



## **WestminsterResearch**

<http://www.westminster.ac.uk/westminsterresearch>

### **Advanced digital predistortion of power amplifiers for mobile and wireless communications.**

**Dmytro Bondar**

School of Electronics and Computer Science

This is an electronic version of a PhD thesis awarded by the University of Westminster. © The Author, 2009.

This is an exact reproduction of the paper copy held by the University of Westminster library.

---

The WestminsterResearch online digital archive at the University of Westminster aims to make the research output of the University available to a wider audience. Copyright and Moral Rights remain with the authors and/or copyright owners.

Users are permitted to download and/or print one copy for non-commercial private study or research. Further distribution and any use of material from within this archive for profit-making enterprises or for commercial gain is strictly forbidden.

---

Whilst further distribution of specific materials from within this archive is forbidden, you may freely distribute the URL of WestminsterResearch:  
(<http://westminsterresearch.wmin.ac.uk/>).

In case of abuse or copyright appearing without permission e-mail [repository@westminster.ac.uk](mailto:repository@westminster.ac.uk)

**ADVANCED DIGITAL PREDISTORTION OF  
POWER AMPLIFIERS FOR MOBILE AND  
WIRELESS COMMUNICATIONS**

DMYTRO BONDAR

A thesis submitted in partial fulfillment of the  
requirements of the University of Westminster for the  
degree of Doctor of Philosophy

September 2009

## **ACKNOWLEDGEMENT**

I would like to thank my director of studies Dr. D. Budimir for his excellent supervision, guidance and encouragement throughout the research work. I am also grateful to my supervisor Dr. A. Tarczynski for his useful suggestions and assistance.

The financial support provided by the University of Westminster is gratefully acknowledged.

To my mother Valentina, who always supported me.

# ABSTRACT

This research work focuses on improving the performances of digital predistorters while maintaining low computational complexity for mobile and wireless communication systems. Initially, the thesis presents the fundamental theory of power amplifiers, overview of existing linearisation and memory-effects compensation techniques and reveals the current issues in the field. Further, the thesis depicts the proposed solutions to the problems, including the developed in-band distortion modelling technique, model extraction methods, memoryless digital predistortion technique based on distortion components iterative injection, baseband equalisation technique for minimising memory effects, Matlab-ADS co-simulation system and adaptation circuit with an offline training scheme. The thesis presents the following contributions of the research work.

A generalized in-band distortion modelling technique for predicting the nonlinear behaviour of power amplifiers is developed and verified experimentally. Analytical formulae are derived for calculating predistorter parameters.

Two model extraction techniques based on the least-squares regression method and frequency-response analysis are developed and verified experimentally. The area of implementation and the trade-off between the methods are discussed.

Adjustable memoryless digital predistortion technique based on the distortion components iterative injection method is proposed in order to overcome the distortion compensation limit peculiar to the conventional injection techniques.

A baseband equalisation method is developed in order to provide compensation of memory effects for increasing the linearising performance of the proposed predistorter.

A combined Matlab-ADS co-simulation system is designed for providing powerful simulation tools.

An adaptation circuit is developed for the proposed predistorter for enabling its adaptation to environmental conditions.

The feasibility, performances and computational complexity of the proposed digital predistortion are examined by simulations and experimentally. The proposed method is tuneable for achieving the best ratio of linearisation degree to computational complexity for any particular application.

# CONTENTS

|  |              |
|--|--------------|
| <b>ACKNOWLEDGEMENT .....</b>                             | <b>ii</b>    |
| <b>ABSTRACT .....</b>                                    | <b>iii</b>   |
| <b>LIST OF TABLES.....</b>                               | <b>x</b>     |
| <b>LIST OF FIGURES .....</b>                             | <b>xi</b>    |
| <b>LIST OF ABBREVIATIONS .....</b>                       | <b>xxiii</b> |
| <b>1. INTRODUCTION .....</b>                             | <b>1</b>     |
| 1.1. Introduction to Wireless Communication Systems..... | 1            |
| 1.2. Aims and Objectives .....                           | 4            |
| 1.2.1. Aims.....   | 4            |
| 1.2.2. Objectives .....                                  | 5            |
| 1.3. Outline of the Thesis.....                          | 7            |
| 1.4. References.....                                     | 10           |
| <b>2. RF AMPLIFIER THEORY.....</b>                       | <b>12</b>    |
| 2.1. Introduction.....                                   | 12           |
| 2.2. Power Amplifier Fundamentals .....                  | 13           |
| 2.2.1 Amplification Principle.....                       | 14           |
| 2.2.2 Conduction Angle .....                             | 16           |
| 2.2.3 Gain.....  | 17           |
| 2.2.4 1dB Compression Point .....                        | 18           |
| 2.2.5 Second- and Third-Order Intercept Points.....      | 19           |
| 2.2.6 Back-Off .....                                     | 21           |
| 2.2.7 Efficiency .....                                   | 22           |

|           |   |           |
|-----------|---|-----------|
| 2.3.      | Methods of Amplification.....                     | 24        |
| 2.3.1     | Class-A Amplifiers .....                          | 25        |
| 2.3.2     | Class-B Amplifiers.....                           | 27        |
| 2.3.3     | Class-AB Amplifiers.....                          | 29        |
| 2.3.4     | Class-C Amplifiers.....                           | 29        |
| 2.3.5     | Efficiency Trade-Off.....                         | 32        |
| 2.4.      | Nonlinear Analysis.....                           | 33        |
| 2.4.1     | Approaches to Analysis .....                      | 33        |
| 2.4.2     | Nonlinear Analysis using Power Series .....       | 35        |
| 2.4.3     | Two-Tone Test.....                                | 36        |
| 2.4.4     | AM/AM and AM/PM Distortions.....                  | 39        |
| 2.4.5     | Saturation and Desensitisation.....               | 41        |
| 2.4.6     | Error Vector Magnitude .....                      | 41        |
| 2.4.7     | Harmonic Distortion .....                         | 43        |
| 2.4.8     | Intermodulation Distortion.....                   | 45        |
| 2.4.9     | Cross Modulation Distortion.....                  | 47        |
| 2.4.10    | Adjacent Channel Power Ratio.....                 | 48        |
| 2.5.      | Conclusion .....                                  | 50        |
| 2.6.      | References.....                                   | 50        |
| <b>3.</b> | <b>OVERVIEW OF LINEARISATION TECHNIQUES .....</b> | <b>53</b> |
| 3.1.      | Introduction.....                                 | 53        |
| 3.2.      | Feedback Linearisation Techniques.....            | 54        |
| 3.2.1     | RF Feedback .....                                 | 56        |
| 3.2.2     | Modulation Feedback.....                          | 59        |
| 3.2.3     | Polar Loop.....                                   | 60        |
| 3.2.4     | Cartesian Loop .....                              | 61        |
| 3.3.      | Feedforward Linearisation Techniques.....         | 63        |
| 3.4.      | Envelope Elimination and Restoration .....        | 65        |

|           |  |           |
|-----------|--|-----------|
| 3.5.      | Linear Amplification using Nonlinear Components.....     | 67        |
| 3.6.      | Injection Techniques.....                                | 69        |
| 3.7.      | Analogue Predistortion.....                              | 72        |
| 3.8.      | Digital Predistortion.....                               | 75        |
| 3.8.1     | Look-Up-Table Digital Predistortion.....                 | 78        |
| 3.8.2     | Polynomial Digital Predistortion.....                    | 83        |
| 3.8.3     | Baseband Components Injection Digital Predistortion..... | 86        |
| 3.9.      | Conclusion.....  | 89        |
| 3.10.     | References.....  | 90        |
| <b>4.</b> | <b>MEMORY EFFECTS IN POWER AMPLIFIERS.....</b>           | <b>97</b> |
| 4.1.      | Introduction.....  | 97        |
| 4.2.      | Linearisation and Memory Effects.....                    | 97        |
| 4.2.1     | Origins of Memory Effects.....                           | 98        |
| 4.2.2     | Bandwidth-Dependent Behaviour.....                       | 99        |
| 4.3.      | Classification of Memory Effects.....                    | 102       |
| 4.3.1     | Electrical Memory Effects.....                           | 103       |
| 4.3.2     | Thermal Memory Effects.....                              | 106       |
| 4.4.      | Quantifying Memory Effects.....                          | 108       |
| 4.4.1     | Single-Tone Analysis.....                                | 111       |
| 4.4.2     | Two-Tone Analysis.....                                   | 113       |
| 4.4.3     | Digitally Modulated Test.....                            | 115       |
| 4.5.      | Memory Effects Compensation Techniques.....              | 119       |
| 4.5.1     | Impedance Optimisation.....                              | 119       |
| 4.5.2     | Envelope Filtering.....                                  | 122       |
| 4.5.3     | Envelope Injection.....                                  | 124       |
| 4.5.4     | Baseband Equalisation.....                               | 125       |

|      |                  |     |
|------|------------------|-----|
| 4.6. | Conclusion ..... | 127 |
| 4.7. | References.....  | 128 |

**5. NONLINEAR MODELLING OF POWER AMPLIFIERS WITH MEMORY EFFECTS .....131**

|         |  |     |
|---------|--|-----|
| 5.1.    | Introduction.....  | 131 |
| 5.2.    | Overview of Memory Modelling Techniques.....                                 | 132 |
| 5.2.1   | Volterra Series .....  | 134 |
| 5.2.2   | Models Addressing Linear Memory .....  | 136 |
| 5.2.2.1 | Two-Box Wiener Model.....  | 137 |
| 5.2.2.2 | Two-Box Hammerstein Model .....  | 137 |
| 5.2.2.3 | Three-Box Wiener-Hammerstein Model .....                                     | 138 |
| 5.2.3   | Models Addressing Nonlinear Memory.....                                      | 139 |
| 5.2.3.1 | Nonlinear Feedback Model.....  | 140 |
| 5.2.3.2 | Nonlinear Cascade Model.....   | 141 |
| 5.2.3.3 | Parallel Wiener Model .....  | 143 |
| 5.3.    | Memoryless Nonlinear Modelling for the Purpose of Digital Predistortion..... | 144 |
| 5.3.1   | Proposed In-Band Distortion Modelling of Power Amplifiers.....               | 145 |
| 5.3.2   | Model Extraction Methods .....   | 149 |
| 5.3.2.1 | AM/AM Least-Squares Polynomial Approximation.....                            | 150 |
| 5.3.2.2 | Model Extraction using a PA Frequency Response.....                          | 154 |
| 5.3.3   | Experimental Verification of the Proposed Modelling Technique .....          | 156 |
| 5.4.    | Conclusion .....   | 162 |
| 5.5.    | References.....  | 163 |

**6. MEMORYLESS DIGITAL PREDISTORTION TECHNIQUE WITH ENHANCED LINEARISING PERFORMANCES .....167**

|      |                   |     |
|------|-------------------|-----|
| 6.1. | Introduction..... | 167 |
|------|-------------------|-----|

|           |   |            |
|-----------|---|------------|
| 6.2.      | Adjustable Memoryless DPD System.....   | 169        |
| 6.2.1     | Problem Definition.....   | 169        |
| 6.2.2     | Proposed DPD using Distortion Components Iterative Injection .....                  | 171        |
| 6.2.3     | Operation of the Proposed Digital Predistorter.....                                 | 176        |
| 6.2.4     | Computational Complexity and Linearising Performance .....                          | 178        |
| 6.3.      | Verification of the Proposed DPD by Simulations .....                               | 180        |
| 6.3.1     | Simulations Setup and Results for the Direct Injection DPD .....                    | 181        |
| 6.3.2     | Developed Matlab-ADS Co-Simulation System .....                                     | 184        |
| 6.3.3     | Matlab-ADS Simulation Setup for Verifying the Iterative Injection DPD.....          | 186        |
| 6.3.4     | Simulation Results for the Proposed Iterative Injection DPD .....                   | 190        |
| 6.4.      | Experimental Verification and Results .....   | 195        |
| 6.4.1     | Hardware Setup.....   | 196        |
| 6.4.2     | PA Characterisation .....   | 197        |
| 6.4.3     | 5-MHz QPSK Signal Case.....   | 201        |
| 6.4.4     | 3.5-MHz 16-QAM Signal Case .....  | 204        |
| 6.5.      | Conclusion .....  | 207        |
| 6.6.      | References.....   | 208        |
| <b>7.</b> | <b>DIGITAL PREDISTORTION OF POWER AMPLIFIERS WITH IMPROVED MEMORY EFFECTS .....</b> | <b>209</b> |
| 7.1.      | Introduction.....   | 209        |
| 7.2.      | Baseband Equalisation Technique for Compensating Memory Effects .....               | 210        |
| 7.2.1     | Developed Compensation Algorithm .....  | 211        |
| 7.2.2     | Implementation and Computational Complexity.....                                    | 213        |
| 7.3.      | Verification of the Memory Compensation Technique by Simulations .....              | 216        |
| 7.3.1     | Matlab-ADS Co-Simulation Test Bed.....  | 216        |
| 7.3.2     | PA Characterisation .....   | 218        |
| 7.3.3     | Equaliser Coefficient Extraction.....   | 220        |
| 7.3.4     | Simulated Results.....  | 222        |

|           |   |            |
|-----------|---|------------|
| 7.4.      | Adaptation Procedure using Offline Training.....                          | 225        |
| 7.5.      | Experimental Setup.....   | 230        |
| 7.5.1     | Hardware Setup.....   | 230        |
| 7.5.2     | Implemented Predistorter Configuration .....                              | 231        |
| 7.6.      | Experimental Results for a Power Amplifier Exhibiting Memory Effects..... | 234        |
| 7.6.1     | PA Characterisation .....   | 234        |
| 7.6.2     | 5-MHz WCDMA Signal Case .....   | 239        |
| 7.6.3     | 5-MHz 16-QAM Signal Case .....  | 244        |
| 7.7.      | Conclusion .....  | 249        |
| 7.8.      | References.....   | 250        |
| <b>8.</b> | <b>CONCLUSION.....</b>  | <b>252</b> |
| 8.1.      | Thesis Summary.....   | 252        |
| 8.2.      | Originality and Contribution to Knowledge .....                           | 258        |
| 8.2.1     | Original Developments .....   | 258        |
| 8.2.2     | Contributions to Knowledge.....   | 259        |
| 8.3.      | Future Work.....  | 260        |
|           | <b>LIST OF PUBLICATIONS .....</b>   | <b>262</b> |
|           | <b>APPENDIXES.....</b>  | <b>264</b> |
|           | APPENDIX-A: I/Q Generation using Matlab-ADS .....                         | 264        |
|           | APPENDIX-B: Data Sheets for the Power Amplifiers.....                     | 273        |
|           | APPENDIX-C: Experimental Signal Generation .....                          | 275        |

## LIST OF TABLES

|  |     |
|--|-----|
| <b>TABLE 1.1:</b> Wireless technologies  | 3   |
| <b>TABLE 5.1:</b> Element values of the developed series                             | 149 |
| <b>TABLE 5.2:</b> Measured output harmonics at different power levels for ZFL500     | 157 |
| <b>TABLE 5.3:</b> Linear system coefficients based on the measured results           | 158 |
| <b>TABLE 6.1:</b> Computational complexity of the proposed DPD                       | 179 |
| <b>TABLE 6.2:</b> Voltage and power levels for the experiment                        | 204 |
| <b>TABLE 7.1:</b> Number of stored coefficients for the proposed equalisation method | 215 |
| <b>TABLE 7.2:</b> Voltage and power levels for simulations                           | 220 |
| <b>TABLE 7.3:</b> Voltage and power levels for the experiment                        | 244 |

## LIST OF FIGURES

|   |    |
|---|----|
| Figure 1-1: General block diagram of a transceiver  | 3  |
| Figure 2-1: Examples of transfer characteristics: (a) ideal transfer characteristic; (b) real transfer characteristic   | 12 |
| Figure 2-2: The general amplifier circuit   | 13 |
| Figure 2-3: Example of a common-source MOSFET amplifier with a self-bias circuit  | 14 |
| Figure 2-4: Common-source $n$ -channel MOSFET amplifier characteristics showing signal operation: (a) transfer characteristic curve; (b) drain curves                                       | 15 |
| Figure 2-5: Reduced conduction angle waveforms: (a) input voltage waveform; (b) drain current waveform  | 17 |
| Figure 2-6: The measured characteristics of the PA Mini-Circuits ZFL-500 with the 1dB compression point at 9-dBm output power level: a) Output power characteristic; b) Gain characteristic | 19 |
| Figure 2-7: Relations between the output back-off, peak back-off and peak-to-average ratio for power amplifiers   | 22 |
| Figure 2-8: Measured output power and PAE curves for Mini-Circuits ZFL-500  | 24 |
| Figure 2-9: Configuration of a BJT power amplifier  | 25 |
| Figure 2-10: Voltage and current waveforms for a class-A power amplifier  | 26 |

|  |    |
|--|----|
| Figure 2-11: Voltage and current waveforms for a class-B power amplifier   | 27 |
| Figure 2-12: Voltage and current waveforms for a class-C power amplifier   | 29 |
| Figure 2-13: Collector current waveform for a reduced conduction angle amplifier   | 30 |
| Figure 2-14: Efficiency as a function of conduction angle ( $\Theta$ )   | 32 |
| Figure 2-15: Two-tone test in the frequency domain (a) and in the time domain (b)  | 37 |
| Figure 2-16: Frequency-domain response of a nonlinear PA with a two-tone excitation assuming there is no filtering of DC and harmonic components | 38 |
| Figure 2-17: Example of the AM/AM (a) and AM/PM (b) characteristics for a PA   | 40 |
| Figure 2-18: Error vector in a memoryless system   | 42 |
| Figure 2-19: Error vector in a system exhibiting memory effects  | 42 |
| Figure 2-20: Second- and third-harmonic distortions versus input voltage magnitude   | 44 |
| Figure 2-21: Graphical representation of ACPR  | 49 |
| Figure 3-1: General feedback system for a PA   | 55 |
| Figure 3-2: Active feedback linearisation system   | 57 |
| Figure 3-3: Distortion feedback linearisation system   | 58 |
| Figure 3-4: General layout of a modulation feedback system   | 59 |

|  |    |
|--|----|
| Figure 3-5: Polar-loop feedback system   | 60 |
| Figure 3-6: Cartesian-loop feedback system   | 62 |
| Figure 3-7: General layout of a feedforward system   | 63 |
| Figure 3-8: Block diagram of an adaptive feedforward system                                    | 65 |
| Figure 3-9: Envelope elimination and restoration system  | 66 |
| Figure 3-10: Linear amplification using nonlinear components system                            | 67 |
| Figure 3-11: Second-order products injection system  | 69 |
| Figure 3-12: Feedback-based second-order products injection circuit                            | 71 |
| Figure 3-13: Schematic of an analogue predistortion system                                     | 73 |
| Figure 3-14: Operation of a predistortion system   | 73 |
| Figure 3-15: Block diagram of a cubic analogue predistorter                                    | 74 |
| Figure 3-16: General layout of a digital predistortion system                                  | 75 |
| Figure 3-17: General schematic of an adaptive digital predistortion system                     | 77 |
| Figure 3-18: Block diagram of an adaptive LUT-based DPD system                                 | 79 |
| Figure 3-19: Block diagram of an adaptive polynomial DPD system                                | 84 |
| Figure 3-20: Block diagram of a 3 <sup>rd</sup> -order baseband component injection DPD system | 88 |

|   |     |
|---|-----|
| Figure 4-1: Magnitude of the IM3 component: (a) measured experimentally for the PA Mini-Circuits ZFL-500 at a -10 dBm input power level; (b) calculated theoretically based on a polynomial model | 101 |
| Figure 4-2: Matching and biasing circuits' impedances: (a) common-emitter BJT amplifier; (b) common-source MESFET amplifier   | 103 |
| Figure 4-3: Contribution to the final IM3 from spectral components using a cascaded polynomial model  | 105 |
| Figure 4-4: Block diagram of a thermal power feedback   | 107 |
| Figure 4-5: Normalised thermal impedance of a PA integrated circuit versus frequency  | 107 |
| Figure 4-6: Measured asymmetry in the lower and higher IM3 for the PA Mini-Circuits ZFL-500 due to the thermal memory effects   | 108 |
| Figure 4-7: Simulation testbed for investigating PA memory effects using a single- or multi-tone input signals  | 109 |
| Figure 4-8: Sub-circuit for the PA transistor-level model used in simulations   | 110 |
| Figure 4-9: ADS model for Motorola MOSFET MRF9742 active device   | 111 |
| Figure 4-10: Simulated MRF9742 gain dependence on power level for the frequency range of 835...865 MHz  | 112 |
| Figure 4-11: Simulated MRF9742 gain variations over modulation frequency due to memory effects  | 113 |
| Figure 4-12: Simulated MRF9742 phase variations over modulation frequency due to memory effects   | 113 |

|   |     |
|---|-----|
| Figure 4-13: Simulated MRF9742 IM3 magnitude variations over modulation frequency and output power due to PA memory effects   | 114 |
| Figure 4-14: Simulated MRF9742 IM3 phase variations over modulation frequency and output power due to PA memory effects   | 115 |
| Figure 4-15: Main circuit for the Matlab-ADS connected simulation   | 116 |
| Figure 4-16: Normalised constellation diagram of a 16-QAM signal after passing the PA in a linear mode at -5 dBm input power level. The distortion is caused only by memory effects   | 118 |
| Figure 4-17: Normalised constellation diagram of a 16-QAM signal after passing the PA in a weakly non-linear mode at 13 dBm input power level. The distortion is caused by the nonlinear transfer function and memory effects | 118 |
| Figure 4-18: Norton equivalent for the active device nonlinear circuit  | 120 |
| Figure 4-19: Test setup for optimising envelope impedance   | 121 |
| Figure 4-20: A general block diagram of the envelope filtering technique  | 122 |
| Figure 4-21: Examples of the symmetrical (a)-(b) and asymmetrical (c)-(d) memory effects  | 123 |
| Figure 4-22: A general block diagram of the envelope injection technique  | 125 |
| Figure 5-1: Volterra-series representation of a system  | 135 |
| Figure 5-2: Wiener memory nonlinear model   | 137 |
| Figure 5-3: Hammerstein memory nonlinear model  | 138 |
| Figure 5-4: Wiener-Hammerstein memory nonlinear model   | 139 |

|  |     |
|--|-----|
| Figure 5-5: Nonlinear feedback structure of a PA for modelling the nonlinear behaviour and the thermal and electrical memory effects                               | 140 |
| Figure 5-6: Nonlinear cascade model of a PA representing the nonlinear behaviour and the thermal and electrical memory effects                                     | 142 |
| Figure 5-7: Parallel Wiener model of a PA representing the nonlinear behaviour and the thermal and electrical memory effects                                       | 143 |
| Figure 5-8: AM/AM characteristic used to extract the memoryless fundamental-frequency model for a MOSFET PA  | 151 |
| Figure 5-9: Frequency response of a PA with the 5 <sup>th</sup> -order nonlinearity  | 155 |
| Figure 5-10: Experimental test bench   | 156 |
| Figure 5-11: Comparison of the voltage curves: measured experimentally and calculated analytically using the LSR model extraction method for the PA (ZFL500)       | 159 |
| Figure 5-12: Measured frequency response of the PA (ZFL500) at -8 dBm input power  | 160 |
| Figure 5-13: Comparison of the voltage curves: measured experimentally and calculated analytically using the frequency-response model extraction method for ZFL500 | 160 |
| Figure 5-14: Simulated 16-QAM output spectrum for the developed ZFL500 model   | 161 |
| Figure 5-15: Measured 16-QAM output spectrum for ZFL500  | 161 |

|   |     |
|---|-----|
| Figure 6-1: Block diagram of the proposed digital baseband predistorter using iterative injection of the in-band distortion components  | 177 |
| Figure 6-2: Hardware implementation of the simplified for weakly nonlinear systems proposed digital baseband predistorter using direct generation of the injected in-band distortion components         | 178 |
| Figure 6-3: Dependence of the spectral regrowth suppression on the number of injections for a 5-MHz 16-QAM signal   | 180 |
| Figure 6-4: Simulation test bed for verifying performances of the predistorter with direct injection of the distortion components   | 181 |
| Figure 6-5: Simulated output power and gain versus input power for the considered PA  | 182 |
| Figure 6-6: Simulated spectral re-growth without and with the proposed DPD using direct injection of the distortion components: (a) QPSK input signal; (b) 16-QAM input signal; (c) 64-QAM input signal | 183 |
| Figure 6-7: General functional diagrams for the Matlab-ADS co-simulation systems: (a) generating a digital baseband signal in Matlab; (b) generating a final RF signal in Matlab                        | 185 |
| Figure 6-8: Main circuit for the designed Matlab-ADS co-simulation system   | 187 |
| Figure 6-9: ADS analogue sub-circuit for the I/Q modulator  | 188 |
| Figure 6-10: ADS analogue sub-circuit for the main PA   | 189 |
| Figure 6-11: Functional diagram for the Matlab signal source  | 190 |

|  |     |
|--|-----|
| Figure 6-12: Simulated output power and gain versus input power for the considered PA  | 190 |
| Figure 6-13: Spectral re-growth improvement for a QPSK signal: (a) without DPD; (b) proposed DPD with 3 injections; (c) proposed DPD with 6 injections   | 191 |
| Figure 6-14: Spectral re-growth improvement for a 256-OFDM 64-QAM signal: (a) without DPD; (b) proposed DPD with 1 injection; (c) proposed DPD with 3 injections; (d) proposed DPD with 6 injections | 192 |
| Figure 6-15: Spectral re-growth improvement for a 7-MHz 256-OFDM 16-QAM signal: (a) without DPD; (b) proposed DPD with 6 injections  | 193 |
| Figure 6-16: ACPR for a 7-MHz 256-OFDM 16-QAM signal at 8-MHz upper and lower offsets without DPD and with the proposed DPD with 6 iterations  | 193 |
| Figure 6-17: EVM verses output power for a 7-MHz 256-OFDM 16-QAM signal without DPD and with the proposed DPD with 6 iterations  | 193 |
| Figure 6-18: Demodulated 16-QAM constellation without DPD ( $P_{in} = -3$ dBm)   | 194 |
| Figure 6-19: Demodulated 16-QAM constellation with 6-iterations DPD ( $P_{in} = -3$ dBm)   | 194 |
| Figure 6-20 Experimental setup for verifying digital predistorters: (a) Functional diagram; (b) Experimental setup; (c) Hardware test-bench  | 196 |
| Figure 6-21: Measured output power and gain versus input power for the considered PA   | 198 |
| Figure 6-22: Measured gain of the PA (ZFL-500) at the input power level of -10 dBm   | 199 |

|   |     |
|---|-----|
| Figure 6-23: Measured IM3 of the PA at the input power level of -10 dBm   | 200 |
| Figure 6-24: Measured gain characteristic of the PA ZFL-500 versus output power and modulation frequency  | 200 |
| Figure 6-25: Measured IM3 characteristic of the PA ZFL-500 versus output power and modulation frequency   | 201 |
| Figure 6-26. Measured output spectra of a 5-MHz QPSK signal at the output of the PA ZFL-500: (a) without DPD; (b) with the proposed DPD using 3 injections                                    | 203 |
| Figure 6-27. Measured ACPRs for 7-MHz offsets of a 5-MHz QPSK signal at the output of the PA ZFL-500 without DPD and with the proposed DPD using 3 injections                                 | 204 |
| Figure 6-28. Measured output spectra of a 3.5-MHz 16-QAM signal at the output of the PA ZFL-500: (a) without DPD; (b) conventional baseband DPD; (c) proposed baseband DPD using 2 injections | 206 |
| Figure 6-29. Measured ACPRs for 5-MHz offsets of a 3.5-MHz 16-QAM signal at the output of the PA ZFL-500 without DPD and with the proposed DPD using 2 injections                             | 206 |
| Figure 7-1: Block diagram of the developed baseband equalisation method   | 213 |
| Figure 7-2: General block diagram of the proposed memory-compensating method  | 214 |
| Figure 7-3: Block diagram of the proposed memory-compensating method for an OFDM system   | 215 |
| Figure 7-4: Main circuit for the designed Matlab-ADS co-simulation system   | 216 |

|  |     |
|--|-----|
| Figure 7-5: ADS analogue sub-circuit for the PA  | 217 |
| Figure 7-6: ADS sub-circuit for the PA transistor-level model  | 217 |
| Figure 7-7: Simulated output power and gain versus input power for the considered PA   | 218 |
| Figure 7-8: Simulated MRF9742 gain variations over modulation frequency due to memory effects  | 219 |
| Figure 7-9: Simulated MRF9742 phase variations over modulation frequency due to memory effects   | 219 |
| Figure 7-10: Magnitude of the normalised frequency response $H_{\text{NORM}}(f_k, P_{\text{IN}})$ for three power levels   | 221 |
| Figure 7-11: Phase of the normalised frequency response $H_{\text{NORM}}(f_k, P_{\text{IN}})$ for three power levels   | 221 |
| Figure 7-12: Demodulated constellation for the considered PA (MRF9742) without compensation of memory effects at $P_{\text{in}} = 0$ dBm (EVM = 5.3 %)                       | 222 |
| Figure 7-13: Demodulated constellation for the considered PA (MRF9742) using the developed baseband equalisation method at $P_{\text{in}} = 0$ dBm (EVM = 0.97 %)            | 223 |
| Figure 7-14: EVM versus input power with and without pre-equalisation for the considered PA exited with a 3.5-MHz 256-OFDM 16-QAM signal                                     | 224 |
| Figure 7-15: ACPRs at 4-MHz higher and lower offsets versus input power with and without pre-equalisation for the considered PA exited with a 3.5-MHz 256-OFDM 16-QAM signal | 225 |

|   |     |
|---|-----|
| Figure 7-16: Close-loop adaptive implementation of the proposed predistorter using a feedback-based offline training scheme                                 | 227 |
| Figure 7-17: Experimental setup for verifying digital predistorters: (a) Functional diagram; (b) Experimental setup; (c) Hardware test-bench                | 230 |
| Figure 7-18: Block diagram of the proposed predistorter   | 233 |
| Figure 7-19: Measured output power and gain versus input power for the considered PA ZHL-1042J at 2.1 GHz   | 235 |
| Figure 7-20: Measured output power and gain versus input power for the considered PA ZHL-1042J at 3.5 GHz   | 235 |
| Figure 7-21: Comparison of the measured and 5 <sup>th</sup> -order polynomial model transfer characteristics for the DUT ZHL-1042J at 2.1 GHz               | 236 |
| Figure 7-22: Comparison of the measured and 5 <sup>th</sup> -order polynomial model transfer characteristics for the DUT ZHL-1042J at 3.5 GHz               | 237 |
| Figure 7-23: Comparison of the measured and 7 <sup>th</sup> -order polynomial model transfer characteristics for the DUT ZHL-1042J at 3.5 GHz               | 238 |
| Figure 7-24: Measured gain of the PA ZHL-1042J versus modulation frequency  | 238 |
| Figure 7-25: Measured higher and lower IM3 of the PA ZHL-1042J versus modulation frequency at the input power level of -3 dBm                               | 239 |
| Figure 7-26: Magnitude of the normalised frequency response $H_{\text{NORM}}(f, P_{\text{IN}})$ for the considered PA ZHL-1042J at -3 dBm input power level | 240 |

Figure 7-27: Phase of the normalised frequency response  $H_{\text{NORM}}(f, P_{\text{IN}})$  for the considered PA ZHL-1042J at -3 dBm input power level 240

Figure 7-28: Measured output spectra of a 5-MHz WCDMA signal with a 2.1 GHz carrier at the output of the PA ZHL-1042J: (a) without DPD; (b) conventional DPD; (c) proposed DPD using 3 injections and pre-compensation of the memory effects 243

Figure 7-29: Measured ACPRs for 7-MHz offsets of a 5-MHz WCDMA signal with 2.1 GHz carrier at the output of the PA ZHL-1042J without DPD and with the proposed DPD using 3 injections and pre-compensation of the memory effects 243

Figure 7-30: Magnitude of the normalised frequency response  $H_{\text{NORM}}(f, P_{\text{IN}})$  for the considered PA ZHL-1042J at three input power levels 245

Figure 7-31: Phase of the normalised frequency response  $H_{\text{NORM}}(f, P_{\text{IN}})$  for the considered PA ZHL-1042J at three input power levels 245

Figure 7-32. Measured output spectra of a 5-MHz 16-QAM signal at the output of the PA ZHL-1042J at 3.5 GHz: (a) without DPD; (b) proposed baseband DPD using 3 injections and pre-compensation of the memory effects 248

Figure 7-33. Measured ACPRs for 7-MHz offsets of a 5-MHz 16-QAM signal at the output of the PA ZHL-1042J without DPD and with the proposed DPD using 3 injections and pre-compensation of the memory effects 248

## **LIST OF ABBREVIATIONS**

ACPR - Adjacent Channel Power Ratio  
ACPRH - ACPR of the Higher Adjacent Channel  
ACPRL - ACPR of the Lower Adjacent Channel  
ADC - Analogue-to-Digital Converter  
ADS - Advanced Design System  
AGC - Automatic Gain Control  
AM - Amplitude Modulation  
ANN - Artificial Neural Network  
ARMA - Auto-Regressive Moving Average  
BJT - Bipolar Junction Transistor  
BPF - Band-Pass Filters  
CDMA - Code Division Multiple Access  
CM - Cross Modulation  
CW - Carrier Wave  
DAC - Digital-to-Analogue Converter  
DC - Direct Current  
DFT - Discrete Fourier Transform  
DPD - Digital Predistortion  
DSP - Digital Signal Processing  
DSSS - Direct Sequence Spread Spectrum  
DUT - Device Under Test  
EER - Envelope Elimination and Restoration  
ESG - Electronic Signal Generator  
EVM - Error Vector Magnitude  
FDMA - Frequency Division Multiple Access  
FFT - Fast Fourier Transform  
FIR - Finite Impulse Response  
GSM - Group System Mobile  
HD - Harmonic Distortion  
HD2 - Second-Order Harmonic Distortion  
HD3 - Third-Order Harmonic Distortion

I-Component - In-Phase Component  
IDFT - Inverse Discrete Fourier Transform  
IF - Intermediate Frequency  
IFFT - Inverse Fast Fourier Transform  
IIR - Infinite Impulse Response  
IM - Intermodulation  
IM2 - Second-Order Intermodulation  
IM3 - Third-Order Intermodulation  
IM3H - IM3 of the Higher Intermodulation Product  
IM3L - IM3 of the Lower Intermodulation Product  
IMD - Intermodulation Distortion  
IS-95 - Interim Standard 95  
ITU - International Telecommunication Union  
LAN - Local Area Network  
LINC - Linear Amplification using Nonlinear Components  
LMDS - Local Multipoint Distribution Systems  
LMMDS - Low-Power MMDS  
LNA - Low Noise Amplifier  
LO - Local Oscillator  
LPF - Low-Pass Filter  
LSR - Least-Squares Regression  
LUT - Look-Up-Table  
MMDS - Multichannel Multipoint Distribution Systems  
MOSFET - Metal Oxide Semiconductor Field-Effect Transistor  
NF - Noise Floor  
OBO - Output Back-Off  
OFDM - Orthogonal Frequency Division Multiplexing  
PA - Power Amplifier  
PAE - Power-Added Efficiency  
PAN - Personal Area Network  
PAR - Peak-to-Average Ratio  
PBO - Peak Back-Off  
PC - Personal Computer  
PD - Predistortion

PM - Phase Modulation  
PNA - Performance Network Analyser  
PSTN - Public Switched Telephone Network  
Q-Component - Quadrature Component  
QAM - Quadrature Modulation  
QM - Quadrature Modulator  
QPSK - Quadrature Phase Shift Keying  
RCE - Received Constellation Error  
RF - Radio Frequency  
RFC - Radio Frequency Choke  
RMS - Root Mean Square  
SOI - Second-Order Intercept  
TDMA - Time Division Multiple Access  
THD - Total Harmonic Distortion  
TOI - Third-Order Intercept  
TPF - Thermal Power Feedback  
TWT - Travelling Wave Tube  
UMTS - Universal Mobile Telecommunication System  
VCO - Voltage-Controlled Oscillator  
VSA - Vector Signal Analyzer  
WCDMA - Wideband CDMA  
WiMAX - Worldwide Interoperability for Microwave Access

# 1. Introduction

## 1.1. Introduction to Wireless Communication Systems

Wireless communication has been an area of intensive research for many decades. An explosive demand for portable connectivity driven by cellular systems and wireless data applications has stipulated rapid progress in the area. Overall, wireless communication systems can be roughly classified as cellular, fixed wireless, Local Area Networks (LANs), Personal Area Networks (PANs) and ad hoc devices [1.1]-[1.3].

Current cellular telephony includes analogue first-generation (1G) systems based on Frequency Division Multiple Access (FDMA), digital second-generation (2G) systems further divided into European Group System Mobile (GSM) standard based on combined Time and Frequency Division Multiple Access (FDMA/TDMA) and the USA Interim Standard 95 (IS-95) based on Code Division Multiple Access (CDMA), and third-generation (3G) Universal Mobile Telecommunication System (UMTS) based on a hybrid TDMA/CDMA technology.

In GSM, a radio channel at 900-MHz carrier with 200 kHz bandwidth is shared between eight users using TDMA. As several radio channels are allocated to a cell, the system utilises both FDMA and TDMA.

In CDMA, the users share the same radio channel and time intervals, but have different codes. Under IS-95, the bandwidth increases to 1.25 MHz by a long code, whereas the RF carrier frequency is around 1900 MHz.

In UMTS, CDMA-2000 has been employed in the USA and W-CDMA in the rest of the world. The RF operating frequency is in the range of 1.9-2.5 GHz. W-CDMA utilises a 5-MHz channel bandwidth, which is much higher than the CDMA-2000 carrier size of 1.25 MHz. The wider bandwidth serves to enhance performances in a multi-path environment [1.3]-[1.4].

Fixed wireless communication systems aimed mainly at providing a connection from Public Switched Telephone Networks (PSTN) to homes or businesses include Multichannel Multipoint Distribution Systems (MMDS), Low-Power MMDS (LMMDS) and Local Multipoint Distribution Systems (LMDS) [1.5]-[1.7]. MMDS retransmits programs on a point-to-multipoint basis. The system utilises different

frequency bands, e.g. 2 GHz, 3.6-3.9 GHz, 12 GHz, for the channel distribution. LMDS is intended for data, internet and video transmissions in the 25 GHz and higher frequencies.

LAN networks including the IEEE 802.11 and HiperLAN standards are typically comprised on a cellular configuration. Various spectrums, data rates and frequency selections are used in the LAN systems. For instance, 802.11 and 802.11b utilise 2.4 GHz carriers offering 1.2 Mbps and 5 Mbps maximum user data rates respectively, whereas 802.11a and HiperLAN2 operate at 5 GHz providing 32 Mbps maximum data rates for users [1.2]-[1.3]. The first two standards incorporate Direct Sequence Spread Spectrum (DSSS), whereas the last two use Orthogonal Frequency Division Multiplexing (OFMD).

PAN systems include the devices a person may carry with, like a mobile phone, laptop or personal stereo [1.2]. These are the short-range devices facing the requirements of low cost, small size and low power consumption. Among them is the Bluetooth standard operating at the centre frequency of 2.45 GHz with a 1-MHz transmission bandwidth, which can be selected by the device in the range of 80 MHz depending on the environmental conditions. The standard uses a TDMA framing structure for the voice and data transmission.

The ad hoc group includes uni-purpose everyday-use devices like garage door opener, television remote control, car alarm control etc. The devices typically utilise unlicensed spectrum with small transmission power.

As all the wireless systems use the common medium, an issue of spectrum allocation arises. Table 1.1 presents the modulation formats, centre frequencies and frequency bands for some commonly used wireless standards.

In a wireless communication system, the key role plays the circuitry, which assigns the appropriate frequency to the signal and increases its power to the necessary level before transmitting and after receiving. The circuitry is called a transceiver/receiver (transceiver) front-end. Designing of transceivers with high efficiency and linearity is a major task for wireless engineers [1.8]. Figure 1-1 presents a generalised block diagram of a transceiver.

**TABLE 1.1:** Wireless technologies

| Standard  | Modulation Format              | Multiple Access | Centre Frequency              | Frequency Band                 |
|-----------|--------------------------------|-----------------|-------------------------------|--------------------------------|
| GSM       | GMSK                           | FDMA/TDMA       | 900 MHz                       | 800 kHz                        |
| IS-95     | QPSK                           | CDMA            | 450 MHz                       | 1.25 MHz                       |
| CDMA-2000 | QPSK                           | CDMA            | 2.1 GHz                       | 1.25 MHz                       |
| W-CDMA    | QPSK                           | CDMA            | 1.9 - 2.1 GHz                 | 5-MHz                          |
| WiMAX     | BPSK<br>QPSK<br>16QAM<br>64QAM | OFDM            | 2.3 GHz<br>2.5 GHz<br>3.5 GHz | 1.25-20 MHz<br>(3.5, 5, 7 MHz) |
| WLAN      | BPSK<br>QPSK<br>16QAM<br>64QAM | CSMA-CA         | 2.4 GHz                       | 10 MHz<br>25 MHz               |
| Bluetooth | GFSK<br>QPSK                   | TDMA            | 2.4 GHz                       | 1 MHz                          |

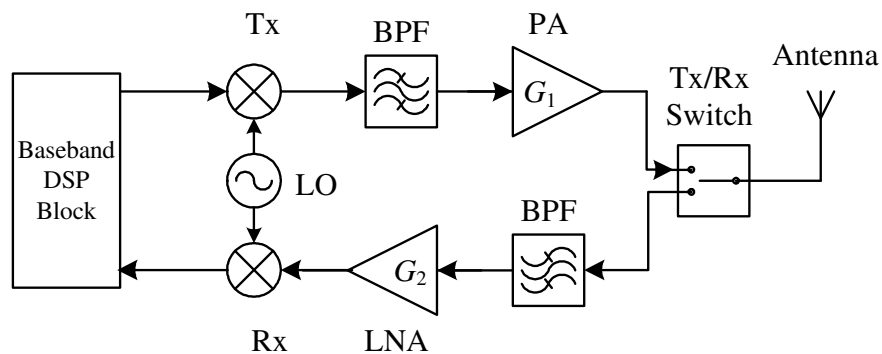


Figure 1-1: General block diagram of a transceiver

As can be seen from the Figure, the transceiver includes a baseband Digital Signal Processing (DSP) block, modulators, Band-Pass Filters (BPF), a Power Amplifier (PA) in the Transmitter (Tx) part, which rises the signal power to the appropriate level for transmission through the propagation medium, a Low Noise Amplifier (LNA) in the Receiver (Rx) part, which rises the received signal to the necessary power level for demodulating and processing.

As discussed above, the most challenging issue in a transceiver design is achieving its high linearity and efficiency. The efficiency can be increased if the PA operates in a nonlinear mode. Therefore, the problem of linearisation is becoming extremely important. The focus of this thesis is the development of advanced linearisation techniques, which would bring significant improvements in the linearity while maintaining a low circuit size, complexity and power consumption.

## **1.2. Aims and Objectives**

Current research work aims at developing digital predistorters with enhanced linearising performances for mobile and wireless communications. This goal will be achieved by analysing existing predistorters, studying phenomena that limit their functioning and developing methods to overcome them. The whole task can be divided into two major categories: attaining enhanced linearising performance for a power amplifier in compression mode and maintaining this performance constant over a high frequency band, which is typical for modern wireless communications. Achieving these targets will result in improving the Intermodulation Distortion (IMD) performance, reducing the spectral re-growth, decreasing the Adjacent Channel Power Ratio (ACPR) and Error Vector Magnitude (EVM), and improving the constellation diagram.

### **1.2.1. Aims**

- Distortion analysis and behaviour modelling of power amplifiers including a memoryless non-linear modelling and investigation of the impact of memory effects.
- Development of a new baseband digital predistortion system for memoryless non-linearity compensation with enhanced linearising performances.
- Development of a digital pre-compensation system for minimising memory effects of power amplifiers.
- Designing a combined simulation system using the software products MathWorks Matlab and Agilent ADS for advanced simultaneous simulation of

the Digital Signal Processing (DSP) and Radio Frequency (RF) parts of the transmitter.

- Practical implementation and experimental validation of the proposed digital predistortion method with compensation of memory effects using different signal types and power amplifiers.

### **1.2.2. Objectives**

1. Study the nonlinear analysis of power amplifiers and applying models for analytical prediction of distortion behaviour.
2. Provide a literature overview on recent advancements in the area of predistortion linearisation and revealing the unresolved problems in this field.
3. Review modelling techniques for representing memory effects and nonlinear behaviour of PAs, particularly Wiener, Hammerstein and polynomial models.
4. Develop an in-band distortion modelling technique for fast and convenient analytical prediction of the PA distortion behaviour and calculating the predistorter parameters.
5. Develop methods for extracting PA polynomial models from instantaneous nonlinear behaviour based on the least-squares regression method and frequency response analysis.
6. Experimentally verify the polynomial model extraction methods with a real power amplifier using analog signal generator Hewlett Packard A6488, Electronic Signal Generator (ESG) Agilent E4433B, spectrum analyzer Hewlett Packard 8594EM and Vector Signal Analyzer (VSA) Agilent E4406A.
7. Provide a comparative overview of existing linearisation techniques.
8. Develop a new memoryless Digital Predistortion (DPD) with enhanced linearising performances based on iterative injecting of distortion components into the original baseband signal.
9. Investigate computational complexity and linearising performances of the proposed DPD technique.

10. Design a Matlab-ADS co-simulation system for advanced simultaneous simulation of transistor-level PA circuits in ADS and DSP-controlled signal sources in Matlab, taking advantages of both the software products (the digital predistortion system is implemented in Matlab and a transistor-level power amplifier model is designed in ADS).
11. Verify the proposed DPD method by simulations in Agilent ADS and the developed Matlab-ADS co-simulation system with different types of signals, such as QPSK, 16-QAM, 64-QAM, 256-OFDM 64-QAM, and 256-OFDM 16-QAM.
12. Implement and experimentally verifying the proposed memoryless DPD method with a real power amplifier Mini-Circuits ZFL-500 and different types of signals, particularly 5-MHz QPSK and 3.5-MHz 16-QAM cases.
13. Study memory effects of power amplifiers, their causes and influence on IMD and frequency-dependent distortions.
14. Quantify PA memory effects by different methods, including a single-tone test, two-tone test and digitally modulated signal test.
15. Provide a comparative overview of techniques used to compensate for memory effects.
16. Develop a baseband equalisation technique for minimising memory effects in wideband wireless transmitters.
17. Verify the proposed memory effects compensation method by Matlab-ADS co-simulation.
18. Investigate the tunability of the proposed linearisation technique and optimising the DPD system for the best ratio of linearisation degree to computational complexity.
19. Develop an offline training scheme for providing adaptation of the proposed predistorter to environmental conditions.
20. Implement the complete predistorter including the memoryless DPD and memory effects compensating parts for linearising a nonlinear PA exhibiting memory effects.

21. Experimentally verify the complete DPD system with Mini-Circuits ZHL-1042J power amplifier and different types of signals, particularly 5-MHz WCDMA at 2.1 GHz and 5-MHz 16-QAM at 3.5 GHz cases.

### **1.3. Outline of the Thesis**

Recent development of wireless and mobile communication systems with high data rates and advanced modulation schemes imposes exacting requirements on the electronic devices. Particularly, linearity and efficiency of wireless transmitters is a key issue for providing users with required quality and range of services. As the efficiency and linearity are mutually exclusive characteristics, the common practice is to enhance the efficiency at the price of linearity and to provide linearisation by an external unit. Therefore, linearisation of wireless transmitters is becoming a primary concern for the design of wireless and mobile communication systems. This research work concentrates on the topic of linearising wireless transmitters by digital methods, which are cost effective, small size, easily integrated, tuneable and maintain high overall efficiency of the system. The thesis presents the work carried out over the period of three years aimed at contributing to the development of mobile and wireless technology. The thesis is organised as follows:

Chapter 2 covers the general theory of RF amplifiers, including PA fundamentals, traditional methods of amplification and nonlinear analysis. Definitions of PA parameters and characteristics are given and analytical relationships between them derived. Methods of amplification are discussed, while the trade-off between efficiency and linearity is revealed. An overview of approaches to nonlinear analysis is carried out. A comprehensive theoretical nonlinear analysis of power amplifiers using power series is provided. The main nonlinear measures and characteristics are defined in the Chapter.

Chapter 3 presents a comparative overview of existing linearisation techniques including the feedback-based methods, feedforward technique, Envelope Elimination and Restoration (EER), Linear Amplification using Nonlinear Components (LINC),

injection techniques, analogue predistortion and digital predistortion. The theoretical concept, main advantages and drawbacks of each of the linearisation technique are presented and discussed. The most commonly used digital predistortion methods are depicted in the Chapter. The recent developments and existing problems in the area of predistortion linearisation are highlighted.

Chapter 4 concentrates on memory effects in power amplifiers, which traditionally degrade performances of predistortion linearisers. Initially, the physical reasons behind memory effects are discussed, which categorise the phenomena into electrical and thermal memory effects. Then, classification of memory effects and their impact on PA frequency-dependent behaviour for narrowband and wideband communication systems are presented. Further, the Chapter provides an overview and depicts practical implementation of the methods used to quantify memory effects in power amplifiers. Finally, a comparative overview of memory compensation techniques is presented in the Chapter, including the impedance optimisation, envelope filtering, envelope injection and baseband equalisation methods.

Chapter 5 is dedicated to the issue of nonlinear modelling of power amplifiers with memory effects. Initially, a comprehensive overview of techniques used for modelling memory nonlinear behaviour is presented, including the Volterra series; the models addressing linear memory, which are a two-box Wiener, two-box Hammerstein and three-box Wiener-Hammerstein models; and the models addressing nonlinear memory, which are a nonlinear feedback, nonlinear cascade and parallel Wiener models. Further, an advanced memoryless nonlinear modelling technique is developed with the aim to simplify and generalise the process of PA characterisation, analytical prediction of its distortion behaviour and calculating the predistorter parameters. The proposed generalised in-band distortion modelling technique is presented, discussed and verified experimentally with different signal types. Two model extraction methods based on AM/AM least-squares polynomial regression approximation and PA instantaneous frequency response analysis are developed. The feasibility and accuracy of the proposed model extraction methods are verified experimentally. The trade-off between the model accuracy and complexity/time consumption of the extraction methods is revealed and discussed.

---

Chapter 6 presents the proposed adjustable memoryless digital predistortion technique based on distortion components iterative injection. The theoretical concept of the proposed DPD technique and verification of its feasibility and linearising performances by simulations and experiments are presented in the Chapter. Initially, an existing problem of limited linearising performance in injection techniques is discussed and defined mathematically. Then, the proposed solution for overcoming the distortion compensation limit by iterative injection of distortion components into the original baseband signal is described mathematically. The practical implementation of the proposed DPD technique in a direct and iterative format is presented and discussed. Further, the computational complexity and corresponding linearising performance are analysed. The trade-off between the computational complexity and linearising performance for the proposed method is quantified and discussed. The adjustability of the DPD system for a particular application is demonstrated. Further, the proposed digital predistortion technique is verified by simulations with different types of signals including QPSK, 16-QAM, 64-QAM, 256-OFDM 64-QAM, and 256-OFDM 16-QAM cases. A developed Matlab-ADS co-simulation system providing powerful tools for simultaneous simulation of the DSP part of a transmitter in Matlab and the RF subsystem in ADS is presented in the Chapter. Different implementation layouts for the co-simulation system are developed for different applications. Further, the simulation results are presented demonstrating a high linearising performance of the proposed method. Finally, the Chapter presents experimental setup and measured results for verifying the feasibility and linearising performances of the proposed DPD. The hardware setup is described and a PA characterisation procedure is demonstrated. The measured results are presented for 5-MHz QPSK and 3.5-MHz 16-QAM cases, which show high performances and reasonably low computational complexity of the method compared to the conventional DPD.

Chapter 7 presents the proposed memory effects compensation technique based on the adaptive baseband equalisation method and demonstrates the implementation of the complete DPD system. The theoretical concept of the proposed equalisation technique and verification of its feasibility and linearising performances by simulations are presented in the first part of the Chapter. Initially, the proposed compensation algorithm is described mathematically and its implementation and computational complexity are analysed. The process of PA characterisation and quantification of the memory effects

is described and demonstrated. Also, the equaliser coefficients extraction procedure is discussed. Further, the developed Matlab-ADS co-simulation system is utilised for verifying the proposed memory effects compensation technique by simulations. The simulated results with a 256-OFDM 16-QAM signal are presented, which demonstrate a high distortion compensation performance of the method. The second part of the Chapter presents the implementation and verification of the complete predistortion system developed during the research work. A close-loop and open-loop implementations of the proposed digital predistorter are depicted. An adaptation circuit based on the offline training scheme is developed for providing adaptation of the predistorter to environmental conditions, such as sample deviations, temperature variations, or aging. Further, experimental setup and results are presented for verifying the feasibility and performances of the complete DPD system including the proposed iterative injection and memory-compensating techniques. The hardware setup and the implemented predistorter configuration are described. The experimental results with a nonlinear PA exhibiting memory effects are presented. The PA characterisation and measured linearising performances of the proposed DPD system with improved memory effects are presented for 5-MHz WCDMA at 2.1 GHz and 5-MHz 16-QAM at 3.5 GHz cases.

Chapter 8 presents the overall conclusions of the research work, including the thesis overview, summary of original developments and contributions to knowledge followed by the suggested directions for the future work.

#### **1.4. References**

- [1.1] D. Tse and P. Viswanath, *Fundamentals of Wireless Communication*, Cambridge University Press, 2005, ISBN 0521845270.
- [1.2] W. Webb, *The Future of Wireless Communication*, Artech House, 2001, ISBN 1580532489.
- [1.3] A. Goldsmith, *Wireless Communications*, Cambridge University Press, 2005, ISBN 0521837162.

- [1.4] A. Hussain, *Advance RF Engineering for Wireless Systems and Networks*, John Wiley, New Jersey, 2005, ISBN 0471674214.
- [1.5] E. Bostick, G. Bostick, *The basic Description of MMDS Television Systems*, Electric Press, New York, 1995, ISBN 1888552026.
- [1.6] P. M. Shankar, *Introduction to Wireless Systems*, John Wiley & Sons, Inc., 2002, ISBN 0471321672.
- [1.7] W. E. Evans, K. G. Balb, “Application Consideration for Low-Power MMDS”, *Private cable magazine (USA) and Cable communications (Canada)*, October 1991.
- [1.8] Y. Sun, *Wireless Communication Circuits and Systems*, IEE Press, London, UK, 2004, ISBN 0852964439.

## 2. RF AMPLIFIER THEORY

### 2.1. Introduction

An amplifier is an electronic device used to increase the strength of the signal fed into it. A Power Amplifier (PA) is an amplifier that is usually the final amplification stage and is designed to give a signal the necessary power for transmission via a propagation medium.

An ideal PA would have an output signal equal to a scalar multiple of the input signal, i.e. a linear transfer characteristic. For such a PA, the input and output voltages are connected using a relationship:

$$V_{OUT}(t) = K_1 \cdot V_{IN}(t), \quad (2.1)$$

where  $K_1$  is the voltage gain of the PA. An example of an ideal transfer characteristic is illustrated in Figure 2-1.

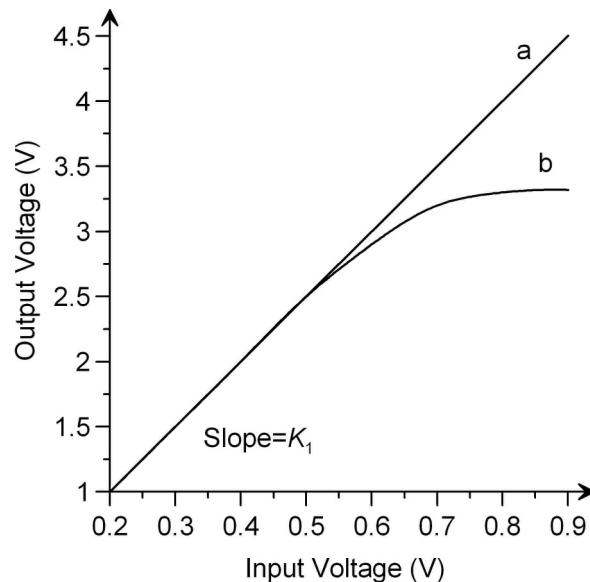


Figure 2-1: Examples of transfer characteristics: (a) ideal transfer characteristic; (b) real transfer characteristic

The real transfer characteristic of a PA differs from the ideal one by having a compression region, where the output voltage does not increase or increase slightly with the increase of the input voltage. Figure 2-1 (b) shows a real transfer characteristic with two regions: a linear region, where the transfer characteristic is close to the ideal; and a compression region, where the output voltage is compressed and not amplified linearly.

## 2.2. Power Amplifier Fundamentals

A typical amplifier as shown in Figure 2-2 consists of an active device and input and output matching circuits, which are necessary to transform the input and output impedances of the active device  $Z_{IN}$  and  $Z_{OUT}$  into the source and load impedances  $Z_S$  and  $Z_L$  respectively [2.1].

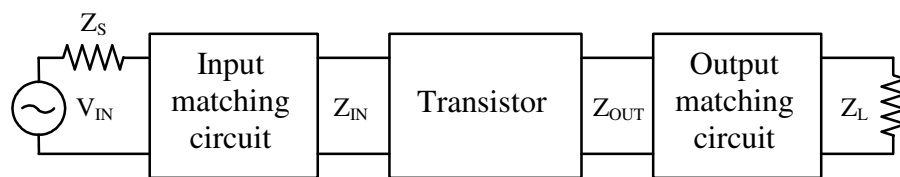


Figure 2-2: The general amplifier circuit

At present, power amplifiers are usually based on transistor active devices. Most commonly used types of transistors are Bipolar Junction Transistor (BJT) and Metal Oxide Semiconductor Field-Effect Transistors (MOSFET). The advantages of the modern MOS devices over the BJT transistors are: easier design of the biasing circuit, thermal stability, and higher reliability due to higher resistance to excessive power levels, which can cause breakdown effects [2.2]. However, the MOSFET transistors have a significant drawback in comparison with the BJT active devices, which is a drift of the threshold voltage within the different samples of the same transistor.

Generally, a transistor has three regions of operation: cut-off, active and saturation. Cut-off occurs when the input bias voltage is less than the threshold necessary to open the semiconductor: for a BJT, the base-emitter voltage is less than the threshold  $V_{BE} < V_{T\_BJT}$ ; for a MOSFET, the gate-source voltage is less than the threshold  $V_{GS} < V_{T\_MOSFET}$ . Active region refers to a situation, when the input bias voltage is equal or

higher than the threshold, and the output bias voltage (collector-emitter voltage  $V_{CE}$  for a BJT and drain-source voltage  $V_{DS}$  for a MOSFET) is lower than the difference between the input bias voltage and the threshold voltage:  $V_{BE} \geq V_{T\_BJT}$  and  $V_{CE} < V_{BE} - V_{T\_BJT}$  for a BJT;  $V_{GS} \geq V_{T\_MOSFET}$  and  $V_{DS} < V_{GS} - V_{T\_MOSFET}$  for a MOSFET. Finally, saturation takes place when the input bias voltage is higher than the threshold and the output bias voltage is equal or higher than the difference between the input bias voltage and the threshold voltage:  $V_{BE} \geq V_{T\_BJT}$  and  $V_{CE} \geq V_{BE} - V_{T\_BJT}$  for a BJT;  $V_{GS} \geq V_{T\_MOSFET}$  and  $V_{DS} \geq V_{GS} - V_{T\_MOSFET}$  for a MOSFET. The saturation region is characterised by a relatively constant load voltage limited by a certain value  $V_{L\_SAT}$ .

### 2.2.1 Amplification Principle

The main idea of an amplifier is the transformation of the Direct Current (DC) power supply energy into the Radio-Frequency (RF) signal energy. The amplification concept can be described using Figures 2-3 and 2-4.

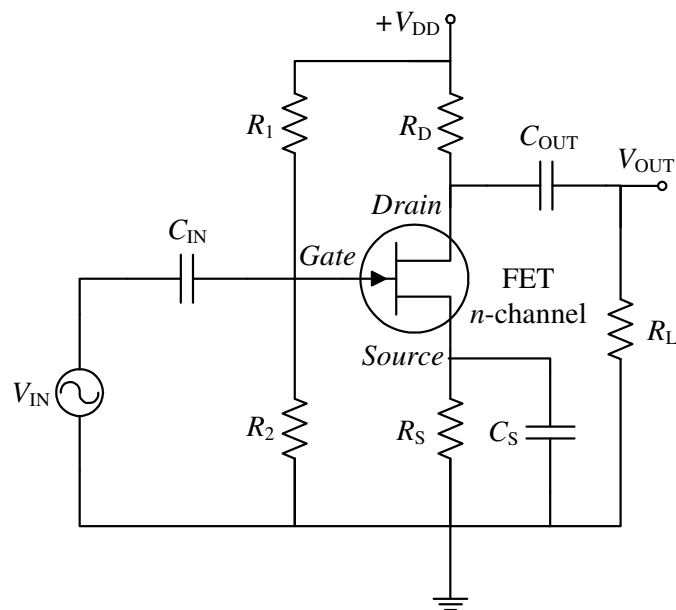


Figure 2-3: Example of a common-source MOSFET amplifier with a self-bias circuit

Figure 2-3 shows an example of a common-source MOSFET amplifier. It includes a voltage divider formed by resistors  $R_1$  and  $R_2$ , which is used to provide self-biasing.

Such a configuration requires only one DC supply to establish the operation point  $Q$  (Figure 2-4). The transistor is biased with a positive drain-to-source voltage  $V_{DS}>0$  and a negative gate-to-source voltage  $V_{GS}<0$  (on Figure 2-3 as the current through  $R_2$  is very small compared to the current through  $R_S$ , the voltage drop  $I_2R_2<I_S R_S$ . Therefore, the potential at the gate is smaller than that at the source and the negative gate-to-source voltage is obtained).

Figure 2-4 (a) shows the transfer characteristic curve for the considered amplifier. When  $V_{GS}=0$ , the drain current is high, but when the negative  $V_{GS}$  is applied, the current decreases as the channel width reduces. After a certain value  $V_{GS}=V_{GS\_OFF}$ , the channel closes and the drain current disappears.

Figure 2-4 (b) shows the drain curves and the load line for the amplifier. The top-curve corresponds to the case of  $V_{GS1}=0$  V,  $V_{GS1}>V_{GS2}>V_{GS3}>\dots$ . When  $V_{GS}<V_{GS\_OFF}$ , the cut-off region occurs. When  $V_{GS}\geq V_{GS\_OFF}$  and  $0<V_{DS}<V_{DS\_SAT}$ , the transistor is in the active region. After a further increase of  $V_{DS}$ , the transistor enters the saturation region. Considering the drain-source branch in Figure 2-3, an equation can be written:

$$V_{DD} = I_D \cdot R_D + V_{DS}. \quad (2.2)$$

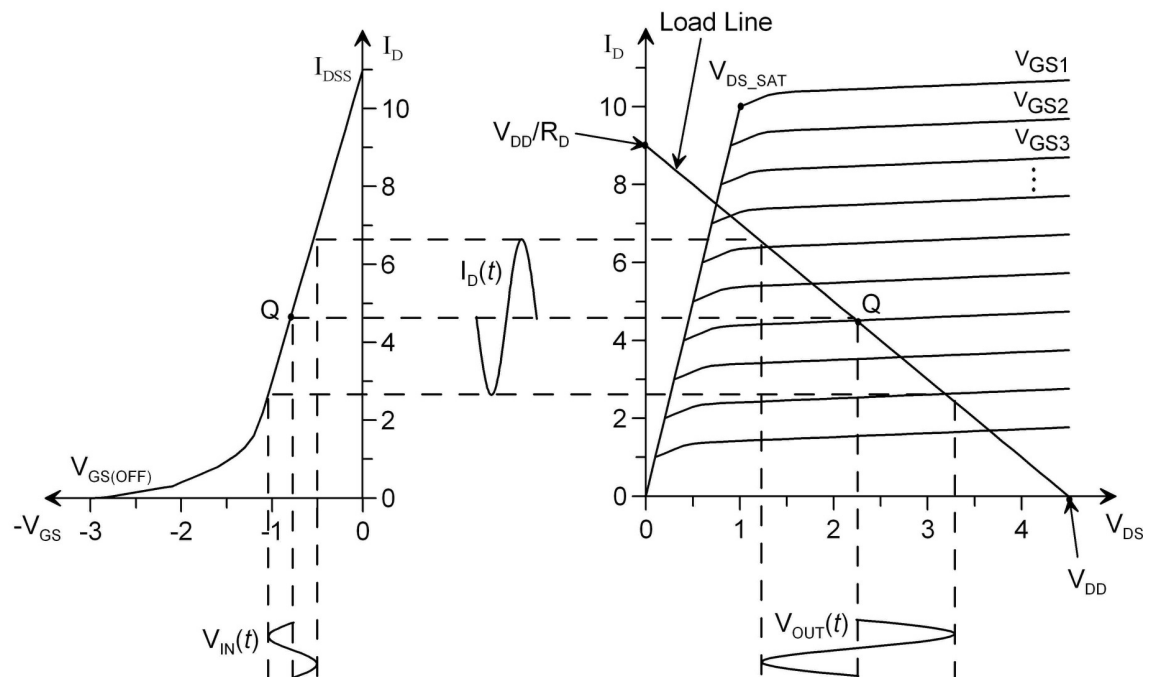


Figure 2-4: Common-source  $n$ -channel MOSFET amplifier characteristics showing signal operation: (a) transfer characteristic curve; (b) drain curves

From (2.2), two points of the load line (Figure 2-4b) are determined by putting  $I_D=0$ ,  $V_{DS}=V_{DD}$ , and  $V_{DS}=0$ ,  $I_D=V_{DD}/R_D$ .

The operation point  $Q$ , also called the bias quiescent point [2.3], refers to the quiescent state, when the input alternating voltage is not applied. Quiescent current  $I_Q$  is the current flowing into the transistor, when the input voltage is zero. In Figure 2-4, the drain current corresponding to the operation point  $Q$  is the quiescent current.

When the input alternating voltage is applied ( $V_{IN}$ ), it causes variations of the gate-to-source voltage. The positive half-period of the input sinusoid results in  $V_{GS}$  being less negative, causing a strong increase in the drain current  $I_D$  (Figure 2-4). It results in a higher voltage drop across  $R_D$ . Therefore, the value of  $V_{OUT}$  would be lower. Consequently, the drain current  $I_D$  alternates in phase with the input voltage  $V_{IN}$ , whereas the output voltage  $V_{OUT}$  is  $180^\circ$  out of phase with the input voltage  $V_{IN}$ . As small variations in the input voltage result in large variations in the output voltage, the concept of amplification is realised.

### 2.2.2 Conduction Angle

In order to provide a non-distorted amplification and to handle maximum possible amplitudes of the input signal, the operation point  $Q$  should be selected in the middle of the linear region on the transfer characteristic (Figure 2-4). This is realised by applying a relevant gate-source DC voltage  $V_{GSQ}$ . If an amplifier is biased in this way, it operates in class A. It is a linear mode of operation, which ideally does not distort the signal. However, the other classes are often preferable, particularly in order to increase efficiency, which will be described later in Sections 2.2.6-2.2.7. If the operation point  $Q$  is moved towards the cut-off region (Figure 2-4), the transistor is only open during a part of the input signal cycle. This is called a reduced conduction angle mode.

Conduction angle  $\Theta$  is the part of the input signal period, when the transistor is conductive. Reduced conduction angle waveforms with the corresponding quiescent current and voltage are shown in Figure 2-5. In terms of conduction angle, four main classes of operation can be described: class A, B, AB, and C. These classes are also known as classical modes of operation [2.3]. In class A, the transistor is conductive for the whole period, hence the conduction angle equals to  $2\pi$ :  $\Theta_A=2\pi$ . A class-AB amplifier has the conduction angle between  $\pi$  and  $2\pi$ :  $\pi < \Theta_{AB} < 2\pi$ . In class B, the

transistor conducts only half of the sinusoid, hence the conduction angle equals to  $\pi$ :  $\Theta_B = \pi$ . Finally, a class-C amplifier has the conduction angle between 0 and  $\pi$ :  $0 < \Theta_C < \pi$ .

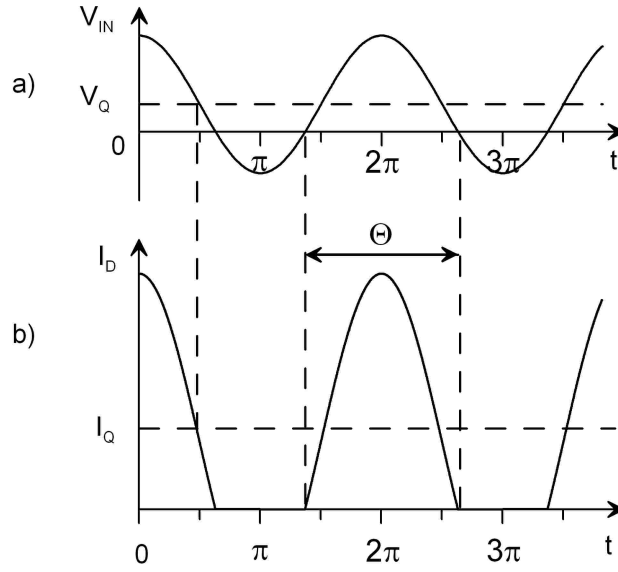


Figure 2-5: Reduced conduction angle waveforms: (a) input voltage waveform; (b) drain current waveform

### 2.2.3 Gain

Gain is one of the most important characteristics of a PA. It is a measure of the amplification degree. There are three main definitions of gain: transducer gain ( $G_t$ ), power gain ( $G_p$ ) and available gain ( $G_a$ ) [2.4]:

$$G_t = \frac{P_d^{Out}}{P_{av}^{In}}, \quad (2.3)$$

$$G_p = \frac{P_d^{Out}}{P_d^{In}}, \quad (2.4)$$

$$G_a = \frac{P_{av}^{Out}}{P_{av}^{In}}, \quad (2.5)$$

where  $P_{av}^{In}$  and  $P_{av}^{Out}$  are the power available at the input and output respectively;  $P_d^{In}$  and  $P_d^{Out}$  are the power delivered at the input and output respectively.

The delivered power differs from the available power because of matching imperfections [2.4]. Practically, when the input of a PA is connected to a signal

generator, and the output is connected to a power meter, the power meter shows the power delivered to the load ( $P_d^{Out}$ ), and the signal generator has the information about the power available at the input of the PA ( $P_{av}^{In}$ ). Therefore, the transducer gain of a PA can be easily measured. As it is often impossible to determine the input and output impedances or reflection coefficients to calculate  $P_d^{In}$  and  $P_{av}^{Out}$ , the other gain definitions are less useful.

Thus, the transducer gain is commonly used to characterise a PA. The shortened term “gain” is used with the intended meaning of “transducer gain”. The gain of a PA is simply defined as the ratio of the output power to the input power:

$$G = 10 \cdot \log\left(\frac{P_{OUT}}{P_{IN}}\right) = P_{OUT\_dBm} - P_{IN\_dBm}, \quad (2.6)$$

where  $P_{IN}$  and  $P_{OUT}$  are the input and output powers expressed in watts, whereas  $P_{IN\_dBm}$  and  $P_{OUT\_dBm}$  are the input and output power in dBm. Gain is usually expressed in dB, whereas power is shown in dBm.

#### 2.2.4 1dB Compression Point

A 1dB compression point is one of the measures to characterise the nonlinearity of a PA. By definition, the 1dB compression point of a PA is the output power level, at which the transfer characteristic of the PA deviates from the ideal linear transfer characteristic by 1 dB. In terms of gain, the 1dB compression point is the PA output power level, at which the gain decreases by 1 dB with respect to the gain in the linear region. The above statement is illustrated in Figure 2-6. In this Figure, the measured output power and gain dependences over input power are presented for a commercially available power amplifier Mini-Circuits ZFL-500. The 1dB compression point is shown on the output power and gain characteristics. The output power and the gain at the 1dB compression point are denoted by  $P_{1dB}$  and  $G_{1dB}$  respectively. For the gain, a relationship can be written:

$$G_{1dB} = G_{LIN} - 1dB, \quad (2.7)$$

where  $G_{LIN}$  is the PA gain in linear mode.

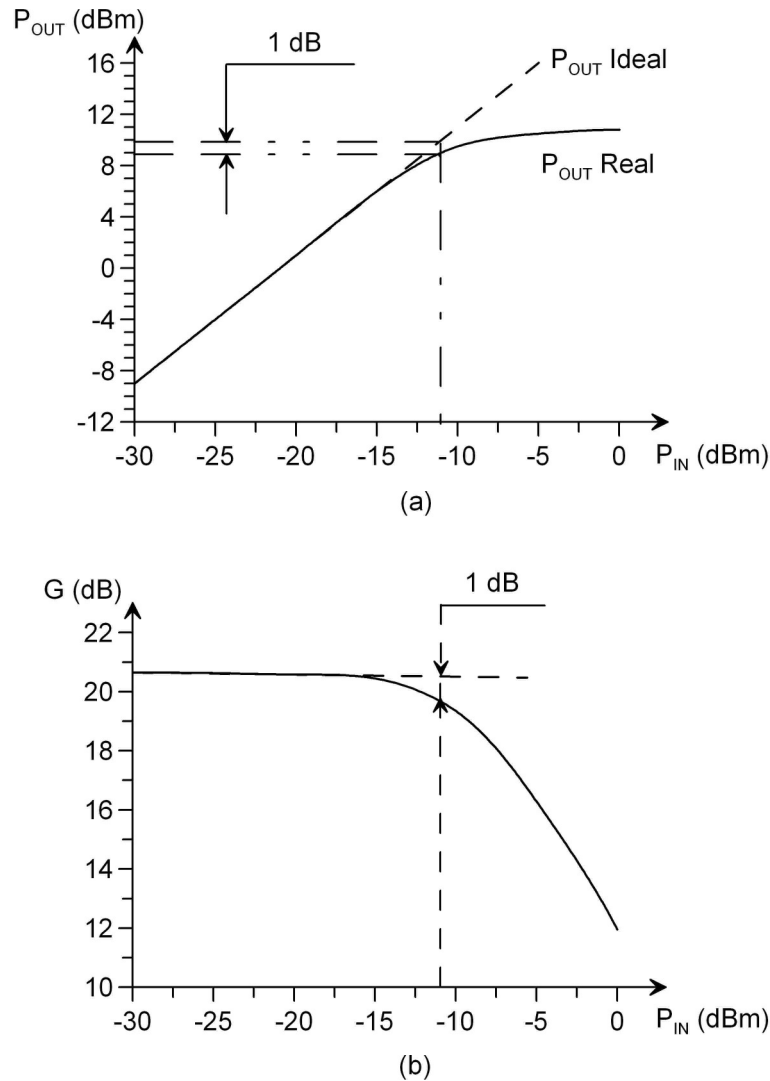


Figure 2-6: The measured characteristics of the PA Mini-Circuits ZFL-500 with the 1dB compression point at 9-dBm output power level: (a) Output power characteristic (b) Gain characteristic

### 2.2.5 Second- and Third-Order Intercept Points

A real nonlinear transfer characteristic, plotted in Figure 2-1 (b), can be approximated using a second-order and/or a third order characteristic [2.2]. If a second-order term is used, the output voltage can be written as:

$$V_{OUT}(t) = K_1 \cdot V_{IN}(t) + K_2 \cdot V_{IN}^2(t), \quad (2.8)$$

where  $K_1$  and  $K_2$  are coefficients. Assuming a sinusoid input signal is fed,

$$V_{IN}(t) = V_m \sin(\omega t), \quad (2.9)$$

after substituting (2.9) into (2.8) and completing trigonometric transformations, the output signal (2.8) can be re-written as:

$$V_{OUT}(t) = \frac{K_2 V_m^2}{2} + K_1 V_m \sin(\omega t) - \frac{K_2 V_m^2}{2} \cos(2\omega t). \quad (2.10)$$

In (2.10), except from the fundamental-frequency signal  $K_1 V_m \sin(\omega t)$ , a DC component and a second-harmonic component  $\frac{K_2 V_m^2}{2} \cos(2\omega t)$  appears. Therefore, in the frequency domain, a second-order component (2.8) appears at twice the original frequency  $2\omega$ . This is called the second Harmonic Distortion (HD). As the second harmonic component is proportional to the square of the input signal, whereas the fundamental component is in proportion to the input signal, the magnitude of the second harmonic increases at a higher rate. Therefore, at some value of the input signal, the fundamental and second harmonic magnitudes are equal. This is called the Second-Order Intercept point (SOI), usually expressed in logarithmic values of dBm for the input or output power. As can be seen from (2.10), the second-order characteristic produces harmonic distortions, but does not produce in-band distortion components.

If a third-order term is present in the PA characteristic, the output voltage can be written as:

$$V_{OUT}(t) = K_1 \cdot V_{IN}(t) + K_3 \cdot V_{IN}^3(t). \quad (2.11)$$

After substituting (2.9) into (2.11) and completing trigonometric transformations, the output signal (2.11) can be re-written as:

$$V_{OUT}(t) = (K_1 V_m + \frac{3K_3 V_m^3}{4}) \cdot \sin(\omega t) - \frac{K_3 V_m^3}{4} \sin(3\omega t). \quad (2.12)$$

A term at three times the original frequency is present in (2.12). This term is the third harmonic, and such a distortion is called the third-harmonic distortion. From (2.12), one can observe that the third-harmonic distortion produces an additional harmonic and an in-band distortion component, whereas the DC component is not generated. By analogy with SOI, as the magnitude of the third harmonic component rises at a higher rate than the fundamental-component magnitude, at a certain level of the input voltage, the magnitudes will be equal. The power level, at which the magnitudes of the fundamental and third harmonic components are equal, is called the

Third-Order Intercept point (TOI). TOI is also usually expressed in dBm and related to the input or output power level. As the third harmonic component brings an in-band distortion, the linear part of the fundamental characteristic must be extrapolated in order to find the TOI.

The SOI and TOI intercept points are a convenient way of describing the PA nonlinearity, as they have fixed values for each PA, and therefore can be used to predict the distortion behaviour in a particular mode of operation.

### 2.2.6 Back-Off

For a power amplifier, the back-off is a measure of how distant is the output power from the saturated output power. There are two commonly used definitions of back-off: output back-off and Peak Back-Off (PBO) [2.5]. Output Back-Off (OBO) is the ratio of saturated output power ( $P_{SAT}$ ) to average output power ( $P_{OUT\_AV}$ ). OBO is usually expressed in dB, and can be found as:

$$\text{OBO}[\text{dB}] = 10 \log \left[ \frac{P_{SAT}}{P_{OUT\_AV}} \right] P_{SAT} [\text{dBm}] - P_{OUT\_AV} [\text{dBm}]. \quad (2.13)$$

Peak Back-Off (PBO) is the ratio of saturated output power ( $P_{SAT}$ ) to peak output power ( $P_{OUT\_MAX}$ ). PBO also can be found as the difference between OBO and Peak-to-Average Ratio (PAR):

$$\text{PBO}[\text{dB}] = 10 \log \left[ \frac{P_{SAT}}{P_{OUT\_MAX}} \right] = \text{OBO}[\text{dB}] - \text{PAR}[\text{dB}], \quad (2.14)$$

where:

$$\text{PAR}[\text{dB}] = 10 \log \left[ \frac{P_{OUT\_MAX}}{P_{OUT\_AV}} \right]. \quad (2.15)$$

Figure 2-7 illustrates relations between the output back-off, peak back-off and peak-to-average ratio for power amplifiers.

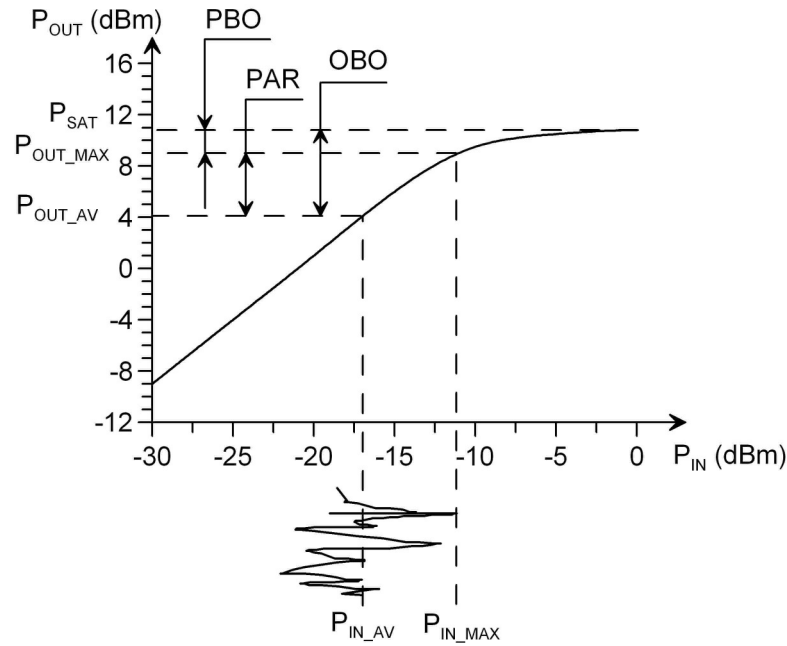


Figure 2-7: Relations between the output back-off, peak back-off and peak-to-average ratio for power amplifiers

The linearity of a conventional PA is related to its back-off: with an increase of the back-off, the linearity of the PA increases and vice versa. An example of the real-life values for OBO and PBO can be found in [2.5], where a PA has the PBO equal to 0.22 dB and the OBO equal to 3.22 dB with a 3-dB peak-to-average ratio.

### 2.2.7 Efficiency

Efficiency is an important PA parameter, which characterises how much of the DC power supply energy is converted into the RF signal. The efficiency of a PA should be as high as possible in order to make the PA consume less power. This is particularly important for battery-operated handset applications.

There are three main definitions of efficiency [2.6]. DC-to-RF efficiency (or drain efficiency) is the ratio of RF output power to DC input power and is given as:

$$\eta = \frac{P_{RF}^{OUT}}{P_{DC}^{IN}}. \quad (2.16)$$

Power-Added Efficiency (PAE) is the ratio of the additional RF power provided by the PA (the difference between the RF output power and the RF input power) to the DC input power:

$$PAE = \frac{P_{RF}^{OUT} - P_{RF}^{IN}}{P_{DC}^{IN}}. \quad (2.17)$$

If the gain is high, the PAE and drain efficiency are approximately equal. In this case, the drain efficiency is commonly used for simplicity. It can be easily shown that:

$$PAE = \eta \cdot \left(1 - \frac{1}{G_p}\right). \quad (2.18)$$

Overall efficiency can be defined as the ratio of the RF output power to the sum of DC and RF input powers:

$$\eta_{OE} = \frac{P_{RF}^{OUT}}{P_{DC}^{IN} + P_{RF}^{IN}}. \quad (2.19)$$

The instantaneous efficiency, which is the efficiency at a particular power level, is usually highest at the peak power level. The average efficiency is the ratio of the average RF output power to the average DC input power [2.7], which can be calculated as:

$$\eta_{AVG} = \frac{\sum_{k=1}^n p_k P_k^{RF-OUT}}{\sum_{k=1}^n p_k P_k^{DC-IN}}, \quad (2.20)$$

where  $p_k$  is the probability of  $k$ -th output power, and  $P_k^{RF-OUT}$  and  $P_k^{DC-IN}$  are the RF output and DC input powers respectively.

From formulae (2.16)-(2.20), one can see that the efficiency increases with the rise of the RF power level. This is also illustrated in Figure 2-8, where the dependences of the output power and the PAE on the input power are presented for a commercially available amplifier Mini-Circuits ZFL-500. The amplifier has a 20-dB gain and a 1-dB compression point at 9-dBm output power.

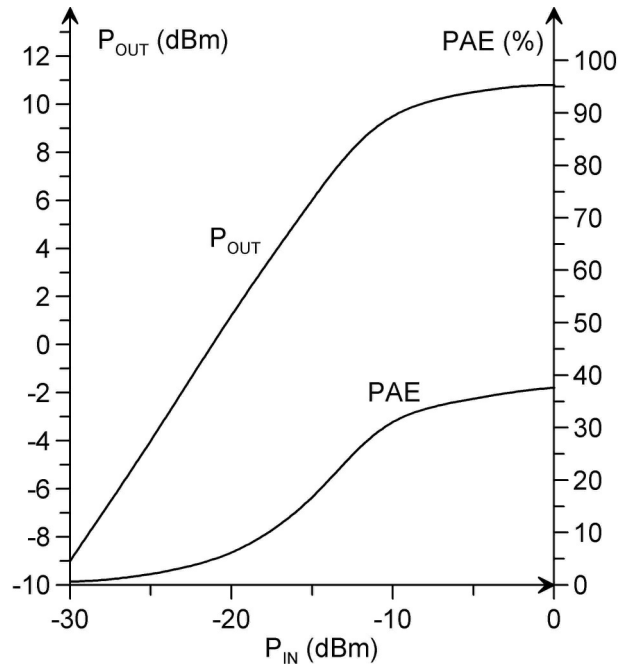


Figure 2-8: Measured output power and PAE curves for Mini-Circuits ZFL-500

Figure 2-8 shows that the efficiency is maximised when the PA operates in a near compression region. Consequently, non-linear distortions may appear at the output. Therefore, linearisation techniques are becoming very important with the purpose to keep the output signal linearly amplified.

### 2.3. Methods of Amplification

Generally, Power Amplifiers (PAs) can be divided into two categories: linear amplifiers, which preserve the input signal waveform, and nonlinear or constant envelope amplifiers, which do not make the preservation of the input signal waveform [2.2]. Linear amplifiers include three main classes: A, AB and B. The main classes within nonlinear amplifiers are: C, D, E, F, G, H and S.

Class-D, -E and -S amplifiers operate in a switching mode. They can approach a theoretical efficiency of 100%.

Class-F, -G and -H amplifiers are new configurations based on class-B or -C amplifier topologies with some modifications in order to increase efficiency.

The main amplification classes A, B, AB and C are described below. A general configuration of a BJT power amplifier is shown in Figure 2-9. The main purpose of the

Radio Frequency Choke (RFC) is to prevent the RF signal from being drawn from the supply, as well as the output capacitor  $C_{out}$  prevents the bias current from being fed to the load.

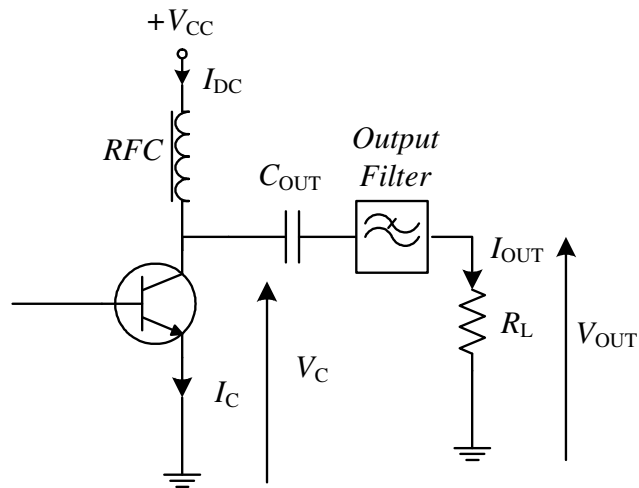


Figure 2-9: Configuration of a BJT power amplifier

### 2.3.1 Class-A Amplifiers

Class-A amplifiers are the most linear and least efficient amongst the other classes. The conduction angle of an amplifier operating in class A equals to  $\Theta_A=2\pi$ , and hence the output current flows at all times. The voltage and current waveforms for a class-A amplifier are illustrated in Figure 2-10. The transistor is biased in the middle of its linear region with  $V_{CC}$  voltage and direct current  $I_{DC}$ . The RF signal voltage is superimposed on this bias level. The collector current consists of the quiescent current  $I_{CQ}$  and RF current:

$$i_c(t) = I_{CQ} - I_{max} \cdot \sin(\omega t), \quad (2.21)$$

where  $I_{max}$  is the amplitude of the RF collector current.

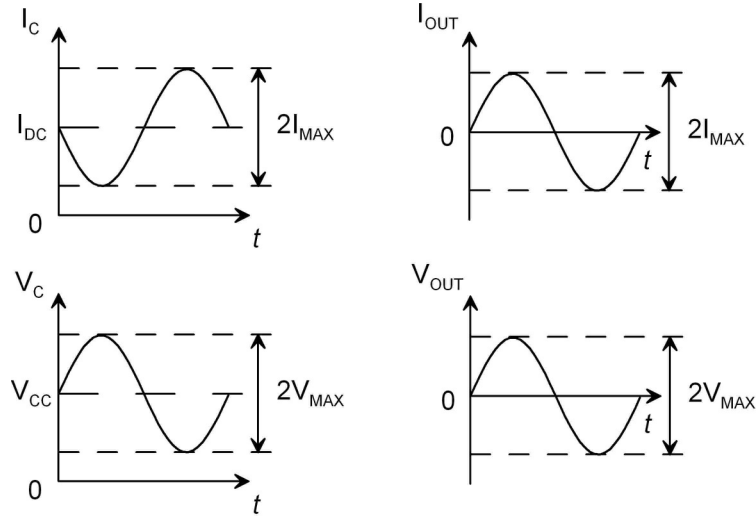


Figure 2-10: Voltage and current waveforms for a class-A power amplifier

As the choke and output capacitor were implemented to separate the RF and DC parts of the collector current, the input current from the supply  $I_{DC}$  is equal to the amplifier's quiescent current  $I_{CQ}$  and the output RF current  $i_{out}(t)$  is equal to the collector RF current:

$$I_{DC} = I_{CQ}, \quad (2.22)$$

$$i_{out}(t) = I_{max} \cdot \sin(\omega t). \quad (2.23)$$

The output voltage can be written as:

$$v_{out}(t) = i_{out}(t) \cdot R_L = I_{max} \cdot R_L \cdot \sin(\omega t). \quad (2.24)$$

The collector voltage  $v_c(t)$  has two components: a DC voltage from the supply  $V_{CC}$  and an RF output voltage  $v_{out}(t)$ :

$$v_c(t) = V_{CC} + V_{max} \cdot \sin(\omega t). \quad (2.25)$$

In order to keep the transistor out of the cut-off region, the collector voltage  $v_c(t)$  must be positive. Therefore, considering (2.25) and Figure 2-10, one can conclude that the voltage magnitude of the RF signal must not exceed the DC voltage from the supply:

$$V_{max} \leq V_{CC}. \quad (2.26)$$

The supply power is:

$$P_S = V_{CC} \cdot I_{DC} = \frac{V_{CC}^2}{R_L}. \quad (2.27)$$

The RF output power is:

$$P_L = \frac{V_{\max} \cdot I_{\max}}{2} = \frac{V_{\max}^2}{2 \cdot R_L}. \quad (2.28)$$

Then the DC-to-RF efficiency can be calculated as:

$$\eta = \frac{P_L}{P_S} = \frac{V_{\max}^2 \cdot R_L}{2 \cdot R_L \cdot V_{CC}^2} = \frac{V_{\max}^2}{2 \cdot V_{CC}^2} \leq \frac{V_{CC}^2}{2 \cdot V_{CC}^2} = \frac{1}{2}. \quad (2.29)$$

Therefore, the maximum instantaneous efficiency of a class-A amplifier is 50%. However, in a real class-A PA, harmonics will be present. The maximum practically achievable efficiency of a class-A PA is 40-45% [2.8].

### 2.3.2 Class-B Amplifiers

Class-B amplifiers are significantly more efficient than those operating in class-A. On the other hand, class-B operation provides lower level of linearity. The conduction angle of an amplifier operating in class B equals to  $\Theta_B = \pi$ , and consequently, for a sinusoidal excitation, the output current flows for one-half of a cycle. The ideal class-B PA has a bias voltage equal to the threshold voltage. This results in a zero quiescent current, so the PA consumes no power in the absence of excitation. The voltage and current waveforms for a class-B amplifier are illustrated in Figure 2-11.

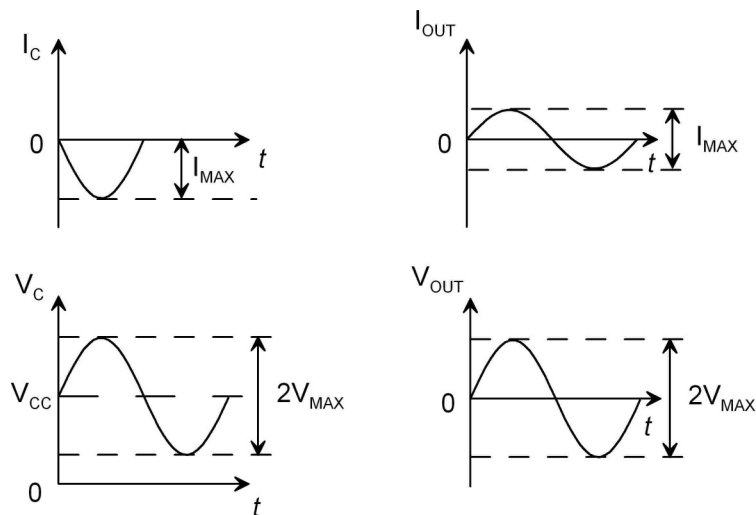


Figure 2-11: Voltage and current waveforms for a class-B power amplifier

When the input signal is positive, the bias voltage is higher than the threshold and the transistor conducts current. Therefore, the collector current looks like a pulse train with each pulse equal to a half-sine (Figure 2-11). As the circuit is designed to allow only the fundamental and DC components to appear, the RF part of the collector voltage is a continuous sinusoid, which also equals to the output voltage [2.4]. The output RF current is the fundamental-frequency part of the collector current, which is a half-sine pulse train with the amplitude  $I_{\max}$ . From Fourier analysis, one can write:

$$i_{out}(t) = i_C^{Fund}(t) = \frac{1}{2} i_C(t) = \frac{1}{2} I_{\max} \cdot \sin(\omega t). \quad (2.30)$$

The DC collector current is the average value of the half-sine pulse train with the amplitude  $I_{\max}$ , which can be found as the constant component of the Fourier series of the half-sine pulse train:

$$I_{DC} = \frac{1}{\pi} \cdot I_{\max} = \frac{I_{\max}}{\pi}. \quad (2.31)$$

Therefore, the power consumed from the supply can be found as:

$$P_S = V_{CC} \cdot I_{DC} = V_{CC} \cdot \frac{I_{\max}}{\pi}. \quad (2.32)$$

The RF output power is:

$$P_L = \frac{|v_{out}(t)| \cdot |i_{out}(t)|}{2} = \frac{V_{\max} \cdot I_{\max}}{2 \cdot 2} = \frac{V_{\max} \cdot I_{\max}}{4}. \quad (2.33)$$

Then the DC-to-RF efficiency can be calculated:

$$\eta = \frac{P_L}{P_S} = \frac{V_{\max} \cdot I_{\max} \cdot \pi}{4 \cdot V_{CC} \cdot I_{\max}} = \frac{V_{\max} \cdot \pi}{4 \cdot V_{CC}} \leq \frac{V_{CC} \cdot \pi}{4 \cdot V_{CC}} = \frac{\pi}{4} = 0.785. \quad (2.34)$$

Therefore, the maximum instantaneous efficiency of a class-B amplifier is 78.5%. However, in a real class-B PA, the maximum practically achievable efficiency is 60-70% [2.8]. A theoretically linear amplifier can be designed using two class-B amplifiers connected according to a push-pull configuration [2.2]. Each of the amplifiers conducts a separate half of the input signal, either positive or negative. The amplifiers operate in antiphase; hence, when one of them is conducting, the other is in the cut-off region and does not consume power. Theoretically, such a configuration should produce a linear output; however, in practice, due to the nonlinear transition from the cut-off to the active mode, a significant crossover distortion will appear.

### 2.3.3 Class-AB Amplifiers

Class-AB amplifiers were introduced to achieve a compromise between class-A and class-B modes. The conduction angle of an amplifier operating in class AB is between  $\pi$  and  $2\pi$ :  $\pi < \Theta_{AB} < 2\pi$ . For a sinusoidal excitation, the output current flows for less than a cycle, but more than one-half of a cycle. Obviously, the maximum theoretical instantaneous efficiency of a class-AB amplifier is between 50% and 78.5% depending on the conduction angle.

### 2.3.4 Class-C Amplifiers

Class-C amplifiers are the most efficient among the amplifiers with conventional modes of amplification, with a maximum theoretical efficiency reaching 100%. The conduction angle of an amplifier operating in class C is between 0 and  $\pi$ :  $0 < \Theta_C < \pi$ . The transistor is biased in the cut-off region. For a sinusoidal excitation, the output current flows for less than one-half of a cycle. The voltage and current waveforms for a class-C amplifier are illustrated in Figure 2-12.

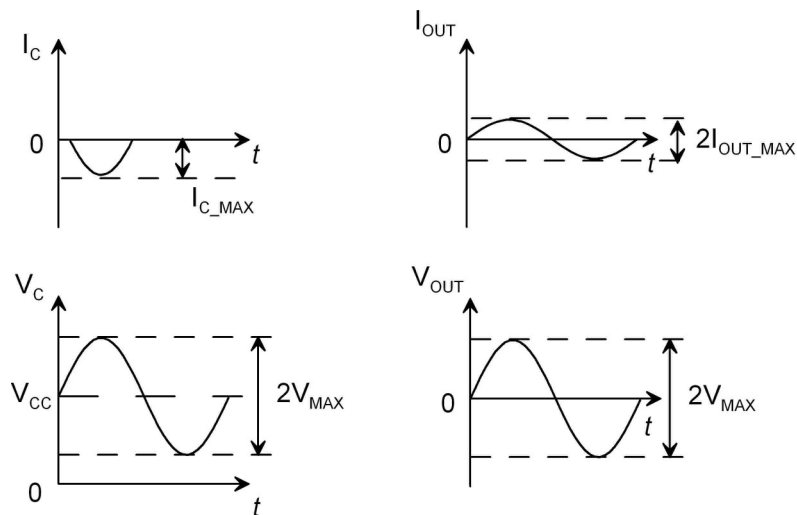


Figure 2-12: Voltage and current waveforms for a class-C power amplifier

The efficiency of a class-C PA is clearly dependent on the conduction angle. In order to find it, the general formula for the efficiency as a function of conduction angle

will be derived. This formula is applicable for class-A, -B and -AB as well as for class-C amplifiers.

A detailed illustration of the collector current waveform for a reduced conduction angle amplifier is presented in Figure 2-13.

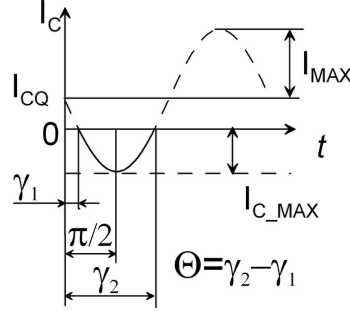


Figure 2-13: Collector current waveform for a reduced conduction angle amplifier

The collector current can be written as:

$$i_c(t) = \begin{cases} I_{CQ} - I_{\max} \cdot \sin(\gamma), & I_{CQ} - I_{\max} \cdot \sin(\gamma) \leq 0, \\ 0, & I_{CQ} - I_{\max} \cdot \sin(\gamma) \geq 0, \end{cases} \quad (2.35)$$

where  $\gamma = \omega t$ . Using Figure 2-13 and (2-35), the relationship between the conduction angle  $\Theta$  and the collector quiescent current  $I_{CQ}$  can be found as:

$$\begin{cases} I_{CQ} - I_{\max} \cdot \sin(\gamma_1) = 0, \\ I_{CQ} - I_{\max} \cdot \sin(\gamma_2) = 0, \end{cases} \quad (2.36)$$

$$2 \cdot I_{CQ} = I_{\max} \cdot (\sin(\gamma_1) + \sin(\gamma_2)), \quad (2.37)$$

$$I_{CQ} = I_{\max} \cdot \sin\left(\frac{\gamma_1 + \gamma_2}{2}\right) \cdot \cos\left(\frac{\gamma_1 - \gamma_2}{2}\right). \quad (2.38)$$

As  $\gamma_1 + \gamma_2 = \pi$  and  $\gamma_1 - \gamma_2 = \Theta$  (Figure 2-13), the following expression can be obtained:

$$I_{CQ} = I_{\max} \cdot \cos\left(\frac{\Theta}{2}\right). \quad (2.39)$$

As the PA is designed to allow only DC components and the fundamental RF harmonics to exist (Figure 2-9), the collector voltage is a continuous sinusoid, which is equal to the output voltage [2.4]. This is illustrated in Figure 2-12. The DC current flowing from the supply, when the transistor is open,  $I_{DC}$ , can be found as a constant component of the Fourier series of the collector current. The magnitude of the output

RF current (the current flowing through the load) can be found as the fundamental component of the same series:

$$I_{DC} = \frac{1}{2\pi} \int_0^{2\pi} i_C(\gamma) d\gamma = \frac{1}{2\pi} \int_{\frac{\pi-\Theta}{2}}^{\frac{\pi+\Theta}{2}} (I_{CQ} - I_{\max} \cdot \sin(\gamma)) d\gamma = \frac{I_{\max}}{\pi} \left( \frac{\Theta}{2} \cdot \cos\left(\frac{\Theta}{2}\right) - \sin\left(\frac{\Theta}{2}\right) \right), \quad (2.40)$$

$$I_{OUT\_MAX} = \frac{1}{\pi} \int_0^{2\pi} i_C(\gamma) \cdot \sin(\gamma) d\gamma = \frac{1}{\pi} \int_{\frac{\pi-\Theta}{2}}^{\frac{\pi+\Theta}{2}} (I_{CQ} - I_{\max} \cdot \sin(\gamma)) \cdot \sin(\gamma) d\gamma, \quad (2.41)$$

$$I_{OUT\_MAX} = \frac{1}{\pi} \int_{\frac{\pi-\Theta}{2}}^{\frac{\pi+\Theta}{2}} \left( I_{CQ} \cdot \sin(\gamma) - \frac{I_{\max}}{2} \cdot \sin(2\gamma) \right) d\gamma. \quad (2.42)$$

After taking the integral and applying trigonometric transformations, the expression for the magnitude of the output RF current can be written as:

$$I_{OUT\_MAX} = \frac{1}{2\pi} \left( 4 \cdot I_{CQ} \cdot \sin\left(\frac{\Theta}{2}\right) - I_{\max} \cdot \Theta - I_{\max} \cdot \sin(\Theta) \right). \quad (2.43)$$

Substituting for  $I_{CQ}$  from (2.39) gives:

$$I_{OUT\_MAX} = \frac{I_{\max}}{2\pi} \cdot (\sin(\Theta) - \Theta). \quad (2.44)$$

Finally, the efficiency can be found as:

$$\eta = \frac{P_L}{P_S}, \quad (2.45)$$

where  $P_L = \frac{I_{OUT\_MAX} \cdot V_{OUT\_MAX}}{2}$ ,  $P_S = I_{DC} \cdot V_{CC}$ . After substituting  $I_{DC}$  and  $I_{OUT\_MAX}$

from (2.40) and (2.44) into  $P_L$  and  $P_S$  respectively, the efficiency can be written as:

$$\eta = \frac{\Theta - \sin(\Theta)}{4 \cdot \left( \sin\left(\frac{\Theta}{2}\right) - \frac{\Theta}{2} \cdot \cos\left(\frac{\Theta}{2}\right) \right)} \cdot \frac{V_{OUT\_MAX}}{V_{CC}}. \quad (2.46)$$

As  $V_{OUT\_MAX} \leq V_{CC}$ , the highest efficiency is achieved, when the output voltage  $V_{OUT\_MAX}$  is equal to the supply voltage  $V_{CC}$ . Therefore, the maximum instantaneous efficiency is:

$$\eta_{MAX} = \frac{\Theta - \sin(\Theta)}{4 \cdot \left( \sin\left(\frac{\Theta}{2}\right) - \frac{\Theta}{2} \cdot \cos\left(\frac{\Theta}{2}\right) \right)}. \quad (2.47)$$

Formula (2.47) is the generalised dependence of the efficiency of a reduced-conduction-angle PA on the value of the conduction angle. For class-C amplifiers, the maximum theoretical efficiency is between 78.5% and 100%.

### 2.3.5 Efficiency Trade-Off

The dependence of efficiency on conduction angle is illustrated in Figure 2-14. The graph is based on the data obtained from (2.47). As can be observed from the Figure, the maximum theoretical efficiency of 100% is achievable in class-C operation by decreasing the conduction angle to zero. However, in this case, the output power also tends to zero, as can be seen from (2.44), where by putting  $\Theta=0$  the value of the output current equals to zero:  $I_{OUT\_MAX}=0$ . Moreover, in a real PA, the efficiency is lower than the theoretical efficiency predicted by (2.47) due to the imperfections of the elements. Therefore, a compromise between the linearity, efficiency and output power is usually sought for each particular application.

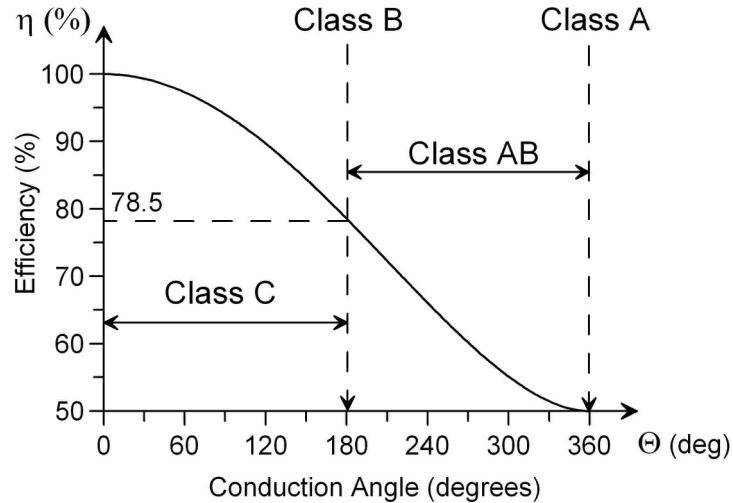


Figure 2-14: Efficiency as a function of conduction angle ( $\Theta$ )

## 2.4. Nonlinear Analysis

### 2.4.1 Approaches to Analysis

The main approaches for the analysis of electronic circuits can be classified as the following four categories [2.4]: load pulling, scattering parameters analysis, time-domain (transient) analysis, and frequency-domain methods. The last category can further be divided into two subcategories: strongly nonlinear circuit analysis incorporating harmonic balance and related techniques, and weakly nonlinear circuit analysis including power-series and Volterra-series analysis.

*Load pulling* is a straightforward method to analyse a large-signal circuit. It includes plotting the contours of load impedances of a circuit on a Smith chart. In order to obtain these contours, different loads are connected to the circuit, and electrical parameters, such as the input and output power level, are measured. The load pulling approach is applicable to power amplifiers. In this case, the gain and output power of the PA are measured with various loads. The obtained contours can be used to find the optimal load impedance to achieve the best compromise between the gain and output power. Load pulling has three major drawbacks: the practical difficulty of measuring load impedances at terminals, the weak possibilities of measuring circuit performances under a multi-tone excitation, and the limited number of properties that can be quantified using this approach.

*Scattering parameters analysis* is another approach to analyse a large-signal nonlinear circuit. The main idea is measuring a set of two-port scattering parameters (S-parameters) under a large-signal input. This approach is based on the assumption that by using the large-signal S-parameters it is possible to apply a linear circuit theory to nonlinear circuits. The main obvious drawback of this approach is that two-port parameters are fundamentally linear parameters, and their application in nonlinear analysis is limited. However, this approach can be used to determine matching impedances for the input and output of a circuit.

*Time-domain analysis* or transient analysis is based on the description of a circuit by time-domain differential equations. This method is commonly used for digital or low-frequency circuits. However, the application of the time-domain analysis is limited for

the circuits, which contain components characterised in the frequency domain, or which are subjected to multiple excitation frequencies. Therefore, the time-domain analysis is not usually used as a primary method to characterise wideband nonlinear PAs operating at high frequencies. Nevertheless, the time-domain analysis has a significant advantage in its capability to analyse very strong nonlinearities in large circuits. This is because as long as the nonlinearities are continuous, the steps used in the time-domain integration can be chosen small enough, that the corresponding voltages and currents change a little between the steps.

*Frequency-domain analysis* is a powerful method for analysing strongly and weakly nonlinear circuits with multi-tone excitations. The most important frequency-domain methods are: harmonic balance analysis, power-series analysis, and Volterra-series analysis. Harmonic balance is mainly used for strongly nonlinear circuits with one large-signal source. Harmonic balance is appropriate for a large number of applications, particularly to the design of power amplifiers, mixers and frequency multipliers. The method calculates a steady-state response of a circuit. A related method, large-signal/small-signal analysis, is usually applied for nonlinear circuits with two-tone inputs, one of which is large and the other is relatively small. This approach is useful in practice for mixers, which have a large Local Oscillator (LO) signal and a smaller RF signal. The Volterra-series analysis is used for analysing weakly nonlinear circuits with multiple small-signal excitations. In such circuits, nonlinearities are relatively small compared to the linear responses. However, they affect the whole system performance. The Volterra-series method is useful for quantifying intermodulation distortions in small-signal circuits, particularly in power amplifiers. The Power-series analysis is a simple technique based on the assumption that circuits contain ideal memoryless nonlinear components. This technique is useful for the theoretical analysis with the aim of describing empirically the nonlinear circuits' behaviour. Due to its convenience, the power-series analysis has become a commonly accepted method for the theoretical analysis of different types of nonlinear circuits, including power amplifiers.

In this chapter, a power-series analysis is used to show phenomena, which appear in nonlinear power amplifiers and to derive relationships for the PA characteristics and nonlinearity measures.

### 2.4.2 Nonlinear Analysis using Power Series

It is widely accepted in the community that the nonlinear behaviour of a PA can be represented by a power series [2.4], [2.9]. Therefore, a nonlinear transfer characteristic curve, similar to those presented in Figure 2-1, can be approximated by a polynomial expression:

$$V_{OUT}(t) = \sum_{n=1}^{\infty} g_n V_{IN}^n(t), \quad (2.48)$$

where  $g_n$  are coefficients near the corresponding terms.

The series (2.48) is a useful tool for the theoretical analysis of nonlinearity-related characteristics of PAs, such as intermodulation products, harmonic distortions, error vectors and others. However, with the aim of describing PA behaviour more precisely, another phenomenon should be taken into account. Due to the fact that a PA circuit contains reactive elements, i.e. inductances and capacitances, which are known to store energy, the PA response is likely to depend not only on the instant excitation signal, but also on the previous excitations. Moreover, the transistor itself is able to store energy due to the presence of a parasitic capacitance in its  $p$ - $n$  junctions. This phenomenon is known as memory effects of power amplifiers, and will be described in details in Chapter 4. Therefore, the memory effects should be considered during the nonlinear analysis of a PA. This can be accomplished by introducing time constants  $\tau_n$  into the power series [2.10]:

$$V_{OUT}(t) = \sum_{n=1}^{\infty} g_n V_{IN}^n(t - \tau_n). \quad (2.49)$$

The input signal in wireless communication systems is usually modulated with amplitude and phase modulation:

$$V_{IN}(t) = V_S(t) \cdot \cos(\omega t + \varphi(t)). \quad (2.50)$$

where  $V_S(t)$  is the Amplitude Modulation (AM), and  $\varphi(t)$  is the Phase Modulation (PM) on the input signal.

Considering a third-order polynomial in (2.49) under a low-distortion condition, after substituting (2.50) into (2.49), the output can be written as:

$$\begin{aligned} V_{OUT}(t) = & g_1 \cdot V_S(t - \tau_1) \cdot \cos(\omega t - \omega\tau_1 + \varphi(t - \tau_1)) \\ & + g_2 \cdot V_S^2(t - \tau_2) \cdot \cos^2(\omega t - \omega\tau_2 + \varphi(t - \tau_2)) \\ & + g_3 \cdot V_S^3(t - \tau_3) \cdot \cos^3(\omega t - \omega\tau_3 + \varphi(t - \tau_3)). \end{aligned} \quad (2.51)$$

Having denoted  $\varphi_1=\omega\tau_1$ ,  $\varphi_2=\omega\tau_2$ , and  $\varphi_3=\omega\tau_3$ , after completing trigonometric transformations, (2.51) can be rewritten as:

$$\begin{aligned}
V_{OUT}(t) = & \frac{g_2}{2} \cdot V_S^2(t - \tau_2) + g_1 \cdot V_S(t - \tau_1) \cdot \cos(\omega t + \varphi(t - \tau_1) - \varphi_1) \\
& + \frac{3g_3}{4} \cdot V_S^3(t - \tau_3) \cdot \cos(\omega t + \varphi(t - \tau_3) - \varphi_3) \\
& + \frac{g_2}{2} \cdot V_S^2(t - \tau_2) \cdot \cos(2\omega t + 2\varphi(t - \tau_2) - 2\varphi_2) \\
& + \frac{g_3}{4} \cdot V_S^3(t - \tau_3) \cdot \cos(3\omega t + 3\varphi(t - \tau_3) - 3\varphi_3).
\end{aligned} \tag{2.52}$$

In (2.52), the first term is a DC signal, which results in a bias shift from the operating point. The second term relates to the linear output signal equal to the input signal times the gain  $g_1$ . The third term is the in-band distortion component produced by an odd-order polynomial term. The fourth and fifth terms are the out-of-band distortions or harmonic distortions at the second and third harmonics respectively. As can be seen from (2.52), the nonlinearity results in the amplitude and phase distortions of the power amplifier.

### 2.4.3 Two-Tone Test

Two-tone test is a widely used method of evaluating PA behaviour over the modulation frequency ( $f_2-f_1$ ), also called the envelope frequency [2.11]. Two RF unmodulated signals of equal amplitudes with the frequencies  $f_2$  and  $f_1$  are generated and passed through the PA. The signals in the time and frequency domains are shown in Figure 2-15. In practice, the power of the tones is adjusted in order to have the peak envelope power of the two-tone signal equal to the full power level, at which the amplifier will be used. The peak envelope power of the two-tone signal is 6 dB higher than the power of each of the Carrier Waves (CW), whereas the mean envelope power is 3 dB higher than the CW power.

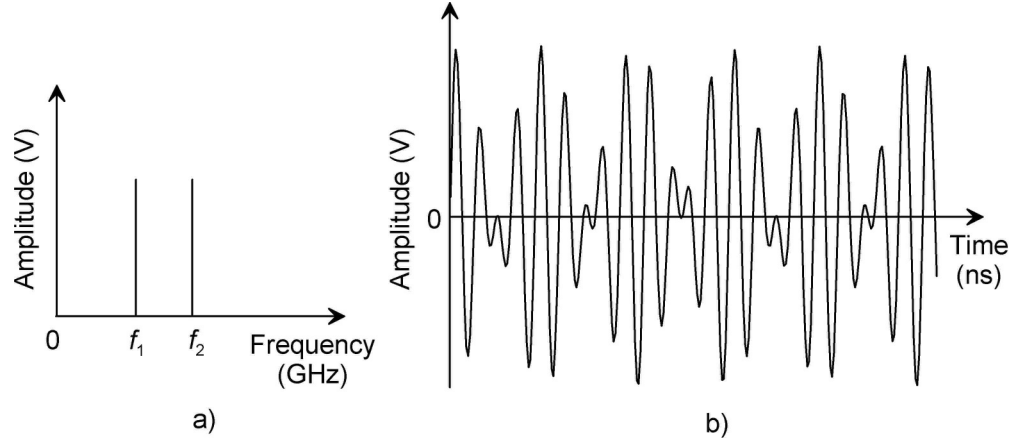


Figure 2-15: Two-tone test in the frequency domain (a) and in the time domain (b)

Both the amplitude and phase distortions of a PA can be characterised using a two-tone test. Below, a two-tone test analysis is carried out with the input signal given by:

$$V_{IN}(t) = V_1 \cdot \cos(\omega_1 t) + V_2 \cdot \cos(\omega_2 t). \quad (2.53)$$

Substituting (2.53) into (2.49) with consideration of a 3<sup>rd</sup>-order polynomial gives:

$$\begin{aligned}
 V_{OUT}(t) = & \left. \begin{aligned} & \frac{g_2}{2} \cdot (V_1^2 + V_2^2) \\ & + g_2 \cdot V_1 \cdot V_2 \cdot \cos[(\omega_1 - \omega_2)t - (\varphi_{12} - \varphi_{22})] \end{aligned} \right\} \begin{array}{l} DC \\ Zone \end{array} \\
 & + g_1 \cdot (V_1 \cdot \cos(\omega_1 t - \varphi_{11}) + V_2 \cdot \cos(\omega_2 t - \varphi_{21})) \\
 & + \frac{3g_3}{4} \cdot (V_1^3 \cdot \cos(\omega_1 t - \varphi_{13}) + V_2^3 \cdot \cos(\omega_2 t - \varphi_{23})) \\
 & + \frac{3g_3}{2} \cdot V_1 \cdot V_2 \cdot (V_2 \cdot \cos(\omega_1 t - \varphi_{13}) + V_1 \cdot \cos(\omega_2 t - \varphi_{23})) \\
 & + \frac{3g_3}{4} \cdot V_1 \cdot V_2 \cdot \left( \begin{array}{l} V_1 \cdot \cos[(2\omega_1 - \omega_2)t - (2\varphi_{13} - \varphi_{23})] \\ + V_2 \cdot \cos[(2\omega_2 - \omega_1)t - (2\varphi_{23} - \varphi_{13})] \end{array} \right) \left. \vphantom{\frac{3g_3}{4}} \right\} \begin{array}{l} \text{Fundamental} \\ \text{Zone} \end{array} \\
 & + \frac{g_2}{2} \cdot (V_1^2 \cdot \cos(2\omega_1 t - 2\varphi_{12}) + V_2^2 \cdot \cos(2\omega_2 t - 2\varphi_{22})) \\
 & + g_2 \cdot V_1 \cdot V_2 \cdot \cos[(\omega_1 + \omega_2)t - (\varphi_{12} + \varphi_{22})] \left. \vphantom{\frac{g_2}{2}} \right\} \begin{array}{l} \text{Second} \\ \text{Harmonic} \\ \text{Zone} \end{array} \\
 & + \frac{g_3}{4} \cdot (V_1^3 \cdot \cos(3\omega_1 t - 3\varphi_{13}) + V_2^3 \cdot \cos(3\omega_2 t - 3\varphi_{23})) \\
 & + \frac{3g_3}{4} \cdot V_1 \cdot V_2 \cdot \left( \begin{array}{l} V_1 \cdot \cos[(2\omega_1 + \omega_2)t - (2\varphi_{13} + \varphi_{23})] \\ + V_2 \cdot \cos[(2\omega_2 + \omega_1)t - (2\varphi_{23} + \varphi_{13})] \end{array} \right) \left. \vphantom{\frac{g_3}{4}} \right\} \begin{array}{l} \text{Third} \\ \text{Harmonic} \\ \text{Zone} \end{array} \quad (2.54)
 \end{aligned}$$

where  $\varphi_{11}=\omega_1\tau_1$ ,  $\varphi_{12}=\omega_1\tau_2$ ,  $\varphi_{21}=\omega_2\tau_1$ ,...  $\varphi_{ij}=\omega_i\tau_j$  are phase shifts corresponding to each polynomial term.

As can be seen from equation (2.54), new spectral components in the DC, fundamental, second-harmonic and third-harmonic zones appear. The physical meaning of the obtained terms is described below.

The first term in the DC zone is a bias shift from the quiescent point. The second term is a second-order intermodulation product (IM2), which is formed by the tone difference ( $\omega_2 - \omega_1$ ).

The first term in the fundamental zone is the desired linear amplification of the input signal. The second term in the same zone represents the in-band distortion components, which result in the output signal amplitude (AM/AM) and phase (AM/PM) conversions. The third term represents the Cross-Modulation (CM) between the input tones. Finally, the last term in the fundamental zone is a third-order intermodulation product (IM3), which is formed by ( $2\omega_i - \omega_j$ ).

The first term in the second-harmonic zone represents the second harmonic of the input signal. The last term in this zone is a second-order intermodulation product (IM2), which is formed by the sum of the input tones ( $\omega_1 + \omega_2$ ).

The first term in the third-harmonic zone represents the third harmonic of the input signal. The last term in this zone is a third-order intermodulation product (IM3), which is formed by ( $2\omega_i + \omega_j$ ).

The complete spectrum at the output of a nonlinear PA represented by a third-order polynomial model with a two-tone excitation is presented in Figure 2-16, assuming there is no filtering of the DC and harmonic components. The Figure illustrates (2.54) in the frequency domain.

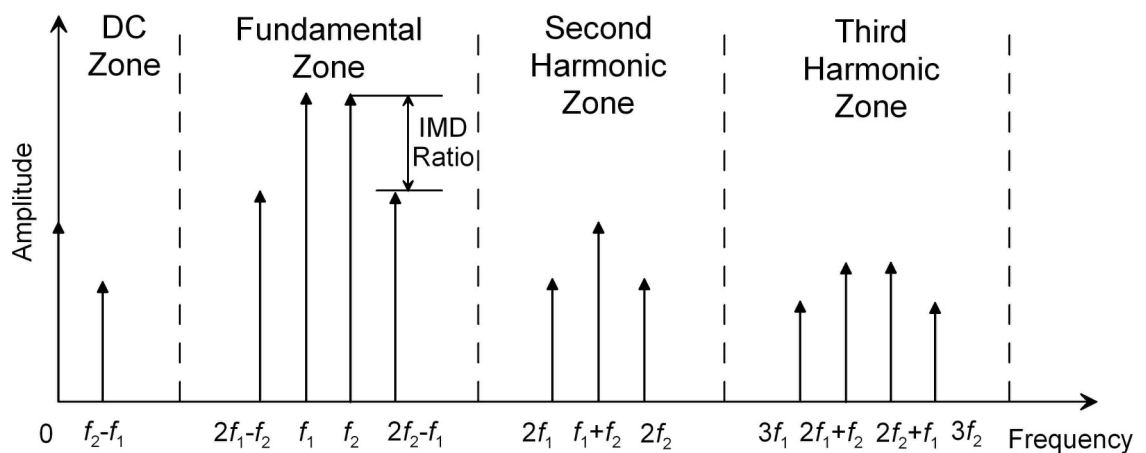


Figure 2-16: Frequency-domain response of a nonlinear PA with a two-tone excitation assuming there is no filtering of DC and harmonic components

The distortion components produced by a nonlinear PA can be classified as the in-band and out-of-band distortions. The out-of-band distortion components, such as the DC and harmonics, can be easily filtered. Therefore, they do not cause significant problems. The in-band distortion components directly affect the fundamental-frequency output and hence present challenges for the design of a linear PA. The ratio of the amplitude of an intermodulation component to the fundamental tone amplitude, called Intermodulation Distortion (IMD), is illustrated in Figure 2-16. The remainder of this chapter contains descriptions of different types of distortions and derivations of the most important relationships, which are used to analyse the nonlinear behaviour of a PA.

#### **2.4.4 AM/AM and AM/PM Distortions**

AM/AM and AM/PM characteristics represent the amplitude and phase dependence of the fundamental output signal on the input signal amplitude. In other words, AM/AM is a conversion between the input signal AM and the modified output AM; AM/PM is a conversion from the input signal AM to the output signal PM [2.2]. The reason behind the AM/AM distortion is the nonlinearity of the transfer characteristic, particularly when the PA operates in its compression region. The AM/PM distortion occurs as a consequence of memory effects. Indeed, a shift in phase at the output can appear due to signal delays in the PA caused by its reactive elements. In addition, the energy stored in the reactive elements and unequal node impedances for different modulation frequencies contribute to the phase swing. Consequently, the AM/AM distortion occurs in any nonlinear PA, whereas the AM/PM distortion only appears in a PA exhibiting memory effects [2.10]-[2.11]. An example of AM/AM and AM/PM characteristics for a MOSFET PA is shown in Figure 2-17.

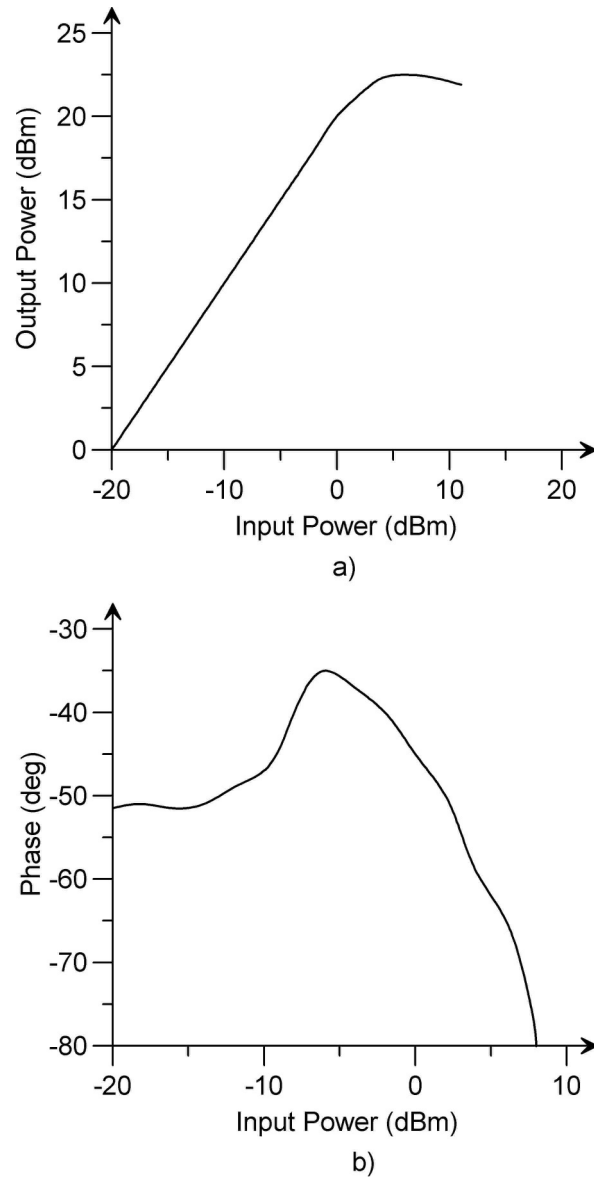


Figure 2-17: Example of the AM/AM (a) and AM/PM (b) characteristics for a PA

Considering a fundamental-frequency response to the two-tone excitation at one particular frequency  $\omega_1$ , (2.54) leads to:

$$\begin{aligned}
 V_{OUT\_o1}^{FUND}(t) &= g_1 \cdot V_1 \cdot \cos(\omega_1 t - \varphi_{11}) \\
 &+ \frac{3g_3}{4} \cdot V_1^3 \cdot \cos(\omega_1 t - \varphi_{13}) + \frac{3g_3}{2} \cdot V_1 \cdot V_2^2 \cdot \cos(\omega_1 t - \varphi_{13}).
 \end{aligned}
 \tag{2.55}$$

In (2.55), the first term is the linear response, whereas the second and the third terms cause distortions in the amplitude and phase of the signal. The second term is the AM/AM and AM/PM term, as it is produced by the input signal amplitude. The third

term is the cross-modulation term caused by the third-order response to the second tone  $\omega_2$  at the first-tone frequency  $\omega_1$ .

### 2.4.5 Saturation and Desensitisation

Examining the fundamental-frequency output signal (2.55), one can conclude that additional components, which appear as a result of the PA nonlinearity, cause changes in the gain. If the coefficient  $g_3$  is negative, the second and third terms in (2.55) will result in a gain reduction. This is typical for all PAs due to the fact that the available output power is limited. The phenomenon described above is known as saturation. In other words, saturation is a decrease in gain with an increase in the input power level, which occurs due to the nonlinearity in the PA transfer characteristics.

Considering a two-tone test with a large and a small input signal, another phenomenon, called desensitisation, can be described. When the large input signal drives a PA into saturation, the gain for the large signal decreases, as well as it does for the small signal. This is known as desensitisation. In other words, desensitisation is a decrease in the system's sensitivity due to the appearance of a large signal at the input.

### 2.4.6 Error Vector Magnitude

Error vector is the difference between the linear PA output signal, in other words the desired signal, and the overall output signal composed by the sum of the linear term and the nonlinear distortions [2.2], [2.10]. Considering (2.55), the error vector is the difference between the first linear term and the total output signal. Error Vector Magnitude (EVM) can be calculated as:

$$EVM = g_3 \cdot \left[ \frac{3}{4} \cdot V_1^3 + \frac{3}{2} \cdot V_1 \cdot V_2^2 \right]. \quad (2.56)$$

Usually AM/AM distortion is defined for a single-tone input; hence (2.56) can be simplified as [2.10]:

$$EVM = \frac{3g_3}{4} \cdot V_1^3. \quad (2.57)$$

If the system is memoryless, the phase shift equals to zero:  $\varphi_{11} = \varphi_{13} = 0$ . Therefore, the nonlinearity distorts only the magnitude of the linear term, but does not affect its phase:

$$V_{OUT\_ \omega_1}^{FUND}(t) = \left[ g_1 \cdot V_1 + \frac{3g_3}{4} \cdot V_1^3 + \frac{3g_3}{2} \cdot V_1 \cdot V_2^2 \right] \cdot \cos(\omega_1 t). \quad (2.58)$$

This is illustrated in Figure 2-18. The angle between the AM and the Cross Modulation (CM) component is zero. There is no phase distortion, and the error vector is simply the magnitude of the error. If the system exhibits memory effects, the phase change occurs. This results in the error vector having a non-zero angle. This case is illustrated in Figure 2-19, where the linear response is plotted on the horizontal axes and the total signal at the fundamental frequency is the sum of the linear vector and the error vector. The AM and CM vectors make a non-zero angle and produce a phase distortion.

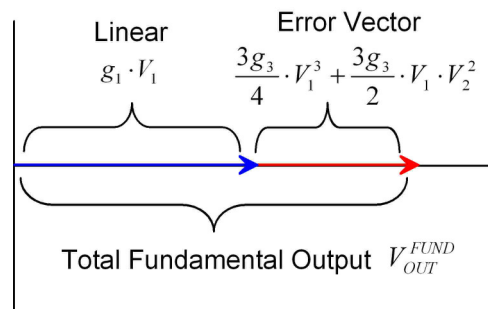


Figure 2-18: Error vector in a memoryless system

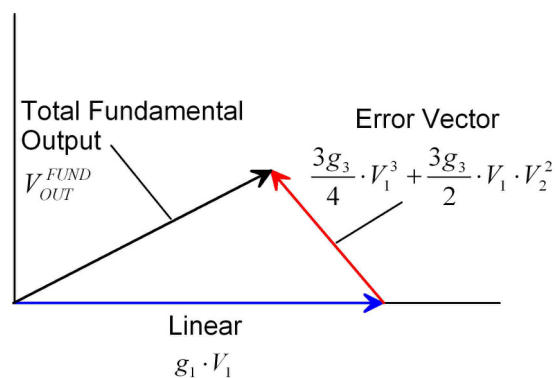


Figure 2-19: Error vector in a system exhibiting memory effects

For digitally modulated signals, EVM, also called the Received Constellation Error (RCE), is calculated as the difference between the actually received symbols and the ideal symbols. EVM is calculated as the average power of the error vector normalised to the signal power using a Root-Mean-Square (RMS) average [2.12]. A general formula for calculating the EVM for a digitally modulated signal is:

$$EVM = \sqrt{\frac{\sum_{k=1}^N |S_r(k) - S_i(k)|}{\sum_{k=1}^N |S_i(k)|}}, \quad (2.59)$$

where  $k$  is the sample index,  $S_i(k)$  and  $S_r(k)$  are the ideal and received symbols respectively.

Typical values of the EVM for modern wireless communication systems are in the range of several percent [2.13]. Normally, the EVM is highly dependent on the PA back-off: an increase in the OBO results in an EVM reduction.

#### 2.4.7 Harmonic Distortion

Harmonic distortion in a PA is the out-of-band type of distortions. Usually, second- and third-harmonic distortions are evaluated. The second-harmonic distortion is defined as the ratio of the amplitude of the second harmonic to the amplitude of the fundamental signal [2.10]:

$$HD_2 = \frac{V_{SEC}}{V_{FUND}}. \quad (2.60)$$

Harmonic distortion can be analysed using a single-tone or two-tone excitation. A single tone, applied to the PA nonlinearity, will result in new harmonics generated at the output. Using (2.52), the second- harmonic distortion (2.60) can be rewritten as:

$$HD_2 = \frac{\frac{g_2}{2} \cdot V}{g_1 + \frac{3g_3}{4} \cdot V^2}, \quad (2.61)$$

where  $V$  is the magnitude of the input signal.

Usually, for small nonlinearity, i.e. when the gain compression due to  $g_3$  coefficient is small, its value can be neglected [2.14]-[2.15], and (2.61) reduces to:

$$HD_2 = \frac{g_2}{2g_1} \cdot V. \quad (2.62)$$

Similarly, the third-harmonic distortion is defined as the ratio of the amplitude of the third harmonic to the amplitude of the fundamental signal [2.10]:

$$HD_3 = \frac{V_{THIRD}}{V_{FUND}}. \quad (2.63)$$

Substituting the expressions for the third-harmonic and fundamental terms from (2.52) into (2.63) results in:

$$HD_3 = \frac{g_3 \cdot V^3}{4 \cdot (g_1 \cdot V + \frac{3g_3}{4} \cdot V^3)}. \quad (2.64)$$

For a small nonlinearity, having neglected the gain compression due to  $g_3$  coefficient [2.14]-[2.15], the third-harmonic distortion can be simplified to:

$$HD_3 = \frac{g_3}{4g_1} \cdot V^2. \quad (2.65)$$

From (2.62) and (2.65), one can see that the  $HD_2$  is proportional to the input signal magnitude  $V$ , whereas the  $HD_3$  is proportional to the square of the magnitude  $V^2$ . Consequently, for low levels of distortion,  $HD_3$  increases faster than  $HD_2$  with increasing  $V$ . For larger values of the input signal magnitude, which exceed the low-distortion conditions, harmonic distortions flatten off with increasing  $V$  [2.16]. This is illustrated in Figure 2-20.

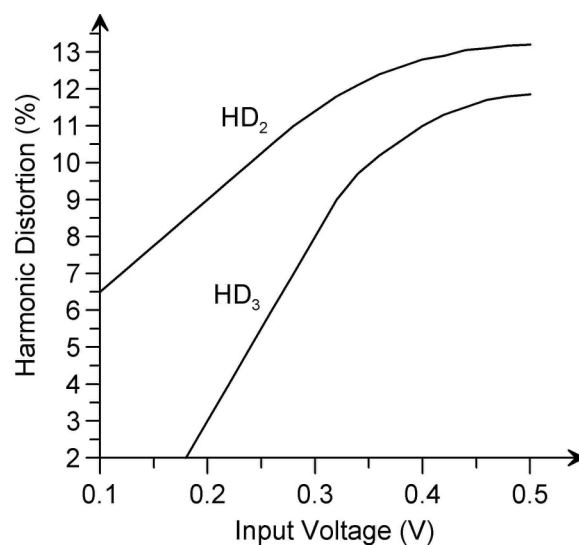


Figure 2-20: Second- and third-harmonic distortions versus input voltage magnitude

Another parameter for analysing harmonic distortion in a nonlinear PA is the Total Harmonic Distortion (THD), defined by the following:

$$\text{THD} = \sqrt{\text{HD}_2^2 + \text{HD}_3^2 + \dots} \quad (2.66)$$

THD is not a widely used parameter due to its incapability to clearly quantify the dependence of harmonic distortion on the input signal level.

### 2.4.8 Intermodulation Distortion

Intermodulation (IM) products are additional signals generated by two or more different-frequency excitation signals. Generally, IM products have frequencies different from the fundamental or harmonic frequencies. Intermodulation products can be classified as in-band and out-of-band. In (2-54), the out-of-band IM products are the components at  $\omega_2 \pm \omega_1$  frequencies, called the sum and difference second-order IM terms; and the in-band IM products are the third-order components at  $2\omega_2 - \omega_1$  and  $2\omega_2 - \omega_1$  frequencies. In general, there are higher-order IM products, caused by the forth-, fifth-, and higher polynomial terms. The even-order IM products usually occur at frequencies situated far from the fundamental, and produce out-of-band distortion, whereas the odd-order ones take place near the desired signal and produce in-band distortion [2.10]. The out-of-band products can be easily filtered out, unlike the in-band ones, which are the most challenging IM products in power amplifiers.

An  $n$ -order Intermodulation Distortion (IMD) is defined as the ratio of the  $n$ -order IM product to the fundamental-frequency term. Thus, the second-order intermodulation distortion (IM2) is the ratio of the components at  $\omega_2 \pm \omega_1$  to the one at  $\omega_2$  or  $\omega_1$ . From (2-54), considering  $V_1=V_2=V$  and ignoring the phase shift, one can obtain:

$$\text{IM}_2 = \frac{g_2}{g_1} \cdot V \quad (2.67)$$

As can be seen from (2.67), the IM2 grows proportionally with the input-signal magnitude.

The odd-order IM products are close to the fundamental-frequency signal and hence cannot be filtered out. Among all the odd-order IM products, the third-order one is the strongest, and consequently causes the highest distortion. The third-order intermodulation distortion (IM3) is defined as the ratio of the components at  $2\omega_2 - \omega_1$  or

$2\omega_1 - \omega_2$  to the one at  $\omega_2$  or  $\omega_1$ . Similarly, from (2-54) considering  $V_1=V_2=V$  and ignoring the phase shift, the following can be obtained:

$$\text{IM}_3 = \frac{3g_3}{4g_1} \cdot V^2. \quad (2.68)$$

As can be seen from (2.68), the IM3 grows proportionally with the square of the input-signal magnitude. It means that for a certain value of the input voltage, the IM product becomes equal to the fundamental-frequency signal. This occurs at the Third Order Intercept (TOI) point. At this magnitude of the input signal, the IM3 equals to one. Having denoted the value of the input voltage at TOI as  $V_{IP3}$ , the following expression can be written:

$$1 = \frac{3g_3}{4g_1} \cdot V_{IP3}^2. \quad (2.69)$$

From (2.69), the TOI input voltage can be determined:

$$V_{IP3} = \sqrt{\frac{4g_1}{3g_3}}. \quad (2.70)$$

Therefore, (2.68) can be rewritten as:

$$\text{IM}_3 = \left( \frac{V}{V_{IP3}} \right)^2. \quad (2.71)$$

Using logarithmic units, the relation between IMD and IP3 can be obtained:

$$\text{IM}_3[\text{dBm}] = 2 \cdot (V[\text{dBm}] - V_{IP3}[\text{dBm}]). \quad (2.72)$$

This relation can also be written for power expressed in dBm:

$$P_{IM3} = 2 \cdot (P - P_{IP3}), \quad (2.73)$$

where  $P$  is the input signal power in dBm,  $P_{IP3}$  is the input power in dBm at the TOI point, and  $P_{IM3}$  is the third-order intermodulation distortion power ratio in dB.

For example, a power amplifier with an input intercept point of +20 dBm and a two-tone excitation at 0-dBm power level per tone generates a third-order intermodulation product with  $P_{IM3} = 2 \cdot (0 - 20) = -40$  dBc. The unit dBc means the IMD ratio in dB with respect to the carrier level.

Having compared (2.62) with (2.67) and (2.65) with (2.68), the relations between HD and IMD can be written:

$$\text{IM}_2 = 2 \cdot \text{HD}_2, \quad (2.74)$$

$$\text{IM}_3 = 3 \cdot \text{HD}_3. \quad (2.75)$$

Consequently, under small-nonlinearity conditions, there is a univocal correspondence between the HD and IMD; hence, only one of them needs to be specified [2.16]. Practically, it is preferable to measure IM3 rather than HD3 for two reasons. Firstly, as it has been mentioned above, the IM3 is a more important characteristic due to its higher contribution to the output-signal distortion. Secondly, IM3 is easier to measure as it is three times larger than HD3. For these reasons, IM3 has become a commonly used measure for the characterisation of PA distortions. Numerous methods have been developed with the aim to improve the IM3 performance [2.17]. These methods will be examined minutely in Chapter 3.

### 2.4.9 Cross Modulation Distortion

Cross Modulation (CM) in a nonlinear circuit with a multi-tone excitation is the phenomenon of transferring amplitude modulation from one signal to another. CM occurs because under a multi-tone excitation the degree of compression for a given signal depends on the instantaneous level of the other signals. Therefore, the amplitude modulation of one of the signals can appear on the other carriers.

CM is usually analysed using a two-tone signal with one unmodulated signal and the other being AM-modulated [2.4]:

$$V_{IN}(t) = V_1 \cdot \cos(\omega_1 t) + V_{2\_AM}(t) \cdot \cos(\omega_2 t), \quad (2.76)$$

$$V_{2\_AM}(t) = V_2 \cdot (1 + m \cdot \cos(\omega_m t)), \quad (2.77)$$

where  $m$  is the modulation index, and  $\omega_m$  is the modulating frequency.

Substituting (2.76) into (2.48) and completing trigonometric transformations gives the expression for the fundamental-frequency output signal:

$$\begin{aligned} V_{OUT}^{FUND}(t) = & g_1 \cdot (V_1 \cdot \cos(\omega_1 t) + V_{2\_AM}(t) \cdot \cos(\omega_2 t)) \\ & + \frac{3g_3}{4} \cdot (V_1^3 \cdot \cos(\omega_1 t) + V_{2\_AM}^3(t) \cdot \cos(\omega_2 t)) \\ & + \frac{3g_3}{2} \cdot V_1 \cdot V_{2\_AM}(t) \cdot (V_{2\_AM}(t) \cdot \cos(\omega_1 t) + V_1 \cdot \cos(\omega_2 t)). \end{aligned} \quad (2.78)$$

In (2.78), the last term is the CM product. The CM is produced by the odd-order terms in (2.48). After substituting (2.77) into (2.78) and completing trigonometric transformations, the CM product at  $\omega_1$  can be written as:

$$V'_{\text{CM}}(t) = \frac{3g_3}{2} \cdot V_1 \cdot V_2^2 \cdot (1 + m \cdot \cos(\omega_m t))^2 \cdot \cos(\omega_1 t). \quad (2.79)$$

In (2.79), the distorted AM of the signal at  $\omega_2$  appears at  $\omega_1$ . After expanding (2.79), one can see that the CM is produced by the  $\cos(\omega_m t)$  and  $\cos^2(\omega_m t)$  terms of (2.79). The term at  $\cos^2(\omega_m t)$  can be ignored because it is small, and the resulting CM product looks like:

$$V_{\text{CM}}(t) = 3g_3 \cdot V_1 \cdot V_2^2 \cdot m \cdot \cos(\omega_m t) \cdot \cos(\omega_1 t). \quad (2.80)$$

The overall output signal formed by the linear and CM term is:

$$V_{\text{OUT\_CM}}(t) = g_1 \cdot V_1 \cdot \left[ 1 + \frac{3g_3}{g_1} \cdot V_2^2 \cdot m \cdot \cos(\omega_m t) \right] \cdot \cos(\omega_1 t). \quad (2.81)$$

A measure of the CM is the cross-modulation distortion factor, which is defined as the ratio of the transferred amplitude modulation index to the original amplitude modulation index [2.10], [2.18]. In (2.81), the transferred amplitude modulation index equals to  $\frac{3g_3}{g_1} \cdot V_2^2 \cdot m$ , and hence:

$$\text{CM} = \frac{3g_3}{g_1} \cdot V_2^2, \quad (2.82)$$

where CM is the cross-modulation distortion factor.

From (2.82), it can be concluded that the CM on the first carrier is independent of the magnitude of this carrier, and depends only on the square magnitude of the second carrier. Comparing (2.68) and (2.82), one can see that the ratio  $\text{CM}/\text{IM}_3 = 4$ .

### 2.4.10 Adjacent Channel Power Ratio

Adjacent Channel Power Ratio (ACPR) is a characteristic aimed at quantifying intermodulation distortions of modulated signals in wireless communication systems. ACPR shows how much a signal spreads into adjacent channels due to nonlinearities of a PA. ACPR is defined as the ratio of the total adjacent-channel integrated power (intermodulation signal) to the power of the useful signal band [2.19]:

$$\text{ACPR} = \frac{P_{\text{ACL}} + P_{\text{ACH}}}{P_{\text{S}}}, \quad (2.83)$$

or

$$\text{ACPR} = \frac{\int_{\omega_L}^{\omega_1} S(\omega) d\omega + \int_{\omega_2}^{\omega_U} S(\omega) d\omega}{\int_{\omega_1}^{\omega_2} S(\omega) d\omega}, \quad (2.84)$$

where  $P_{\text{ACL}}$  and  $P_{\text{ACH}}$  is the total integrated power of the lower and upper adjacent channels,  $P_{\text{S}}$  is the total integrated power of the considered fundamental signal (useful signal);  $S(\omega)$  is the power spectral density function of the output signal,  $\omega_1$  and  $\omega_2$  are the band limits of the fundamental signal, and  $\omega_L$  and  $\omega_U$  are the limits of the total considered band. A graphical representation of the used parameters is given in Figure 2-21.

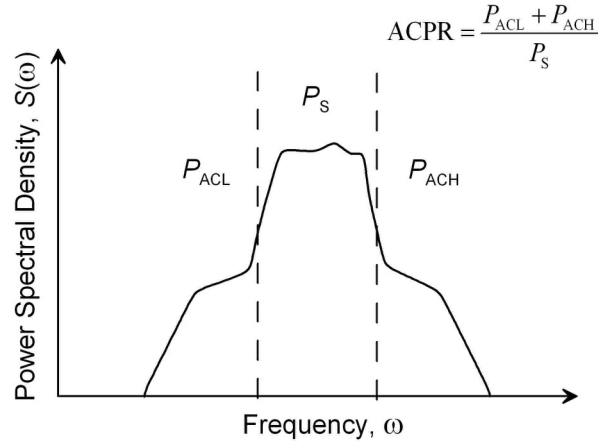


Figure 2-21: Graphical representation of ACPR

ACPR is related to IMD. N. B. De Carvalho and J. C. Pedro in [2.9], [2.19]-[2.20] derived empirical relationships between the ACPR of a multi-tone or complex signal and the two-tone IMD ratio  $P_{\text{IM3}}$ :

$$\text{ACPR}_{\text{dBc}} = P_{\text{IM3}} + 10 \log \left[ \frac{n^3}{4A + B} \right], \quad (2.85)$$

where  $P_{\text{IM3}}$  is the third-order intermodulation distortion ratio in dBc given by (2.73),  $n$  is the number of carriers,  $A$  and  $B$  are coefficients given by the following:

$$A = \frac{2n^3 - 3n^2 - 2n}{24} + \frac{\text{mod}(n/2)}{8}, \quad (2.86)$$

$$B = \frac{n^2 - \text{mod}(n/2)}{4}, \quad (2.87)$$

where  $\text{mod}(x/y)$  is the remainder of  $x$  divided by  $y$ .

There are two ways of measuring ACPR. The first way is measuring the total output power and the power in adjacent channels and calculating their ratio in logarithmic units. The second way is based on calculating the logarithmic ratio of the measured output power in a small bandwidth around the carrier to the power in the adjacent channel, which has the bandwidth equal to those of the main-channel signal. Due to easier practical implementation, the second way is more popular.

## 2.5. Conclusion

In this Chapter, the fundamental parameters of power amplifiers, traditional methods of amplification and nonlinear analysis have been presented. Power amplifiers are characterised by their efficiency and linearity, which depend on the mode of operation. Classes A, B, and AB preserve the input signal waveform and hence offer more linear but less efficient amplification compared to classes C, D, E, F, G, H and S. In order to increase the efficiency, a PA is designed to operate in a nonlinear mode, and an additional device is used for its linearisation. A nonlinear analysis is carried out for characterising the PA distortions in a nonlinear mode of operation. The power series analysis is a convenient and powerful tool for deriving the relations between the PA parameters and nonlinearity measures as well as for designing and quantifying the performances of linearising circuits.

## 2.6. References

- [2.1] D. Pozar, *Microwave Engineering*, 3<sup>rd</sup> edition, John Wiley & Sons, 2004, ISBN 0471170968.
- [2.2] P. B. Kenington, *High Linearity RF Amplifier Design*, Artech House Inc., 2000, ISBN 1580531431.
- [2.3] S. C. Cripps, *RF Power Amplifiers for Wireless Communications*, Artech House Inc., 1999, ISBN 0890069891.
- [2.4] S. Maas, *Nonlinear Microwave and RF Circuits*, Artech House Publishers, 2003, ISBN 1580534848.
- [2.5] J. K. Cavers, "Amplifier linearization using a digital predistorter with fast adaptation and low memory requirements," *IEEE Transactions on Vehicular Technology*, vol. 39, no. 4, pp. 374–382, Nov. 1990.
- [2.6] F. H. Raab, et al., "Power amplifiers and transmitters for RF and microwave," *IEEE Transactions on Microwave Theory and Techniques*, vol. 50, no. 3, pp. 814–826, Mar. 2002.
- [2.7] B. Sahu, and G. A. Rincon-Mora, "A high-efficiency linear RF power amplifier with a power-tracking dynamically adaptive buck-boost supply," *IEEE Transactions on Microwave Theory and Techniques*, vol. 52, no. 1, pp. 112–120, Jan. 2004.
- [2.8] M. Albulet, *RF power amplifiers*, Noble Publishing, Atlanta, GA, 2001.
- [2.9] J. C. Pedro, and N. B. De Carvalho, "On the use of multitone techniques for assessing RF components' intermodulation distortion," *IEEE Transactions on Microwave Theory and Techniques*, vol. 47, no. 12, pp. 2393–2402, Dec. 1999.
- [2.10] G. Collins, and D. W. Runton, "Nonlinear analysis of power amplifiers," *Microwave Journal*, vol. 50, no. 9, p. 164, Sept. 2007.
- [2.11] J. Vuolevi, T. Rahkonen, *Distortion in RF Power Amplifiers*, Artech House Inc., 2003, ISBN 1580535399.

- [2.12] P. Jardin, and G. Baudoin, "Filter look up table method for power amplifiers linearization," *IEEE Transaction on Vehicular Technology*, vol. 56, no. 3, pp. 1076–1087, Apr. 2007.
- [2.13] S. Yoon, "Static and dynamic error vector magnitude behavior of 2.4-GHz power amplifier," *IEEE Transactions on Microwave Theory and Techniques*, vol. 55, no. 4, pp. 643-647, Apr. 2007.
- [2.14] R.G. Meyer, and A.K. Wong, "Blocking and desensitization in RF amplifiers," *IEEE Journal of Solid-State Circuits*, vol. 30, no. 8, pp. 944-946, Aug. 1995.
- [2.15] G. Palumbo, and S. Pennisi "High-frequency harmonic distortion in feedback amplifiers: analysis and applications." *IEEE Transactions on Circuits and Systems-I: Fundamental Theory and Applications*, vol. 50, no. 3, pp. 328-340, Mar. 2003.
- [2.16] W. Sansen, "Distortion in elementary transistor circuits," *IEEE Transactions on Circuits and Systems-II: Analog and Digital Signal Processing*, vol. 46, no. 3, pp. 315-325, Mar. 1999.
- [2.17] C. S. Aitchison, M. Mbabele, M. R. Moazzam., D. Budimir, and F. Ali, "Improvement of third order intermodulation products of RF and microwave amplifiers by injection," *IEEE Transactions on Microwave Theory and Techniques*, vol. 49, no. 6, pp. 1148-1154, June 2001.
- [2.18] R. G. Meyer, M. J. Shensa, and R. Eschenbach, "Cross modulation and intermodulation in amplifiers at high frequencies," *IEEE Journal of Solid-State Circuits*, vol. 7, no. 1, pp. 16-23, Feb. 1972.
- [2.19] N. B. De Carvalho, and J. C. Pedro, "Compact formulas to relate ACPR and NPR to two-tone IMR and IP3," *Microwave Journal*, vol. 42, no. 2, pp. 70–84, Dec. 1999.
- [2.20] N. B. Carvalho and J.C. Pedro, "Multi-tone intermodulation distortion performance of 3<sup>rd</sup> order microwave circuits," *IEEE International Microwave Theory and Techniques Symposium Digest*, pp. 763–766, June 1999.

---

## 3. OVERVIEW OF LINEARISATION TECHNIQUES

### 3.1. Introduction

Power amplification of RF signals faces a problem of achieving high linearity and efficiency at the same time. Efficiency is maximised when a PA operates with a small back-off, i.e. close to the saturation region. However, in this mode of operation, nonlinear distortions are produced, which degrade the system linearity. It means that efficiency and linearity are mutually exclusive requirements. A trade-off between them is usually sought for each particular application [3.1]-[3.2]. For handset applications, the most important requirement is efficiency, as it is important to use the handset battery efficiently in order to increase the talk-time. For base stations, the major issue is linearity, as the down-link signal must be highly-linear in order to achieve a small error rate and a good quality of reception in mobile terminals. Solutions to the efficiency problem, called efficiency enhancement techniques, are already well-developed and investigated whereas the existing linearity improvement techniques still have considerable limitations and are being the subject of many recent research works [3.2].

A general practical approach for achieving a highly linear efficient transmitter is increasing the PA efficiency at the cost of linearity at the first stage and providing external linearisation afterwards in order to fulfil the linearity requirements [3.3]. Consequently, linearisation of power amplifiers is an important task aimed to satisfy the exacting requirements put on modern wireless transmitters.

Many linearisation techniques have been developed recently. They can be classified into three major categories:

- feedback methods;
- feedforward linearisation;
- predistortion techniques.

However, the classification of linearisation techniques is arguable. For example, some authors separate techniques based on the injection of second-order products into an independent group [3.4]-[3.6] whereas others place them within the mentioned categories [3.1], [3.7]-[3.8]. There are also Envelope Elimination and Restoration (EER) and Linear Amplification using Nonlinear Components (LINC) methods traditionally

associated with the efficiency enhancement techniques, however, being capable of increasing linearity as well [3.1]-[3.2].

The feedback methods incorporate RF feedback techniques, divided into passive and active RF feedback, and envelope or modulation feedback techniques, including polar and Cartesian loops. The predistortion methods are divided into analogue predistortion and Digital Predistortion (DPD). The latter includes Look-Up-Table (LUT), polynomial and baseband-components injection DPD techniques.

The current chapter presents an overview of all the major techniques used to increase the linearity of wireless transmitters, describing the concepts of the techniques and highlighting their advantages and drawbacks.

### 3.2. Feedback Linearisation Techniques

Feedback is a relatively simple and straightforward method based on the idea of comparing the linear input signal with the attenuated distorted output signal available through the feedback chain and correcting the input signal according to the results of that comparison. There are many types of feedback linearisation techniques [3.9]-[3.20]. They can be classified as RF feedback, further divided into active and passive RF feedback, and modulation or envelope feedback, including polar and Cartesian loops. The former is also known as direct feedback techniques, and the latter refers to indirect feedback techniques [3.2]. The main difference between the RF and modulation feedback is that the first method implies comparison between the RF signals whereas the second one includes comparison between the modulation components of the signal (e.g. I and Q components).

The generalised feedback system for a PA is illustrated in Figure 3-1. It consists of an amplifier with the gain  $G$ , a feedback path and a comparator. The feedback chain in the simplest case contains only a voltage divider with the gain  $1/K$ , but in real systems it may include many signal-processing components. The comparator produces an error signal  $x_e(t)$  from the linear input signal  $x(t)$  and the reference signal  $y_r(t)$ , obtained from the distorted output signal  $y(t)$  attenuated in the feedback path. In the simplest case the comparator is a subtracter, which calculates the error signal by subtracting the reference signal from the system input signal.

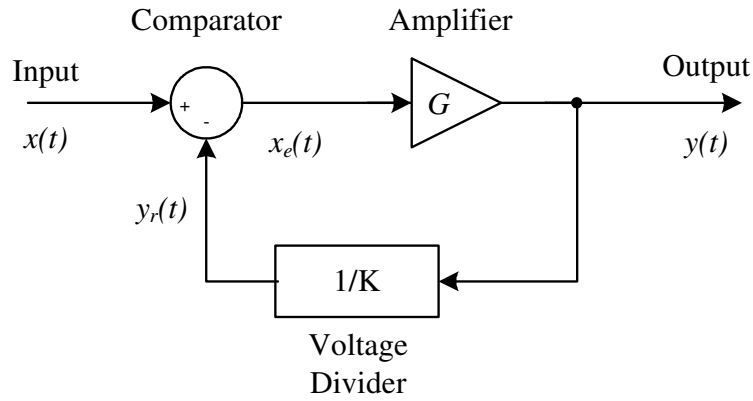


Figure 3-1: General feedback system for a PA

For the feedback system presented in Figure 3-1 an input signal  $x(t)$  outcomes in an error signal  $x_e(t)$  appearing at the input of the PA. The amplified output signal can be found as:

$$y(t) = G \cdot x_e(t). \quad (3.1)$$

Further, this signal is forwarded back to the comparator through the voltage divider producing a reference signal:

$$y_r(t) = \frac{y(t)}{K}. \quad (3.2)$$

Using this reference signal a new error signal is obtained:

$$x_e(t) = x(t) - y_r(t). \quad (3.3)$$

After combining (3.1), (3.2) and (3.3), a relationship between the system input and output signals can be obtained:

$$y(t) = \frac{G \cdot K}{G + K} \cdot x(t). \quad (3.4)$$

Using the gain of the feedback chain  $G_{FB} = \frac{1}{K}$  in place of the attenuation ratio, (3.4) can be re-written as:

$$y(t) = \frac{G}{1 + G \cdot G_{FB}} \cdot x(t). \quad (3.5)$$

From (3.5) one can see that the composite gain of the entire circuit is:

$$G_C = \frac{G}{1 + G \cdot G_{FB}}. \quad (3.6)$$

The relationship demonstrates that the price of achieving a more stable amplified output signal by a feedback method is a reduction in the composite gain.

The effect of distortion reduction by a feedback method can be described empirically as following. The noise and distortion introduced by the PA are included in (3.1) by adding a new summand  $d(t)$ :

$$y(t) = G \cdot x_e(t) + d(t). \quad (3.7)$$

Combining (3.1), (3.2) and (3.3) yields:

$$y(t) = \frac{K \cdot (G \cdot x(t) + d(t))}{G + K}. \quad (3.8)$$

If the amplifier gain  $G$  is much greater than the division ratio  $K$  of the feedback chain,  $G \gg K$ , then  $G + K \approx G$  and (3.8) can be approximated by:

$$y(t) \approx K \cdot x(t) + \frac{K}{G} \cdot d(t). \quad (3.9)$$

From the obtained relation one can see that the feedback chain reduces the distortion of the PA by the factor  $K/G$  at a price of degrading the overall gain.

### 3.2.1 RF Feedback

RF feedback systems imply subtracting of the output signal from the input signal at RF frequencies without demodulation or downconversion. They are used mainly to linearise individual amplification stages rather than the whole transmitter due to stability problems in feedback loops. RF feedback can be implemented as a passive or active feedback.

Passive RF feedback systems [3.1], [3.9] use passive components in the feedback path similar to the voltage divider shown in Figure 3-1. Such systems have a stable performance at a price of losing the overall gain. They are used mainly to improve the broadband performance of an amplifier by gain levelling, rather than to reduce IMD or harmonic distortions [3.1]. As the gain of a PA is usually higher at lower frequencies, the levelling is achieved by reducing the gain at lower frequencies by the action of feedback in order to attain the equal gain over the whole frequency range. Consequently, the chain must provide a greater feedback at lower frequencies, in other words to have a low-frequency response.

Active RF feedback systems [3.10]-[3.11] include an auxiliary amplifier in the feedback path in place of the voltage divider as shown in Figure 3-2. It helps to reduce the power dissipated in the feedback components.

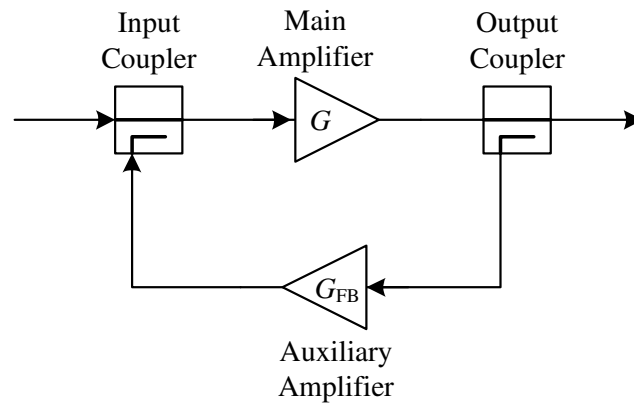


Figure 3-2: Active feedback linearisation system

The overall gain of an active RF feedback system can be found according to (3.6), where  $G$  stands for the main amplifier's gain and  $G_{FB}$  denotes the gain of the auxiliary amplifier. Using an additional amplifier it is possible to reduce the distortion introduced by the main PA. If the auxiliary amplifier operates in a nonlinear mode and produces distortion of the fed-back signal, with the proper adjustment of its gain and phase it is possible to obtain the compensation of the main amplifier's distortion. Employing this method a 12-dB reduction in IMD was reported in [3.10]-[3.11]. However, the gain reduction and dependence of the IMD improvement on the input power level were discovered as well. These disadvantages limit potential applications of the conventional active RF feedback techniques.

Several modified feedback techniques have been proposed in order to remove the mentioned drawbacks [3.12]-[3.13]. Distortion feedback is one of the techniques aimed at overcoming the disadvantages of the conventional RF feedback methods [3.1], [3.13]. The block diagram shown in Figure 3-3 describes the operation of the distortion feedback technique.

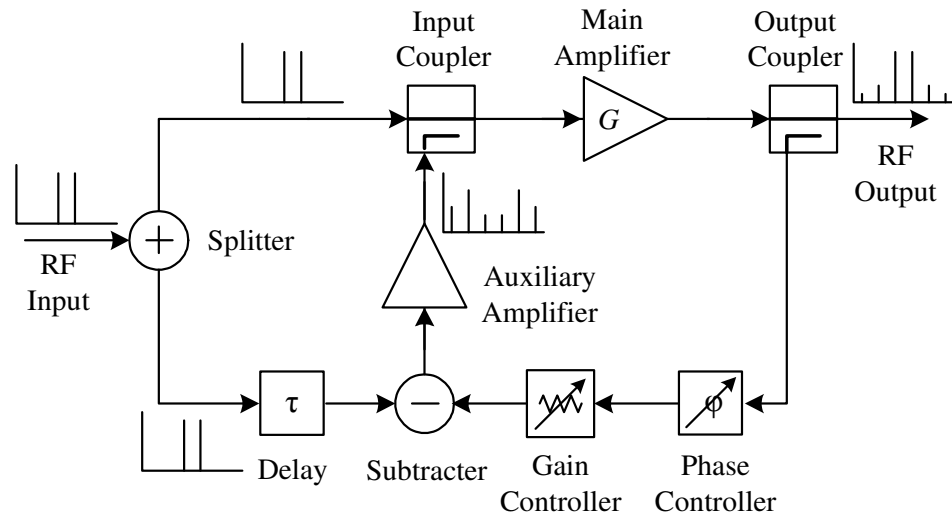


Figure 3-3: Distortion feedback linearisation system

The input signal is divided into two parts: one part is used to obtain an error signal by comparison with the output signal; and the other part with addition of the error signal is delivered to the PA input. The fundamental components of the fed-back signal are cancelled in the subtractor and only nonlinear distortion components are added to the PA input signal, providing compensation of the main amplifier's distortion. The technique is a combination of the feedback and feedforward approaches. Its performance depends on the quality of the cancellation process, putting exacting requirements on the gain and phase controllers, which ideally should be able to adjust to the shift in PA electrical parameters caused by different signal loading, aging or temperature change.

Distortion feedback technique was investigated in [3.13], where the improvements in IMD of 6 dB were achieved for a 300-MHz PA with a 10-MHz bandwidth. The small linearity attained by this technique is not enough for modern communication systems. Moreover, feedback systems have a significant problem at RF frequencies due to the time delay between the appearance of the signal at the PA output and the subtraction of the input and reference signals. Higher delays result in a smaller signal bandwidth in which a stable operation can be achieved. With increase in the RF frequency or modulation bandwidth it is becoming difficult to achieve operation stability in the feedback system. Therefore, RF feedback is not suitable for wideband applications, and various forms of indirect feedback, such as polar or Cartesian loop, are used.

### 3.2.2 Modulation Feedback

The modulation or envelope feedback technique [3.14]-[3.18] is an indirect feedback technique which aims to reduce stability problems inherent to RF feedback systems by operating at modulation frequencies. The general layout of a modulation feedback system is illustrated in Figure 3-4.

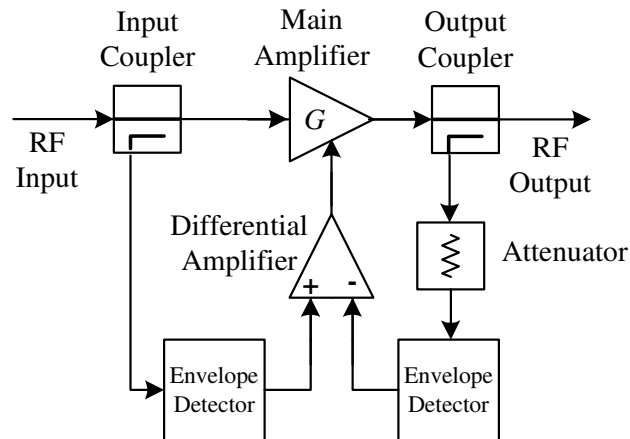


Figure 3-4: General layout of a modulation feedback system

The system has two matched envelope detectors coupled to the input and output of the main amplifier, and a differential amplifier, which produces an amplitude error-correction signal from the comparison of the detected envelopes. The error signal controls the gain of the main PA. In such a system, the output envelope is forced to replicate the input envelope, which leads to reduction in spectral distortion. However, this is valid only for power levels below saturation whereas in saturation the system performance degrades dramatically. The non-coherent envelope detection is not able to correct phase distortions, hence the considered technique does not correct AM/PM distortions. Moreover, the gain of the differential amplifier needs to be higher for lower power levels, which leads to stability problems. Wideband performance of the modulation feedback system is also limited by the differential amplifier, which may be not fast enough to proceed signals with high bit rates in order of megahertz.

The inability of non-coherent envelope feedback to correct phase distortions in a PA stimulated the development of new methods capable of compensating AM/AM and AM/PM distortions. Two techniques which realise this are polar and Cartesian loops.

Both of them refer to the linearisation of a complete transmitter rather than a single PA. The main difference between the polar and Cartesian systems is the form in which the signal information is processed, either a polar form with the separate consideration of the amplitude and phase modulation or a Cartesian form with the separate processing of the in-phase I and quadrature Q components.

### 3.2.3 Polar Loop

The polar loop [3.15]-[3.16] is an extension of the modulation feedback technique, which performs both amplitude and phase corrections. A block diagram of the polar loop system is shown in Figure 3-5.

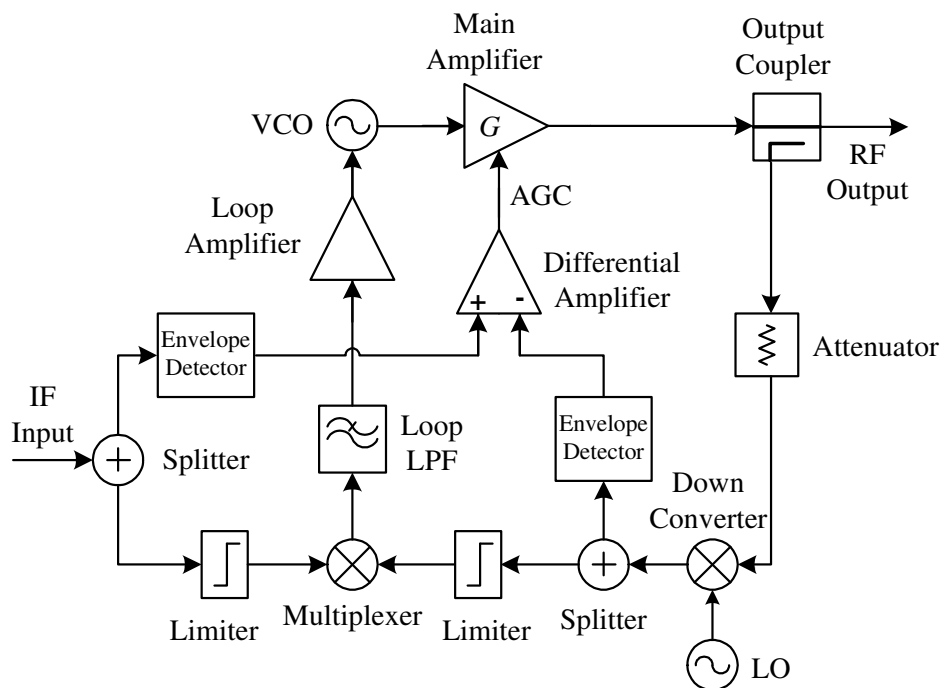


Figure 3-5: Polar-loop feedback system

The system uses downconversion and corrects AM/AM and AM/PM distortions by two separate loops. The input is an amplitude and phase modulated Intermediate Frequency (IF) signal. The PA output signal is coupled, attenuated and downconverted to IF. Both input and output signals are divided into the amplitude and phase parts using envelope detectors and limiters respectively. As a result, two separate signals are

obtained, one of them containing only the amplitude modulation and the other having only the phase modulation of the initial signal. The amplitude-modulated signals are compared in the differential amplifier. Its output error signal provides Automatic Gain Control (AGC) for the main amplifier. The phase-modulated signals are compared using the multiplexer and the low-pass filter. The output error signal controls the Voltage-Controlled Oscillator (VCO). Therefore, both the AM/AM and AM/PM distortion compensations are achieved.

The advantage of the polar loop technique is its ability to provide the amplitude and phase corrections and hence to increase the linearity of a PA with the envelope peaks going into the compression region. The major drawback is the bandwidth limitation due to limited comparison speed of the differential amplifier and phase delays in the feedback loop, resulting in the technique being unsuitable for wideband and multi-carrier applications.

### 3.2.4 Cartesian Loop

The Cartesian loop [3.17]-[3.18] is another type of the modulation feedback technique that offers amplitude and phase corrections. A block diagram of the Cartesian loop system is shown in Figure 3-6.

The system uses a baseband form of the input signal  $S(t)$ , splitting it into the in-phase  $I(t)$  and quadrature  $Q(t)$  components, which contain both the AM and PM information:

$$S(t) = I(t) \cdot \cos(\omega_c t) + Q(t) \cdot \sin(\omega_c t), \quad (3.10)$$

where  $\omega_c$  is the RF carrier frequency.

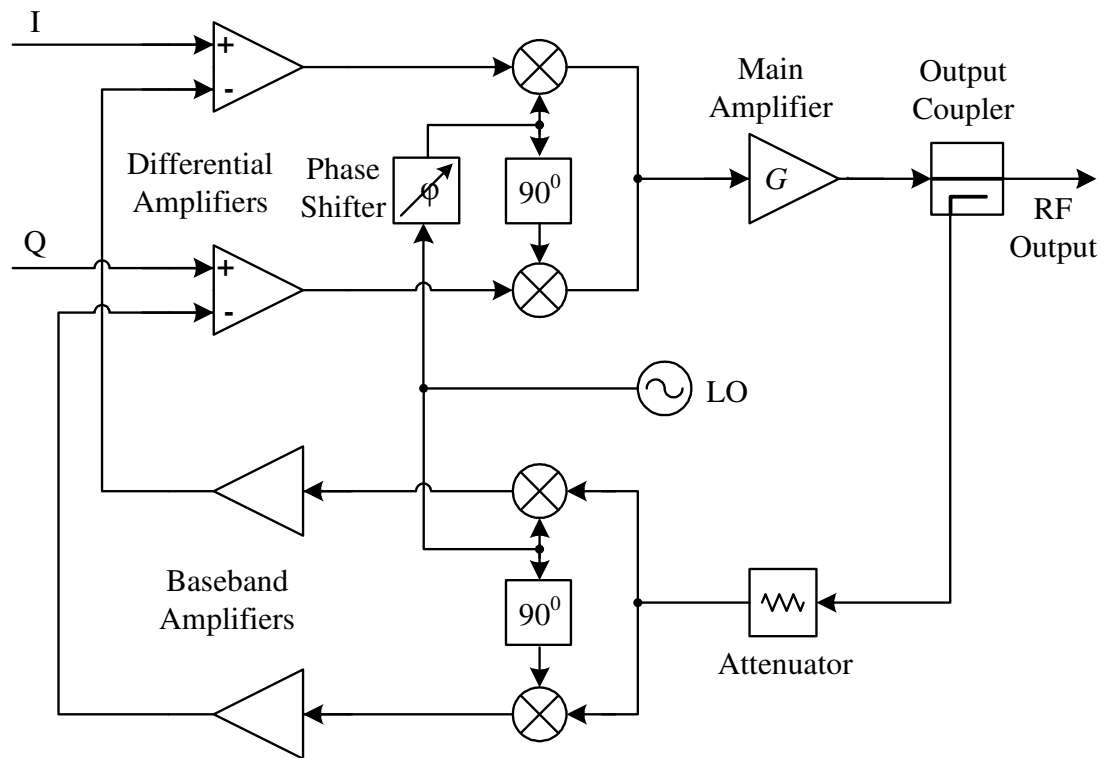


Figure 3-6: Cartesian-loop feedback system

The operation of Cartesian loop is similar to those of polar loop. The input and output signals are split into the I and Q components by the broadband phase-shifting network and compared in differential amplifiers. The output signals of the I- and Q-chain differential amplifiers are upconverted and combined to produce the complex RF signal, which is fed into the main PA. The phase shifter is introduced with the aim of maintaining the constant relationship between the input and fed-back signals. The phase shift of the Local Oscillator (LO) varies with the change in temperature and power levels; hence the system may suffer from stability problems. The wideband performance of the Cartesian loop is better than those of the polar loop; however it is also limited by delays in the feedback chain and bandwidth properties of the feedback-loop components. Another advantage over the polar loop is its easier implementation, because a baseband signal in the I/Q form is usually available from the digital circuit.

Cartesian loop forms a background for digital linearisation techniques, based on correcting I and Q signals by Digital Signal Processing (DSP) methods [3.2], [3.19]. Such an approach allows overcoming the bandwidth limitation issue inevitable in feedback techniques. However, in order to achieve this, the DSP operations with I and Q signals need to be pre-programmed and performed in an open-loop circuit [3.20],

because the close-loop DSP operations have a low speed, which limits the system bandwidth.

### 3.3. Feedforward Linearisation Techniques

Feedforward is an old technique used to linearise power amplifiers for many years [3.8], [3.12], [3.21]-[3.24]. It is based on the idea of compensating a PA distortion at the output by subtracting the distortion components from the overall output signal. The distortion components are obtained and delivered to the output through the feedforward chain. The general layout of a feedforward system is presented in Figure 3-7. It consists of two loops: a signal cancellation loop and an error cancellation loop. The first one is used to remove the fundamental signal and obtain the IMD products. The second loop is necessary to subtract the adjusted distortion products from the overall output in order to obtain the linear amplified signal.

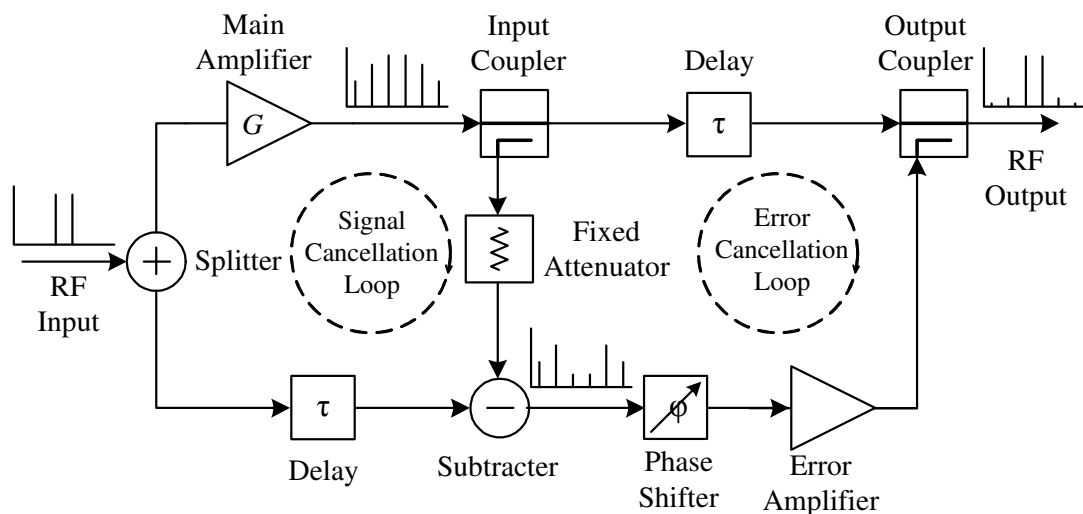


Figure 3-7: General layout of a feedforward system

The input signal is split into two parts: one is amplified in the main nonlinear amplifier and the other delayed and used as a reference signal to obtain IMD components. The part of the amplified signal is coupled, attenuated and fed into the subtractor, where after subtracting the reference signal the resulting distortion components are achieved. The obtained error signal is amplified in the error amplifier to

achieve the proper level and added in antiphase to the main amplified output signal using the output coupler and phase shifter.

By applying the distortion compensation process at the output of the circuit the fundamental drawbacks of the feedback methods, instability and bandwidth limitations due to time delays, are removed. Among all the close-loop techniques, feedforward has the best linearising performance and a wideband signal capability. Improvements of 20-30 dB in ACPR and IMD are expected to be achieved in a single-loop feedforward system and an up to 50 dB improvement can be obtained using multiple loops [3.2]. Feedforward methods have found a wide application for linearising transmitters in wireless base stations.

However, the price of this improvement is the need of an additional class-A amplifier necessary to boost the correction signal. The gain of this amplifier must be high, close to the main PA gain. Also a high accuracy in gain and phase tracking must be maintained over the frequency band and kept constant with time and environmental changes. These lead to the reduced efficiency of the feedforward system and the increased complexity of the overall circuit. Moreover, the linear properties of the auxiliary amplifier limit the potential performance, as a possibility of introducing additional distortions by the auxiliary amplifier appears.

An adaptive feedforward linearisation system, proposed by S. P. Stapleton in [3.24] is shown in Figure 3-8. The adaptation is introduced by the complex gain adjusters and adaptation controllers in both the signal cancellation and error cancellation loops. The adaptation controller in the signal cancellation loop manages the adjustments of the gain and phase of the input signal in such a way that the reference signal is precise enough to eliminate the fundamental components from the main amplifier's output by subtraction. This adaptation controller uses the reference and error signals in order to provide the adjustments. The second adaptation controller, situated in the error compensation loop, regulates the adjustments of the gain and phase of the error signal with the aim of achieving a precise compensation of the distortion at the output of the circuit. This controller uses the error signal and the total system output in order to run the adjustments.

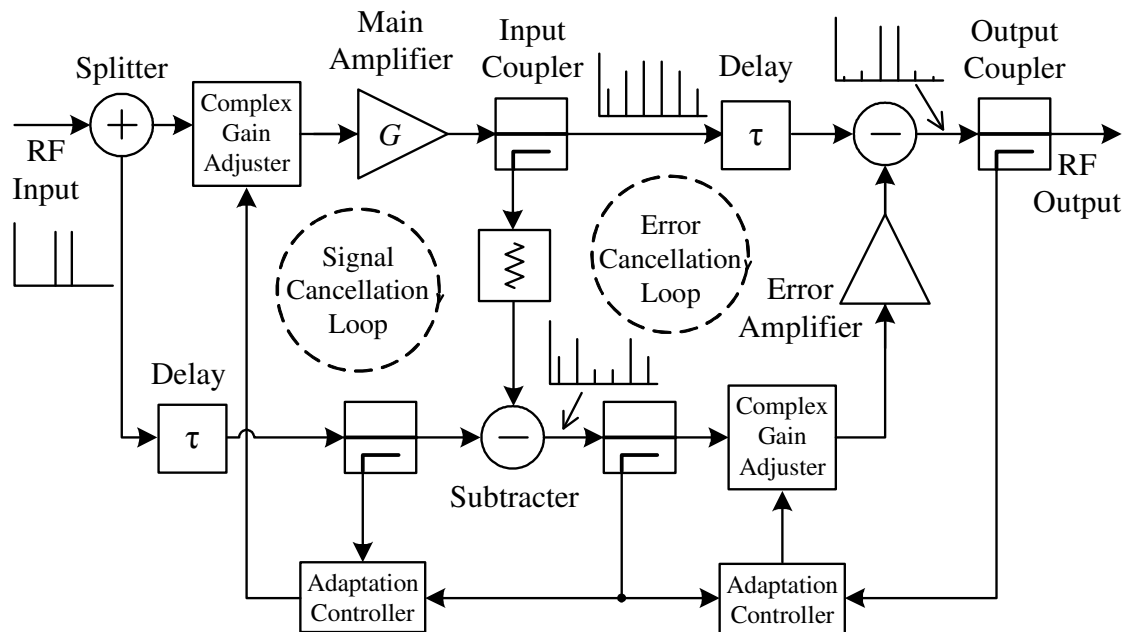


Figure 3-8: Block diagram of an adaptive feedforward system

Summarising the stated above, the main strengths and weaknesses of the feedforward technique can be formulated. Generally, feedforward methods exhibit a good linearising performance with a high stability and wideband signal capability. They are also able to lower memory-related distortions because the error signal includes distortions produced by the PA memory effects [3.24]. The main drawbacks of the feedforward techniques are their low efficiency and high complexity resulting in the high cost and big size of the circuit.

### 3.4. Envelope Elimination and Restoration

Envelope Elimination and Restoration (EER) is a technique suitable for linearity and efficiency enhancement proposed by Kahn in [3.25]. The main idea is based on separating the input signal into two parts, one containing the AM and the other having the PM information, amplifying of the PM modulated signal and adding the envelope information by a conventional amplitude modulation [3.1], [3.26]-[3.27]. A block diagram explaining the operation of the EER technique is shown in Figure 3-9.

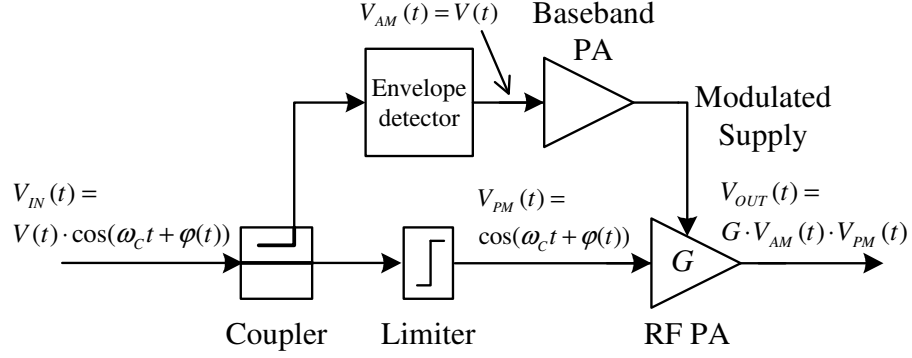


Figure 3-9: Envelope elimination and restoration system

The input signal, given by:

$$V_{IN}(t) = V(t) \cdot \cos(\omega_c t + \varphi(t)), \quad (3.11)$$

where  $V(t)$  and  $\varphi(t)$  is the amplitude and phase modulation on the input signal and  $\omega_c$  is the carrier frequency, is separated into the AM and PM parts using an envelope detector and a limiter. The envelope detector produces a baseband signal, which includes the amplitude modulation of the input signal:

$$V_{AM}(t) = V(t). \quad (3.12)$$

The limiter forms an RF phase-modulated signal with a constant envelope:

$$V_{PM}(t) = \cos(\omega_c t + \varphi(t)). \quad (3.13)$$

The limiter ideally removes AM/PM distortions of the system. The obtained PM signal is amplified in a high-efficiency power amplifier operating in class-C or switch modes, class-D or -E. These modes preserve the PM information while maintaining a high efficiency. The AM signal is amplified in a baseband amplifier and used to modulate the final RF signal. The modulation of the final RF signal, or restoration of the envelope, is achieved by modulating the collector or power supply of the final RF amplifier:

$$V_{OUT}(t) = G \cdot V_{AM}(t) \cdot V_{PM}(t), \quad (3.14)$$

where  $G$  is the gain of the RF amplifier.

As mentioned above, such an approach achieves high efficiency by using the RF amplifier in class-C, -D or -E. It also eliminates AM/PM distortions of the fundamental signal in the RF PA and hence increases linearity of the system. However, a practical implementation of the EER technique is challenging because of the following issues. Firstly, the amplification of a baseband signal to a sufficient level consumes much

power, and hence degrades the overall efficiency [3.2]. Furthermore, high linearity in the baseband amplifier must be maintained during the process. Secondly, the EER system has a large number of potential sources of IMD, such as: bandwidth of the envelope modulator, delays between the AM and PM paths, nonlinearity of the envelope detector, AM/PM conversions in the limiter and RF amplifier while applying a high-level amplitude modulation, and cut-off in the RF PA at low envelope levels [3.1]. Finally, EER is extremely sensitive to possible delays between the envelope and phase-modulated paths [3.3].

### 3.5. Linear Amplification using Nonlinear Components

Linear Amplification using Nonlinear Components (LINC) is a technique aimed at achieving linear amplification at microwave frequencies originally proposed by Chireix in [3.28] and further developed by Cox in [3.29]. The main idea is achieving a linear input-output relation by a circuit containing nonlinear intermediate components [3.1], [3.30]-[3.31]. A simple block diagram illustrating the operation of the LINC technique is presented in Figure 3-10. It includes two highly-efficient nonlinear RF power amplifiers.

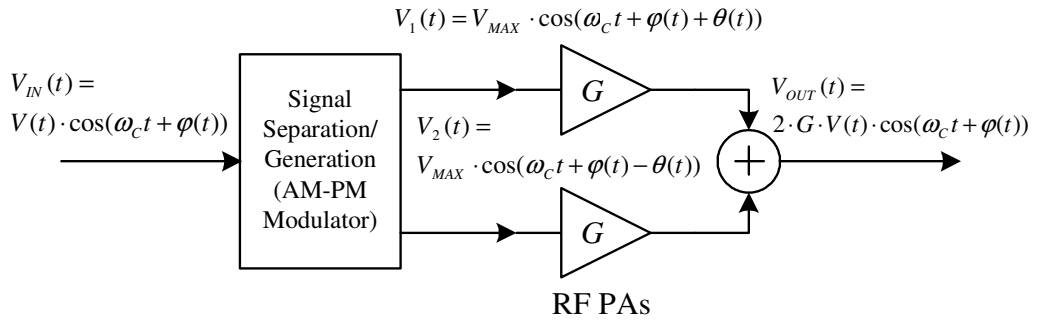


Figure 3-10: Linear amplification using nonlinear components system

The input signal, given by:

$$V_{IN}(t) = V(t) \cdot \cos(\omega_c t + \varphi(t)), \quad (3.15)$$

where  $V(t)$  and  $\varphi(t)$  is the amplitude and phase modulation on the input signal and  $\omega_c$  is the carrier frequency, is split into two phase-modulated signals with constant envelopes

by the AM-PM modulator, which acts as a signal separation component. The obtained signals are derived from (3.15) as follows. Using trigonometric transformations, (3.15) can be rewritten as:

$$V_{IN}(t) = \frac{V_{MAX}}{2} \cdot [\cos(\omega_c t + \varphi(t) + \theta(t)) + \cos(\omega_c t + \varphi(t) - \theta(t))], \quad (3.16)$$

where  $V_{MAX}$  is the amplitude of the input AM signal and  $\theta(t)$  is given by the following:

$$\theta(t) = \cos^{-1}\left(\frac{V(t)}{V_{MAX}}\right). \quad (3.17)$$

The obtained constant-envelope phase-modulated signals are:

$$V_1(t) = V_{MAX} \cdot \cos(\omega_c t + \varphi(t) + \theta(t)), \quad (3.18)$$

$$V_2(t) = V_{MAX} \cdot \cos(\omega_c t + \varphi(t) - \theta(t)). \quad (3.19)$$

Hence after amplifying in the PAs and combining the obtained signals, the resulting output signal will be:

$$V_{OUT}(t) = 2 \cdot G \cdot V(t) \cdot \cos(\omega_c t + \varphi(t)). \quad (3.20)$$

As can be seen from (3.20), the output signal is a linear amplification of the input signal, containing both the AM and PM modulation. The used RF power amplifiers are required to preserve only the phase information of the signal and hence can operate in a highly-efficient class-C, -D or -E. Theoretically, LINC is a very simple and elegant method of achieving both high linearity and efficiency. However, in practice, LINC has a number of limitations. First of all, the method is extremely sensitive to a gain or phase imbalance between the two paths [3.32]. If the amplifiers are not perfectly identical, they may introduce a significant distortion into the output signal. Secondly, it is practically difficult to realise a precise AM-PM modulator. Usually it has some inaccuracy in the signal separation and phase modulation [3.1]. Furthermore, its circuit has a high complexity, which increases the overall complexity of the system. Finally, LINC exhibits bandwidth limitations due to the gain and phase imbalance between the two paths and due to the fact that the bandwidths of the generated modulation signals are extremely high, usually 10 times more than the original bandwidth [3.1].

### 3.6. Injection Techniques

The most developed injection techniques [3.4]-[3.7], [3.33]-[3.35] imply injection of the distortion products generated by the second-order nonlinearity of the PA, which are either the difference frequency component or the second harmonic of the nonlinear PA output. These components can improve the IMD of the PA by mixing with the fundamental signal. Under a two-tone test, the difference frequency component is the one containing  $\cos(\omega_2 - \omega_1)t$ , which being mixed with the fundamental-frequency signal at  $\cos\omega_1t$  produces an additional IMD component at  $\cos(2\omega_1 - \omega_2)t$ . With the carefully selected phase shift, this “false” IMD component can decrease the “real” one, and hence improve the PA linearity. Similarly, the second harmonic at  $\cos 2\omega_1t$  after mixing with the fundamental harmonic at  $\cos\omega_2t$  generates an IMD term at  $\cos(2\omega_1 - \omega_2)t$ , which interferes with the IMD term produced by the amplifier’s nonlinearity, and, if the phase adjusted properly, decreases it. Consequently, the second-order products injection techniques are divided into two groups: difference-frequency and second-harmonic injection techniques.

The general block diagram illustrating operation of the second-order products injection technique is presented in Figure 3-11.

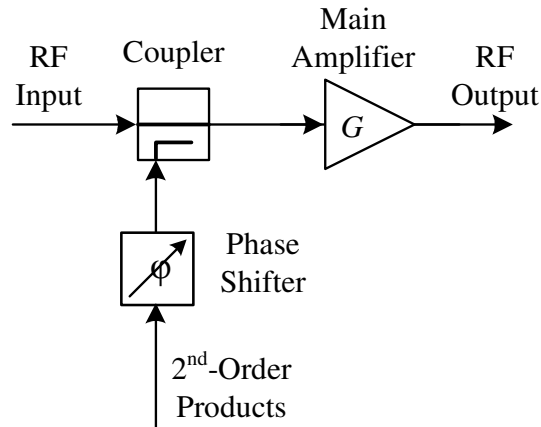


Figure 3-11: Second-order products injection system

The output voltage  $V_{OUT}(t)$  of the PA can be represented by the power series of the input voltage  $V_{IN}(t)$ :

$$V_{OUT}(t) = g_1 V_{IN}(t) + g_2 V_{IN}^2(t) + g_3 V_{IN}^3(t). \quad (3.21)$$

For a two-tone input signal, given by

$$V_{IN}(t) = V \cdot (\cos(\omega_1 t) + \cos(\omega_2 t)), \quad (3.22)$$

the output signal (3.21) can be calculated. As it was described in Section 2.4.3, the most dangerous in-band distortion component, IM3, which cannot be filtered out, presents the challenge for a linear PA design. Consequently, it must be eliminated or at least decreased. The analytical expression for the IM3 component, obtained by substituting of (3.22) into (3.21) and completing trigonometric transformations, looks like:

$$V_{IM3}(t) = \frac{3}{4} \cdot g_3 \cdot V^3 \cdot [\cos((2\omega_1 - \omega_2)t) + \cos((2\omega_2 - \omega_1)t)]. \quad (3.23)$$

In the obtained expression each summand represents an IM3 component situated on either side of the output signal.

If a difference-frequency component at  $\omega_2 - \omega_1$  is injected into the fundamental one, the input signal may be re-written as:

$$V_{IN}(t) = V_1 \cdot (\cos(\omega_1 t) + \cos(\omega_2 t)) + V_2 \cdot (\cos(\omega_2 - \omega_1)t + \varphi), \quad (3.24)$$

where  $\varphi$  is the phase of the phase shifter.

Substituting of (3.24) into (3.21) and completing trigonometric transformations gives the expression for the new IM3 products:

$$\begin{aligned} V_{IM3}(t) &= \frac{3}{4} \cdot g_3 \cdot V_1^3 \cdot [\cos((2\omega_1 - \omega_2)t) + \cos((2\omega_2 - \omega_1)t)] \\ &+ g_2 \cdot V_1 \cdot V_2 \cdot [\cos((2\omega_1 - \omega_2)t - \varphi) + \cos((2\omega_2 - \omega_1)t + \varphi)] \\ &+ \frac{3}{4} \cdot g_3 \cdot V_1 \cdot V_2^2 \cdot [\cos((2\omega_1 - \omega_2)t - 2\varphi) + \cos((2\omega_2 - \omega_1)t + 2\varphi)]. \end{aligned} \quad (3.25)$$

From the obtained expression one can see that the injected difference-frequency component results in the appearance of the new IM3 terms at the output. In (3.25) the first line represents the original IM3 produced by the PA. The second line contains the additional IM3 components obtained as a result of mixing the fundamental signal with the difference-frequency product. If the phase of the phase shifter is selected to be  $\varphi=180^\circ$ , and the amplitude of the injected component is properly adjusted,

$$V_2 = \frac{3g_3}{4g_2} \cdot V_1^2, \quad (3.26)$$

the terms in the first and second line of (3.25) will compensate each other. Consequently, the linearity of the PA will be improved. However, the last line in (3.25) contains the components which limit the performance of the system. They are smaller than the original IMD and have a negligible effect when the PA operates with a high

back-off, but they significantly degrade the difference-frequency technique performance when the PA goes into compression [3.4]. Moreover, practical difficulty to control the magnitude and phase adjustments results in imperfections of the circuit, which again decreases the overall linearity.

If second harmonics at  $2\omega_2$  and  $2\omega_1$  are injected, the input signal may be re-written as:

$$V_{IN}(t) = V_1 \cdot (\cos(\omega_1 t) + \cos(\omega_2 t)) + V_2 \cdot (\cos(2\omega_1 t + \varphi_1) + \cos(2\omega_2 t + \varphi_2)), \quad (3.27)$$

where  $\varphi_1$  and  $\varphi_2$  are the corresponding phase shifts.

By substituting (3.27) into the expression for output signal (3.21), the new IM3 can be found:

$$\begin{aligned} V_{IM3}(t) = & \frac{3}{4} \cdot g_3 \cdot V_1^3 \cdot [\cos((2\omega_1 - \omega_2)t) + \cos((2\omega_2 - \omega_1)t)] \\ & + g_2 \cdot V_1 \cdot V_2 \cdot [\cos((2\omega_1 - \omega_2)t + \varphi_1) + \cos((2\omega_2 - \omega_1)t + \varphi_2)] \\ & + \frac{3}{2} \cdot g_3 \cdot V_1 \cdot V_2^2 \cdot [\cos((2\omega_1 - \omega_2)t + \varphi_1 - \varphi_2) + \cos((2\omega_2 - \omega_1)t + \varphi_2 - \varphi_1)]. \end{aligned} \quad (3.28)$$

Similarly to (3.25), the obtained expression contains the new IM3 components, which can influence the original one. If the phase shifts  $\varphi_1 = \varphi_2 = 180^\circ$  and the magnitude of the injected second harmonic adjusted properly, according to (3.26), the IM3 is reduced. The linearising performance is also limited by the last line in (3.28) and the accuracy of practical gain and phase adjustments.

Conventionally, the source of the second-order injected products is a feedback chain of the PA [3.1], as shown in Figure 3-12.

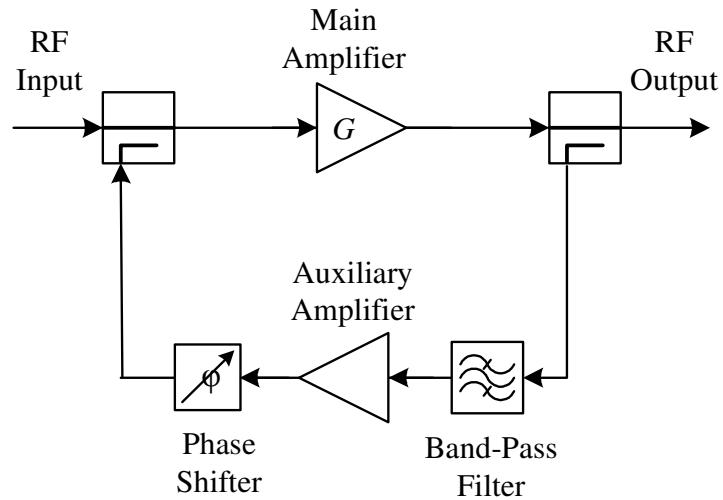


Figure 3-12: Feedback-based second-order products injection circuit

In Figure 3-12 the band-pass filter is used to select the necessary injected component, auxiliary amplifier acts as a gain controller in order to achieve the proper relation between the amplitudes of the fundamental signal and the injected signal, and finally the phase shifter controls the phase of the produced IM3 by the injection is opposite to the original one produced by the main PA. The main advantage of such a system is its simplicity. The main drawbacks are those typical for the feedback techniques and the inability to linearise a wideband PA. This is due to the fact that the signals with large frequency differences cause large phase differences in the created IMD products. Consequently, it is difficult to adjust the phase of the injected signals and the created IMD components add with the original one with not a 180-degree phase shift.

In order to avoid the mentioned drawbacks, the injected signals can be obtained not from a feedback loop, but generated by another nonlinear component, which precedes the PA. Also, DSP operations can be used to provide injection of the signals at baseband, which will be precisely described bellow in Section 3.8.3.

### 3.7. Analogue Predistortion

Predistortion is the simplest and least expensive method among the PA linearisation techniques. The main idea is creating before the PA a distortion characteristic, which is the inverse replica of the PA distortion characteristic, and cascading them with the aim of achieving a linearly amplified signal at the output [3.36]-[3.55].

Predistortion can be implemented as analogue or digital. In the case of analogue predistortion, the inverse AM/AM and AM/PM characteristics are created in the predistorter using analogue components. Such systems are usually implemented at RF or IF frequencies. In the case of Digital Predistortion (DPD), the distortion characteristic is created using digital components and DSP operations. Such systems are realised at baseband frequencies.

The basic principle of analogue predistortion is illustrated in Figures 3-13, 3-14, where  $V_i$  and  $V_o$  is the input and output voltage correspondently,  $\alpha(V_i)$  is the distortion characteristic of the PA, and  $\beta(V_i)$  is the distortion characteristic of the predistorter.

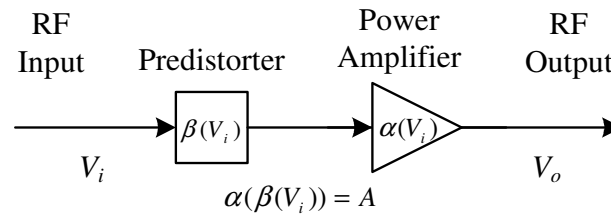


Figure 3-13: Schematic of an analogue predistortion system

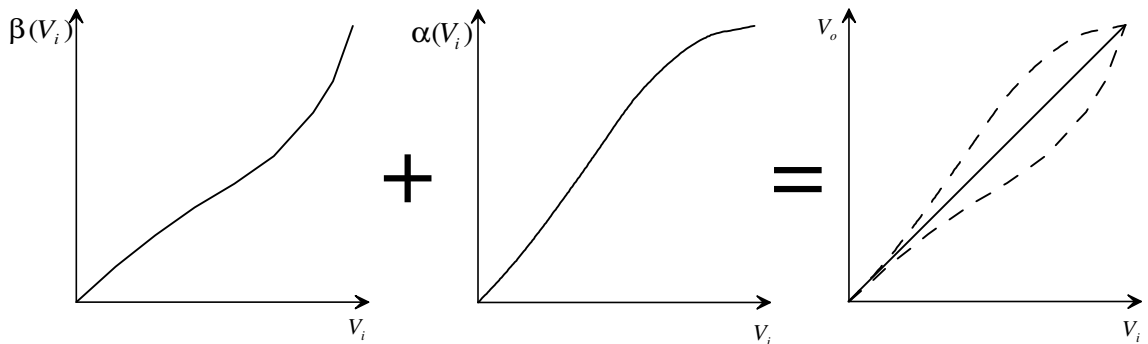


Figure 3-14: Operation of a predistortion system

The figures present the operation of a predistortion system in a very simplified way. In Figure 3-13 the predistortion function  $\beta(V_i)$  is the inverse replica of the distortion function of the PA  $\alpha(V_i)$ . It is applied to the input signal in such a way, that the PA distortion is compensated and the output signal is an amplified non-distorted reproduction of the input signal. In Figure 3-14 the inverse AM/AM characteristic of a PA is created in the predistorter. Usually the AM/PM characteristic is also considered and its inverse replica is generated in the predistorter. In practice, the distortion characteristic of the predistorter is not a mirror image of that of the PA, because only odd-order components of the nonlinear response are considered [3.1].

If a linearising element is placed after the PA, the technique is called postdistortion [3.36]. There are several obvious drawbacks of this approach, which are: necessity of the distortion element to be able to handle the full power range of the final PA stage and the losses in the element, which degrade the overall efficiency.

The implementation of an analogue predistortion implies generation of the expansive characteristic up-front. Expansive means that the gain increases with the increase in input power level. This can be accomplished by several methods: by the use of other nonlinear components, such as diodes or transistors [3.37]-[3.38], by

introducing a polynomial nonlinearity, e.g. cubic predistorters [3.39], or by injecting of harmonics using a feedback or feedforward chain [3.40].

An example of analogue predistortion based on cubic nonlinear element is presented in Figure 6.3. This type of analogue predistortion circuits has become popular for Travelling-Wave-Tube (TWT) amplifiers because they exhibit mainly third-order nonlinearity. A higher-order polynomial predistorter can also be created by the same principle.

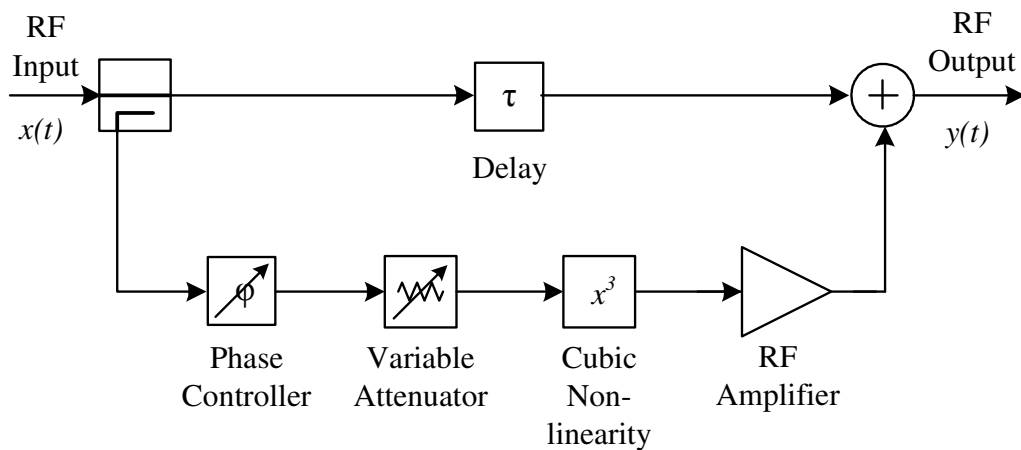


Figure 3-15: Block diagram of a cubic analogue predistorter

The circuit in Figure 3-15 contains a time-delay element in the main path to compensate for the delay in the secondary path, which includes a cubic nonlinearity element, variable attenuator, phase controller and a small-signal amplifier. The components of the secondary path regulate the proper relationship of the predistortion signal to the fundamental one. The presented predistorter is implemented in RF. However, an implementation at IF is also possible. In this case, the system can be used for many RF frequencies by choosing the proper LO.

Typical improvements in ACPR achieved by the analogue predistortion technique are up to 10 dB [3.37], [3.41]. The main advantages of the analogue predistortion are simplicity of realisation, low cost, simple integration procedure, and possibility to linearise wideband power amplifiers. The drawbacks are: small-to-moderate linearising performance, power loss in the additional RF components and hence decrease of the overall efficiency, and difficulty to provide adaptation, which significantly increases complexity of the circuit.

### 3.8. Digital Predistortion

Digital Predistortion (DPD) is a popular linearisation technique [3.42]-[3.55], which is based on the idea of creating the predistortion characteristic for a PA in digital domain. It uses a similar principle to analogue predistortion, but operations are carried out at baseband frequencies using DSP methods, as shown in Figure 3-16. The circuit includes a digital predistorter operating with a baseband input signal, a Digital-to-Analogue Converter (DAC), a modulator with Local Oscillator (LO), and a power amplifier. With the recent development in high-speed and miniaturised digital signal processing chips, the idea of providing linearisation by digital methods is becoming more and more attractive.

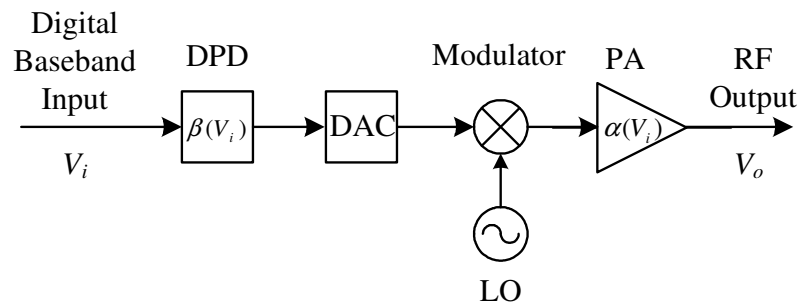


Figure 3-16: General layout of a digital predistortion system

DPD takes advantage of the already existing digital part of a transmitter and eliminates problems regarding RF hardware adjustments and loss of power in additional RF components. Creating of a predistortion characteristic at baseband is simple to realise and the digital linearisation system is stable and precise in operation. DPD also benefits from high flexibility, controllability and possibilities to provide adaptation by combining with feedback and feedforward techniques. DSP provides a wide possibility of generation of the predistortion characteristic, and different combinations with the other linearisation techniques can be used in order to improve the DPD performance.

The main drawbacks of the conventional DPD methods can be summarised as follows. First of all, DPD increases complexity of the circuit and the amount of DSP operations, which put limitations on the choice of DSP components and may result in bandwidth limitations due to the limited signal processing speed of the digital circuit.

Secondly, DPD is quite sensitive to memory effects of PAs. Unlike feedback or feedforward techniques, where the information about memory effects is already contained in the added error signal, DPD systems must provide additional compensation of memory effects for wideband applications. Finally, adaptation procedures further increase the complexity of the circuit resulting in higher power consumption and bandwidth limitations.

Generally, adaptation of DPD circuits is achieved by incorporating a feedback and feedforward paths, as shown in Figure 3-17. The forward part is the main chain with addition of a predistorter block. The feedback part, which includes attenuator, analogue feedback component and Analogue-to-Digital Converter (ADC), is used to calculate the reference signal, which is compared to the input signal in order to control the adaptation procedure. The analogue feedback component is the one used to implement the chosen adaptation procedure, which can be based on minimising the square error between the fed-back and fed-forward signals or it can be based on minimising the ACPR or EVM of the PA output signal. In the first case, the analogue feedback component includes a demodulator or envelope and phase detectors. In the second case, it includes a circuit detecting power in the adjacent channel or an EVM-measuring circuit. The feedback path of the circuit presented in Figure 3-17 has a high mathematical complexity and includes RF components, which potentially can cause problems similar to those inherent in feedback techniques: efficiency degradation due to power loss and limitation of bandwidth due to delays and limited signal processing speed. However, in DPD systems the feedback path is only used for control and does not need to operate constantly. It can be activated when the adaptation is required or during the defined operation cycle. Consequently, the power loss in the feedback part can be kept low and the operational bandwidth is not reduced by implementation of the feedback, but it is limited by the amount of required operations in the forward path.

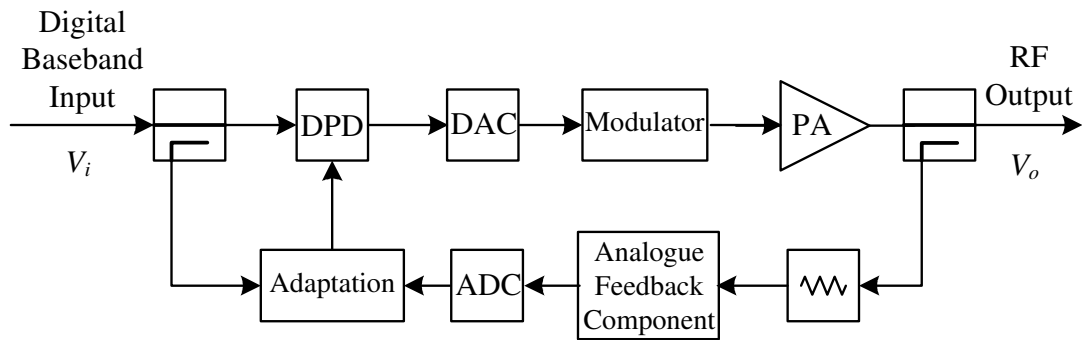


Figure 3-17: General schematic of an adaptive digital predistortion system

There are three main types of digital predistortion:

- look-up-table DPD;
- polynomial DPD;
- baseband-distortion-components injection DPD.

The first one uses Look-Up Tables (LUT) to store coefficients for all values of the input signal and provides sample-by-sample multiplication of the input signal by these coefficients. Adaptation of LUT DPD circuits is usually accomplished by minimising the square error between the fed-back reference and fed-forward signals. If the comparison is carried out in the Cartesian form of signal (I and Q components are compared), the analogue feedback component in the feedback path includes demodulator, which significantly increases the circuit's complexity. If the comparison is accomplished in the polar form of signal, the analogue feedback component includes envelope and phase detectors. The second method uses polynomial functions to describe the characteristics of the PA and the predistorter. It provides multiplication of the incoming signal by the polynomial coefficients of the predistorter, which are adjusted to compensate for the polynomial distortion of the PA. Adaptation of polynomial DPD circuits is usually based on minimising the square error between the fed-back reference and fed-forward signals by direct search or gradient (indirect) methods. The first two methods are conventional types of DPD. They increase complexity of the circuit and number of DSP computations by adding a large LUT or polynomial block to the circuit. The third method, based on the baseband injecting of distortion components, is a relatively new technique aimed at decreasing the DSP complexity of conventional DPD. The method implies injecting the baseband equivalent of the in-band distortion components produced by the odd-order nonlinearities of the

PA into the digital input signal. As the distortion components are generated directly from the input I and Q signals, there is no need in storage of the LUT, whereas only a small number of coefficients need to be tabulated. The main advantages of the baseband components injection DPD comparing to the conventional DPD is its simplicity, low computational complexity, low amount of stored coefficients, and possibility of adjusting the ratio between computational complexity and linearising performance, which allows achieving the optimal compromise for a particular application. The three main DPD methods are described in details in the remainder of this Chapter.

### 3.8.1 Look-Up-Table Digital Predistortion

LUT based DPD is a well-developed linearisation technique described in [3.42]-[3.49]. The idea behind is creating the predistorter characteristic by multiplying each sample of the input signal by coefficients, which have magnitude and phase depending on the AM/AM and AM/PM distortions of the PA at the present input signal power level. When LUT is used, several issues need to be taken into account: LUT architecture; optimum size of the LUT (compromise between accuracy and the number of stored coefficients); indexing or addressing of the LUT and spacing between the LUT entries (equispaced or non-uniformly distributed coefficients).

The LUT architecture, determined by the method of complex envelope processing, can be classified as:

- mapping (two two-dimensional LUTs);
- polar (two one-dimensional LUTs);
- complex gain (one one-dimensional LUT).

Mapping LUT predistorters [3.46] process the input signal in the Cartesian form by separate predistortion of the  $I$ - and  $Q$ -components:  $y_I = x_I + f_I(x_I, x_Q)$ ,  $y_Q = x_Q + f_Q(x_I, x_Q)$ , where  $x_I, x_Q$  are the input  $I$  and  $Q$  components,  $y_I, y_Q$  – output  $I$  and  $Q$  components,  $f_I, f_Q$  – are predistortion functions applied respectively by the first LUT used to predistort the  $I$  component and the second LUT used to predistort the  $Q$  component of the input signal. Consequently, the size of the LUT is  $2 \cdot k^2$ , where  $k$  is the number of the quantisation levels in the input  $I$  and  $Q$  branches. The advantage of

this architecture is high accuracy, whereas the drawback is a large size of the LUT, resulting in large adaptation time, high complexity and power consumption.

Polar LUT architecture [3.47] is based on polar coordinates, employing two one-dimensional tables containing magnitude  $R_{OUT} = f_R(R_{IN})$  and phase  $\Theta_{OUT} = f_\Theta(R_{OUT})$  addressing information correspondingly. The required number of stored coefficients or the size of LUT is  $2 \cdot k$ . The advantage of this method is a significantly reduced size of LUT and a simplified predistortion process. The drawback is increased signal processing time, up to 83% [3.1], due to complexity of rectangular-to-polar conversion.

Complex gain LUT predistorters [3.49] use one LUT containing complex gain factors in the Cartesian form. The indexing is accomplished by calculating the power of the input signal  $R = x^2$  and using it to address the corresponding complex LUT coefficient  $G_{LUT}(R)$ . Hence the output predistorted signal is calculated:  $y = x \cdot G_{LUT}(R)$ . The size of LUT using a complex-gain architecture equals to  $k$ . The advantage of this LUT architecture is the reduced LUT size, time and power required for predistortion and adaptation. The drawback is low predistortion accuracy and consequently low linearising performance.

The operation of a LUT-based adaptive digital predistorter can be described using a detailed block diagram presented in Figure 3-18.

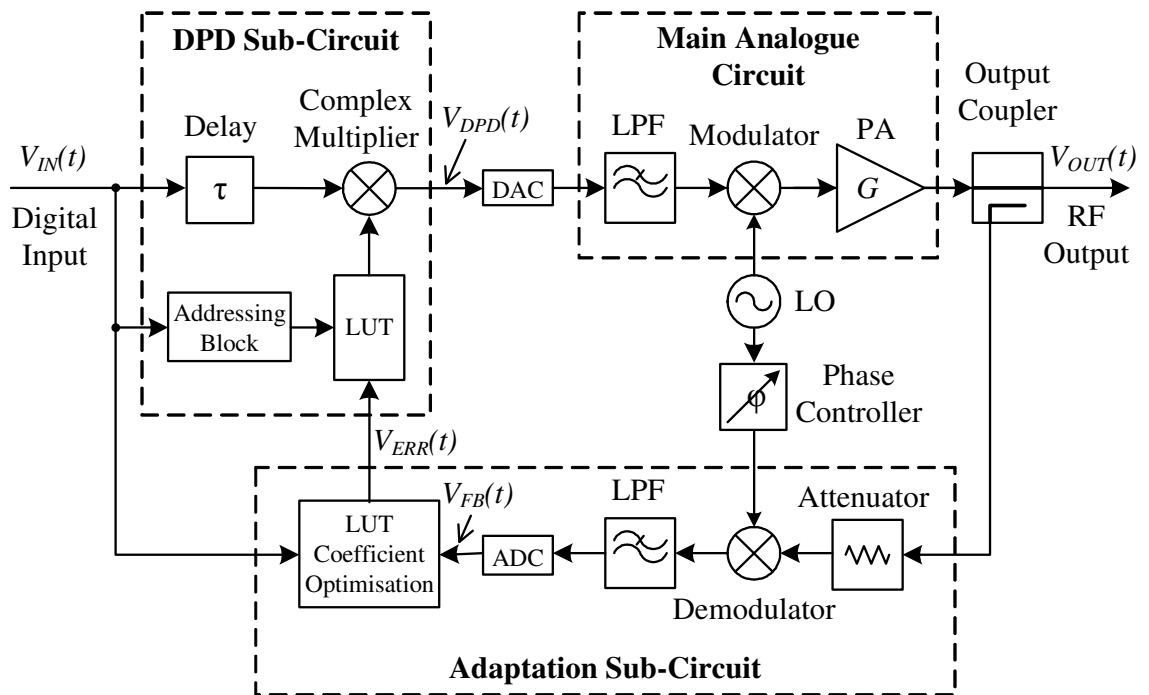


Figure 3-18: Block diagram of an adaptive LUT-based DPD system

The system consists of a DPD part, including a delay block, a LUT block, an addressing unit, and a complex multiplier; a main RF part, including a Low-Pass Filter (LPF), a modulator, and the power amplifier; and an adaptation sub-circuit, containing an attenuator, a demodulator, a LPF, and a LUT coefficient optimisation block.

The input signal  $V_{IN}(t)$ , usually processed in the Cartesian form, is separated into two parts, one of which is fed into the digital predistorter and the other directed to the adaptation sub-circuit. In the DPD sub-circuit the input signal is predistorted by multiplying its each sample with the complex LUT coefficient corresponding to the magnitude of this sample. The LUT coefficients are addressed by calculating the input signal magnitude and referring it to the quantised index of the LUT. A delay element is introduced with the aim to compensate delays in the addressing and LUT blocks. The predistorted signal  $V_{DPD}(t)$  is converted to the analogue form by the Digital-to-Analogue Converter (DAC), filtered with a Low-Pass Filter (LPF), modulated, and sent to the input of the PA. Ideally the magnitude of the signal at the PA input is equal to that of the predistorted signal  $V_{DPD}(t)$ . In reality it may be slightly different due to imperfections of the modulator and other signal-processing components. For analytical description, those magnitudes are assumed to be equal.

In order to analytically describe the operation of a LUT predistorter, magnitudes of the complex signal on each stage of the DPD operation are denoted as follows, where the time dependence is not shown for simplicity. The magnitude of the input signal, predistorted signal and signal after modulator are denoted as  $x_i = |V_{IN}(t)|$ ,  $x_d = x_q = |V_{DPD}(t)|$  respectively.

The PA has a complex gain  $G(x_q)$  dependent on the PA input signal magnitude, which is the magnitude of the signal after the modulator:

$$V_{OUT}(t) = G(x_q) \cdot V_{DPD}(t). \quad (3.29)$$

The predistorter also has a complex gain  $F(x_i)$  dependent on the magnitude of the signal at the input of the predistorter:

$$V_{DPD}(t) = F(x_i) \cdot V_{IN}(t). \quad (3.30)$$

The DPD circuit aims at keeping a constant overall gain of the system  $K$  for all the input power levels up to a deep saturation:

$$V_{OUT}(t) = K \cdot V_{IN}(t). \quad (3.31)$$

Combining (3.29)-(3.31) yields:

$$K = F(x_i) \cdot G(x_q). \quad (3.32)$$

Taking into account that  $x_q = |V_{DPD}(t)|$  and  $x_i = |V_{IN}(t)|$  after substituting  $V_{DPD}(t)$  from (3.30), the last equation can be re-written as:

$$K = F(x_i) \cdot G(x_i \cdot |F(x_i)|). \quad (3.33)$$

In order to compensate for AM/PM distortions of the PA, in other words to keep the phase of the whole system constant, the phase distortion of the predistorter must be 180°-opposite to those of the PA:

$$\Theta_F(x_i) = -\Theta_G(x_q), \quad (3.34)$$

or using similar reasoning, the following expression can be obtained:

$$\Theta_F(x_i) = -\Theta_G(x_i \cdot |F(x_i)|). \quad (3.35)$$

The PA output generally includes an error signal:

$$V_{OUT}(t) = K \cdot V_{IN}(t) + V_{OUT\_ERR}(t). \quad (3.36)$$

Then the fed-back signal can be calculated assuming that after loss in the coupler, attenuator and other signal processing devices, the resulting signal is a fraction of the output signal divided by coefficient  $S$ :

$$V_{FB}(t) = \frac{V_{OUT}(t)}{S}. \quad (3.37)$$

Therefore,

$$V_{FB}(t) = \frac{K \cdot V_{IN}(t) + V_{OUT\_ERR}(t)}{S}. \quad (3.38)$$

The error signal is calculated as the difference between the fed-back signal and the product of the input signal and the coefficient  $\frac{K \cdot V_{IN}(t)}{S}$ :

$$V_{ERR}(t) = V_{FB}(t) - \frac{K \cdot V_{IN}(t)}{S} = \frac{V_{OUT\_ERR}(t)}{S}. \quad (3.39)$$

The adaptation process optimises the LUT coefficients in order to minimise the error signal  $V_{ERR}(t)$ . Adaptation can be accomplished by several methods. The most commonly used adaptation techniques are linear and secant algorithms [3.48]-[3.49].

The linear adaptation algorithm [3.48] can be derived using iterative form of (3.33):

$$F(x_i, j+1) = \frac{K}{G(x_i \cdot |F(x_i, j)|)}, \quad (3.40)$$

where  $F(x_i, j)$  is the coefficient corresponding to the  $x_i$  input magnitude level on the  $j$ -th iteration. Combining (3.29) and (3.30) yields:

$$G(x_q) = \frac{V_{OUT}(t)}{F(x_i) \cdot V_{IN}(t)}. \quad (3.41)$$

The obtained equation gives the value of  $G(x_q) = G(x_i \cdot |F(x_i)|)$ , which after substituting into (3.40) outcomes in:

$$F(x_i, j+1) = F(x_i, j) \cdot K \cdot \frac{V_{IN}(t)}{V_{OUT}(t)}. \quad (3.42)$$

From (3.37)-(3.39):

$$K \cdot V_{IN}(t) = V_{OUT}(t) - S \cdot V_{ERR}(t). \quad (3.43)$$

After substituting (3.43) and (3.37) into (3.42), the formula for linear iterative adaptation algorithm can be obtained:

$$F(x_i, j+1) = F(x_i, j) \cdot \left(1 - \frac{V_{ERR}(t)}{V_{FB}(t)}\right). \quad (3.44)$$

The secant adaptation algorithm [3.49] is also an iterative algorithm based on calculating the error signal according to (3.39):

$$V_{ERR}(t) = V_{FB}(t) - \frac{K \cdot V_{IN}(t)}{S}. \quad (3.45)$$

The iterative adaptation secant algorithm modifies coefficients of the look-up-table according to [3.49]:

$$F(x_i, j+1) = \frac{F(x_i, j-1) \cdot V_{ERR}(x_i, j) - F(x_i, j) \cdot V_{ERR}(x_i, j-1)}{V_{ERR}(x_i, j) - V_{ERR}(x_i, j-1)}, \quad (3.46)$$

where  $V_{ERR}(x_i, j)$  is the error signal obtained at the j-th iteration for  $x_i$  input signal.

The advantages of the secant adaptation algorithm is its faster convergence and possibility of removing the phase shifter from the circuit (Figure 3-18) due to the fact that the same behaviour is obtained for every value of phase shift [3.49]. The drawback is higher computational complexity of the method comparing to the linear adaptation algorithm.

### 3.8.2 Polynomial Digital Predistortion

Polynomial DPD is another well-developed type of digital predistortion [3.50]-[3.53]. It uses a polynomial function in place of LUT to create the predistortion characteristic. The predistortion function is usually based on an odd-order polynomial, 3<sup>rd</sup> or 5<sup>th</sup> order, which determines the linearising performance and computational complexity of the circuit. The polynomial function is an inverse characteristic of the PA distortion, approximated by a polynomial nonlinearity.

The operation of a polynomial adaptive digital predistorter can be described using a detailed block diagram presented in Figure 3-19. It includes a DPD part, composed of a delay block, a polynomial-function block, an addressing unit, which is usually implemented as a square magnitude addressing, and a complex multiplier; a main RF part, including a Low-Pass Filter (LPF), a modulator, and the power amplifier; and an adaptation sub-circuit, which is usually accomplished according to ACPR minimisation algorithm and includes a demodulator, a Band-Pass Filter (BPF), an adjacent channel power detector and a polynomial coefficient optimisation block. The main difference to the LUT-based predistorter is highly reduced size of the coefficient storage block at the price of higher computational complexity in the forward path, where complex multiplications of polynomial is required in place of multiplications of the signal by complex coefficients at LUT DPD. The increase number of mathematical operations may result in bandwidth limitations of the modulation signal due to the limited system clock frequency. Moreover, the linearising performance of the polynomial DPD is usually lower than that of the LUT DPD and highly depends on the order of polynomial function.

In order to describe analytically the operation of a polynomial predistorter, squared magnitudes of the complex signal on each stage of the DPD operation are denoted in a similar way as before in the LUT-based DPD case: the squared magnitude of the input signal, predistorted signal and signal after modulator are denoted as  $x_i(t) = |V_{IN}(t)|^2$ ,  $x_d(t) = x_q(t) = |V_{DPD}(t)|^2$  respectively.

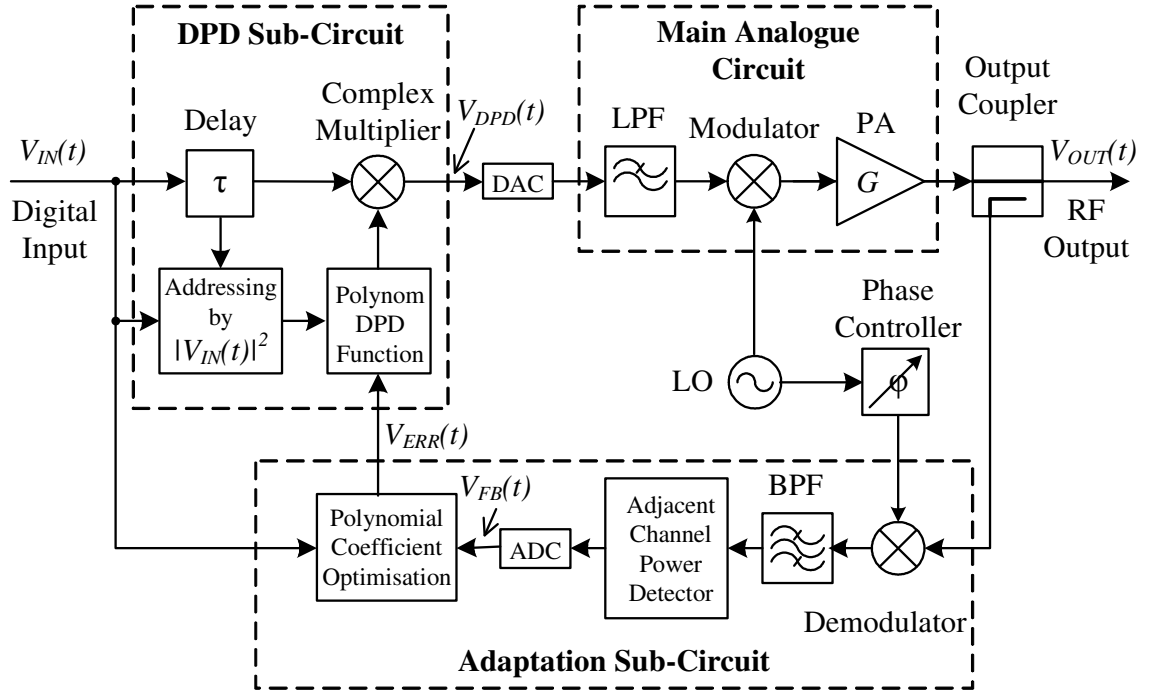


Figure 3-19: Block diagram of an adaptive polynomial DPD system

For a 5<sup>th</sup>-order nonlinearity, the polynomial distortion characteristic of a PA is defined as [3.53]:

$$G(x_d(t)) = \beta_1 + \beta_3 \cdot x_d(t) + \beta_5 \cdot x_d^2(t), \quad (3.47)$$

where  $\beta_1, \beta_3, \beta_5, \dots$  are complex coefficients that account for both AM/AM and AM/PM distortions of the PA. The PA has a complex gain  $G(x_q)$  dependent on the PA input signal square magnitude  $x_q(t)$ , which equals to the square magnitude of the signal after the predistorter  $x_d(t)$ :

$$V_{OUT}(t) = G(x_d) \cdot V_{DPD}(t). \quad (3.48)$$

Combining (3.47) and (3.48) gives:

$$V_{OUT}(t) = \beta_1 \cdot V_{DPD}(t) + \beta_3 \cdot V_{DPD}^3(t) + \beta_5 \cdot V_{DPD}^5(t). \quad (3.49)$$

From (3.49) one can see that the PA has a 5<sup>th</sup>-order nonlinearity and that only odd-order terms are taken into account because they produce in-band distortion unlike the even-order ones.

For a 5<sup>th</sup>-order nonlinearity, the polynomial distortion characteristic of the predistorter  $F(x_i(t))$  is defined as:

$$F(x_i(t)) = \alpha_1 + \alpha_3 \cdot x_i(t) + \alpha_5 \cdot x_i^2(t), \quad (3.50)$$

where  $\alpha_1, \alpha_3, \alpha_5, \dots$  are complex coefficients.

The polynomial predistorter presented in Figure 3-19 performs calculation of  $F(x_i(t))$  for each sample of the input signal and executes the complex multiplication of the input signal with the calculated polynomial function (3.50).

The complex composite gain  $K(x_i(t))$  of the polynomial DPD system can be derived similarly to (3.33):

$$K(x_i(t)) = F(x_i(t)) \cdot G(x_d(t)), \quad (3.51)$$

$$K(x_i(t)) = F(x_i(t)) \cdot G\{x_i(t) \cdot |F(x_i(t))|^2\}. \quad (3.52)$$

The composite gain of the system is also expressed as a polynomial function:

$$K(x_i(t)) = \gamma_1 + \gamma_3 \cdot x_i(t) + \gamma_5 \cdot x_i^2(t), \quad (3.53)$$

where the complex coefficients  $\gamma_1, \gamma_3, \gamma_5$ , can be obtained as follows [3.53]:

$$\gamma_1 = \alpha_1 \beta_1, \quad (3.54)$$

$$\gamma_3 = \alpha_3 \beta_1 + \alpha_1 \beta_3 |\alpha_1|^2, \quad (3.55)$$

$$\gamma_5 = \alpha_5 \beta_1 + \alpha_3 \beta_3 |\alpha_1|^2 + \alpha_1 \beta_5 |\alpha_1|^4 + 2\alpha_1 \beta_3 \operatorname{Re}\{\alpha_1 \alpha_3^*\} \quad (3.56)$$

The linearising performance of a polynomial predistorter is achieved when the complex coefficients  $\gamma_1, \gamma_3, \gamma_5$  are minimised by proper choosing the  $\alpha_1, \alpha_3, \alpha_5$  coefficients of the predistorter.

Adaptation methods for polynomial predistorters can be divided into direct search and gradient algorithms. The first group offers good stability and low computational complexity, whereas the second one has faster convergence. Consequently, direct search methods are mainly used in applications which do not require fast adaptation. In general, the drifts in the PA characteristics occur due to changes in temperature, variations in power supply, aging, and application of different signals; for these cases adaptation can be slow [3.53]. A basic direct search algorithm can be described as follows. A function of ACPR or EVM  $F(x)$  defined over a multi-dimensional space  $x = \{x_1, x_2, \dots, x_n\}$  is minimised by an iterative algorithm. From a starting point  $x^k$ , where  $k$  is the number of iteration, the search over all coordinates is performed until a local minimum is found at  $x^{k+1}$ , such as:

$$F(x^{k+1}) < F(x^k), \quad (3.57)$$

then the approximate gradient direction is calculated as:

$$s^k = x^{k+1} - x^k, \quad (3.58)$$

and the next point  $x^{k+2}$  is obtained by:

$$x^{k+2} = x^{k+1} + s^k. \quad (3.59)$$

The procedure continues with the described searching steps until the function minimum is found. The practical adaptation time of 100s, reported in [3.53] for a 16-QAM signal operating at 64 kb/s rate, was necessary reduce IM power by 1/2. Faster adaptation may be offered by gradient methods at the price of higher computational complexity. In this case, the derivative of the function  $F(x)$  is calculated at each step in order to determine the gradient direction. The derivative approach results in the fastest conversion time.

Summarising the state above, the main advantage of the polynomial predistortion over the LUT-based DPD is the significant reduction of the coefficients-storage block. The fundamental drawback of the polynomial DPD arises from the fact that the product of the predistorter and PA polynomial distortion characteristics results in a large number of unwanted terms, which, on one hand, increase the signal processing complexity of the system and, on the other hand, limit the potential distortion compensation performance, particularly IMD reduction.

A solution to the mentioned issues of the traditional digital predistortion techniques, LUT-based and polynomial DPD, may be offered by a baseband-components injection technique, which unlike the polynomial DPD does not recreate the whole polynomial nonlinearity of the PA in the predistorter, but only injects the baseband equivalent of the PA in-band distortion components with the same magnitude and opposite phase to those generated by the PA.

### 3.8.3 Baseband Components Injection Digital Predistortion

The baseband components injection technique is a new DPD technique proposed in [3.54] in 2005 and significantly developed in this thesis with the aim of eliminating the drawbacks of the conventional DPD methods. In [3.54] the idea of injecting of the third- and fifth-order in-band distortion components in a baseband block is proposed and investigated for a hardware implementation. This technique is described below in the current Section. However the so-called distortion compensation limit inherent to this technique and its inability to compensate memory effects of PAs significantly limit the possible applications of the method. The new DPD, based on the idea of baseband

components iterative injection incorporates an improved memory-compensation technique is then proposed in Chapters 6 and 7 of this thesis.

In order to explain the idea of baseband distortion components injection to linearise a PA, the third- and fifth-order component injection technique is presented below. The PA nonlinearity is modelled by a fifth-order polynomial expression as follows:

$$V_{OUT}(t) = g_1 \cdot V_{IN}(t) + g_2 \cdot V_{IN}^2(t) + g_3 \cdot V_{IN}^3(t) + g_4 \cdot V_{IN}^4(t) + g_5 \cdot V_{IN}^5(t), \quad (3.60)$$

where  $V_{IN}(t)$  is the input voltage of the PA and  $g_1, g_2, g_3, g_4, g_5$  are coefficients of the nonlinear polynomial function. A cosine input signal with the amplitude  $V_S(t)$  and phase  $\varphi(t)$  looks like:

$$V_{IN}(t) = V_S(t) \cos(\omega t + \varphi(t)). \quad (3.61)$$

The input signal (3.61) can be re-written in the Cartesian form as follows [3.54]:

$$V_{IN}(t) = V \cdot (I(t) \cdot \cos(\omega t) - Q(t) \cdot \sin(\omega t)), \quad (3.62)$$

where:  $I(t) = \frac{V_S(t)}{V} \cdot \cos(\varphi(t))$ ,  $Q(t) = \frac{V_S(t)}{V} \cdot \sin(\varphi(t))$  and  $V = \text{average}(|V_S(t)|)$ .

Consequently  $\text{average}(I^2(t) + Q^2(t)) = 1$ .

After substituting (3.62) into (3.60) and completing trigonometric transformations the fundamental-frequency part of the output signal, including the amplified original signal and the in-band distortion components, produced by the third- and fifth-order terms of the PA nonlinearity polynomial expression (3.60), can be written:

$$\begin{aligned} V_{OUT}^{FUND}(t) = & g_1 \cdot V_{IN}(t) + \frac{3V^2 g_3 (I^2(t) + Q^2(t))}{4} \cdot V_{IN}(t) \\ & + \frac{5V^4 g_5 (I^2(t) + Q^2(t))^2}{8} \cdot V_{IN}(t). \end{aligned} \quad (3.63)$$

In the obtained expression, the first summand is the linear amplified input signal, whereas the second and the third ones are the in-band distortion components produced by the 3<sup>rd</sup>- and 5<sup>th</sup>-term in (3.60) respectively.

The idea behind the considered DPD method is to inject those components in the baseband block with the same amplitude and 180° phase shift in order to compensate for the in-band distortion of the PA. For a system injecting the 3<sup>rd</sup>-order distortion component, the input signal can be written:

$$V_{IN}^{DPD}(t) = V \cdot \{1 + a \cdot (I^2(t) + Q^2(t))\} \cdot [I(t) \cdot \cos(\omega t) - Q(t) \cdot \sin(\omega t)], \quad (3.64)$$

where

$$a = -\frac{3V^2 g_3}{4g_1}. \quad (3.65)$$

Figure 3-20 shows the schematic of the predistorter based on injecting the 3<sup>rd</sup>-order distortion component [3.54]. The  $I$ ,  $Q$ , and  $I^2+Q^2$  signals are generated in the baseband block and used for creating the predistorted signal according to (3.64). The needed magnitude and phase of the injected component is obtained by the  $a$ -blocks and phase shifters  $\varphi$  correspondingly. The predistorted signal is filtered with LPF, modulated in the Quadrature Modulator (QM) and passed thorough the PA.

After substituting (3.64) into (3.60), the new fundamental-frequency output signal can be written as:

$$\begin{aligned} V_{OUT}^{FUND}(t) &= g_1 \cdot V_{IN}(t) \\ &+ g_1 \cdot a \cdot [I^2(t) + Q^2(t)] \cdot V_{IN}(t) \\ &+ \frac{3}{4} \cdot g_3 \cdot V^2 \cdot [I^2(t) + Q^2(t)] \cdot V_{IN}(t) \\ &+ \frac{9}{4} \cdot g_3 \cdot a \cdot V^2 \cdot [I^2(t) + Q^2(t)]^2 \cdot V_{IN}(t) \\ &+ \frac{9}{4} \cdot g_3 \cdot a^2 \cdot V^2 \cdot [I^2(t) + Q^2(t)]^3 \cdot V_{IN}(t). \end{aligned} \quad (3.66)$$

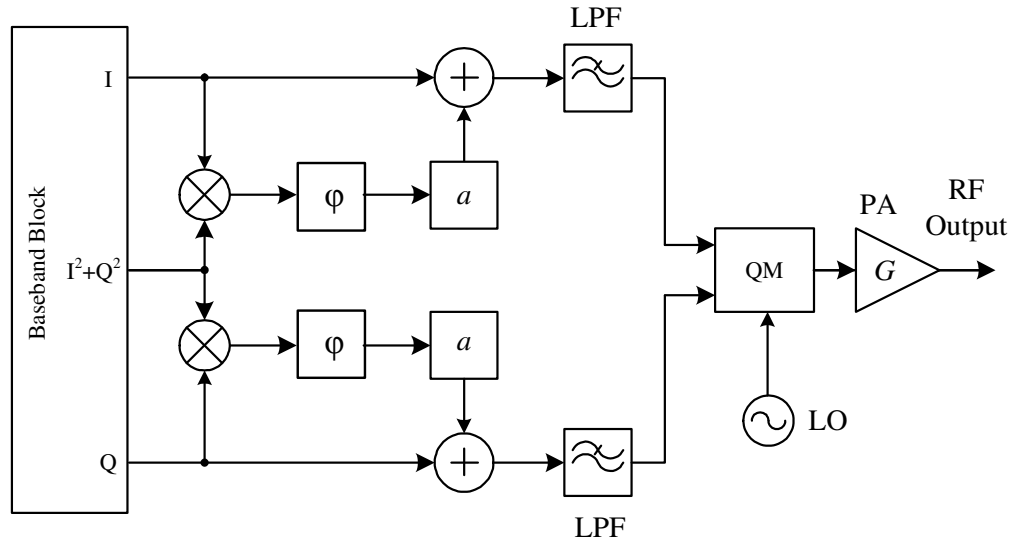


Figure 3-20: Block diagram of a 3<sup>rd</sup>-order baseband component injection DPD system

In (3.66) the second and third terms compensate each other due to (3.65), whereas the fourth and fifth terms appear as the new distortion introduced by the injection. These new distortion components are smaller than the original distortion; however they limit the potential linearising performance of this technique. This phenomenon, known as the

distortion compensation limit [3.55] is inherent in the conventional distortion-component injection DPD.

Summarising the stated above, the main advantages and drawbacks of the conventional distortion-component injection DPD can be highlighted. The advantages are small size and low computational complexity as well as high integrability and simple practical realisation of the method comparing to the LUT-based and polynomial DPD. The disadvantages are limited linearising performance due to the distortion compensation limit and inability to compensate for PAs memory effects by the conventional distortion-component injection DPD. Moreover, despite the technique is more stable to the drifts in the PA power characteristics than the polynomial or LUT-based DPD, an adaptation algorithm should be developed in such a way, that it will not increase the system's complexity significantly.

Possible solutions to the problems of distortion compensation limit and memory effects compensation are proposed in Chapters 6 and 7 of this thesis.

### **3.9. Conclusion**

In this Chapter, an overview of linearisation techniques has been presented. The main classes of linearisation include feedback, feedforward, envelop elimination and restoration, linear amplification using nonlinear components, second-order injection and predistortion techniques. The feedback methods are able to provide good linearising performance at the cost of increased circuit's complexity and potential stability problems inherent in feedback loops. The feedforward methods offer the most superior linearising performance with high stability, but they have low efficiency and high circuit complexity. The EER technique can be highly-efficient and able to minimise the AM/PM distortion, but has a number of practical issues and stability problems. The LINC method is theoretically suitable for increasing both the efficiency and linearity of a PA, but is extremely sensitive to the real-life device imperfections, and hence is difficult for practical implementation. The second-order product injection techniques are simple and efficient, as they require less RF modifications, but the methods are extremely sensitive to the phase shift, and hence are instable and problematic for the wideband linearisation. Analogue predistortion is simple in implementation and able to linearise wideband PAs, but suffers from low-to-moderate linearising performance and

adaptation difficulties. The digital predistortion methods are simple in implementation and integration, exhibiting high efficiency, as they do not require additional RF components. However, the conventional LUT and polynomial DPD techniques offer only moderate linearising performance and have high DSP computational complexity. The baseband components injection DPD has a potential of achieving high linearising performance, while maintaining relatively low computational complexity. For this reason, the method is assumed as the basis for the advanced DPD technique developed in this thesis.

### 3.10. References

- [3.1] P. B. Kenington, *High Linearity RF Amplifier Design*, Artech House Inc., 2000, ISBN 1580531431.
- [3.2] S. C. Cripps, *RF Power Amplifiers for Wireless Communications*, Artech House Inc., 1999, ISBN 0890069891.
- [3.3] J. Vuolevi, T. Rahkonen, *Distortion in RF Power Amplifiers*, Artech House Inc., 2003, ISBN 1580535399.
- [3.4] C. S. Aitchison, M. Mbabele, M. R. Moazzam., D. Budimir, and F. Ali, "Improvement of third order intermodulation products of RF and microwave amplifiers by injection," *IEEE Transactions on Microwave Theory and Techniques*, vol. 49, no. 6, pp. 1148-1154, June 2001.
- [3.5] C. W. Fan, and K. K. M. Cheng, "Theoretical and experimental study of amplifier linearization based on harmonic and baseband signal injection technique," *IEEE Transactions on Microwave Theory and Techniques*, vol. 50, no. 7, pp. 1801-1806, July 2002.
- [3.6] S. Kusunoki, K. Kawakami, and T. Hatsugai, "Load impedance and bias-network dependence of power amplifier with second-harmonic injection," *IEEE Transactions on Microwave Theory and Techniques*, vol. 52, no. 9, pp. 2169–2176, Sep. 2004.
- [3.7] Y. Hu, J. C. Mollier, and J. Obregon, "A new method of third-order intermodulation reduction in nonlinear microwave systems," *IEEE Transactions on Microwave Theory and Techniques*, vol. MTT-34, no. 2, pp 245 – 250, Feb. 1986.
- [3.8] Y. Yang, and B. Kim, "A new linear amplifier using low-frequency second-order intermodulation component feedforwarding," *IEEE Microwave and Guided Wave Letters*, vol. 9, no. 10, pp. 419–421, Oct. 1999.
- [3.9] A. F. Mitchell, "A 135 MHz feedback amplifier," *IEE Colloq. Broadband High Frequency Amplifiers: Practice and Theory*, pp. 2/1-2/6, London, Nov. 1979.

- [3.10] F. Perez, E. Ballesteros, J. Perez, "Linearisation of microwave power amplifiers using active feedback networks," *IEE Electronics Letters*, vol. 21, no. 1, pp. 9-10, Jan. 1985.
- [3.11] E. Ballesteros, F. Perez, J. Perez, "Analysis and design of microwave linearized amplifiers using active feedback" *IEEE Transactions on Microwave Theory and Techniques*, vol. 36, no. 3, pp. 499-504, Mar. 1988.
- [3.12] M. Faulkner, "Amplifier linearization using RF feedback and feedforward techniques," *IEEE Transactions on Vehicular Technology*, vol. 47, pp. 209-215, Feb., 1998.
- [3.13] G. Gajda, and R. Douville, "A linearization system using RF feedback," in *Proc. IEEE International Electrical and Electronics Conference*, Toronto, Canada, pp. 30-33, 1983.
- [3.14] T. Arthanayake, and H. B. Wood, "Linear amplification using envelope feedback," *IEE Electronics Letters*, vol. 7, no. 7, pp. 145-146, Apr. 1971.
- [3.15] V. Petrovic, and W. Gosling, "Polar-loop transmitter", *IEE Electronics Letters*, vol. 15, no. 10, pp. 286-288, May 1979.
- [3.16] T. Sowlati, D. Rozenblit, E. MacCarthy, M. Damgaard, R. Pullela, D. Koh, D. Ripley, "Quad-band GSM/GPRS/EDGE polar loop transmitter," *IEEE Journal of Solid-State Circuits*, vol. 39, no 12, pp. 2179- 2189, Dec. 2004.
- [3.17] J. L. Dawson, and T. H. Lee, "Automatic phase alignment for a fully integrated cartesian feedback power amplifier system," *IEEE Journal of Solid-State Circuits*, vol. 38, no. 12, pp. 2269-2279, Dec. 2003.
- [3.18] M. Johansson, and L. Sundstrom, "Linearisation of RF multicarrier amplifiers using Cartesian feedback," *IEE Electronics Letters*, vol. 30, no. 14, pp. 1110-1111, Jul. 1994.
- [3.19] S. Chung, J. W. Holloway, and J. L. Dawson, "Energy-efficient digital predistortion with lookup table training using analog cartesian feedback," *IEEE Transactions on Microwave Theory Tech.* vol. 56, no. 10, pp. 385-392, Oct. 2008.
- [3.20] S. Chung, J. W. Holloway, and J. L. Dawson, "Open-loop digital predistortion using Cartesian feedback for adaptive RF power amplifier linearization," in *Proc. IEEE MTT-S Int. Microw. Symp. Dig.*, Jun. 2007, pp. 1449-1452.

- [3.21] M. T. Hickson, D. K. Paul, P. Gardner, and K. Konstantinou, "High efficiency feedforward linearizers," In *Proc. 24<sup>th</sup> European Microwave Conference*, vol. 1, pp. 819-824, 1994.
- [3.22] Y. K. G. Hau, V. Postoyalko, and J. R. Richardson, "Design and characterization of a microwave feed-forward amplifier with improved wide-band distortion cancellation," *IEEE Transactions on Microwave Theory Tech.* vol. 49, no. 1, pp. 200-203, Jan. 2001.
- [3.23] H. Seidel, "A feedforward experiment applied to an L-4 carrier system amplifier," *IEEE Transactions on Communication Technology*, vol. COM-19, no. 3, pp.320-325, Jun.1971.
- [3.24] S. P. Stapleton, "Adaptive feedforward linearization for RF power amplifiers," *55<sup>th</sup> ARFTG Conference Digest-Spring*, vol. 37, pp. 1-7, Jun. 2000.
- [3.25] L. R. Kahn, "Single sideband transmission by envelope elimination and restoration," *Proc. of the Institute of Radio Engineers*, vol.40 no.7, pp.803-806, Jul. 1952.
- [3.26] F. H. Raab, "Intermodulation distortion in Kahn-technique transmitter," *IEEE Transactions on Microwave Theory Tech.*, vol. 44, no 12, pp 2273-2278, Dec. 1996.
- [3.27] F. H. Raab, "Envelope-elimination-and-restoration system concepts," In *Proc. 1987-RF Expo East, Boston, MA*, pp. 167 - 177, Nov. 1987.
- [3.28] H. Chireix, "High power outphasing modulation," *Proc. of the Institute of Radio Engineers*, vol. 23, pp. 1370-1392, Nov. 1935.
- [3.29] D.C. Cox, "Linear amplification with nonlinear components", *IEEE Transactions on Communication Technology*, vol. 22, no 12, pp 1942-1945, Dec. 1974.
- [3.30] F. H. Raab, "Efficiency of outphasing RF power-amplifier systems," *IEEE Transactions on Communication Technology*, vol. 33, no. 10, pp. 1094 - 1099, Oct. 1985.
- [3.31] X. Zhang, L. E. Larson, "Gain and phase error-free LINC transmitter," *IEEE Transactions on Vehicular Technology*, vol. 49, no. 5, pp. 1986-1994, Sept. 2000.

- [3.32] F. J. Casadevall, and A. Valdorinos, "Performance analysis of QAM modulations applied to the LINC transmitter," *IEEE Trans. Veh. Technol.*, vol. 42, no. 4, pp. 399-406, Nov. 1993.
- [3.33] M. Modeste, et al., "Analysis and Practical Performance of Difference Frequency Technique for Improving the Multicarrier IMD Performance of RF Amplifiers," *IEEE MTT Symposium on Technologies for Wireless Applications*, Vancouver, pp.53-56, Febr. 1999.
- [3.34] N. Males-Ilic, B. Milovanovic, and D. Budimir, "Improvement in second harmonics linearization technique for multichannel amplifiers," *Microwave and Optical Technology Letters*, vol.38, no. 2, pp. 150-153, Jul. 2003.
- [3.35] M. R. Moazzam, C. S. Aitchison, "A low third order intermodulation amplifier with harmonic feedback circuitry," *IEEE MTT-S Int. Microwave Symp. Dig.*, vol. 2, pp.827-830, 1996.
- [3.36] A. Prochazka, P. Lancaster, R. Neumann, "Amplifier linearization by complementary pre-or post-distortion," *IEEE Transactions on Cable Television*, vol.CATV-1, no.1, pp.31-39, Oct. 1976.
- [3.37] K. Yamauchi, et al., "A novel series diode linearizer for mobile radio power amplifiers," *1996 IEEE MTT-S International Microwave Symposium Digest*, vol.2, pp.831-834, Jun. 1996.
- [3.38] W. Huang, R.E. Sand, "Novel third-order distortion generator with residual IM2 suppression capabilities," *IEEE Transactions on Microwave Theory and Techniques*, vol.46, no.12, pp.2372-2382, Dec 1998.
- [3.39] P. B. Kenington, K. J. Parsons, and D.W. Bennett, "Broadband linearisation of high-efficiency power amplifiers," In *Proc. Third Int. Mobile Satellite Conf.*, pp. 59-64, June 1993.
- [3.40] M. Maeda, et al., "Source second-harmonic control for high efficiency power amplifiers," *IEEE Trans. Microwave Theory Tech.*, vol. 43, pp. 2952-2958, Dec. 1995.
- [3.41] F. H. Raab, et al., "Power amplifiers and transmitters for RF and microwave," *IEEE Transactions on Microwave Theory and Techniques*, vol. 50, no. 3, pp. 814–826, Mar. 2002.

- [3.42] T. Liu, S. Boumaiza, and F. M. Ghannouchi, "Augmented Hammerstein predistorter for linearization of broad-band wireless transmitters", *IEEE Trans. on Microwave Theory and Techniques*, vol. 54, no. 4, pp. 1340-1349, June 2006.
- [3.43] S. Boumaiza, et al., "Adaptive digital/RF predistortion using a nonuniform LUT indexing function with built-in dependence on the amplifier nonlinearity," *IEEE Transactions on Microwave Theory and Techniques*, vol.52, no.12, pp. 2670-2677, Dec. 2004.
- [3.44] P.L. Gilabert, et al., "Multi-lookup table FPGA implementation of an adaptive digital predistorter for linearizing RF power amplifiers with memory effects," *IEEE Transactions on Microwave Theory and Techniques*, vol.56, no.2, pp.372-384, Feb. 2008.
- [3.45] K.J. Muhonen, M. Kavehrad, R. Krishnamoorthy, "Look-up table techniques for adaptive digital predistortion: a development and comparison," *IEEE Transactions on Vehicular Technology*, vol.49, no.5, pp.1995-2002, Sep 2000.
- [3.46] Nagata, Y., "Linear amplification technique for digital mobile communications," *IEEE 39<sup>th</sup> Vehicular Technology Conference*, vol.1, pp.159-164, May 1989.
- [3.47] M. Faulkner, T. Mattsson, W. Yates, "Adaptive linearisation using pre-distortion," *IEEE 40<sup>th</sup> Vehicular Technology Conference*, pp.35-40, 6-9 May 1990.
- [3.48] J. K. Cavers, "The effect of quadrature modulator and demodulator errors on adaptive digital predistorters for amplifier linearization," *IEEE Trans. Veh. Technol.*, vol. 46, pp. 456-466, May 1997.
- [3.49] J.K. Cavers, "Amplifier linearization using a digital predistorter with fast adaptation and low memory requirements," *IEEE Transactions on Vehicular Technology*, vol.39, no.4, pp.374-382, Nov 1990.
- [3.50] M. Ghaderi, S. Kumar, D.E. Dodds, "Adaptive predistortion lineariser using polynomial functions," *IEE Proceedings on Communications*, vol.141, no.2, pp.49-55, Apr 1994.
- [3.51] L. Ding, et al., "A robust digital baseband predistorter constructed using memory polynomials," *IEEE Transactions on Communications*, vol.52, no.1, pp. 159-165, Jan. 2004.

- 
- [3.52] S. Hong, et al., "Weighted polynomial digital predistortion for low memory effect doherthy power amplifier," *IEEE Transactions on Microwave Theory and Techniques*, vol.55, no.5, pp.925-931, May 2007.
- [3.53] S.P. Stapleton, F.C. Costescu, "An adaptive predistorter for a power amplifier based on adjacent channel emissions," *IEEE Transactions on Vehicular Technology*, vol.41, no.1, pp.49-56, Feb 1992.
- [3.54] N. Mizusawa, and S. Kusunoki, "Third- and fifth-order baseband component injection for linearization of the power amplifier in a cellular phone," *IEEE Trans. Microw. Theory Tech.*, vol. 53, no. 4, pp. 3327-3334, Apr. 2005.
- [3.55] N. Mizusawa, and S. Kusunoki, "Third and fifth order base-band component injection for linearization of the power amplifier in a cellular phone," In *2005 IEEE MTT-S International Microwave Symposium Digest*, pp. 1565-1568, June 2005.

## **4. MEMORY EFFECTS IN POWER AMPLIFIERS**

### **4.1. Introduction**

Power amplifiers play an important role in wireless communication systems. The requirements of high linearity and efficiency are commonly satisfied by designing a highly-efficient PA at the price of linearity and providing a compensation of nonlinear distortions by an external lineariser. Linearisation techniques, described in the previous Chapter, treat the PA nonlinear behaviour with respect to its input signal. However, in reality the PA behaviour depends not only on the current input signal, but on the previous inputs. This phenomenon, called memory effects, may significantly degrade the performance of linearisers and require a close examination.

This Chapter covers memory effects in power amplifiers. It describes the reasons behind memory effects, their impact on the performance of power amplifiers and discusses the methods used to quantify and compensate for memory effects.

### **4.2. Linearisation and Memory Effects**

Linearisation techniques are traditionally intended for compensating nonlinear distortions in power amplifiers. The performance is determined by the degree of cancelling the distortion components produced by a PA. Theoretically the performance can be attained high by one of the linearisation techniques described in the previous Chapter. The techniques are based on compensating the instantaneous nonlinear behaviour of a PA, assuming that the generated distortion products are dependent only on the current input signal. However, in reality PAs exhibit memory effects and their distortion behaviour depends not only on the instantaneous input, but on the previous inputs as well. Memory effects result in the distortion products generated by a PA being variable and dependent on many conditions, such as the input signal's magnitude, carrier frequency, and bandwidth. Consequently, the distortion-compensation performance of a memoryless lineariser is also variable and not stable.

The impact of memory effects on the linearising performance is different for different types of linearisation [4.1]. Thus the linearisation techniques, which process the actual distortion signals, e.g. feedforward or feedback, are less sensitive to memory effects, whereas the linearisation techniques, which aim to predict the distortion generated by a PA, e.g. ERR or predistortion methods, are more exposed to memory effects. Consequently, in order to improve the performance of predictive linearisation techniques, the compensation of memory effects must be incorporated.

The current section presents a description of the physical phenomena behind memory effects and the impact of memory effects on the PA behaviour.

### 4.2.1 Origins of Memory Effects

Any power amplifier topology includes reactive elements like capacitances and inductances. Moreover, the PA active device also has parasitic capacitance in its  $p$ - $n$  junctions [4.2]. A capacitor is defined by the following differential equation:

$$i_C(t) = C \cdot \frac{dv_C(t)}{dt}, \quad (4.1)$$

where,  $v_C(t)$  is the voltage applied to the capacitor,  $i_C(t)$  is the current flowing through the capacitor, and  $C$  is a constant called capacitance.

Similarly, an inductor is defined as:

$$v_L(t) = L \cdot \frac{di_L(t)}{dt}, \quad (4.2)$$

where,  $i_L(t)$  is the current flowing through the inductor,  $v_L(t)$  is the voltage drop on the inductor, and  $L$  is a constant called inductance.

If a capacitor is driven by a current source  $i_C(t)$ , the voltage between the capacitor's nodes can be obtained as the integral of (4.1) from  $\tau = -\infty$  to  $\tau = t$ :

$$v_C(t) = \frac{1}{C} \int_{-\infty}^t i_C(\tau) d\tau. \quad (4.3)$$

From (4.3) one can see, that the output voltage depends not only on the instantaneous input signal, but on the entire past history.

If at some time  $t_0$ ,  $t_0 < t$ , the value of voltage  $v_C(t_0)$  is known, (4.3) can be re-written using the integral from  $t_0$  to  $t$ :

$$v_C(t) = v_C(t_0) + \frac{1}{C} \int_{t_0}^t i_C(\tau) d\tau. \quad (4.4)$$

As the initial condition  $v_C(t_0)$  summarises the history until the moment  $t_0$ , there is no need in specifying the entire history.

Similarly, an inductor can be described by the following relationship:

$$i_L(t) = i_L(t_0) + \frac{1}{L} \int_{t_0}^t v_L(\tau) d\tau. \quad (4.5)$$

Equations (4.4)-(4.5) show that reactive elements are able to store energy and hence have memory. Therefore, power amplifiers exhibit memory due to the presence of reactive elements in their circuits.

## 4.2.2 Bandwidth-Dependent Behaviour

The time response of power amplifiers with memory depends not only on the instantaneous input signal, but on the previous inputs as well. This can be represented as a convolution of the input signal samples with the PA impulse response. The convolution in the time domain corresponds to the multiplication in the frequency domain. Consequently, memory effects result in the frequency-dependent gain and phase shifts of the signal passing through the PA. For this reason, in literature memory effects are often defined as the dependence of the magnitude and phase of the output signal on modulation frequency [4.3].

In a memoryless system, the signal distortion does not depend on frequency, whereas in a system exhibiting memory effects, the signal distortion varies with frequency. Another consequence of memory effects is a phase shift. Generally, memoryless systems do not cause phase shifts, whereas those containing energy-storing elements introduce a phase distortion dependent on frequency. Indeed, for a circuit composed of a resistive element with the impedance  $Z_R=R$  and a reactive element, capacitor, with the impedance  $Z_C=1/j\omega C$ , the total impedance is given by:

$$Z_0 = R + \frac{1}{j\omega C}. \quad (4.6)$$

From (4.6) it is obvious that after passing a circuit containing resistive and reactive elements, the signal magnitude and phase will be affected, and this impact is dependent

on frequency. This notation leads to a major difference between the memoryless systems and those with memory, which is used to quantify memory effects. The common approach for quantifying memory effects of a nonlinear system is to analyse the phase distortion introduced by the system and the dependence of its gain and phase on frequency. For this purpose, phasors analysis can be used [4.1]. The signal in sinusoidal form,

$$s(t) = V \cdot \cos(\omega t + \varphi), \quad (4.7)$$

is re-written as a sum of two complex phasors using the Euler's equation:

$$s(t) = \frac{V}{2} \cdot e^{j\varphi} \cdot e^{j\omega t} + \frac{V}{2} \cdot e^{-j\varphi} \cdot e^{-j\omega t}. \quad (4.8)$$

In the last equation the phasors containing  $\omega t$  represent the phase shift over frequency and the factors containing magnitude  $V$  and phase  $\varphi$  information completely represent the initial signal given by (4.7). Such an approach simplifies the process of analysing memory effects because the operations of integration and differentiation used to describe energy-storing elements are replaced by multiplications or divisions with  $j\omega$ .

If time constants of a nonlinear system are much smaller than the inverse value of the maximum envelope frequency of the input signal, the system is considered to have small memory and can be treated as a quasi-memoryless system. Such systems can be accurately represented by their AM/AM and AM/PM characteristics, which depend only on the instantaneous value of the input signal [4.4]. On the contrary, systems with large memory cannot be accurately modelled only by their AM/AM and AM/PM characteristics. For such systems other modelling approaches are used, which will be described later. Using the same reasoning, a system may be considered to be a quasi-memoryless system for narrow-band signals, whereas it exhibits large memory for wide-band signals. This leads to another definition of memory effects as bandwidth-dependent effects.

For characterisation of bandwidth-dependent effects, a two-tone test with variable tone spacing is commonly used. Alternatively, a digitally-modulated signal test may be used for this purpose. The first method has advantages of lower computational complexity and possibility of analytical calculation of the spectral components.

Generally, in order to evaluate memory effects, a single tone test can be applied as well as the two-tone test. The fundamental output signal being affected by the PA memory will demonstrate amplitude and phase distortions even in a linear mode. These

distortions can be used to quantify memory effects. However, as the fundamental signals are strong comparing to the distortions produced by the PA memory, the described approach may suffer from poor accuracy. More precise results can be achieved by analysing the intermodulation components' behaviour under a two-tone test.

A polynomial model of a memoryless system excited with a two-tone signal produces in-band IM3 components, which are invariable with the change in tone spacing and have the amplitude proportional to the third power of the input signal amplitude, as described in Chapter 2. However, the practical measurement of IM3 components for a PA exhibiting memory effects shows that their magnitude and phase are dependent on tone difference. This is shown in Figure 4-1, where the experimental (a) and theoretical (b) IM3 magnitude curves are presented. The experimental results are obtained by measuring the magnitude of the IM3 component for a Mini-Circuits ZFL-500 power amplifier under a two-tone excitation at -10 dBm input power with variable tone spacing in the range of 0.01 – 10 MHz. From the Figure one can conclude that the IM3 component of a PA exhibiting memory effects is dependent on the input signal bandwidth and is higher than the theoretically predicted level.

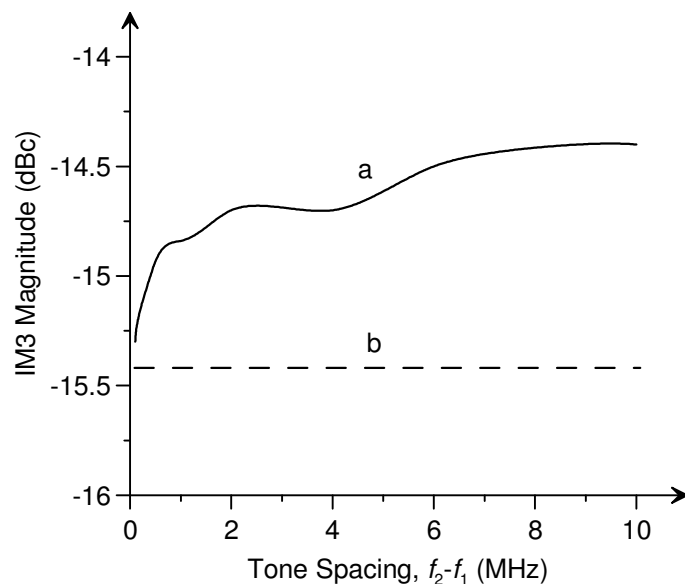


Figure 4-1: Magnitude of the IM3 component: (a) measured experimentally for the PA Mini-Circuits ZFL-500 at a -10 dBm input power level; (b) calculated theoretically based on a polynomial model

### 4.3. Classification of Memory Effects

Memory effects in RF power amplifiers can be classified as electrical and thermal (or electrothermal) [4.5]-[4.7]. The electrical memory effects occur because of the dependence of PA node impedances, particularly the impedances of the biasing and matching circuits, on signal bandwidth. In other words, the electrical memory effects are caused by the variable frequency response of the PA due to the presence of reactive elements in the circuit. The thermal memory effects appear because of the dependence of electrical characteristics of the active device on temperature. Changes in the junction temperature due to self-heating and different input signal strength as well as the power supply fluctuations result in variations of the transistor temperature-dependent electrical parameters. This, in turns, modifies the behaviour of the whole amplifier and introduces additional distortions. Consequently, the main locations of the electrical memory effects are the biasing and matching circuits of the PA, while the thermal memory effects are primarily located within the PA active device.

Due to the nature of electrical and thermal memory, their time duration is different: the electrical memory effects impact the signal passing through the PA during a short time interval, comparing to the thermal memory effects, which appear during a longer period. For this reason, the electrical and thermal memory effects are also called short-term and long-term memory effects correspondingly [4.7].

From the modelling point of view, a nonlinear system exhibiting electrical memory can be represented by a model consisted of two separate blocks, one of which contains a model for the nonlinear behaviour and the other one accounts for the memory effects; whereas a nonlinear system with thermal memory exhibits some dynamic effects and cannot be modelled by a linear cascade of two non-interacting blocks [4.6]-[4.7]. For this reason, the electrical memory effects are also known as linear memory, whereas the thermal memory effects represent nonlinear memory [4.7].

It is commonly accepted that the thermal memory effects typically appear at low modulation frequencies up to 1 MHz, while the electrical memory effects occur at higher frequencies in order of several MHz [4.3]-[4.6]. Consequently, narrow-band signals, such as EDGE or GSM, are more sensitive to the PA thermal memory; and wide-band signals, such as WCDMA or WiMAX, are more exposed to the electrical memory effects.

### 4.3.1 Electrical Memory Effects

The electrical memory effects are mainly produced by the reactive elements of the PA biasing and matching circuits. In order to investigate physical phenomena behind the electrical memory effects, the complex impedances of the PA nodes are considered below. The general layouts for the common-emitter BJT and common-source MESFET PA circuits are presented in Figure 4-2 (a) and (b) respectively [4.1].

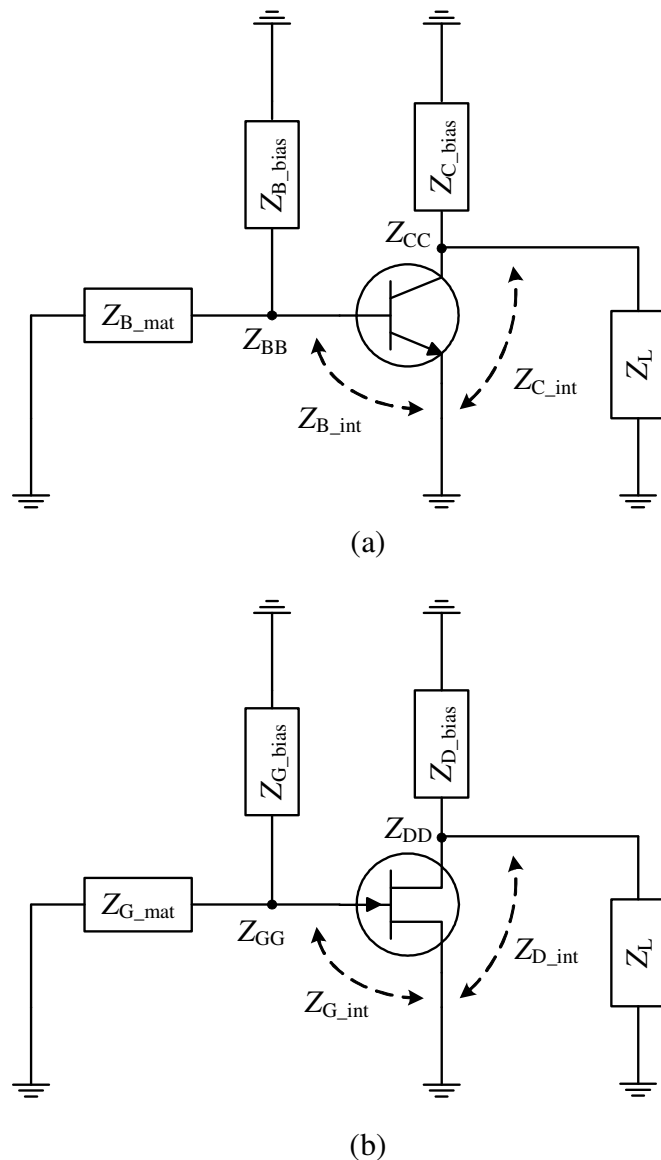


Figure 4-2: Matching and biasing circuits' impedances: (a) common-emitter BJT amplifier; (b) common-source MESFET amplifier

In Figure 4-2  $Z_{B\_mat}$  and  $Z_{G\_mat}$  are the complex impedances of the input matching circuits connected to the base of the BJT transistor (a) and to the gate of the MESFET transistor (b) respectively.  $Z_{B\_bias}$ ,  $Z_{C\_bias}$ ,  $Z_{G\_bias}$ , and  $Z_{D\_bias}$  are the complex impedances of the corresponding base, collector, gate, and drain biasing circuits.  $Z_{B\_int}$ ,  $Z_{C\_int}$ ,  $Z_{G\_int}$ , and  $Z_{D\_int}$  are the internal impedances of the base, collector, gate, and drain of the corresponding active devices.  $Z_L$  is the load impedance. For the BJT PA the node impedance of the base node  $Z_{BB}$  can be calculated as a parallel connection of the base matching  $Z_{B\_mat}$ , base biasing  $Z_{B\_bias}$  and internal base impedances  $Z_{B\_int}$ . In the same way, the node impedance of the collector node  $Z_{CC}$  can be calculated as a parallel connection of the load  $Z_L$ , collector biasing  $Z_{C\_bias}$  and internal collector  $Z_{C\_int}$  impedances. A similar notation can be made for the MESFET PA.

The difference between the theoretically predicted by polynomial modelling nonlinear behaviour and the measured characteristic, as shown in Figure 4-1, appears because of two main reasons: the presence of several nonlinear sources in a PA and the phenomenon that the input distortion components at one node having a complex impedance generate higher-order frequency-dependent distortion components, which sum up and form the resulting behaviour. Therefore, the node impedances must be carefully considered during the design of a highly-linear PA. The described phenomenon of a consecutive distortion generation can be represented as a simplified cascade of two polynomials [4.6]. Hereby, for a BJT PA (Figure 4-2a) the first polynomial models the nonlinearity between the base-emitter voltage and the input voltage, whereas the second one stands for the nonlinearity between the output current and the base-emitter voltage. A similar notation can be written for a MESFET PA (Figure 4-2b).

Consequently, the multi-tone signal, obtained at the output of the first polynomial, shown in Figure 4-3, is applied to the second nonlinearity. The IM3 magnitude of the input signal with the magnitude  $V_{max}$  is evaluated in dBm by the following (see Section 2.4):

$$V_{\max\_IM3} = \frac{3g_3}{4} \cdot V_{\max}^3 \quad (4.9)$$

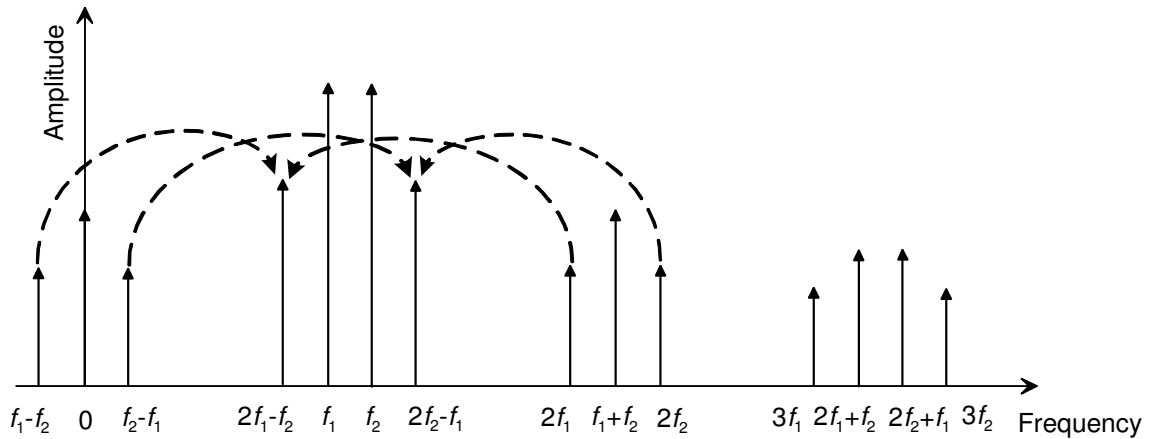


Figure 4-3: Contribution to the final IM3 from spectral components using a cascaded polynomial model

Being fed to the input of the second nonlinearity, this multi-tone signal produces the output IM3, which is a result of mixing of many spectral components. For example, the output IM3 at  $2\omega_2 - \omega_1$  is contributed by mixing the envelope signal at  $\omega_2 - \omega_1$  with the fundamental tone at  $\omega_2$  in the second polynomial block. Consequently, the final IM3 is formed not only by the fundamental signal, but also by the envelope frequency components from different nodes. Similarly, the second harmonics at  $2\omega_1$  and  $2\omega_2$  being mixed with the fundamental signal in the second polynomial block contribute to the output IM3.

The varying node impedances for the envelope, fundamental and second-harmonic signals cause the electrical memory effects. As the frequency-dependent deviation range for the fundamental and second-harmonic impedances is relatively small in comparison with the variations of the envelope impedances over frequency, the electrical memory effects are mainly caused by varying node impedances at the envelope frequency [4.1]. As described above, the node impedances are composed of the impedances of the biasing and matching circuits and the internal impedance of the active device. The latter plays a minor role, and the impedance of the matching circuit can be minimised by a careful design. However, due to large time constants, biasing circuits produce the main inevitable part of the electrical memory effects [4.6].

### 4.3.2 Thermal Memory Effects

The thermal memory effects are caused by the varying temperature-dependent electrical parameters of power amplifiers. The varying input signal strength results in a non-constant power dissipated in the active device. The dissipated power outcomes in the self-heating of the active device and its temperature change. The thermal impedance  $Z_{TH}$  is used to describe temperature variations  $\Delta T$  due to power dissipation  $P_{DISS}$ :

$$Z_{TH} = \frac{\Delta T}{P_{DISS}}. \quad (4.10)$$

$Z_{TH}$  quantifies the dependence of heat flow out of the device on its temperature. As the heat flow does not occur instantly, but has some phase delay due to the mass of the device, the thermal impedance also has a phase shift, and hence is a complex-valued quantity. Consequently, the thermal impedance is not constant over frequency, and acts as a low-pass filter with the bandwidth of up to 1 MHz [4.1].

As only the DC and envelope frequencies are within the filter bandwidth, the resulting temperature of the active device consists of three main summands [4.6], the ambient temperature  $T_{AMB}$ , the heat generated by the dissipation of direct current and the frequency-dependent temperature produced by the dissipation of envelope components:

$$T = T_{AMB} + Z_{TH}(DC) \cdot P_{DISS}(DC) + Z_{TH}(\omega_2 - \omega_1) \cdot P_{DISS}(\omega_2 - \omega_1), \quad (4.11)$$

where  $Z_{TH}(DC)$  and  $Z_{TH}(\omega_2 - \omega_1)$  are the thermal impedances at the DC and envelope frequencies;  $P_{TH}(DC)$  and  $P_{TH}(\omega_2 - \omega_1)$  are the power dissipations at the DC and envelope frequencies. As can be seen from (4.11), the temperature variations depend on signal frequency. Consequently, the temperature-dependent electrical parameters of the device change with the input signal frequency, causing the thermal memory effects.

The described phenomenon can be modelled by a Thermal Power Feedback (TPF) circuit, presented in Figure 4-4 [4.1]. The thermal low-pass filter models the temperature change due to power dissipation  $P_{DISS}$ , proportional to the square of the input signal magnitude,

$$P_{DISS} \propto V_{IN}^2, \quad (4.12)$$

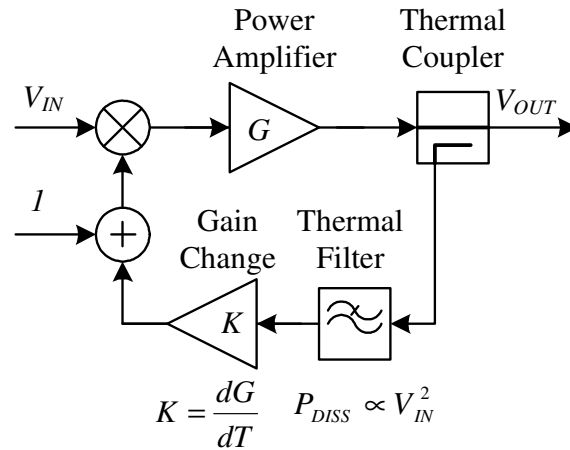


Figure 4-4: Block diagram of a thermal power feedback

whereas the block “K” represents the PA gain  $G$  change with temperature  $T$ :

$$K = \frac{dG}{dT}. \quad (4.13)$$

The thermal impedance frequency-dependent behaviour was investigated and reported in [4.1], [4.8]. The normalised magnitude and phase of thermal impedance variations over frequency for a PA integrated circuit is presented in Figure 4-5. From the Figure two main conclusions can be made: the thermal impedance at DC is pure resistive as the phase equals to zero, and the thermal impedances for the positive and negative frequencies have opposite phases.

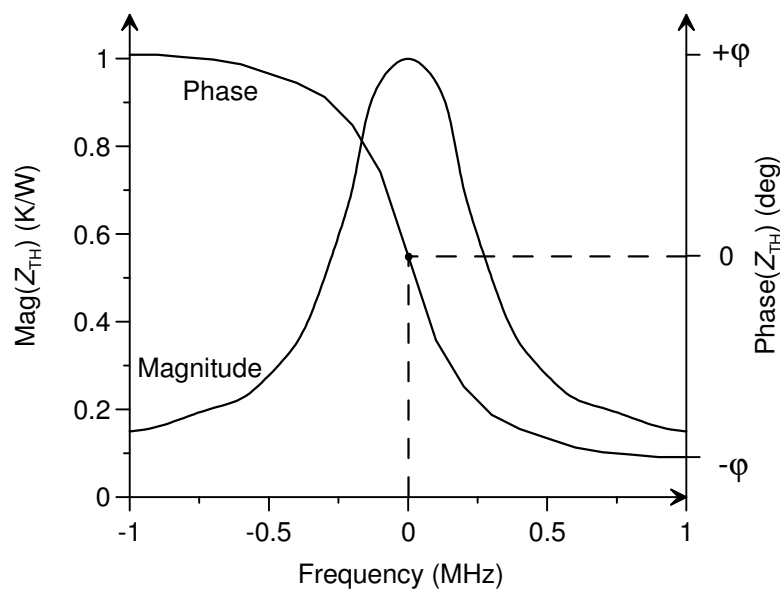


Figure 4-5: Normalised thermal impedance of a PA integrated circuit versus frequency

The latter notation outcomes in asymmetry between the higher and lower third-order intermodulation products IM3H and IM3L at low modulation frequencies. This is illustrated in the Figure 4-6, where the measured IM3H and IM3L components are presented for the power amplifier Mini-Circuits ZFL-500. The experimental results are obtained using a two-tone test with the input power level of -10 dBm and varying tone spacing in the range of 1 kHz - 10 MHz.

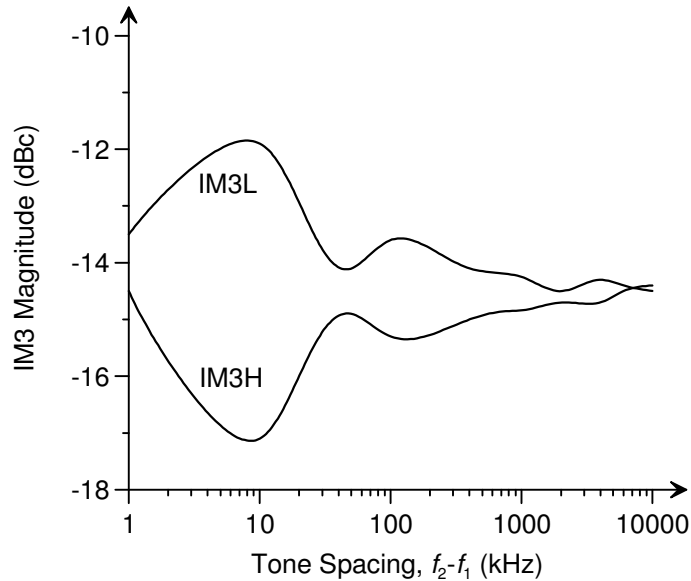


Figure 4-6: Measured asymmetry in the lower and higher IM3 for the PA Mini-Circuits ZFL-500 due to the thermal memory effects

The presented IM3 asymmetry (Figure 4-6) is observed at low modulation frequencies up to 1 MHz due to the thermal memory effects of the power amplifier. Analysis of the IM3 frequency-dependent behaviour is one of the methods used to quantify memory effects. This method and the other measurement techniques used to analyse memory effects in power amplifiers are described in the next Section.

#### 4.4. Quantifying Memory Effects

Memory effects of power amplifiers result in additional distortions of the output signal even if operating in a linear mode. These distortions can be minimised by implementing a sub-circuit compensating for memory effects. In order to design such a

circuit, PA memory effects must be quantified. There are several methods aimed at measuring and quantifying memory effects. The main techniques, which provide information about the dependence of memory-related distortions on power level and modulation frequency, can be classified into the following three categories: a single-tone test with analysis of the gain and phase dependence on frequency and power level [4.4], a two-tone test with analysis of the IM3 dependence on tone spacing and power level [4.9], and a digitally-modulated signal test with analysis of the distorted constellation diagram in a linear mode [4.10].

In the current Section, quantification of memory effects by the mentioned methods is carried out using Advance Design System (ADS) simulations of a power amplifier exhibiting memory effects. A transistor-level model of a MOSFET PA based on Motorola MRF9742 active device is used in the simulations. The simulation testbed incorporating a harmonic balance controller for executing a single-tone or two-tone test is presented in Figure 4-7. The PA used in simulations is represented by its transistor-level model shown in Figure 4-8. The MRF9742 active device model used in the PA design is presented in Figure 4-9.

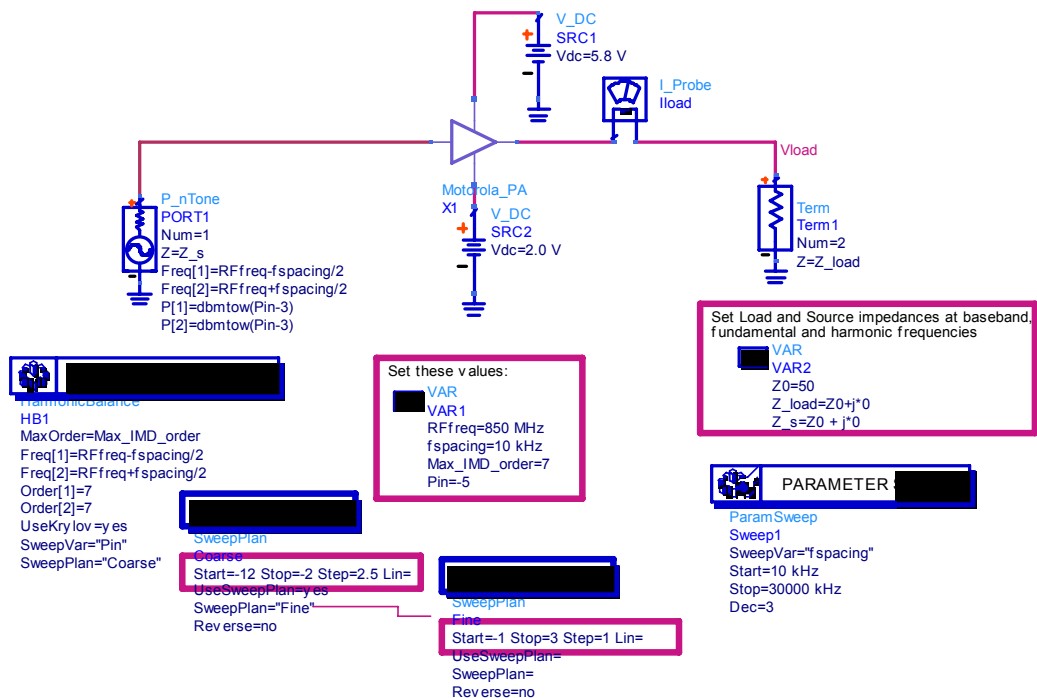


Figure 4-7: Simulation testbed for investigating PA memory effects using a single- or multi-tone input signals

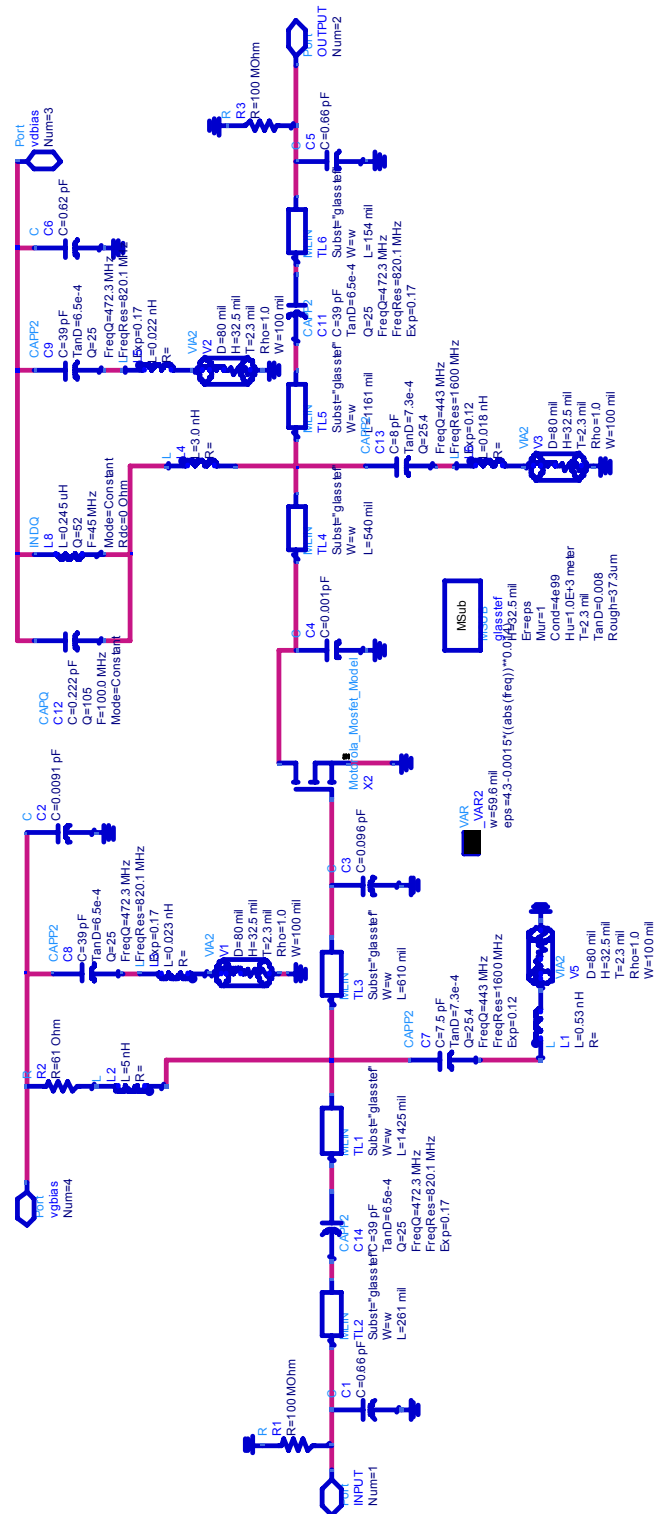


Figure 4-8: Sub-circuit for the PA transistor-level model used in simulations

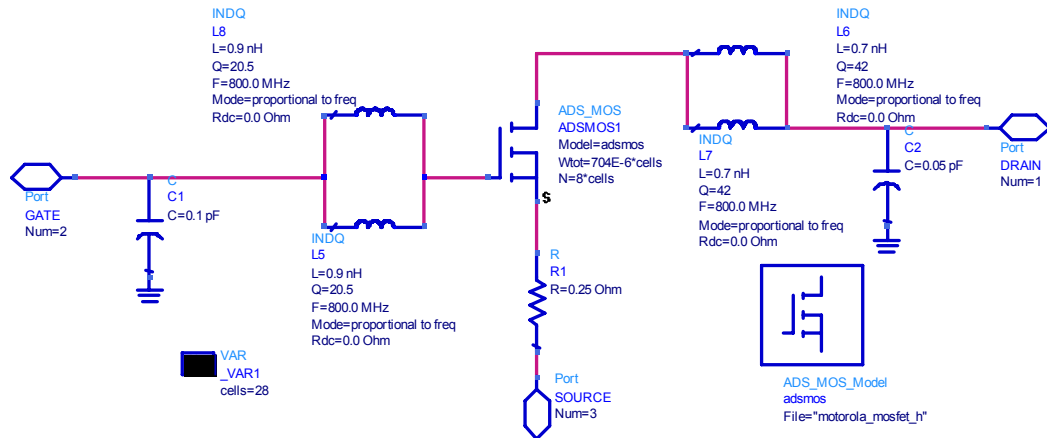


Figure 4-9: ADS model for Motorola MOSFET MRF9742 active device

#### 4.4.1 Single-Tone Analysis

The first method used to quantify memory effects in power amplifiers is a single-tone test using a power and frequency sweep. The main idea is excitation of a PA with RF carrier input signal having the frequency swept over the whole operation bandwidth and the power level swept over the whole operating power range. The measured characteristics include the dependence of AM/AM and AM/PM curves on input signal's frequency and power. Alternatively, variations of the PA gain and phase versus input signal's frequency and power are measured and analysed.

For the considered PA based on a Motorola MRF9742 active device, the ADS simulation testbed presented in Figures 4-7 – 4-9 is configured as follows. The PA has a 12 dB gain and the 1-dB compression point at 25 dBm output power. The centre operation frequency of the PA is  $f_{RF\_C} = 850$  MHz. In order to quantify only memory effects, but not saturation, the output power range is chosen as  $P_{OUT} = 0 \dots 15$  dBm, which corresponds to the input power of  $P_{IN} = -12 \dots 3$  dBm. The RF tone frequency is swept around the centre frequency in the range of 30 MHz, which corresponds to the signal bandwidth when a digital modulation is used. Hence the tested RF frequencies are  $f_{RF} = 835 \dots 865$  MHz. Figure 4-10 shows the dispersion of the PA gain for different modulation frequencies versus output power level. As can be seen from the Figure, the dispersion is stronger for higher power levels.

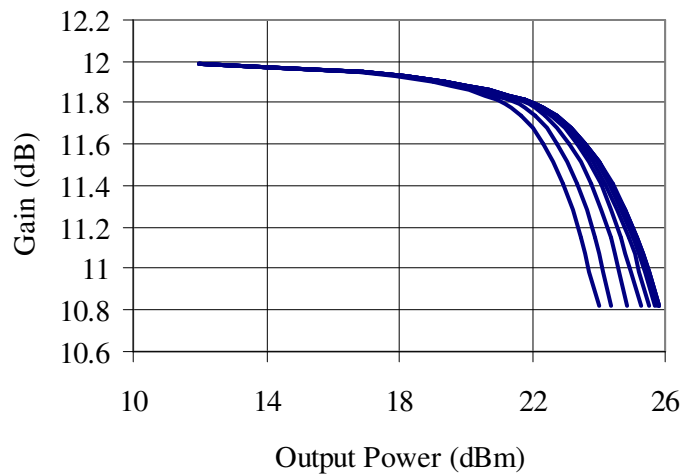


Figure 4-10: Simulated MRF9742 gain dependence on power level for the frequency range of 835...865 MHz

Figures 4-11 and 4-12 show respectively the simulated dependence of PA gain and phase on modulation frequency for different power levels. As the power range is chosen to provide the PA operation with a significant back-off, the observed gain and phase distortions are caused purely by memory effects. From the Figures 4-11 and 4-12 one can conclude that the memory-related distortions depend on power level. For  $P_{\text{OUT}} = 0$  dBm the gain is almost independent from the modulation frequency and the phase is linear, whereas for  $P_{\text{OUT}} = 15$  dBm the characteristics are significantly varying with frequency.

The main advantages of the single-tone analysis are its simplicity and convenience of processing the measured results, which can be directly used for calculating the pre-compensation circuit's parameters. As memory-compensating techniques are often based on constructing the inverse frequency-dependent gain and phase characteristics, the single-tone analysis provides the required data. However, the accuracy of memory effects quantification by this method is limited, because the frequency-dependent distortions of AM/AM and AM/PM characteristics are very small comparing to the fundamental signal. This makes the measurement of memory effects practically difficult by a single-tone test. Another drawback of this method is its inability to analyse intermodulation distortions related to memory effects. This can be accomplished by a two-tone analysis.

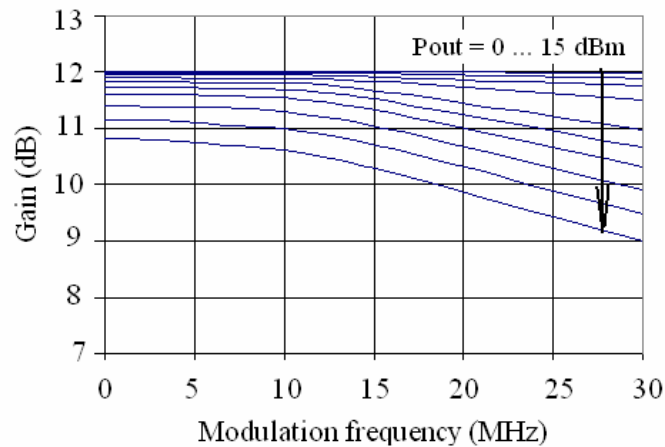


Figure 4-11: Simulated MRF9742 gain variations over modulation frequency due to memory effects

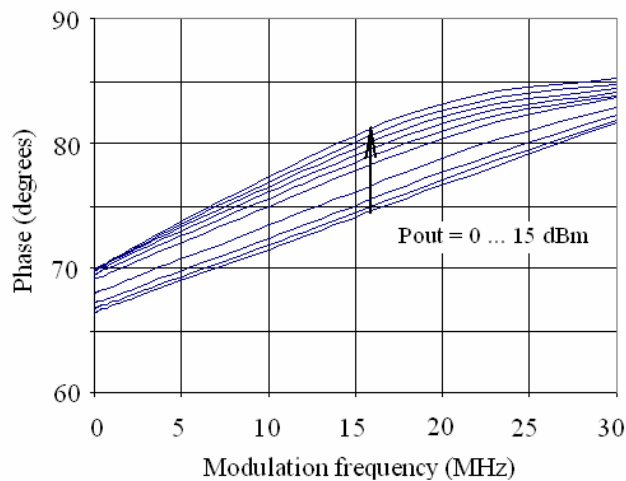


Figure 4-12: Simulated MRF9742 phase variations over modulation frequency due to memory effects

#### 4.4.2 Two-Tone Analysis

The second method used to quantify memory effects in power amplifiers is a two-tone test with variable tone-spacing and input power level. A PA is excited with two RF carriers of equal magnitudes. Similarly to the previously described technique, the power of the input tones is swept in order to cover the whole dynamic range of the PA, and the difference between the tone frequencies is swept over the whole PA operating

bandwidth. Using this method, the dependence of the magnitude and phase of higher and lower third-order intermodulation products IM3H and IM3L on frequency and power is measured.

For the considered 12-dB gain and the 1-dB compression point at 25 dBm output power amplifier, the output power is varying in the range of  $P_{\text{OUT}} = 0 \dots 15$  dBm in order to quantify only memory effects but not the distortion caused by the PA transfer characteristic nonlinearity. The ADS simulation testbed is configured similarly to the single-tone test. The unmodulated RF signals are placed around the centre frequency  $f_{\text{RF}} = 850$  MHz with the tone spacing varying in the range of  $f_{\text{spacing}} = 10 \text{ kHz} \dots 30$  MHz. Figures 4-13 and 4-14 show respectively the simulated IM3 magnitude and phase variations due to memory effects.

The characteristics are presented in 3D plots versus tone spacing and output power level of the considered PA (MRF9742). In a memoryless system, the IM3 magnitude is proportional to the third power of the input signal magnitude and does not vary with frequency. The observed IM3 magnitude and phase fluctuations are caused by memory effects.

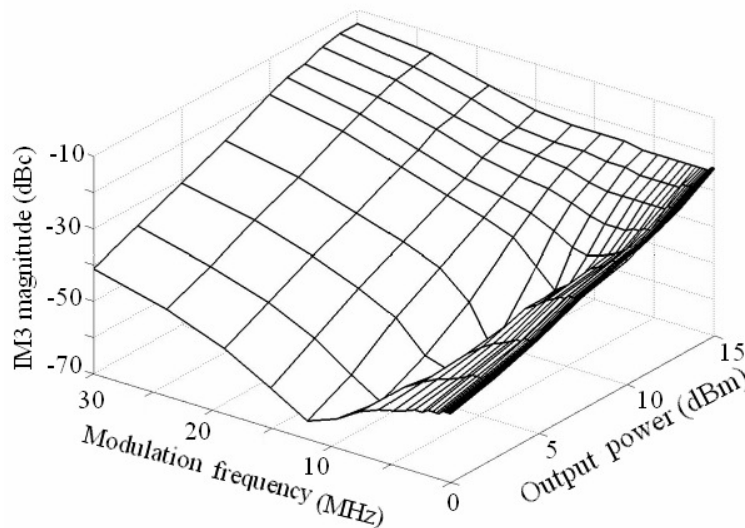


Figure 4-13: Simulated MRF9742 IM3 magnitude variations over modulation frequency and output power due to PA memory effects

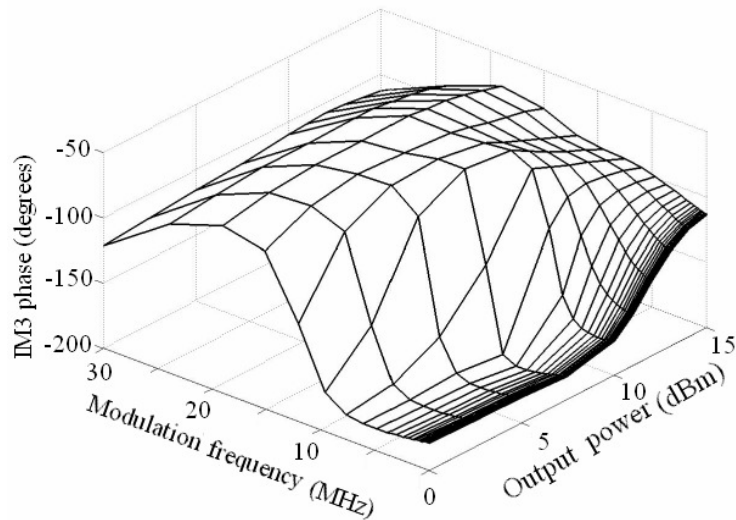


Figure 4-14: Simulated MRF9742 IM3 phase variations over modulation frequency and output power due to PA memory effects

The main advantages of the two-tone analysis are its ability to measure intermodulation distortions and relatively high accuracy due to the fact that memory effects cause significant variations in the IM3 magnitude and phase, which can be easily measured. However, the method does not directly provide the AM/AM and AM/PM characteristics of the PA and hence is not very useful in calculating or optimising parameters of the memory pre-compensation system. Consequently, it is often convenient to use both of the described methods.

#### 4.4.3 Digitally Modulated Test

Another method used to quantify memory effects in power amplifiers is a digitally-modulated signal test. This method is used to analyse the impact of PA memory effects on the output signal constellation diagram. A digitally modulated signal is fed to the PA input with the power level below saturation. The observed distortion in the output constellation diagram when the PA operates in a linear mode shows the impact of memory effects.

In order to carry out a digitally modulated signal test for the considered PA, a combined Matlab-ADS co-simulation setup was created. The main layout for the ADS testbed is shown in Figure 4-15.

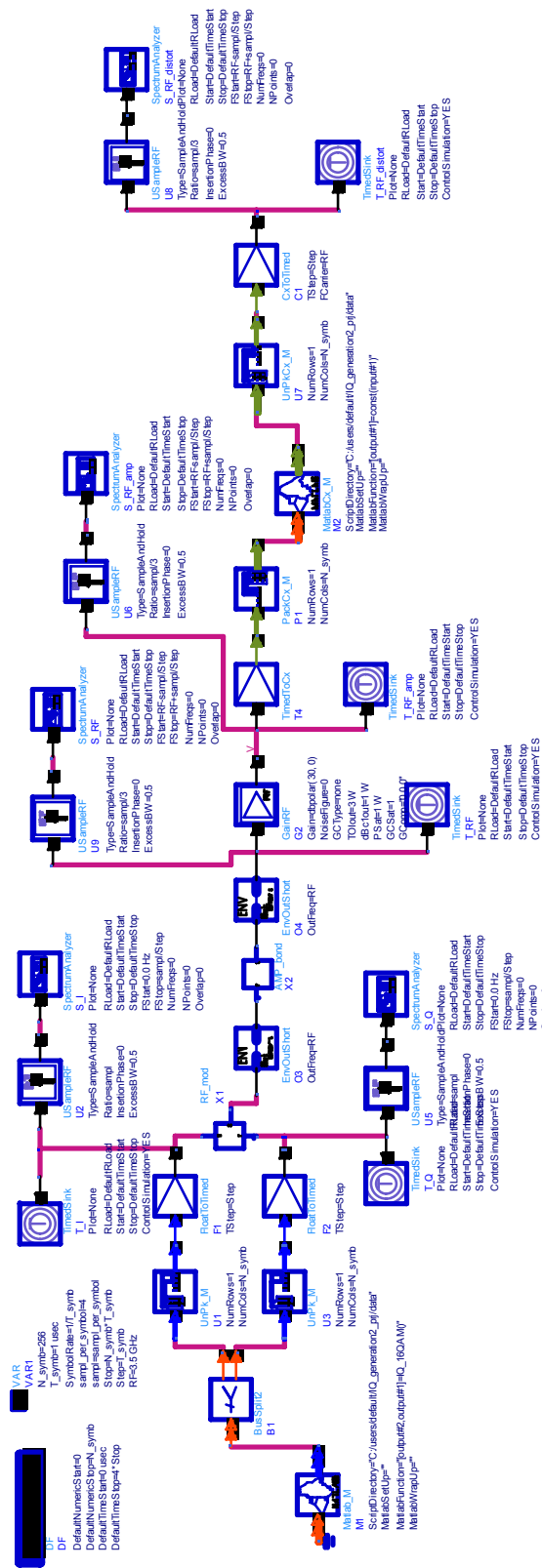


Figure 4-15: Main circuit for the Matlab-ADS connected simulation

The main ADS digital circuit uses a data flow simulation controller in order to execute simulations. The input 256-OFDM 16-QAM modulated signal is generated in Matlab. The considered PA (Figures 4-7 – 4-9) is implemented as an analogue ADS sub-circuit with the envelope simulation controller. The PA output signal is forwarded to Matlab, where the constellation diagram is plotted. The detailed description of the developed Matlab-ADS co-simulation system is presented below in Chapter 6.

In order to demonstrate the impact of memory effects in a pure linear mode and in a weakly non-linear mode, the simulations are carried out at two input power levels:  $P_{IN1} = -5$  dBm, which corresponds to the linear part of the PA transfer characteristic, and  $P_{IN2} = 13$  dBm, which relates to the 1-dB compression point. The corresponding constellation diagrams are presented in Figures 4-16 and 4-17.

As can be seen from the Figures, memory effects in the linear mode cause rotations of the constellation diagram points due to the dependence of PA phase on modulation frequency, whereas in a weakly nonlinear mode both the amplitude and phase nonlinear frequency-dependent distortions cause the dispersion and rotation of the constellation diagram points. The distortion of the constellation diagram due to memory effects is well-consistent with the gain and phase distortions under a single-tone test, presented in Figures 4-10 – 4-12. For a  $P_{IN1} = -5$  dBm corresponding to  $P_{OUT} = 7$  dBm the gain is almost constant, and there is a linear phase shift over modulation frequency. This is reflected in the constellation diagram, where the “circles” are formed by the baseband signal samples of the same magnitude, but appearing at the different OFDM sub-channel frequencies. Moreover, the diameter of the “circles” on the constellation diagram increases for those signal samples, which have greater baseband magnitude. The same behaviour can be observed from the Figures 4-11 and 4-12, where for higher power levels the impact of memory effects is more appreciable. This notation leads to a conclusion that memory effects are dependent on the power level: the impact of memory effects is more considerable for higher amplitudes of the input signal.

The digitally-modulated signal test described above is not useful for obtaining the required data for calculating parameters of the memory-compensating circuit. However, it provides the best measure of the circuit’s performance and is used to evaluate the operation of the overall system including the PA and lineariser.

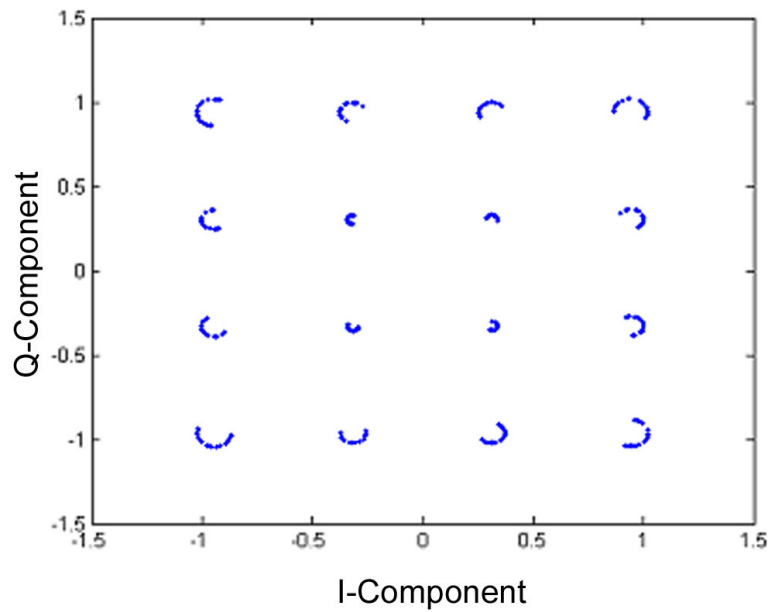


Figure 4-16: Normalised constellation diagram of a 16-QAM signal after passing the PA in a linear mode at -5 dBm input power level. The distortion is caused only by memory effects

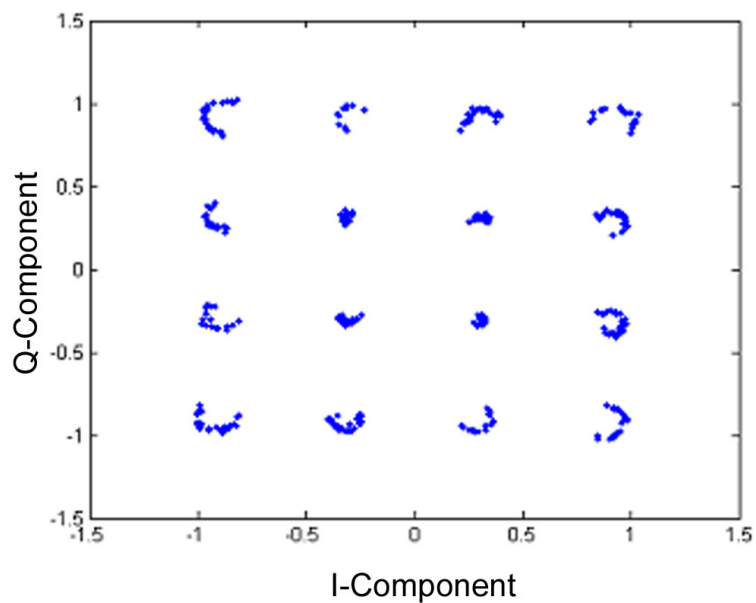


Figure 4-17: Normalised constellation diagram of a 16-QAM signal after passing the PA in a weakly non-linear mode at 13 dBm input power level. The distortion is caused by the nonlinear transfer function and memory effects

## 4.5. Memory Effects Compensation Techniques

Memory effects of power amplifiers cause degradation of the distortion-compensation performance of linearisers. As it has been mentioned in Section 4.2, different linearisation techniques have different sensitivity to memory effects. Thus the feedforward and feedback techniques are able to reduce distortions caused by PA memory, whereas the predictive techniques, particularly digital predistortion, do not cope with memory effects. For such systems, a memory-compensation circuit needs to be implemented if the PA exhibits considerable amount of memory. In the case of DPD, a practically achievable degree of IM3 may be limited to medium-low due to the presence of memory. However, if a memory-compensation circuit is implemented together with the predistorter, the linearising performance can be increased.

The current Section presents an overview of the most commonly used methods for compensating memory effects: impedance optimisation, envelope filtering, envelope injection, and baseband equalisation. The first method is based on the idea of flattening impedances of the biasing and matching circuits over the frequency band in order to reduce the PA frequency-dependent behaviour [4.11]-[4.12]. The envelope filtering and injection methods [4.13]-[4.15] based on the idea of constructing the opposite memory effects in the lineariser using an envelope signal can reduce IM3 of the PA under a range of conditions, but they have stability problems and are difficult for practical implementation due to the requirements for precise tuning of the predistorter and maintenance of the proper phase relation. The baseband equalisation method [4.16] is a powerful tool for minimising memory effects based on the idea of compensating for the PA frequency-dependent behaviour by a filter, which has the frequency response inverse to that of the PA.

### 4.5.1 Impedance Optimisation

The impedance optimisation method is used to compensate for the electrical memory effects. As mentioned in Section 4.3.1, the frequency-dependent behaviour of the output signal is substantially contributed by varying with frequency node impedances at the envelope, fundamental and harmonic bands, which form the

intermodulation distortion IM3. Consequently, making the impedances constant over frequency will reduce the electrical memory effects. As the practical impedance deviation range for the fundamental and harmonic bands is negligibly small compared to that of the envelope band, the impedance optimisation method is used to flatten the envelope impedance [4.1].

Impedance optimisation can be accomplished by the source-pull method, which is described below with an example of a BJT PA. The PA base-emitter nonlinearity produces distortion currents, which result in the output signal distortion. For the common-emitter BJT amplifier shown in Figure 4-2a the base node impedance  $Z_{BB}$  is calculated as the parallel connection of the matching, biasing and internal impedances  $Z_{B\_mat}$ ,  $Z_{B\_bias}$ ,  $Z_{B\_int}$ . The nonlinear BJT circuit can be represented by its Norton equivalent consisted of the input impedance  $Z_{IN}$  and the base-emitter internal impedance  $Z_{BE}$  with the nonlinear current source  $I_{NL}$ , as shown in Figure 4-18. In correspondence to the previous notation, the input impedance is the parallel connection of the matching and biasing impedances:  $Z_{IN}=Z_{B\_mat}\parallel Z_{B\_bias}$ .

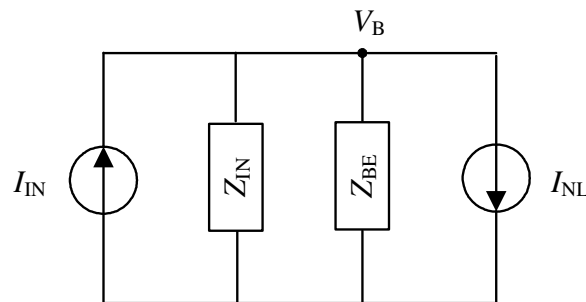


Figure 4-18: Norton equivalent for the active device nonlinear circuit

For a two-tone input signal, the envelope voltage at the base node can be found as:

$$V_B(\omega_2 - \omega_1) = [I_{IN}(\omega_2 - \omega_1) - I_{NL}(\omega_2 - \omega_1)] \cdot Z_{BB}(\omega_2 - \omega_1), \quad (4.14)$$

where  $Z_{BB}=Z_{IN}\parallel Z_{BE}$ . By tuning  $I_{IN}(\omega_2-\omega_1)$ , the base voltage at the envelope frequency can be forced to zero when the following condition is fulfilled:

$$I_{IN}(\omega_2 - \omega_1) = I_{NL}(\omega_2 - \omega_1). \quad (4.15)$$

The effective impedance seen by the nonlinear current is calculated as the ratio of the node voltage to the nonlinear current:

$$Z_{BB\text{eff}} = \frac{V_B(\omega_2 - \omega_1)}{I_{NL}(\omega_2 - \omega_1)} = \left[ \frac{I_{IN}(\omega_2 - \omega_1)}{I_{NL}(\omega_2 - \omega_1)} - 1 \right] \cdot Z_{BB}(\omega_2 - \omega_1). \quad (4.16)$$

Consequently, the effective impedance can be controlled by changing  $I_{IN}$ . If the input current is applied as (4.15), no voltage appears at the base node, meaning that the effective impedance is forced to zero. If the input current is applied with the same magnitude and  $180^\circ$ -phase, the effective impedance equals to the actual base impedance times two, as can be observed from (4.16). This method allows keeping the base envelope voltage equal to zero, which results in reduction of IM3.

The concept of the out-of-band impedance optimisation is to add an external source of the same frequency and tune it in order to fulfil the condition (4.15), producing the second-order distortion products virtually equal to zero, which results in the reduction of final IM3. A test setup for optimising the envelope impedance proposed in [4.11] is shown in Figure 4-19.

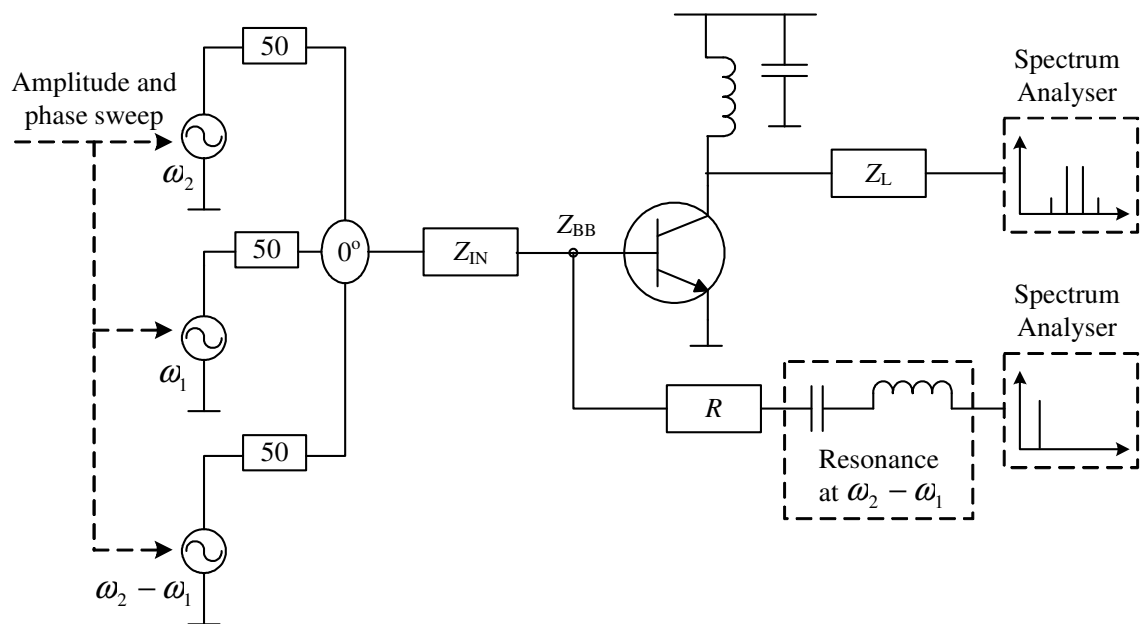


Figure 4-19: Test setup for optimising envelope impedance

Signal generators are used to provide a two-tone input and the envelope signal. The signal generators being phase-locked are tuned by amplitude and phase adjustments. The input signals are combined and fed to the PA input. The envelope component of the base signal is detected using the resonance chain tuned to  $\omega_2 - \omega_1$  and monitored in the spectrum analyser. When the envelope signal disappears, the requirement (4.15) is

fulfilled. Under this condition, the optimal base impedance is calculated using the input and measured voltages and currents. The base impedance is set to its optimal value by modifying the matching or biasing circuit's impedance:  $Z_{B\_mat}$ ,  $Z_{B\_bias}$ .

The impedance optimisation method can provide some improvement in distortion compensation as claimed in [4.11]-[4.12]. However, there are a number of shortcomings inherent to the technique. Firstly, the actual base impedance varies depending on the biasing conditions and signal applied. Secondly, there is a practical difficulty of measuring and generating the optimum impedance. Finally, the requirement for calibration and necessity of an additional signal source make the process time-consuming and difficult to implement.

#### 4.5.2 Envelope Filtering

The idea behind the envelope filtering technique is to create the opposite to PA memory effects in a predistorter by multiplying the filtered and tuned envelope signal with the fundamental signal [4-13]. A general block diagram describing the operation of the envelope filtering technique is presented in Figure 4-20.

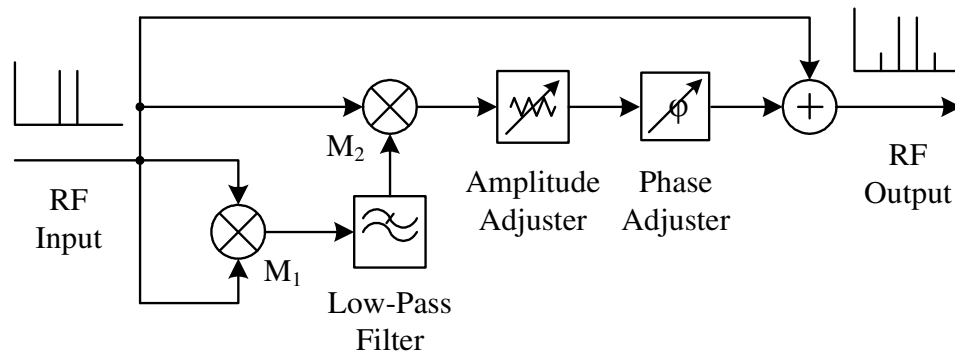


Figure 4-20: A general block diagram of the envelope filtering technique

The input signal is squared in the multiplexer  $M_1$  producing the envelope and second harmonic components. The envelope signal is extracted using the low-pass filter. It is further multiplied with the fundamental signal in the multiplexer  $M_2$  in order to produce additional IM3 components used to eliminate those generated by the PA. Finally, the amplitude and phase of the obtained IM3 signal is tuned using the amplitude

and phase adjusters, and the resulting predistortion signal is summed with the fundamental one. The filter in Figure 4-20 has an even-symmetry in its amplitude response and an odd-symmetry in the phase response, meaning that the amplitudes of responses for the negative and positive frequencies are equal, but their phases are opposite to each other. This results in the opposite phase shift for the generated IM3 sidebands. Such an approach imitates symmetrical memory effects of a PA, which can be successfully cancelled. Symmetrical means that memory effects outcome in the higher and lower IM3, which have equal magnitudes but opposite phases.

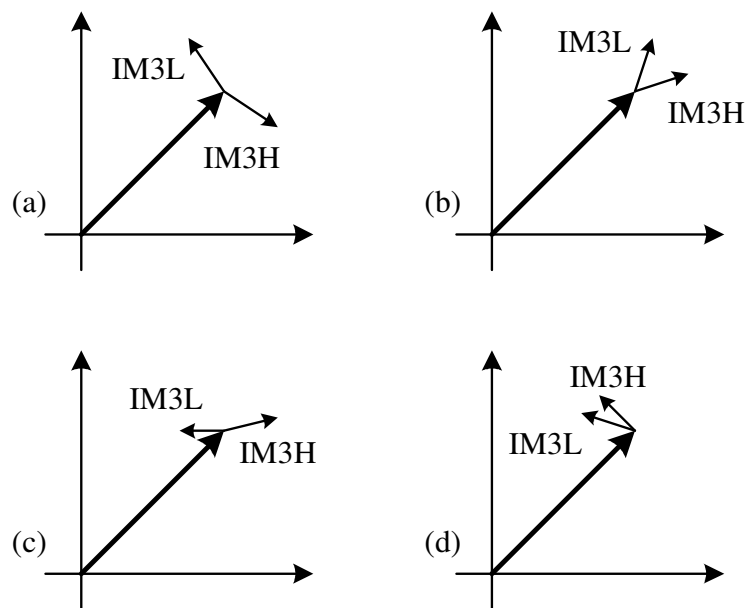


Figure 4-21: Examples of the symmetrical (a)-(b) and asymmetrical (c)-(d) memory effects

Figure 4-21 presents typical examples of the symmetrical and asymmetrical memory effects. The IM3 distortion due to PA nonlinearity is highlighted as the bold arrows, whereas the regular arrows represent IM3 distortions caused by memory effects. Inaccuracies in the memoryless nonlinearity compensation, which can be understood as the phase mismatch between the memoryless predistorter and bold IM3 components in Figure 4-21, outcome in violation of symmetry of memory effects, making the envelope filtering technique ineffective. Therefore, the memoryless part of a predistorter must be tuned accurately in order to make possible compensation of memory effects by the envelope filtering method.

The main advantage of the envelope filtering technique is its relative simplicity. The main disadvantages are: incapability of handling the asymmetric memory effects, practical difficulty of maintaining the precise amplitude and phase relations of the predistortion signal and high accuracy requirements to the envelope filter and memoryless part of the predistorter.

### 4.5.3 Envelope Injection

Envelope injection technique [4.13]-[4.15] is based on the assumption that memory effects are predominantly caused by upconverting the envelope signal to the final IM3. Indeed, considering a PA as a cascade of two nonlinearities (see Section 5.2), the input signal after passing the first nonlinearity produces the envelope and harmonic components at  $\omega_2 - \omega_1$  and  $2\omega_1$  correspondently, which are affected by frequency-dependent impedances. After that the envelope and harmonic signals with the inserted frequency-dependent distortion are passed through the second nonlinearity, and converted to the final IM3, which now includes memory effects. Assuming that the frequency-dependent variations of node impedances are mainly expressed at the envelope frequencies, the main part of the final memory effects is caused by the upconverted envelope signal. Consequently, using an additional envelope signal with the properly tuned amplitude and phase, it is possible to reduce memory effects.

The envelope injection technique can be considered as a real-time source-pull method described above. However, the injected envelope signal is not taken from an additional source, but generated from the input signal by squaring it. A block diagram of the envelope injection technique is presented in Figure 4-22.

Here, the envelope injection technique is implemented together with a polynomial predistorter. The main difference to the envelope filtering technique is that the compensation of memory effects is carried out by modifying the envelope signal, but not the whole IM3 vector. It means that only the part of signal, which produces memory effects, is cancelled by the injected signal. This approach has several advantages, which are: lower accuracy requirements for the low-pass filter and the ability to compensate for the asymmetrical memory effects.

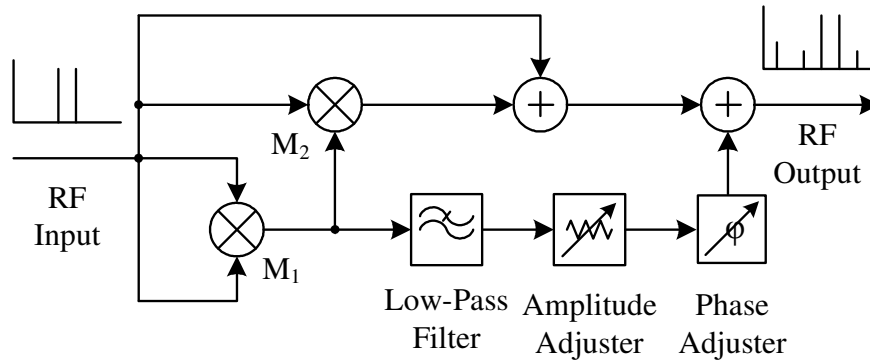


Figure 4-22: A general block diagram of the envelope injection technique

However, the envelope injection method has several problems, which are: practical difficulty to provide initial tuning and maintain the proper phase and amplitude relations of the injected envelope signal, high complexity of the circuit, and low stability due to the fact that the accuracy of source-pulling is highly dependent on the biasing conditions and input signal. Possible solutions to the problems can be sought in providing the properly shaped modulated signal by DSP using digital filtering or baseband equalisation rather than analogue filtering of the envelope signal.

#### 4.5.4 Baseband Equalisation

Equalisation of a signal is a powerful tool used to improve its frequency-dependent behaviour. Recent works [4.5], [4.16] have implemented the equalisation approach to the problem of compensating memory effects in PAs. As memory effects stipulate the dependence of the gain and phase of a PA on modulation frequency and power level, the PA acts as a filter with the frequency response  $H(f, P_{IN})$ . This behaviour is reflected in any of the models used to represent memory nonlinear behaviour (see Section 5.2). Consequently, in order to compensate for the frequency-dependent distortion, the input signal can be pre-equalised or filtered by an additional filter with the impulse response satisfying the following condition in the time domain:

$$h_{eq}(n) * h_{PA}(n) = \delta(n), \quad (4.17)$$

where  $\delta(n)$  denotes the unit impulse response and  $*$  is the operation of convolution.

In the frequency domain the equation (4.17) can be re-written as:

$$H_{eq}(f) \cdot H_{PA}(f) = const. \quad (4.18)$$

A straightforward method to implement an equaliser is to design a digital filter with the transfer characteristic obtained from AM/AM and AM/PM measurements, which was investigated in [4.5]. A Finite Impulse Response (FIR) filter was chosen to avoid potential stability problems of the Infinite Impulse Response (IIR) and Auto-Regressive Moving Average (ARMA) filters. The input-output relation can be written as:

$$y(n) = \sum_{m=0}^{M-1} a(m) \cdot x(n-m), \quad (4.19)$$

where  $M$  is the number of taps in the FIR filter, which stands for the memory depth of the equaliser; whereas  $a(m)$  denotes the coefficients of the filter taps.

Identification of the FIR filter coefficients  $a(m)$  needs to be accomplished during the offline training procedure using the least mean square or recursive least square algorithm. This results in a complex and time-consuming process of the predistorter training. Another drawback of the method is the difficulty of implementing an adaptation procedure, which also requires offline coefficient identification.

Another method to accomplish equalisation of the signal is to extract the complex discrete values of the frequency response  $H(f_i, P_{IN})$  directly from the PA gain and phase characteristics for all power levels and multiply the Fast Fourier Transform (FFT) frequency points of the signal by  $1/H(f_i, P_{IN})$ . This method was proposed to minimise memory effects for OFDM systems in [4.16] and developed to minimise memory effects for single-carrier systems in this thesis. The method is called baseband equalisation as it is implemented at the baseband frequencies before the modulator. Compensating of memory effects by baseband equalisation is described in Chapter 7 of this thesis.

The main advantages of the baseband equalisation method are its flexibility, simplicity of implementation and adaptation. The main shortcoming is the necessity of FFT procedure and hence the difficulty of hardware implementation. However, with the constant development of miniaturised and cheap microprocessors, the baseband equalisation technique is becoming more advantageous comparing to other methods.

## 4.6. Conclusion

This Chapter depicted memory effects in power amplifiers, including their origins and impact on the PA behaviour, classification and compensation methods. Also, the procedures to quantify memory effects were presented and demonstrated by simulations.

Memory effects are classified as electrical and thermal. The electrical memory effects are mainly produced by the reactive elements of the PA biasing and matching circuits, and are typical for wideband transceivers. The thermal memory effects are attributed to varying temperature-dependent electrical parameters of power amplifiers, and are the dominant source of memory effects for the narrowband systems. Also, memory effects can be categorised as symmetrical and asymmetrical, depending on the behaviour of the frequency-dependent IM3 distortion. Symmetrical memory effects are easier to minimise, as they can be compensated for by an ordinary filter with the odd frequency response. Asymmetrical memory effects are more challenging, and hence can be used as an indicator of the predistorter performance.

There are three main methods used to quantify memory effects, which are the single-tone, two-tone and digitally modulated tests. The first two methods are useful for characterising the PA behaviour and extracting the pre-compensation circuits' coefficients, whereas the last one is convenient for assessing the performances of the overall system.

There are four main approaches in compensating for memory effects: impedance optimisation, envelope filtering, envelope injection and baseband equalisation. The first method is able to improve the electrical memory effects by making the impedances constant over frequency. However, the method is difficult in practical implementation, time consuming and requires significant hardware modification. The envelope filtering technique is simple, as it requires only one filter. However, the method is unstable and not suitable for compensating for the asymmetrical memory effects. The envelope injection technique is able to minimise both the symmetrical and asymmetrical memory effects. However, the method increases the circuit's complexity and requires additional RF components. Moreover, the envelope filtering and envelope injection techniques have practical difficulties to provide initial tuning and maintain the proper phase and amplitude relations. The most promising tool for minimising memory effects is

baseband equalisation, which allows pre-compensating the frequency-dependent behaviour by digitally processing the input signal without modifying the RF path. The method is simple and convenient for the software implementation, whereas it may significantly increase the circuit's complexity if implemented in hardware.

#### 4.7. References

- [4.1] J. Vuolevi, T. Rahkonen, *Distortion in RF Power Amplifiers*, Artech House Inc., 2003, ISBN 1580535399.
- [4.2] L. O. Chua, C. A. Desoer, E. S. Kuh, *Linear and Nonlinear Circuits*, McGraw-Hill Book Company, 1987, ISBN 0070108986.
- [4.3] T. Liu, S. Boumaiza, and F. M. Ghannouchi, "Identification and pre-compensation of the electrical memory effects in wireless transceivers", *2006 Radio & Wireless Symposium (RWS-2006)*, San Diego, USA, pp. 535-538, Jan. 2006.
- [4.4] W. Bosch and G. Gatti, "Measurement and simulation of memory effects in predistortion linearizers," *IEEE Transactions on Microwave Theory and Techniques*, vol. 37, no. 12, pp. 1885-1890, Dec. 1989.
- [4.5] T. Liu, S. Boumaiza, and F. M. Ghannouchi, "Augmented Hammerstein predistorter for linearization of broad-band wireless transmitters", *IEEE Transactions on Microwave Theory and Techniques*, vol. 54, no. 4, pp. 1340-1349, Apr. 2006.
- [4.6] J. Vuolevi, T. Rahkonen, and J. Manninen, "Measurement technique for characterizing memory effects in RF power amplifiers," *IEEE Transactions on Microwave Theory and Techniques*, vol. 49, no. 8, pp. 1383-1389, Aug. 2001.
- [4.7] J. C. Pedro, and S. A. Maas, "A comparative overview of microwave and wireless power-amplifier behavioral modeling approaches," *IEEE Transactions on Microwave Theory and Techniques*, vol. 53, no. 4, pp. 1150-1163, Apr. 2005.

- [4.8] J. A. Lonac, A. Santarelli, I. Melczarsky, and F. Filicori, "A simple technique for measuring the thermal impedance and the thermal resistance of HBTs," In *Proc. 2005 European Gallium Arsenide Application Symposium (EGAAS 2005)*, Bologna Univ., Italy, pp. 197–200, Oct. 2005.
- [4.9] J. Vuolevi, T. Rahkonen, "Analysis of amplitude-dependent memory effects in RF power amplifiers", in *Proc. European Conference on Circuit Theory and Design (ECCTD-2001)*, Espoo, Finland, pp. 37-40, Aug. 2001.
- [4.10] A. Chaker, M. Ariaudo, I. Fijalkow, J. Gautier, "Pre-compensation of the frequency-dependence of a non-linear amplifier in a multi-carrier transmission," in *Proc. IEEE International Conference on Communications ICC-2004*, Paris, France, pp. 2464-2467, June 2004.
- [4.11] J. Vuolevi, T. Rahkonen, and J. Manninen, "Measurement technique for improving linearity by optimizing the source impedance of RF power amplifiers," in *Proc. IEEE Radio and Wireless Conference (RAWCON 2000)*, Denver, CO, USA, pp. 227–230, Sept. 2000.
- [4.12] T. Iwai, et al., "High efficiency and high linearity InGaP/GaAs HBT power amplifiers: matching techniques of source and load impedance to improve phase distortion and linearity," *IEEE Transactions on Electron Devices*, vol. 45, no. 12, pp. 1196–1200, Jun. 1998.
- [4.13] J. Vuolevi, J. Manninen, and T. Rahkonen, "Canceling the memory effects in RF power amplifiers," in *Proc. Int. Circuits and Systems Symp.*, Sydney, Australia, vol. 1, pp. 57–60, May, 2001.
- [4.14] J. Vuolevi, J. Manninen, and T. Rahkonen, "Memory effects compensation in RF power amplifiers by using envelope injection technique," in *Proc. Radio and Wireless Conf. Dig.*, Boston, Massachusetts, USA, pp. 257–260, Aug. 2001.
- [4.15] I. Kim, et al., "Envelope injection consideration of high power hybrid EER transmitter for IEEE 802.16e mobile WiMAX application," in *Proc. 2008 IEEE MTT-S International Microwave Symposium Digest*, Atlanta, GA, USA, pp. 411–414, Jun. 2008.

- [4.16] A. Chaker, M. Ariaudo, S. Traverso, J. Gautier, and I. Fijalkow, "Adaptive compensation of high frequency memory effects of a realistic amplifier in an OFDM system", in *Proc. Information and Communication Technologies (ICTTA'06)*, Damascus, Syria, vol. 2, pp. 2629-2633, Apr. 2006.

---

## 5. NONLINEAR MODELLING OF POWER AMPLIFIERS WITH MEMORY EFFECTS

### 5.1. Introduction

Modelling the nonlinear behaviour and memory effects of power amplifiers is an important part of the process of wireless transceivers design. Despite numerous modelling techniques have been reported in literature, there is still a lack of knowledge regarding a universal PA baseband modelling approach, which would be convenient for calculating and optimising the predistorter coefficients. It includes developing analytical description of the output signal distortion caused by the memory effects of the PA and the nonlinearity of its transfer function. Such models are used for analysing performances of the transceiver and developing predistortion linearisers.

Firstly, the Chapter presents an overview of behavioural modelling methods for representing the nonlinear distortion and memory effects of power amplifiers including the conventional Volterra series analysis, simplified two-box and three-box models consisted of independent blocks and models incorporating mutually-dependent interacting blocks. The two-box and three-box models are used to represent so called linear memory, whereas the models containing interacting blocks are applicable for power amplifiers with nonlinear memory.

Secondly, the current Chapter presents the developed memoryless modelling method, which elaborates a fundamental-frequency model for any degree of nonlinearity, and is convenient for calculating and optimising the predistorter coefficients. The method contributes to the state-of-the-art by the developed general formulas, which relate the analytical expression for the fundamental frequency signal and the in-band distortion components to the order of PA polynomial model.

Further, two alternative methods for extracting a PA memoryless model are developed. The first method is grounded on extracting the model from the measured AM/AM characteristics. It uses a least-squares polynomial regression analysis for calculating the model coefficients. The method offers high accuracy at the price of high computational complexity and time-consuming process of AM/AM measurements. The

second method, based on extracting the model from the PA frequency response, is proposed as an alternative to the first one with the aim of reducing the computational complexity and time required for obtaining the model coefficients. It allows accomplishing a quick estimation of initial values of the predistorter coefficients, which can be further optimised during predistorter tuning. The second technique reduces time and hardware requirements for calculating the DPD coefficients at the price of lower accuracy, which can be further increased in the stage of predistorter tuning or for adaptive systems during the adaptation cycle. The feasibility of both the methods is verified experimentally and their accuracy is assessed by calculating the coefficient of determination.

## 5.2. Overview of Memory Modelling Techniques

Modelling of power amplifiers can be accomplished in two ways: using the physical knowledge of the PA internal composition or by an empirical set of the input-output observations. The first approach relates to physical models, whereas the second one implies behavioural models. The physical models are more accurate, but they require precise knowledge of the PA internal structure, which increases simulation time or may be unavailable. For these reasons, when a complete system-level evaluation is required, the behavioural models are usually preferred, which treat a PA as a black-box and are determined by a properly selected set of the input-output relations.

Generally, any power amplifier can be seen as an operator, which transforms an input function  $x(t)$  into the output function  $y(t)$  according to the following nonlinear differential equation:

$$f\left\{y(t), \frac{dy(t)}{dt}, \dots, \frac{d^p y(t)}{dt^p}, x(t), \frac{dx(t)}{dt}, \dots, \frac{d^r x(t)}{dt^r}\right\} = 0, \quad (5.1)$$

which means that the system output and its time derivatives are related in a nonlinear way to the input and its time derivatives [5.1]. A solution to (5.1), which expresses the system output function  $y(t)$  in terms of the input function  $x(t)$  and their time derivatives, serves as a behavioural model for the PA. As the model is intended for implementing in a discrete-time environment of a Personal Computer (PC), the solutions are sought in a discrete-time format, when the continuous functions of time  $x(t)$  and  $y(t)$  are represented

by their uniform time samples  $x(s)$  and  $y(s)$  with the sampling period  $T_s$ . The precise solution to (5.1) has a recursive form as:

$$y(s) = f_R \{y(s-1), \dots, y(s-Q_1), x(s), x(s-1), \dots, x(s-Q_2)\}, \quad (5.2)$$

meaning that the current output at a time sample  $s$  depends on the previous  $Q_1$  outputs, the current input, and the previous  $Q_2$  inputs. However, the recursive form (5.2) is not convenient for practical use due to the difficulty of storing and processing the system output history. With any required small precision the solution to (5.1) can be written in a direct form as [5.1]:

$$y(s) = f_D \{x(s), x(s-1), \dots, x(s-Q)\}. \quad (5.3)$$

There are two main developed approaches in expressing the functions  $f_R$  and  $f_D$  in (5.2) and (5.3): by using polynomial filters or Artificial Neural Networks (ANNs) [5.1]. The first approach has advantages of simplicity of extracting the model parameters and evaluating the model performance, whereas the ANN parameters cannot be extracted in a direct way and need to be obtained by an optimisation procedure. This is due to the fact that the function of a polynomial filter is linearly related to its parameters allowing implementing a systematic extraction procedure, whereas ANNs are nonlinear functions of their parameters and require a nonlinear training process. ANNs also suffer from poor evaluation possibilities, as the number of involved neurons is initially unknown and the dependence of the ANN accuracy on this number cannot be predicted, as well as it cannot be evaluated, whether the obtained ANN is optimal for the given number of neurons. The disadvantage of the polynomial filters modelling approach is a significant deterioration of the performance for inputs, which are beyond the range of signals used in training or extracting the model parameters. This results in the approach being suitable mainly for modelling weakly-nonlinear systems. On contrary, the ANN approach has better extrapolating properties and can be used for modelling strongly-nonlinear systems.

The most developed method of expressing the function (5.3) is approximation by the Taylor series. This is known as the Volterra series analysis, which has several special forms. In fact, the generalised behaviour modelling of power amplifiers capable of representing both linear and nonlinear memory effects can be accomplished by the Volterra series or by a model including several interacting nonlinear and filter blocks. Simplified models used for representing PA nonlinearity and linear memory consist of an independent nonlinear memoryless block and a linear filter, which are known as the

Wiener and Hammerstein models. The latter models being simpler in terms of computational complexity, and extraction and adaptation procedures are often used to represent memory effects in modern wideband communication systems, which are more exposed to linear electrical memory effects. This Section presents a description of the Volterra series, its special cases employed to model linear memory and some common models to represent both nonlinear and linear memory effects.

### 5.2.1 Volterra Series

For a time-invariant or stationary linear system fed with the input signal  $x(t)$ , the output signal  $y(t)$  can be expressed as the following convolution integral [5.2]:

$$y(t) = \int_{-\infty}^{\infty} h(\tau)x(t-\tau)d\tau, \quad (5.4)$$

where  $h(\tau)$  is the system response to a Dirac delta function  $\delta(\tau)$  applied at the time  $\tau$ , which is a unit pulse located at the time  $\tau$  having infinitesimal width, infinite amplitude and energy equal to one. The property of time invariance for the system is specified with the aim to consider the response to a shifted Dirac delta function  $\delta(t-\tau)$  as the shifted response  $h(t-\tau)$ . (5.4) means that the output signal is composed as the sum of the system impulse responses shifted through the time  $\tau$  multiplied by the input signal at that time. In other words, superposition is used to add individual responses.

For a time-invariant or stationary nonlinear system the relation between the input and the output can be found as the generalisation of (5.4), known as Volterra series [5.3]:

$$\begin{aligned} y(t) = & \int_{-\infty}^{\infty} h_1(\tau_1)x(t-\tau_1)d\tau_1 + \int_{-\infty}^{\infty} \int_{-\infty}^{\infty} h_2(\tau_1, \tau_2)x(t-\tau_1)x(t-\tau_2)d\tau_1 d\tau_2 \\ & + \int_{-\infty}^{\infty} \int_{-\infty}^{\infty} \int_{-\infty}^{\infty} h_3(\tau_1, \tau_2, \tau_3)x(t-\tau_1)x(t-\tau_2)x(t-\tau_3)d\tau_1 d\tau_2 d\tau_3 \\ & + \dots + \int_{-\infty}^{\infty} \int_{-\infty}^{\infty} \dots \int_{-\infty}^{\infty} h_n(\tau_1, \tau_2, \dots, \tau_n)x(t-\tau_1)x(t-\tau_2) \dots x(t-\tau_n)d\tau_1 d\tau_2 \dots d\tau_n + \dots \end{aligned} \quad (5.5)$$

The mathematical series was developed by Vito Volterra and first applied to the analysis of nonlinear systems by Norbert Wiener. The function of  $n$  variables  $h_n(\tau_1, \tau_2, \dots, \tau_n)$  called the  $n$ th-order kernel or the  $n$ th-order nonlinear impulse response has the

corresponding frequency-domain nonlinear transfer function  $H_n(\omega_{q1}, \omega_{q2}, \dots, \omega_{qn})$  calculated as its  $n$ -dimensional Fourier transform.

The Volterra series (5.5) can be written as:

$$y(t) = \sum_{n=1}^{\infty} H_n(x(t)), \quad (5.6)$$

where  $H_n(x(t))$  is the  $n$ -th Volterra operator from the input function  $x(t)$ , expressed as:

$$H_n(x(t)) = \int_{-\infty}^{\infty} \dots \int_{-\infty}^{\infty} h_n(\tau_1, \tau_2, \dots, \tau_n) x(t - \tau_1) x(t - \tau_2) \dots x(t - \tau_n) d\tau_1 d\tau_2 \dots d\tau_n. \quad (5.7)$$

Figure 5-1 shows a generalised block diagram of the system modelled by the Volterra series corresponding to (5.6). The output is composed as the sum of the black boxes performing the Volterra operators  $H_n(x(t))$ .

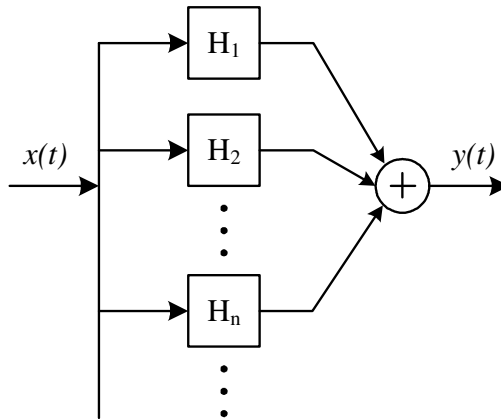


Figure 5-1: Volterra-series representation of a system

The Volterra series can be seen as a generalised power series including memory effects. Indeed, the Volterra kernels in (5.5) are convolution integrals and hence represent the memory of a system, and for the input  $ax(t)$  (5.6) takes the form of:

$$y(t) = \sum_{n=1}^{\infty} a^n H_n(x(t)), \quad (5.8)$$

which is a power series of the gain factor  $a$ .

Determining the Volterra kernels is a complicated time-consuming process, involving a large number of coefficients exponentially increasing with the increase of nonlinearity and memory of the system. It results in a practical difficulty of obtaining

Volterra kernels restricting the application of the Volterra series to weakly nonlinear systems having a small number of kernels, usually not more than five [5.4].

In order to reduce the modelling complexity, simpler models are developed based on the separate consideration of the linear memory and nonlinear memoryless blocks. These models can be divided into two groups: those based on a simple cascade connection of an independent memoryless nonlinear block with a linear filter and the models containing interacting memoryless and filter blocks. The first group being significantly simpler in terms of computational complexity and model extraction procedures is capable of representing the linear memory of a PA, which is the main cause of memory effects for wideband applications. The second group is able to model both the linear and nonlinear memory, crucial for narrowband systems, at the price of high computational complexity and time consuming extraction procedures. Consequently, for wideband applications, models consisting of a memoryless nonlinear block and a linear filter, like Wiener or Hammerstein, are usually implemented, which have good performance in representing the linear memory or the electrical memory effects. The remainder of this section includes an overview of the main models addressing linear and nonlinear memory.

### 5.2.2 Models Addressing Linear Memory

In a discrete-time form the Volterra series for a system can be expressed as a sum of multidimensional convolutions:

$$y(n) = \sum_{k=1}^K y_k(n), \quad (5.9)$$

$$y_k(n) = \sum_{m_1=0}^{M-1} \cdots \sum_{m_k=0}^{M-1} h_k(m_1, \dots, m_k) \prod_{l=1}^k x(n - m_l), \quad (5.10)$$

where  $h_k$  is a  $k$ -th Volterra kernel of the nonlinear system having a finite memory length  $M$  and polynomial length  $K$  [5.5].

The models addressing bandwidth-dependent effects or linear memory described below are the Wiener model, the Hammerstein model and the Wiener-Hammerstein model. They can be derived from the general Volterra series (5.9)-(5.10) by assuming that the nonlinear behaviour and memory effects are analysed separately.

### 5.2.2.1 Two-Box Wiener Model

The two-box Wiener model [5.6]-[5.7] is a special case of the general Volterra series (5.9)-(5.10), composed of a linear filter with the transfer function  $H(\omega_m)$  followed by a memoryless nonlinear block as shown in Figure 5-2.  $\omega_m$  stands for the modulation frequency.

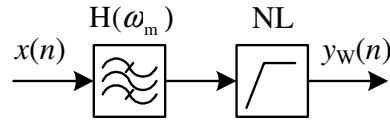


Figure 5-2: Wiener memory nonlinear model

The input-output relation for the Wiener model for a nonlinear system with a finite memory length  $M$  and polynomial length  $K$  looks like:

$$y_w(n) = \sum_{k=1}^K a_k \left[ \sum_{m=0}^{M-1} h(m)x(n-m) \right]^k, \quad (5.11)$$

where  $a_k$  are polynomial coefficients of the nonlinear memoryless block,  $h(m)$  is the input filter impulse response.

As the filter is placed before the nonlinear block, the Wiener structure models the frequency-dependent shift in the input envelope magnitude by the amount of  $|H(\omega_m)|$ . In other words, the model represents the horizontal shift in the AM/AM, AM/PM characteristics due to variations of  $\omega_m$ .

Despite being a convenient and simple method of representing both the nonlinearity and memory effects of a PA, the Wiener structure suffers from a drawback of the nonlinear dependence of the model's output on the coefficients  $h(m)$ , which makes the model parameters extraction procedure more difficult. This problem is overcome in the Hammerstein model.

### 5.2.2.2 Two-Box Hammerstein Model

The two-box Hammerstein model [5.8]-[5.9] is a special case of the general Volterra series (5.9)-(5.10), composed of a memoryless nonlinear block followed by a linear filter with the transfer function  $G(\omega_m)$  as shown in Figure 5-3.

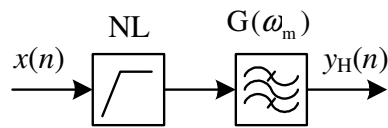


Figure 5-3: Hammerstein memory nonlinear model

The input-output relation for the Hammerstein model looks like:

$$y_H(n) = \sum_{m=0}^{M-1} g(m) \sum_{k=1}^K a_k x^k(n-m), \quad (5.12)$$

where  $a_k$  are polynomial coefficients of the nonlinear memoryless block,  $g(m)$  is the output filter impulse response.

The Hammerstein model is a linear function of its  $g(m)$  parameters, which makes the estimation procedure simple comparing to the Wiener structure. In the works [5.9]-[5.10] it has been shown that the Wiener and Hammerstein models can constitute mutually inverse structures. This has an important consequence for the design of digital predistorters: if a PA is represented by its Wiener model, the predistorter is designed as a Hammerstein structure and vice versa.

As the filter is placed after the nonlinear block, the Hammerstein structure models the frequency-dependent shift in the output envelope magnitude and phase by the amount of  $|G(\omega_m)|$  and  $\angle G(\omega_m)$  correspondingly. In other words, the model represents the vertical shift in the AM/AM, AM/PM characteristics due to variations of  $\omega_m$ . In order to model the horizontal and vertical shifts simultaneously, the three-box Wiener-Hammerstein model is used.

### 5.2.2.3 Three-Box Wiener-Hammerstein Model

The three-box Wiener-Hammerstein model [5.5], [5.11] is a special case of the general Volterra series (5.9)-(5.10), composed of an input linear filter with the transfer function  $H(\omega_m)$ , followed by a memoryless nonlinear block, and an output linear filter with the transfer function  $G(\omega_m)$  as shown in Figure 5-4. In this model, the input filter represents the memory of the input matching and biasing circuits as well as the active device itself and the output filter models those at the PA output.

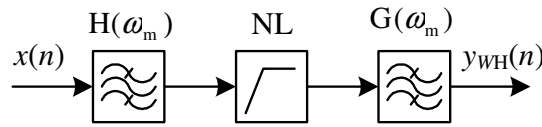


Figure 5-4: Wiener-Hammerstein memory nonlinear model

The input-output relation for the Wiener-Hammerstein model looks like:

$$y_{WH}(n) = \sum_{m_2=0}^{M-1} g(m_2) \sum_{k=1}^K a_k \left[ \sum_{m_1=0}^K h(m_1) x(n - m_1 - m_2) \right]^k, \quad (5.13)$$

where  $a_k$  are polynomial coefficients of the nonlinear memoryless block,  $h(m_1)$  is the input filter impulse response, and  $g(m_2)$  is the output filter impulse response;  $K$  and  $M$  are correspondingly polynomial and memory lengths of the system.

The three-box Wiener-Hammerstein structure is a more generalised model than the two-box Wiener and Hammerstein models. It has a universal modelling capability and is able to represent both the vertical and horizontal shifts in the AM/AM and AM/PM. However, the model is nonlinear in its coefficients  $h(m_1)$  and hence has more complex extraction and optimisation procedures than the Hammerstein model.

### 5.2.3 Models Addressing Nonlinear Memory

The above models are used to represent the major cause of memory effects in wideband nonlinear PAs, which are the electrical memory effects, caused by the input and output matching and biasing circuits' reactive elements. This type of memory is called the linear memory because the effects caused by it are independent of the nonlinear behaviour of the PA, being equally expressed in the linear and nonlinear PA regimes, and can be represented by a single filter independent of the nonlinear block.

Except from the short-term linear memory, there are also effects related to the active device self-heating and varying power supply known as the long-term thermal memory effects, which are dependent on the PA nonlinear regime and are represented as interacting linear filters and nonlinear memoryless blocks. Due to the dependence on the PA nonlinearity and impossibility to be represented by a separate non-interacting filter

and polynomial, the thermal memory effects are also called the nonlinear memory of the PA.

The thermal memory effects have a long-term rather than instantaneous impact on the PA performance and hence affect the low modulation frequencies. They are the main part of memory effects present in the narrowband systems, whereas this type of memory is frequently ignored in the wideband systems.

Many structures have been studied to represent the interaction between the nonlinearity and memory effects of a PA. They can be summarised into the following three main groups: feedback-based models, the models including several alternate filters and polynomials, and the parallel-structure-based models. The stated models are presented below in the remainder of this Section.

### 5.2.3.1 Nonlinear Feedback Model

The nonlinear feedback model is a memory nonlinear model capable of representing both the electrical and thermal memory of a PA together with its nonlinear behaviour. The model, developed by J. C. Pedro et al. in [5.1], [5.12], is presented in Figure 5-5.

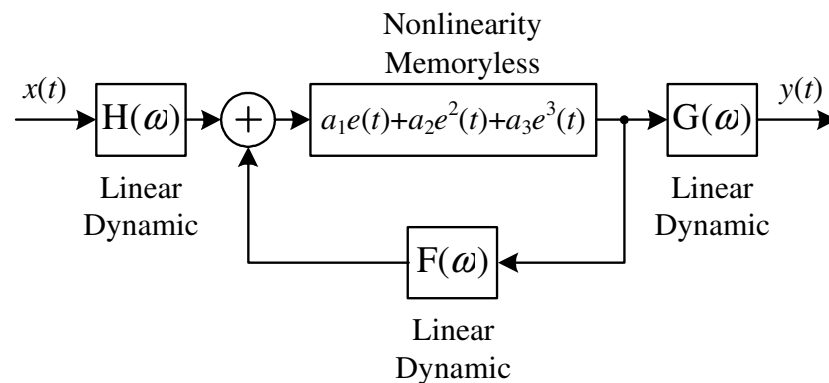


Figure 5-5: Nonlinear feedback structure of a PA for modelling the nonlinear behaviour and the thermal and electrical memory effects

In the Figure, the input and output filters with the corresponding transfer functions  $H(\omega)$  and  $G(\omega)$  model the linear memory attributed to the electrical memory effects placed in the input and output matching and biasing networks, whereas the feedback

filter with the transfer function  $F(\omega)$  is responsible for representing the nonlinear memory effects caused by the thermal dynamics in the active device.

The operation of the nonlinear feedback structure can be understood as applying the polynomial function and generating the third-order degree nonlinearity  $P_3(x(t))$ , passing the signal through the feedback filter realising the linear dynamic operation, and applying the polynomial function again resulting in the output signal in the form of  $P_3[F\{P_3[x(t)]\}]$ . The third-order Volterra nonlinear transfer function of the feedback model can be found as [5.12]:

$$S_3(\omega_1, \omega_2, \omega_3) = \frac{H(\omega_1)H(\omega_2)H(\omega_3)G(\omega_1 + \omega_2 + \omega_3)}{D(\omega_1)D(\omega_2)D(\omega_3)D(\omega_1 + \omega_2 + \omega_3)} \cdot \left\{ a_3 + \frac{2}{3} a_2 \left[ \frac{F(\omega_1 + \omega_2)}{D(\omega_1 + \omega_2)} + \frac{F(\omega_1 + \omega_3)}{D(\omega_1 + \omega_3)} + \frac{F(\omega_2 + \omega_3)}{D(\omega_2 + \omega_3)} \right] \right\}, \quad (5.14)$$

where  $D(\omega) = 1 - a_1 F(\omega)$ .

The nonlinear feedback structure has general modeling capability, being able to represent mixing products of all orders. However the practical implementation of this structure is difficult from the computational and model extraction points of view, additionally facing drawbacks inherit from the feedback structures. A more simple structure without the feedback chain is the nonlinear cascade model presented below.

### 5.2.3.2 Nonlinear Cascade Model

The nonlinear cascade model is another memory nonlinear model capable of representing both the electrical and thermal memory of a PA, proposed by J. Vuolevi et al. in [5.13], [5.14] and used in the future works [5.15]. The model presented in Figure 5-6 is consisted of two 3<sup>rd</sup>-order polynomial blocks with a linear filter between them.

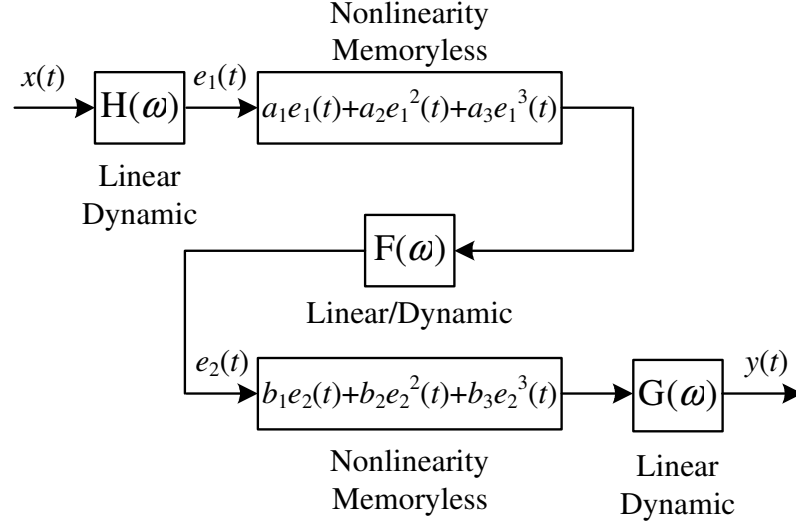


Figure 5-6: Nonlinear cascade model of a PA representing the nonlinear behaviour and the thermal and electrical memory effects

In the Figure, the input and output filters with the corresponding transfer functions  $H(\omega)$  and  $G(\omega)$  model the linear memory attributed to the input and output matching circuits, whereas the filter with the transfer function  $F(\omega)$  situated between two nonlinearities is responsible for representing the nonlinear memory effects caused by the thermal dynamics in the active device. In the PA operational frequency band, the memory effects of the filter  $F(\omega)$  outcome in the AM/PM conversion, whereas at the baseband frequencies the filter represents the long-term memory effects.

The third-order Volterra nonlinear transfer function of the nonlinear cascade model can be found as [5.1]:

$$\begin{aligned}
 S_3(\omega_1, \omega_2, \omega_3) &= H(\omega_1)H(\omega_2)H(\omega_3)G(\omega_1 + \omega_2 + \omega_3) \\
 &\cdot \{a_3F(\omega_1 + \omega_2 + \omega_3)b_1 \\
 &+ \frac{2}{3}a_1a_2[F(\omega_3)F(\omega_1 + \omega_2) + F(\omega_2)F(\omega_1 + \omega_3) + F(\omega_1)F(\omega_2 + \omega_3)]b_2 \\
 &+ a_1^3F(\omega_1)F(\omega_2)F(\omega_3)b_3\}.
 \end{aligned} \tag{5.15}$$

The operation of the nonlinear cascade structure is similar to the those of the feedback model as the signal is passed through the first polynomial function, the linear filter and the second polynomial function, causing the output signal to appear in the form of  $P_3[F\{P_3[x(t)]\}]$ . However, the main difference to the nonlinear feedback model is that the described structure is able to represent not all mixing products but those up to

the ninth order. The model is easier in practical implementation and was used in [5.15] for modeling PA memory effects.

### 5.2.3.3 Parallel Wiener Model

Another approach to accommodate both the electrical and thermal memory of a PA developed by H. Ku et al. in [5.16]-[5.17] is the parallel Wiener model consisted of  $n$  branches, each being composed of a polynomial function and a linear filter. The structure formed by  $n$  parallel Wiener models is presented in Figure 5-7, where the linear filter in each block is coupled with the corresponding nonlinearity. The main difference to the Wiener model is that different filters are used for different nonlinearity orders.

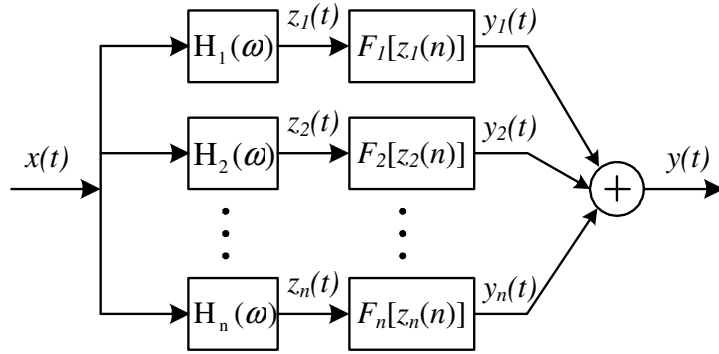


Figure 5-7: Parallel Wiener model of a PA representing the nonlinear behaviour and the thermal and electrical memory effects

For an input signal given by:

$$x(t) = A \cos(\omega_m t), \quad (5.16)$$

the input-output relationship for the parallel Wiener model looks like:

$$y_{PW}(t) = \sum_{i=1}^p \sum_{k=1}^n a_{2k-1,i} \left( A |H_i(\omega_m)| \cos(\omega_m t + \Omega_i(\omega_m)) \right)^{2k-1}, \quad (5.17)$$

where  $p$  is the number of branches,  $n$  is the order of polynomial,  $a_{k-1,i}$  are polynomial coefficients of the nonlinear memoryless blocks, and  $\Omega_i(\omega_m) = \angle H_i(\omega_m)$ .

The presented model has a powerful universal modelling capability similar to those of the Volterra series or the generalised memory polynomial model, but being less complex in terms of practical implementation and training procedures [5.1], [5.5]. The price is the indirect parameter-estimation procedure, which is accomplished by minimising the mean square error between the model outputs and those measured under a single-tone test.

### **5.3. Memoryless Nonlinear Modelling for the Purpose of Digital Predistortion**

Recent achievements in the PA linearity and efficiency enhancement techniques resulted in the development of digital predictive linearising methods. Such methods require a priori knowledge of the PA nonlinear behaviour due to the nature of operation, and hence stipulate for precise and convenient characterisation techniques. Traditionally used for this purpose Volterra series vanishes in the modern DPD systems due to its shortcomings, which are: practical difficulty of implementation and measurement of the Volterra kernels, high computational complexity and limitation to only weakly-nonlinear systems, while exhibiting dramatic performance degradation under strongly nonlinear conditions.

The weaknesses of the Volterra modelling approach described above result in the advancement and wider implementation of the Wiener-based systems, which are founded on the assumption that the nonlinear behaviour and memory effects of a PA can be accurately represented by a separate polynomial model and a linear filter. These models are easier in practical implementation, more convenient for extracting and optimising predistorter coefficients with less computational complexity, and capable of representing strong nonlinearities [5.18]. These advantages make the Wiener-based systems favourable for modelling power amplifiers for the purpose of digital predistortion. The main disadvantage of this approach is the assumption of independence of the nonlinear behaviour and memory effects, which may result in a lower modelling accuracy for the PAs, which do not have this property. However, in the works [5.19]-[5.20] the authors proved that even PAs with mutually-dependent nonlinear behaviour and memory effects can be modelled by several independent

polynomial blocks and linear filters, which interact by either a feedback loop or a three-block series connection. This notation extends the applicability of the digital predistorters based on separate compensation of memoryless nonlinearity and memory effects for linearising modern wireless transmitters.

In this work, nonlinear behaviour and memory effects are considered independently, and separate techniques are developed for providing memoryless linearisation and compensating for memory effects, which can be combined into any of the system models composed of either independent or interacting memory and nonlinear blocks.

In order to provide an efficient memoryless digital predistortion, an accurate and convenient for practical implementation PA characterisation technique is required for extracting and optimising the predistorter coefficients. For weakly-nonlinear systems represented by the third- and fifth-order polynomial models, PA characterisation and DPD coefficients extraction procedures have been widely described in literature [5.21]-[5.23]. However, there is a lack of this information for higher degrees of nonlinearity. This Section presents the developed generalised fundamental-frequency modelling technique suitable for any degree of nonlinearity and proposes compact formulas for analytic representation of the in-band distortion components and the fundamental-frequency signal for any order of the polynomial model. The proposed method allows a quick, convenient and accurate extraction of the predistorter parameters for a given order of nonlinearity using the derived formulas.

### 5.3.1 Proposed In-Band Distortion Modelling of Power Amplifiers

A memoryless polynomial model for representing nonlinear behaviour of a power amplifier with an input signal  $V_{IN}(t)$  and the output signal  $V_{OUT}(t)$  is given by the following expression:

$$V_{OUT}(t) = \sum_{n=1}^{\infty} g_n V_{IN}^n(t), \quad (5.18)$$

where  $g_n$  are coefficients of the corresponding nonlinear terms.

The input signal in modern wireless communication systems is usually modulated with the amplitude  $V_S(t)$  and phase  $\varphi(t)$  modulations and can be written as:

$$V_{IN}(t) = V_S(t) \cdot \cos(\omega t + \varphi(t)). \quad (5.19)$$

As a quadrature modulation is commonly used, it is convenient to re-write the input signal in the Cartesian form by introducing the in-phase  $I(t)$  and quadrature  $Q(t)$  components:

$$V_{IN}(t) = V \cdot [I(t) \cdot \cos(\omega t) - Q(t) \cdot \sin(\omega t)], \quad (5.20)$$

where  $V$  is the mean value of the modulating signal amplitude  $V_S(t)$  expressed as

$$V = \text{average}(|V_S(t)|), \quad (5.21)$$

and the in-phase  $I(t)$  and quadrature  $Q(t)$  components are calculated using the following formulas:

$$I(t) = \frac{V_S(t)}{V} \cdot \cos(\varphi(t)), \quad (5.22)$$

$$Q(t) = \frac{V_S(t)}{V} \cdot \sin(\varphi(t)). \quad (5.23)$$

From (5.21)-(5.23) one can show that:

$$\text{average}[I^2(t) + Q^2(t)] = 1. \quad (5.24)$$

Considering the first three terms in the polynomial model (5.18) after substituting (5.20) into (5.18) and performing trigonometric transformations, the following expression can be obtained:

$$\begin{aligned} V_{OUT}(t) = & \frac{V^2 g_2}{2} \cdot [I^2(t) + Q^2(t)] + \\ & + \left[ Vg_1 + \frac{3V^3 g_3 [I^2(t) + Q^2(t)]}{4} \right] \cdot [I(t) \cdot \cos(\omega t) - Q(t) \cdot \sin(\omega t)] + \\ & + \frac{V^2 g_2}{2} \cdot [\{I^2(t) - Q^2(t)\} \cdot \cos(2\omega t) - 2 \cdot I(t) \cdot Q(t) \cdot \sin(2\omega t)] + \\ & + \frac{V^3 g_3}{4} \cdot [I(t) \cdot \{I^2(t) - 3Q^2(t)\} \cdot \cos(3\omega t) - Q(t) \cdot \{3I^2(t) - Q^2(t)\} \cdot \sin(3\omega t)] \end{aligned} \quad (5.25)$$

In the obtained formula, the first term represents a DC signal, the second term is the fundamental-frequency output signal consisted of the desired linear amplification of the input signal and the in-band distortion component produced by the third-order nonlinearity, the third term is the second harmonic distortion product and the final term is the third harmonic distortion product. The DC and harmonic signals are not important for consideration as they can be easily filtered out. However, the in-band distortion causes a significant degradation of the output signal and is the subject of any linearising

technique. The in-band distortion modelling is an important part of designing a digital predistorter based on injecting the distortion components into the baseband signal. Therefore, the fundamental-frequency modelling is carried out below in order to develop a framework for calculating the DPD injected signals' parameters.

The fundamental-frequency part of the output signal (5.25) is given by following:

$$V_{OUT}^{FUND}(t) = \left[ Vg_1 + \frac{3V^3 g_3 [I^2(t) + Q^2(t)]}{4} \right] \cdot [I(t) \cdot \cos(\omega t) - Q(t) \cdot \sin(\omega t)] \quad (5.26)$$

Considering (5.20), the last expression can be re-written as:

$$V_{OUT}^{FUND}(t) = \left[ g_1 + \frac{3V^2 g_3 [I^2(t) + Q^2(t)]}{4} \right] \cdot V_{IN}(t), \quad (5.27)$$

or

$$V_{OUT}^{FUND}(t) = g_1 V_{IN}(t) + V_{3DIST}^{FUND}(t), \quad (5.28)$$

where  $V_{3DIST}^{FUND}(t)$  is the in-band distortion component produced by the third-order term of the polynomial model (5.18), which is calculated as:

$$V_{3DIST}^{FUND}(t) = \frac{3V^2 g_3 [I^2(t) + Q^2(t)]}{4} \cdot V_{IN}(t). \quad (5.29)$$

For deriving (5.26)-(5.29), the first three terms of the polynomial model (5.18) were considered. Further, the same procedure is used for deriving the expressions for higher-order distortion components. Because only odd-order terms of the polynomial model (5.18) generate the in-band distortion components, the even terms are not included in the reasoning below. Carrying out similar mathematical calculations, for the 5<sup>th</sup>-order polynomial model, the fifth-order in-band distortion component can be expressed as:

$$V_{5DIST}^{FUND}(t) = \frac{5V^4 g_5 [I^2(t) + Q^2(t)]^2}{8} \cdot V_{IN}(t). \quad (5.30)$$

Further, the in-band distortion component produced by the seventh order nonlinear term looks like:

$$V_{7DIST}^{FUND}(t) = \frac{35V^6 g_7 [I^2(t) + Q^2(t)]^3}{64} \cdot V_{IN}(t). \quad (5.31)$$

Having considered the third- (5.29), fifth- (5.30) and seventh-order (5.31) distortion components, it is possible to observe regularity in their expressions. Using the mathematical induction, the general formula can be found:

$$V_{(2k+1)DIST}^{FUND}(t) = b_{2k+1} V^{2k} g_{2k+1} [I^2(t) + Q^2(t)]^k \cdot V_{IN}(t), \quad (5.32)$$

where  $k=1,2,3,..$  and  $b_{2k+1}$  is an element of the developed mathematical series [5.24]-[5.26], which is presented in Table 5.1.

In order to verify the feasibility of the obtained formula, the next two in-band distortion components, which are the ninth- and eleventh-order components, are derived using the described method and calculated by (5.32). The derived components perfectly agree with those obtained by the proposed formula:

$$V_{9DIST}^{FUND}(t) = \frac{63V^8 g_9 [I^2(t) + Q^2(t)]^4}{128} \cdot V_{IN}(t), \quad (5.33)$$

$$V_{7DIST}^{FUND}(t) = \frac{231V^{10} g_{11} [I^2(t) + Q^2(t)]^5}{512} \cdot V_{IN}(t). \quad (5.34)$$

Using (5.32), a compact formula for the PA fundamental-frequency output signal can be written:

$$V_{OUT}^{FUND}(t) = g_1 \cdot V_{IN}(t) + \left[ \sum_{k=1}^{\infty} b_{2k+1} V^{2k} g_{2k+1} [I^2(t) + Q^2(t)]^k \right] \cdot V_{IN}(t). \quad (5.35)$$

In the last expression, the first term is the undistorted desired linear output signal and the second one is the sum of all the in-band distortion components produced by the corresponding terms of the polynomial nonlinearity (5.18). The obtained formula (5.35) gives a compact analytical expression for the distorted output signal at the fundamental frequency. It allows to quickly estimate the distortion generated by a PA and calculate the predistorter coefficients for the required order of polynomial model in one shot without the need of iteratively calculating equations (5.29)-(5.34).

By taking a closer look at

$$G_{2k+1}(t) = b_{2k+1} V^{2k} g_{2k+1} [I^2(t) + Q^2(t)]^k, \quad (5.36)$$

one can see it is dependent on the square magnitude of the baseband signal,

$$G_{2k+1}(t) = b_{2k+1} g_{2k+1} \cdot |V_S(t)|^{2k}, \quad (5.37)$$

and represents the magnitude multiple of a  $(2k+1)$ -order in-band distortion component.

**TABLE 5.1:** Element values of the developed series

| $b_3$         | $b_5$         | $b_7$           | $b_9$            | $b_{11}$          | $b_{13}$           | $b_{15}$             | $b_{17}$              | $b_{19}$               |
|---------------|---------------|-----------------|------------------|-------------------|--------------------|----------------------|-----------------------|------------------------|
| $\frac{3}{4}$ | $\frac{5}{8}$ | $\frac{35}{64}$ | $\frac{63}{128}$ | $\frac{231}{512}$ | $\frac{429}{1024}$ | $\frac{6435}{16384}$ | $\frac{12155}{32768}$ | $\frac{46189}{131072}$ |

The series  $\{b_{2k+1}\}$  is a mathematical series of coefficients for the corresponding in-band distortion components. It is obtained by raising the Cartesian expression for the input signal  $V_{IN}(t) = V \cdot [I(t) \cdot \cos(\omega t) - Q(t) \cdot \sin(\omega t)]$  to the power  $(2k+1)$ ,  $k=1,2,3,\dots$ , simplifying the obtained expression in order to extract the fundamental-frequency part, and taking the coefficients near the fundamental-frequency term. Using Matlab the first nineteen elements of the  $b$ -series have been found. The odd ones, which are important for calculating the digital predistorter parameters, are presented in Table 5.1. The series  $\{b_{2k+1}\}$  and formula (5.35) allow considering as many distortion components as necessary for achieving the required linearising degree of the predistorter.

### 5.3.2 Model Extraction Methods

This Section presents two methods for extracting a memoryless polynomial model for a PA. The first method incorporates the measurement of the AM/AM characteristics and a least-squares polynomial regression analysis for calculating the model coefficients, resulting in a high accuracy, but making the model extraction process computationally complex and time-consuming. The second method includes generating a nonlinear frequency response for the maximum operating power, measuring the magnitudes of the harmonics and calculating the model coefficients using the obtained values. The second method offers a quick and simple estimation of the model coefficients with lower accuracy, which still can be increased in the stage of predistorter tuning.

For designing the memoryless part of the proposed digital predistorter, which is described in Chapter 6, a fundamental-frequency model of the PA must be extracted. This model is composed of the odd-order terms of the PA nonlinearity, as shown in the previous Section. Generally, the model can include both the AM/AM and AM/PM distortions if the coefficients are obtained in the complex form. However, for the

proposed DPD only AM/AM need to be represented by the model as the distortion caused by memory effects is compensated separately by the proposed baseband equalisation method described in Chapter 7.

Consequently, real-valued coefficients are sought for the model (5.35), which is simplified by putting  $\varphi(t)=0$  and assuming the unmodulated input signal in the form  $V_{IN}(t) = V_{MAX} \cdot \cos(\omega t)$ . The last notation results in  $I^2(t)=1$  and  $Q^2(t)=0$ , which after substituting in (5.35), give:

$$V_{OUT}^{FUND}(t) = g_1 \cdot V_{IN}(t) + \left[ \sum_{k=1}^{\infty} b_{2k+1} g_{2k+1} V_{MAX}^{2k} \right] \cdot V_{IN}(t). \quad (5.38)$$

As coefficients  $b_{2k+1}$  are known (see Table 5.1), the task of the fundamental-frequency model extraction procedure is to determine  $g_{2k+1}$  for  $k=1,2,3,\dots$ . Two methods are described below, which accomplish the task by processing the PA AM/AM characteristic and its frequency response respectively.

### 5.3.2.1 AM/AM Least-Squares Polynomial Approximation

Least-Squares Regression (LSR) is used to approximate an empirical set of data by an analytical function. In the case of extracting a model from the AM/AM characteristic, the PA is excited by a tone signal with discretely varying magnitude  $V_{MAX}(i)$  and the corresponding output signal magnitude at the same frequency  $V_{MAX\_OUT}^{FUND}(i)$  is measured, where  $i = 1,2,3,\dots$  stands for the number of the experiment. The relation between  $V_{MAX\_OUT}^{FUND}(i)$  and  $V_{MAX}(i)$ , which is the PA AM/AM characteristic, can be obtained from (5.38) as:

$$V_{MAX\_OUT}^{FUND}(i) = g_1 \cdot V_{MAX}(i) + g_3 \cdot b_3 \cdot V_{MAX}^3(i) + g_5 \cdot b_5 \cdot V_{MAX}^5(i) \dots, \quad (5.39)$$

or writing in another way:

$$V_{MAX\_OUT}^{FUND}(i) = \sum_{k=0}^p a_{2k+1} \cdot V_{MAX}^{2k+1}(i), \quad (5.40)$$

where  $a_{2k+1} = g_{2k+1} b_{2k+1}$ , for  $k=0,1,2,\dots$ ,  $b_1=1$ , and  $m = 2p + 1$  is the order of the extracted model.

The concept of the least-squares regression analysis is minimising the sum of squared residuals between the measured and modelled data sets by calculating the

partial derivatives of the sum with respect to  $a_{2k+1}$ , equating these derivatives to zero and solving the obtained system of linear equations in order to find those values of  $a_{2k+1}$ , which result in the minimum of the sum of square differences between the measured and modelled data samples.

Mathematically the LSR approximation can be described as following. Let us suppose that a set of experimental data is obtained as  $n$  pairs of an input  $x_i$  and the corresponding output  $y_i$  variables:  $(x_1, y_1), (x_2, y_2), (x_3, y_3), \dots, (x_n, y_n)$ , where  $n > m$ .

Then, the sum of squared residuals between the measured and modelled data samples can be written as:

$$S = \sum_{i=1}^n [y_i - \tilde{y}_i]^2, \quad (5.41)$$

where  $\{y_i\}$  and  $\{\tilde{y}_i\}$  are the measured and modelled output data respectively.

In relation to (5.40), the approximating function is given in the form of:

$$y_i = \sum_{k=0}^m a_{2k+1} \cdot x_i^{2k+1}, \quad (5.42)$$

where  $x_i$  corresponds to  $V_{MAX}(i)$ , and  $y_i$  corresponds to  $V_{MAX\_OUT}^{FUND}(i)$ . An example of the measured set of data  $\{x_i, y_i\}$  for a MOSFET PA is illustrated in Figure 5-8.

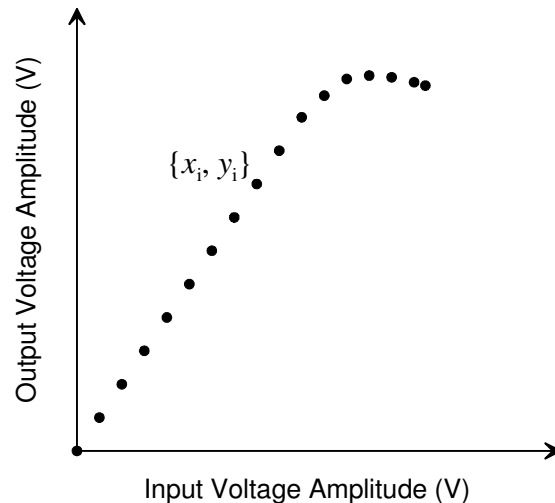


Figure 5-8: AM/AM characteristic used to extract the memoryless fundamental-frequency model for a MOSFET PA

Then, (5.41) can be re-written as:

$$S = \sum_{i=1}^n [y_i - (a_1 x_i + a_3 x_i^3 + a_5 x_i^5 + \dots + a_m x_i^m)]^2, \quad (5.43)$$

or:

$$S = [y_1 - (a_1 x_1 + a_3 x_1^3 + \dots + a_m x_1^m)]^2 + [y_2 - (a_1 x_2 + a_3 x_2^3 + \dots + a_m x_2^m)]^2 \\ + [y_3 - (a_1 x_3 + a_3 x_3^3 + \dots + a_m x_3^m)]^2 + \dots + [y_n - (a_1 x_n + a_3 x_n^3 + \dots + a_m x_n^m)]^2. \quad (5.44)$$

The partial derivatives of  $S$  with respect to  $a_{2k+1}$  look like:

$$\frac{dS}{da_1} = 2x_1[y_1 - (a_1 x_1 + a_3 x_1^3 + a_5 x_1^5 + \dots + a_m x_1^m)] \\ + 2x_2[y_2 - (a_1 x_2 + a_3 x_2^3 + a_5 x_2^5 + \dots + a_m x_2^m)] \\ \dots + 2x_n[y_n - (a_1 x_n + a_3 x_n^3 + a_5 x_n^5 + \dots + a_m x_n^m)], \quad (5.45)$$

$$\frac{dS}{da_3} = 2x_1^3[y_1 - (a_1 x_1 + a_3 x_1^3 + a_5 x_1^5 + \dots + a_m x_1^m)] \\ + 2x_2^3[y_2 - (a_1 x_2 + a_3 x_2^3 + a_5 x_2^5 + \dots + a_m x_2^m)] \\ \dots + 2x_n^3[y_n - (a_1 x_n + a_3 x_n^3 + a_5 x_n^5 + \dots + a_m x_n^m)], \quad (5.46)$$

.....

$$\frac{dS}{da_m} = 2x_1^m[y_1 - (a_1 x_1 + a_3 x_1^3 + a_5 x_1^5 + \dots + a_m x_1^m)] \\ + 2x_2^m[y_2 - (a_1 x_2 + a_3 x_2^3 + a_5 x_2^5 + \dots + a_m x_2^m)] \\ \dots + 2x_n^m[y_n - (a_1 x_n + a_3 x_n^3 + a_5 x_n^5 + \dots + a_m x_n^m)]. \quad (5.47)$$

After equating the obtained derivatives to zero  $\frac{dS}{da_1} = 0$ ,  $\frac{dS}{da_3} = 0$ , ...  $\frac{dS}{da_m} = 0$ , the

following linear with respect to  $a_{2k+1}$  system of equations can be written:

$$x_1 y_1 + x_2 y_2 + \dots + x_n y_n \\ = a_1 (x_1^2 + x_2^2 + \dots + x_n^2) + a_3 (x_1^4 + x_2^4 + \dots + x_n^4) \\ + a_5 (x_1^6 + x_2^6 + \dots + x_n^6) + \dots + a_m (x_1^{m+1} + x_2^{m+1} + \dots + x_n^{m+1}), \quad (5.48)$$

$$x_1^3 y_1 + x_2^3 y_2 + \dots + x_n^3 y_n \\ = a_1 (x_1^4 + x_2^4 + \dots + x_n^4) + a_3 (x_1^6 + x_2^6 + \dots + x_n^6) \\ + a_5 (x_1^8 + x_2^8 + \dots + x_n^8) + \dots + a_m (x_1^{m+3} + x_2^{m+3} + \dots + x_n^{m+3}), \quad (5.49)$$

$$\begin{aligned}
 & \dots\dots\dots \\
 & x_1^m y_1 + x_2^m y_2 + \dots + x_n^m y_n \\
 & = a_1(x_1^{m+1} + x_2^{m+1} + \dots + x_n^{m+1}) + a_3(x_1^{m+3} + x_2^{m+3} + \dots + x_n^{m+3}) \quad (5.50) \\
 & + a_5(x_1^{m+5} + x_2^{m+5} + \dots + x_n^{m+5}) + \dots + a_m(x_1^{2m} + x_2^{2m} + \dots + x_n^{2m}).
 \end{aligned}$$

As  $\{x_i\}$  and  $\{y_i\}$  are the known sets of data, where  $i=1,2,\dots,n$ , the system of equations (5.48)-(5.50) can be written in a compact form:

$$\left\{ \begin{aligned}
 & s_2 a_1 + s_4 a_3 + s_6 a_5 + \dots + s_{m+1} a_m = t_1, \quad (5.51) \\
 & s_4 a_1 + s_6 a_3 + s_8 a_5 + \dots + s_{m+3} a_m = t_3, \quad (5.52) \\
 & \dots\dots\dots \\
 & s_{m+1} a_1 + s_{m+3} a_3 + s_{m+5} a_5 + \dots + s_{2m} a_m = t_m, \quad (5.53)
 \end{aligned} \right.$$

where:

$$s_j = \sum_{i=1}^n x_i^j, \quad (5.54)$$

$$t_j = \sum_{i=1}^n y_i \cdot x_i^j. \quad (5.55)$$

In the system (5.51)-(5.53), the number of equations corresponds to the degree of the model. After solving this system, the values  $a_{2k+1}$  are obtained. Then,  $g_{2k+1}$  are calculated as:

$$g_{2k+1} = \frac{a_{2k+1}}{b_{2k+1}}. \quad (5.56)$$

The method of extracting  $g$ -coefficients described above offers the most superior accuracy of approximation, which will be verified experimentally in Section 5.3.3 and compared to that of the method of extracting  $g$ -coefficients from the PA frequency response. However, the presented method is time-consuming and requires performing a significant amount of computations. Experimentally it was shown that in the most cases a 5<sup>th</sup> or 7<sup>th</sup> order polynomial model provides sufficient accuracy, which will be discussed in details in Chapter 7.

### 5.3.2.2 Model Extraction using a PA Frequency Response

The proposed method of extracting memoryless model coefficients from a PA nonlinear frequency response is based on the analytical dependence of the magnitudes of generated harmonics on the polynomial model coefficients [5.24]. If the PA is excited with a tone signal, which has the amplitude corresponding to the maximum power used in the operational dynamic range, the generated frequency response will include the number of harmonics equal to the degree of the PA nonlinearity. Having measured the magnitudes of all the generated harmonics, it is possible to calculate the polynomial model coefficients. The latter statement is proven analytically in the remainder of this Section.

For a nonlinear PA with the polynomial model described by (5.18) and a tone input signal  $V_{IN}(t) = V_{MAX} \cdot \cos(\omega t)$ , the total output signal can be found as:

$$V_{OUT}(t) = V_{DC} + \left[ \sum_{k=0}^{\infty} b_{2k+1} g_{2k+1} V_{MAX}^{2k+1} \right] \cdot \cos(\omega t) + V_{SEC} \cdot \cos(2\omega t) \quad (5.57)$$

$$+ V_{THIRD} \cdot \cos(3\omega t) + V_{FOURTH} \cdot \cos(4\omega t) + V_{FIFTH} \cdot \cos(5\omega t) + \dots$$

For definiteness, the proposed method is described using a 5th-order nonlinearity. In this case, (5.57) takes the form of:

$$V_{OUT}(t) = \left[ \frac{g_2 V_{MAX}^2}{2} + \frac{3g_4 V_{MAX}^4}{8} \right] + \left[ \sum_{k=0}^2 b_{2k+1} g_{2k+1} V_{MAX}^{2k+1} \right] \cdot \cos(\omega t)$$

$$+ \left[ \frac{g_2 V_{MAX}^2}{2} + \frac{g_4 V_{MAX}^4}{2} \right] \cdot \cos(2\omega t) + \left[ \frac{g_3 V_{MAX}^3}{4} + \frac{5g_5 V_{MAX}^5}{16} \right] \cdot \cos(3\omega t) \quad (5.58)$$

$$+ \frac{g_4 V_{MAX}^4}{8} \cdot \cos(4\omega t) + \frac{g_5 V_{MAX}^5}{16} \cdot \cos(5\omega t).$$

From (5.58) one can see, that the output signal includes 5 harmonics at the frequencies  $k\omega$ :  $k=1, 2, 3, 4, 5$ , and the magnitudes of these harmonics are expressed analytically by the multipliers near the corresponding  $\cos(k\omega t)$  terms in (5.58). Figure 5-9 shows the total output signal of a PA with the 5<sup>th</sup>-order nonlinearity.

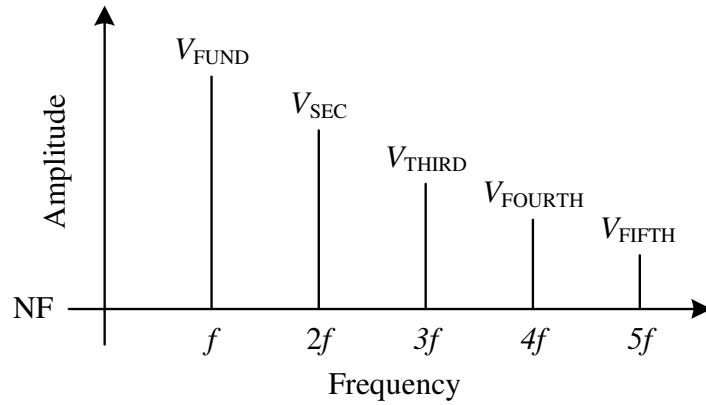


Figure 5-9: Frequency response of a PA with the 5<sup>th</sup>-order nonlinearity

As can be seen from the Figure, a PA with the 5<sup>th</sup>-order nonlinearity produces five harmonics, which can be observed above the Noise Floor (NF). Having measured their magnitudes, a simple system of linear equations can be written:

$$\left\{ \begin{array}{l} g_1 V_{MAX} + \frac{3}{4} g_3 V_{MAX}^3 + \frac{5}{8} g_5 V_{MAX}^5 = V_{FUND}, \\ \frac{g_2 V_{MAX}^2}{2} + \frac{g_4 V_{MAX}^4}{2} = V_{SEC}, \\ \frac{g_3 V_{MAX}^3}{4} + \frac{5g_5 V_{MAX}^5}{16} = V_{THIRD}, \\ \frac{g_4 V_{MAX}^4}{8} = V_{FOURTH}, \\ \frac{g_5 V_{MAX}^5}{16} = V_{FIFTH}. \end{array} \right. \quad (5.59)$$

From the obtained system of equations,  $g$ -coefficients can be easily calculated. The method of extracting memoryless polynomial model described above offers the most quick and computationally simple estimation of the DPD parameters. However, during experimental verifications, the proposed method was found to be less accurate than the one based on the AM/AM measurements since there were inaccuracies involved in measuring the exact values of the harmonics. Therefore, the proposed method is suitable only for initial estimation of  $g$ -coefficients, which then are optimised by simulations during the predistorter tuning or for adaptive DPD systems during the adaptation cycle. The feasibility of the proposed method is verified experimentally in next Section.

### 5.3.3 Experimental Verification of the Proposed Modelling Technique

In order to verify the feasibility of the proposed fundamental-frequency modelling and model extraction techniques, experiments with a power amplifier operating in its saturation region are carried out using harmonic and 16-QAM modulated signal tests. Experimental equipment shown in Figure 5-10 consists of an analog Electronic Signal Generator (ESG) Hewlett Packard A6488, spectrum analyser Hewlett Packard 8594EM, digitally-modulated signal generator Agilent E4433B and Vector Signal Analyser (VSA) Agilent E4406A. A 20-dB gain power amplifier Mini-Circuits ZFL500, which has the 1-dB compression point at 9 dBm output power, is used for experiments.

Initially, an RF tone at the frequency of 500 MHz has been generated and passed through the PA at different power levels with the aim to investigate the nonlinear behaviour and generation of harmonics. Table 5.2 presents the measured amplitudes of the harmonics for different input power levels.

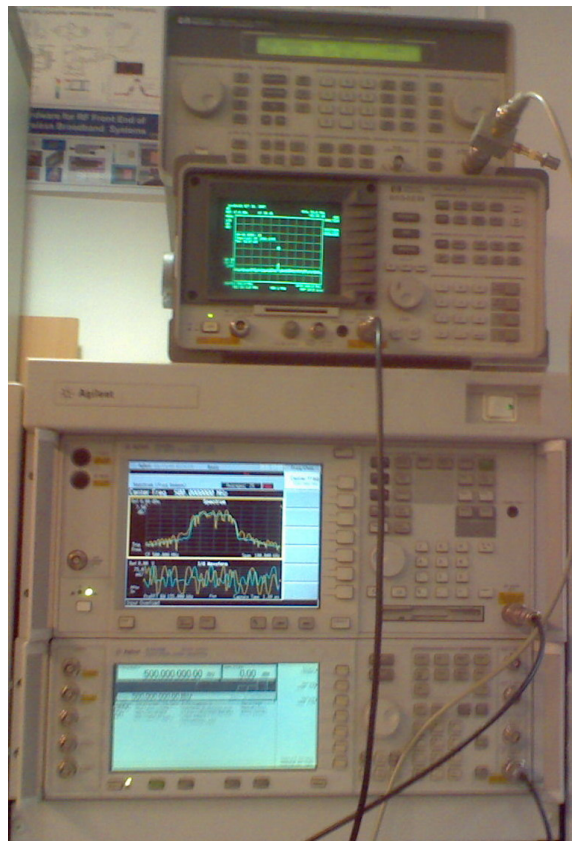


Figure 5-10: Experimental test bench

**TABLE 5.2:** Measured output harmonics at different power levels for ZFL500

| $P_{IN}$ ,<br>dBm | $P_{FUND}$ ,<br>dBm | $P_{SEC}$ ,<br>dBm | $P_{THIRD}$ ,<br>dBm | $P_{FOURTH}$ ,<br>dBm | $P_{FIFTH}$ ,<br>dBm | Higher<br>Odd-<br>Order |
|-------------------|---------------------|--------------------|----------------------|-----------------------|----------------------|-------------------------|
| -30               | -9.3                | -47.5              | -                    | -                     | -                    | -                       |
| -20               | 0.5                 | -38                | -47.3                | -                     | -                    | -                       |
| -15               | 5.4                 | -29.8              | -36                  | -45.5                 | -                    | -                       |
| -10               | 9.3                 | -14.7              | -16                  | -31.8                 | -47                  | -                       |
| -8                | 10.6                | -10.2              | -15                  | -32                   | -36                  | -                       |
| -6                | 11.06               | -9                 | -14.8                | -36                   | -26.7                | +                       |
| -5                | 11.33               | -9.4               | -14.6                | -30                   | -27.5                | +                       |
| -4                | 11.5                | -10                | -13.8                | -24.6                 | -29                  | +                       |

In Table 5.2, signs “plus” indicate the appearance above the noise floor of the odd harmonics of orders greater than five. For both the model extracting techniques, the first step is to determine the polynomial model order, which can be estimated by the number of harmonics appearing at the maximum operational power level. In this experiment, the PA is intended to be used at the power level of its 1-dB compression point, which occurs at 10 dBm output power. At this level, the PA generates five harmonics, and hence a 5<sup>th</sup>-order polynomial model is sought.

In the case of extracting the memoryless fundamental-frequency model using the LSR approximation, the first two columns of Table 5.2 are considered as the input and output data pairs  $\{x_i, y_i\}$ . The number of the measured data sample is greater than the order of the polynomial model:  $n = 8 > m = 5$ . Based on the measured data, the coefficients of the linear system (5.51)-(5.53) are calculated and presented in Table 5.3. The solution to this system is unique and represents the set of coefficients for the PA polynomial model.

With the aid of a PC, the solution can be obtained by either MS Excel or Matlab software:  $a_1 = 10.7$ ;  $a_3 = -188.8$ ;  $a_5 = 1645.9$ . After that, using (5.56), the  $g$ -coefficients of the polynomial model are calculated:

$$\begin{cases} g_1 = 10.7; \\ g_3 = -251.7; \\ g_5 = 2633.4. \end{cases} \quad (5.60)$$

**TABLE 5.3:** Linear system coefficients based on the measured results

|          |             |             |          |
|----------|-------------|-------------|----------|
| S2       | S4          | S6          | t1       |
| 0.126664 | 0.003578049 | 0.000115581 | 0.872438 |
| S4       | S6          | S8          | t3       |
| 0.003578 | 0.000115581 | 3.98319E-06 | 0.023089 |
| S6       | S8          | S10         | t5       |
| 0.000116 | 3.98319E-06 | 1.42723E-07 | 0.000722 |

Finally, the analytical expression for the fundamental-frequency model can be written as:

$$V_{OUT}^{FUND}(t) = 10.7 \cdot V_{IN}(t) - 189 \cdot |V_S(t)|^2 \cdot V_{IN}(t) + 1646 \cdot |V_S(t)|^4 \cdot V_{IN}(t). \quad (5.61)$$

In order to verify accuracy of the model (5.61), the AM/AM characteristic of the PA is plotted using the model and compared to that obtained from the measured data. Further, the coefficient of determination  $r^2$  is calculated, in order to judge the quality of fit of the model to the measured data. The coefficient of determination  $r^2$  is used to evaluate the quality of fit of a statistical model, which aims to predict the future outcomes of a physical phenomenon. The coefficient of determination measures how well the model predicts the real outcomes. It is defined as:

$$r^2 = \frac{\sum_{i=1}^n (\tilde{y}_i - \bar{y})^2}{\sum_{i=1}^n (y_i - \bar{y})^2}, \quad (5.62)$$

where  $\{y_i\}$  and  $\{\tilde{y}_i\}$  are respectively the measured and modelled output data corresponding to the  $\{x_i\}$  input data, whereas  $\bar{y}$  is the mean value for all experimental outcomes  $\{y_i\}$ . The coefficient of determination takes values in the range of  $0 \leq r^2 \leq 1$ , where  $r^2 = 1$  indicates a perfect fit of the model, i.e. the modelled curve passes exactly all the measured data points.

The comparison of the measured and calculated by the model (5.61) AM/AM curves is presented in Figure 5-11.

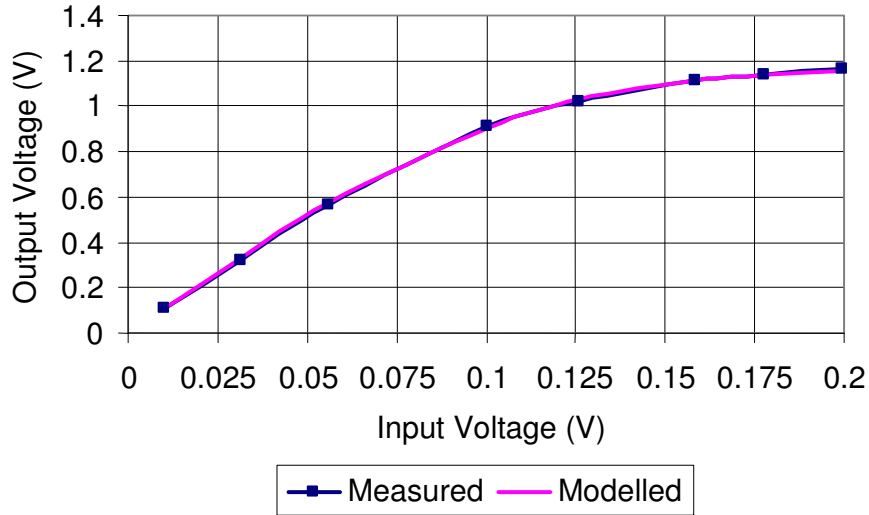


Figure 5-11: Comparison of the voltage curves: measured experimentally and calculated analytically using the LSR model extraction method for the PA (ZFL500)

As can be seen from the Figure 5-11, the LSR polynomial approximation method provides a very high accuracy of the extracted model. This is confirmed by the coefficient of determination, which equals to  $r^2 = 0.99$  in the considered example.

In order to extract the memoryless fundamental-frequency model by the second method, a frequency response for the considered PA is generated. For accurate modelling, the response must include all the harmonics, which appear during PA operation. It is generated at the maximum power level from the PA dynamic range. As mentioned above, the PA operates in the power range up to its 1-dB compression point, which occur at -9...-10 dBm input. In order to take into account all the harmonic products, the frequency response shown in Figure 5-12 is generated at -8 dBm input power. The values of harmonics are measured and substituted into (5.59) for calculating  $g$ -coefficients. After solving the system of equations, the following values are obtained:

$$\begin{cases} g_1 = 10.8; \\ g_3 = -228.7; \\ g_5 = 2260. \end{cases} \quad (5.63)$$

Using (5.60), the analytical expression for the fundamental-frequency model can be written as:

$$V_{OUT}^{FUND}(t) = 10.8 \cdot V_{IN}(t) - 172 \cdot |V_S(t)|^2 \cdot V_{IN}(t) + 1413 \cdot |V_S(t)|^4 \cdot V_{IN}(t). \quad (5.64)$$

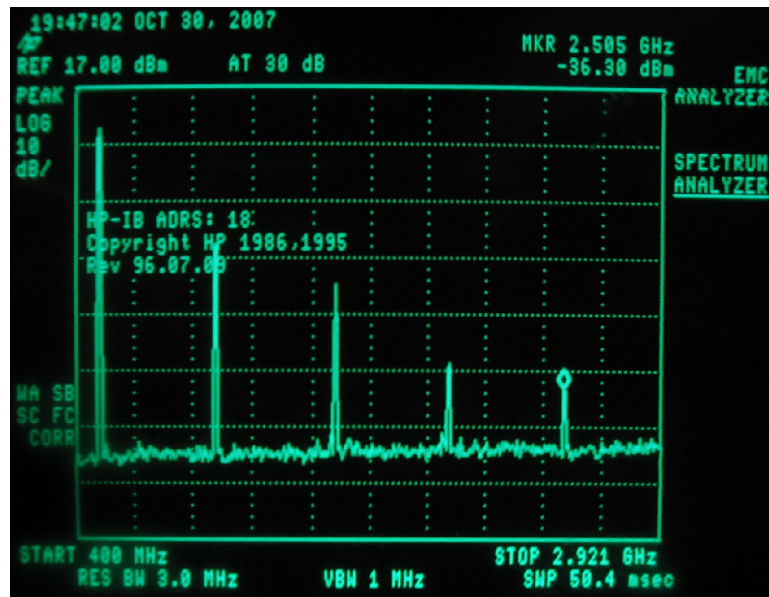


Figure 5-12: Measured frequency response of the PA (ZFL500) at -8 dBm input power

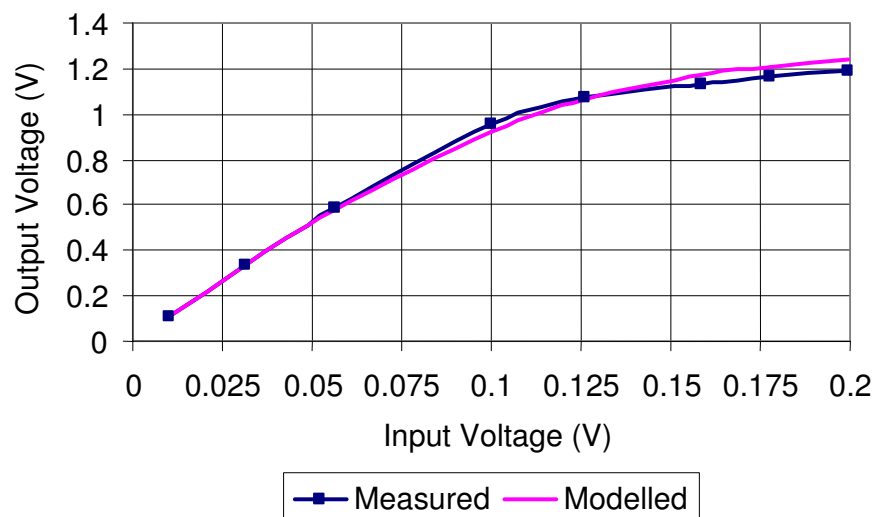


Figure 5-13: Comparison of the voltage curves: measured experimentally and calculated analytically using the frequency-response model extraction method for ZFL500

In order to verify accuracy of the model (5.64), the AM/AM curve of the PA is acquired using the model and compared to that obtained from the measured data. The corresponding voltage curves are shown in Figure 5-13.

Further, the coefficient of determination  $r^2$  is calculated, in order to judge the quality of fit of the model to the measured data. For the considered example, the coefficient of determination equals to  $r^2 = 0.93$ . It means that the proposed method of extracting

polynomial model from the PA frequency response offers sufficiently high accuracy for calculating initial  $g$ -coefficients. However, the accuracy of this method is lower compared to that of the LRS technique.

Finally, the obtained model (5.64) is tested with a digitally-modulated signal excitation. The output spectrum is obtained by simulating the model in a Matlab-ADS co-simulation system and compared to the measured one. The proposed PA model is implemented in Matlab and called from ADS during the simulation. Comparison of the simulated (Figure 5-14) and measured (Figure 5-15) spectrums allows making a conclusion that the developed polynomial model of the power amplifier is accurate and can be used for calculation the predistorter parameters.

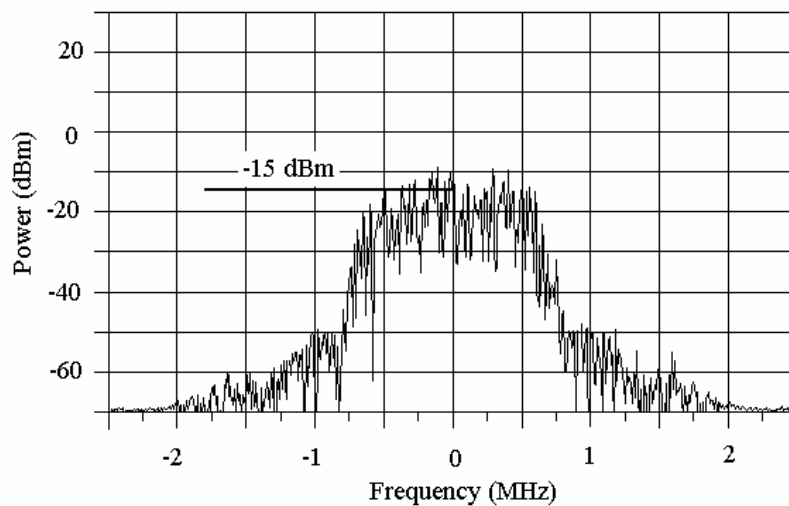


Figure 5-14: Simulated 16-QAM output spectrum for the developed ZFL500 model



Figure 5-15: Measured 16-QAM output spectrum for ZFL500

## 5.4. Conclusion

The current Chapter presented modelling techniques used to analytically represent the nonlinear behaviour and memory effects of power amplifiers. Behavioural modelling of power amplifiers including the nonlinear distortion and memory effects is conventionally accomplished by the Volterra series analysis, which, however, has a number of practical limitations and difficulties. For these reasons, simplified models are usually preferred, which represent the memory effects and nonlinear behaviour of a PA by separate interacting or independent blocks. The first case refers to the nonlinear memory, whereas the second one is used for the linear memory of power amplifiers. The most popular models are the two-box Wiener and Hammerstein models, which are formed of a memoryless nonlinear block and a linear filter. From the overview of existing modelling techniques, a conclusion can be made that the Wiener and Hammerstein models are accurate and convenient for practical use for representing power amplifiers with memory effects and designing predistorter linearisers based on the inverse structure.

The in-band distortion modelling technique together with the model extraction procedures based on the PA frequency-response analysis and least-squares polynomial regression were developed and verified experimentally. The experimental results proved the feasibility and accuracy of the proposed modelling methods and revealed the trade-off between the model extraction techniques: the model extraction procedure based on the least-squares polynomial regression has a higher accuracy, but also a higher time consumption and complexity compared to those of the PA frequency-response analysis.

## 5.5. References

- [5.1] J. C. Pedro, and S. A. Maas, "A comparative overview of microwave and wireless power-amplifier behavioral modeling approaches," *IEEE Transactions on Microwave Theory and Techniques*, vol. 53, no. 4, pp. 1150-1163, Apr. 2005.
- [5.2] S. Maas, *Nonlinear Microwave and RF Circuits*, Artech House Publishers, 2003, ISBN 1580534848.

- 
- [5.3] M. Schetzen, *The Volterra and Wiener Theories of Nonlinear Systems*, New York: Wiley, 1980, ISBN 0894643568.
- [5.4] A. Zhu, J. C. Pedro, and T. R. Cunha, "Pruning the Volterra series for behavioral modeling of power amplifiers using physical knowledge," *IEEE Transactions on Microwave Theory and Techniques*, vol. 55, no. 5, pp. 813–820, May 2007.
- [5.5] D. R. Morgan, Z. Ma, J. Kim, M. G. Zierdt, and J. Pastalan, "A generalized memory polynomial model for digital predistortion of RF power amplifiers," *IEEE Transactions on Signal Processing*, vol. 54, no. 10, pp. 3852–3860, Oct. 2006.
- [5.6] H. W. Kang, Y. S. Cho, and D. H. Youn, "Adaptive precompensation of Wiener systems," *IEEE Transactions on Signal Processing*, vol. 46, no. 10, pp. 2825–2829, Oct. 1998.
- [5.7] P. Celka, N. J. Bershad, and J.-M. Vesin, "Stochastic gradient identification of polynomial Wiener systems: analysis and application," *IEEE Transactions on Signal Processing*, vol. 49, no. 2, pp. 301–313, Feb. 2001.
- [5.8] A. E. Nordsjo and L. H. Zetterberg, "Identification of certain time-varying nonlinear Wiener and Hammerstein systems," *IEEE Transactions on Signal Processing*, vol. 49, no. 3, pp. 577–592, Mar. 2001.
- [5.9] T. J. Liu, S. Boumaiza, F. M. Ghannouchi, "Augmented Hammerstein predistorter for linearization of broad-band wireless transmitters," *IEEE Transactions on Microwave Theory and Techniques*, vol. 54, no. 4, pp. 1340–1349, Apr. 2006.
- [5.10] T. Wang, and J. Ilow, "Compensation of nonlinear distortions with memory effects in OFDM transmitters," in *Proc. IEEE Global Telecommun. Conf.*, vol. 4, pp. 2398–2403, Dallas, USA, Nov. 2004.
- [5.11] N. J. Bershad, P. Celka, and S. McLaughlin, "Analysis of stochastic gradient identification of Wiener–Hammerstein systems for nonlinearities with Hermite polynomial expansions," *IEEE Transactions on Signal Processing*, vol. 49, no. 5, pp. 1060–1072, May 2001.
- [5.12] J. C. Pedro, N. B. Carvalho, and P. M. Lavrador, "Modeling nonlinear behavior of band-pass memoryless and dynamic systems," in *Proc. IEEE MTT-S Int. Microwave Symp. Dig.*, Philadelphia, PA, USA, pp. 2133–2136, Jun. 2003.

- [5.13] J. Vuolevi, T. Rahkonen, *Distortion in RF Power Amplifiers*, Artech House Inc., 2003, ISBN 1580535399.
- [5.14] J. Vuolevi, T. Rahkonen, and J. Manninen, "Measurement technique for characterizing memory effects in RF power amplifiers," *IEEE Transactions on Microwave Theory and Techniques*, vol. 49, no. 8, pp. 1383–1389, Aug. 2001.
- [5.15] W. Huadong, W. Zhengde, B. Jinfu, T. Xiaohong, "Analyzing memory effect in RF power amplifier using three-box modeling", in Proc. *2005 Asia-Pacific Microwave Conference (APMC 2005)*, Suzhou, China, vol. 4, Dec. 2005.
- [5.16] H. Ku, M. Mckinley, and J. S. Kenney, "Quantifying memory effects in RF power amplifiers," *IEEE Transactions on Microwave Theory and Techniques*, vol. 50, no. 12, pp. 2843–2849, Dec. 2002.
- [5.17] H. Ku and J. Kenney, "Behavioral modeling of RF power amplifiers considering IMD and spectral regrowth asymmetries," in Proc. *IEEE Int. Microwave Symp. Dig.*, Philadelphia, PA, USA, pp. 799–802, Jun. 2003.
- [5.18] M. Schetzen, *The Volterra and Wiener Theories of Nonlinear Systems*, New York: Wiley, 1980, ISBN 0894643568.
- [5.19] J. C. Pedro, N. B. Carvalho, and P. M. Lavrador, "Modeling nonlinear behavior of band-pass memoryless and dynamic systems," in Proc. *IEEE MTT-S Int. Microwave Symp. Dig.*, Philadelphia, PA, USA, pp. 2133–2136, Jun. 2003.
- [5.20] J. Vuolevi, T. Rahkonen, and J. Manninen, "Measurement technique for characterizing memory effects in RF power amplifiers," *IEEE Transactions on Microwave Theory and Techniques*, vol. 49, no. 8, pp. 1383–1389, Aug. 2001.
- [5.21] N. Mizusawa, and S. Kusunoki, "Third- and fifth-order baseband component injection for linearization of the power amplifier in a cellular phone," *IEEE Transactions on Microwave Theory and Techniques*, vol. 53, no. 4, pp. 3327–3334, Apr. 2005.
- [5.22] D. Bondar, and D. Budimir, "WiMax power amplifier linearization through injection of base-band components," in Proc. *11<sup>th</sup> Int. Symp. Microw. Opt. Technol.*, Roma, Italy, pp. 293–297, Dec. 2007.
- [5.23] D. Bondar, D. Budimir, and B. Shelkovnikov, "Linearization of power amplifiers by baseband digital predistortion for OFDM transmitters," in Proc. *18<sup>th</sup> Int.*

---

*Crimean Conf. Microw. and Telecommun. Technology*, Sebastopol, Ukraine, vol. 1, pp. 270-271, Sept. 2008.

- [5.24] D. Bondar, D. Budimir, and B. Shelkovnikov, "A new approach for nonlinear analysis of power amplifiers," in *Proc. 18<sup>th</sup> Int. Crimean Conf. Microw. and Telecommun. Technology*, Sebastopol, Ukraine, vol. 1, pp. 125-128, Sept. 2008.
- [5.25] D. Bondar, and D. Budimir, "A digital predistorter for wireless transmitters," *International Journal of RF and Microwave Computer-Aided Engineering*, 2009.
- [5.26] D. Bondar, and D. Budimir, "Digital baseband predistortion of wideband power amplifiers with improved memory effects," in *Proc. IEEE Radio and Wireless Symposium*, pp. 284-287, Jan. 2009.

---

## 6. MEMORYLESS DIGITAL PREDISTORTION TECHNIQUE WITH ENHANCED LINEARISING PERFORMANCES

### 6.1. Introduction

Modern wireless communication systems, such as UMTS and WiMAX, require highly linear and efficient power amplifiers. These contradicting requirements have led to the development of a number of linearisation techniques described in Chapter 3. Among them the techniques that offer the most superior linearising performance, such as the feedforward and feedback methods, require modification of the RF path and implementation of a feedforward or feedback loop, which increases the overall size, complexity and cost of the transmitter.

The recent advancements in DSP and microchip technology together with the need of reducing the size, cost and complexity of transmitters have increased the popularity of digitally-predictive methods for linearising power amplifiers. However, these methods face several severe challenges, which limit the potential performance and applicability of digital predistortion. First of all, the conventional DPD methods possess a low-to-moderate degree of linearity improvement, which is not sufficient for many base station applications. Secondly, the traditional DPD systems require complex LUT or polynomial signal processing units, which significantly increase the complexity of DSP computations, resulting in higher power consumption, limited bandwidth and exacting requirements to the signal processing components. Moreover, the conventional DPD methods do not cope with memory effects of power amplifiers, which severely degrade the linearising performance and limit the operational bandwidth.

Chapters 6 and 7 presents developed solutions to the problems described above and proposes an advanced DPD system, which, on one hand, possesses less computational complexity, as it does not require complex LUT or polynomial blocks, and, on the other hand, exhibits enhanced linearising performance compared to the conventional DPD and injection methods thanks to the developed iterative baseband components injection technique. The DPD system described in this Chapter incorporates the proposed

solutions for increasing memoryless DPD performances by baseband distortion components iterative injection [6.1]-[6.4]. Two DPD techniques with enhanced linearising performances are proposed, which overcome the drawbacks of conventional DPD methods. The techniques are based on injecting the in-band distortion components produced by all the orders of PA nonlinearity into the original baseband signal. The first technique is implemented as the direct injection of baseband distortion components, neglecting the effect of the new cross-modulation distortion components introduced by the injection, whereas the second method incorporates iterative injecting, including compensation of the initial and all the introduced distortion components. Consequently, for the first technique, the predistorter coefficients are calculated by direct formulas, but for the second method the DPD coefficients are iteratively updated for each new injection in order to take into account the new cross-modulation distortion components introduced during the previous iterations. Both the proposed DPD techniques allow overcoming the distortion compensation limit inherent in the injection methods. The proposed techniques are adjustable for achieving the best ratio of linearising degree to computational complexity, allowing to optimise the predistorter for any particular application.

The proposed techniques are verified experimentally. In this Chapter, the experimental investigations are carried out for the memoryless DPD and a low-memory power amplifier Mini-Circuits ZFL-500 excited with different types of signals. In the next Chapter, experiments are conducted for the proposed DPD with improved memory effects and a wideband power amplifier Mini-Circuits ZHL-1042J.

Aiming at corroborating the theory, different scenarios of the test signals are considered, including the QPSK and 16-QAM modulation schemes with 3.5-MHz and 5-MHz bandwidths at 500-MHz carrier frequency. The measured results verify the feasibility of the proposed predistortion and demonstrate improvements in the linearising performance compared to the conventional DPD. The Chapter depicts the experimental setup for verifying the proposed predistorter. Then, the PA characterisation process is executed, which includes quantifying the nonlinear behaviour and memory effects in order to extract the parameters for the predistorter. Finally, the measured performances of the system are presented for the cases without and with the proposed predistortion for digitally modulated signals.

## 6.2. Adjustable Memoryless DPD System

In this Section, the proposed memoryless digital predistortion is presented and investigated. The proposed DPD aims at enhancing the linearising performance of the conventional baseband DPD, while maintaining low computational complexity, size and cost of the predistorter. The developed technique incorporates iterative injection of the in-band distortion components, in order to overcome the distortion compensation limit. Firstly, the shortcomings of the conventional distortion-component injection DPD are defined mathematically. After that, the proposed solutions to the problems and the theoretical concept for the developed DPD are presented in direct and iterative forms. Then, the computational complexity, adjustability and linearising performance of the technique are investigated and discussed. Finally, the feasibility of the proposed DPD is verified experimentally and by simulations in ADS and developed Matlab-ADS co-simulation system for different types of signals.

### 6.2.1 Problem Definition

Conventional distortion-component injection DPD presented in works [6.5]-[6.7] has been described in Section 3.8.3. It implies compensating the PA nonlinear distortion by injecting baseband distortion components into the input signal with the same amplitude and opposite phase. After proper tuning, the injected and original distortion signals eliminate each other at the output of the PA. As described above, the nonlinear behaviour of a PA at the fundamental frequency can be written in the following form:

$$V_{OUT}^{FUND}(t) = (g_1 + \sum_{k=1}^{\infty} G_{2k+1}(t)) \cdot V_{IN}(t), \quad (6.1)$$

where:

$$G_{2k+1}(t) = b_{2k+1} V^{2k} g_{2k+1} [I^2(t) + Q^2(t)]^k. \quad (6.2)$$

For simplicity of explanation, a 3<sup>rd</sup>-order polynomial model is considered below:

$$V_{OUT}(t) = g_1 \cdot V_{IN}(t) + g_2 \cdot V_{IN}^2(t) + g_3 \cdot V_{IN}^3(t). \quad (6.3)$$

In this case, (6.1) is simply composed of two terms: the linear amplified input signal and the in-band distortion component produced by the 3<sup>rd</sup>-order nonlinearity:

$$V_{OUT}^{FUND}(t) = g_1 \cdot V_{IN}(t) + G_3(t) \cdot V_{IN}(t), \quad (6.4)$$

where:

$$G_3(t) = b_3 V^2 g_3 [I^2(t) + Q^2(t)]. \quad (6.5)$$

According to the injection DPD technique described in [6.5]-[6.7], in order to compensate for the distortion present in the output signal (6.4), the input signal is predistorted as:

$$V_{IN}^{DPD}(t) = V_{IN}(t) + \left(-\frac{G_3(t)}{g_1}\right) \cdot V_{IN}(t). \quad (6.6)$$

After substituting (6.6) into (6.3), it can be shown that the inserted distortion component compensates for the distortion of the power amplifier. Indeed, the new output signal at the fundamental frequency looks like:

$$\begin{aligned} V_{OUT}^{FUND}(t) &= g_1 \cdot V_{IN}(t) - G_3(t) \cdot V_{IN}(t) \\ &+ g_3 \cdot V_{IN}^3(t) \cdot \left[1 + \left(-\frac{G_3(t)}{g_1}\right)\right]^3. \end{aligned} \quad (6.7)$$

Considering (6.3)-(6.4), one can see that the 3<sup>rd</sup>-order nonlinear term  $g_3 \cdot V_{IN}^3(t)$  produces the distortion component  $G_3(t) \cdot V_{IN}(t)$  at the fundamental frequency:

$$\left(g_3 \cdot V_{IN}^3(t)\right)^{FUND} = G_3(t) \cdot V_{IN}(t). \quad (6.8)$$

Then, (6.7) can be re-written as:

$$\begin{aligned} V_{OUT}^{FUND}(t) &= g_1 \cdot V_{IN}(t) - G_3(t) \cdot V_{IN}(t) \\ &+ G_3(t) \cdot V_{IN}(t) \cdot \left[1 + \left(-\frac{G_3(t)}{g_1}\right)\right]^3, \end{aligned} \quad (6.9)$$

or:

$$\begin{aligned} V_{OUT}^{FUND}(t) &= g_1 \cdot V_{IN}(t) - G_3(t) \cdot V_{IN}(t) + G_3(t) \cdot V_{IN}(t) \\ &+ G_3(t) \cdot V_{IN}(t) \cdot \left[ -3 \cdot \frac{G_3(t)}{g_1} + 3 \cdot \left(\frac{G_3(t)}{g_1}\right)^2 - \left(\frac{G_3(t)}{g_1}\right)^3 \right]. \end{aligned} \quad (6.10)$$

From the obtained expression, one can see that the initial distortion component  $G_3(t) \cdot V_{IN}(t)$  has been compensated for. Nevertheless, the injected signal has not only compensated for the PA distortion, but also inserted another distortion components

caused by the last term in (6.10). Being smaller than the initial one, the new distortion components, however, lead to degradation of the output signal:

$$V_{OUT}^{FUND}(t) = g_1 \cdot V_{IN}(t) \cdot \left[ 1 - 3 \cdot \left[ \frac{G_3(t)}{g_1} \right]^2 + 3 \cdot \left[ \frac{G_3(t)}{g_1} \right]^3 - \left[ \frac{G_3(t)}{g_1} \right]^4 \right]. \quad (6.11)$$

In (6.11) the expression in brackets consists of four terms. The first one represents the desired undistorted output signal, whereas the last three arise from the new injected component and become the reason for the distortion compensation limit. Therefore, the described distortion-component injection DPD technique has a limited performance due to the inserted distortion. In order to overcome this shortcoming, an iterative injection technique is developed, which is presented below.

### 6.2.2 Proposed DPD using Distortion Components Iterative Injection

Linearising power amplifiers by injecting the in-band distortion components in a baseband block is a new and promising approach, which being implemented by digital processing of the input signal allows maintaining low circuit complexity. However, the straightforward injection outcomes not only in compensating for the original PA distortion, but also in producing other distortion components, as described above. These introduced distortions become a factor that limits the potential performance. In this Section, an advanced component injection DPD technique is proposed, which overcomes the mentioned issue. For a weakly nonlinear system, the technique is developed in a simple direct form suitable for hardware and software implementation. In this case, the additional distortion components arising from the second injection are ignored, as they are negligibly small for the weakly nonlinear systems. For the systems with strong nonlinearities, the proposed technique is developed in its iterative form, including compensation of all the original and introduced in-band distortion components. This method, which is suitable for software implementation, overcomes the distortion compensation limit and has a universal linearising capability with high performance. Theoretical analysis of the proposed direct and iterative injection methods is given below.

For a weakly nonlinear system, the average value  $V$  of the input voltage magnitude  $|V_S(t)|$  is small, and hence  $\frac{G_3(t)}{g_1} \ll 1$ . Therefore, the last two distortion terms in (6.11) can be ignored as they are significantly smaller than the previous summands. In this case, (6.11) can be simplified to

$$V_{OUT}^{FUND}(t) = g_1 \cdot V_{IN}(t) \cdot \left[ 1 - 3 \cdot \left[ \frac{G_3(t)}{g_1} \right]^2 \right], \quad (6.12)$$

or, considering (6.5), the obtained expression can be written in another way:

$$V_{OUT}^{FUND}(t) = g_1 \cdot V_{IN}(t) - \frac{27 \cdot V^4 \cdot g_3^2 [I^2(t) + Q^2(t)]^2}{16 \cdot g_1} \cdot V_{IN}(t). \quad (6.13)$$

The new distortion component caused by the second summand in (6.13) can be compensated for in a similar way by injecting a baseband signal with the same magnitude but  $180^\circ$  phase shift into the input signal  $V_{IN}(t)$ . Therefore, the overall predistorted input signal looks like:

$$V_{IN}^{DPD}(t) = V_{IN}(t) - \frac{G_3(t)}{g_1} \cdot V_{IN}(t) + 3 \cdot \left[ \frac{G_3(t)}{g_1} \right]^2 \cdot V_{IN}(t). \quad (6.14)$$

The obtained predistortion formula is applicable for linearising weakly-nonlinear systems, which obey the condition:  $\frac{G_3(t)}{g_1} \ll 1$ . Substituting (6.5) for  $G_3(t)$  with

consideration of (5.22)-(5.23) outcomes in:  $\frac{3V^2 g_3 [I^2(t) + Q^2(t)]}{4g_1} = \frac{3g_3 V_S^2(t)}{4g_1} \ll 1$ .

Finally, the condition for applicability of (6.14) is derived as:

$$|V_S(t)| \ll \sqrt{\left| \frac{4g_1}{3g_3} \right|}. \quad (6.15)$$

The predistortion technique described by (6.14)-(6.15) is suitable for hardware implementation and can be easily integrated into the baseband block. Indeed, the injected signals can be obtained from the input I and Q components by generating the baseband signals  $I^2(t) + Q^2(t)$  and  $[I^2(t) + Q^2(t)]^2$  and multiplying them by the corresponding coefficients  $\alpha = \frac{3 \cdot V^2 \cdot g_3}{4 \cdot g_1}$  and  $\beta = \frac{27 \cdot V^4 \cdot g_3^2}{16 \cdot g_1^2}$ . The value  $V$  is calculated

as the average input signal magnitude, and the values for  $g_1$  and  $g_3$  are pre-programmed and can be updated during an adaptation procedure if required.

For strongly-nonlinear systems, the assumption of negligibly small values for the introduced distortion components may not be relevant, and hence all the original and additional distortions must be compensated for. In this case, the nonlinearity of a PA can include high-order terms, and the general  $n$ -order in-band distortion modelling technique is required. According to the developed modelling technique described in Chapter 5, if the PA is represented by its  $n$ -order nonlinear polynomial as

$$V_{OUT}(t) = \sum_{k=1}^n g_k V_{IN}^k(t), \quad (6.16)$$

where  $n=2p+1$ , the total output signal at the fundamental frequency including the desired linear-amplified signal and the in-band distortion components is specified by following:

$$V_{OUT}^{FUND}(t) = g_1 \cdot V_{IN}(t) + \left[ \sum_{k=1}^p b_{2k+1} V^{2k} g_{2k+1} [I^2(t) + Q^2(t)]^k \right] \cdot V_{IN}(t). \quad (6.17)$$

In order to compensate for the nonlinearity, the in-band distortion components are injected into the input signal with the same magnitude but out of phase:

$$V_{IN}^{(1)}(t) = V_{IN}(t) - \frac{\sum_{k=1}^p G_{2k+1}(t)}{g_1} \cdot V_{IN}(t), \quad (6.18)$$

where  $V_{IN}^{(1)}(t)$  is the input signal predistorted with one injection of the in-band distortion components, and  $G_{2k+1}(t)$  is defined by following:

$$G_{2k+1}(t) = b_{2k+1} V^{2k} g_{2k+1} [I^2(t) + Q^2(t)]^k. \quad (6.19)$$

After substituting (6.18) into the general  $n$ -order nonlinear model (6.16), the output signal can be written as:

$$\begin{aligned}
V_{OUT}^{(1)}(t) &= g_1 \cdot V_{IN}(t) - \sum_{k=1}^p G_{2k+1}(t) \cdot V_{IN}(t) \\
&+ g_2 \cdot \left(1 - \frac{\sum_{k=1}^p G_{2k+1}(t)}{g_1}\right)^2 \cdot V_{IN}^2(t) + g_3 \cdot \left(1 - \frac{\sum_{k=1}^p G_{2k+1}(t)}{g_1}\right)^3 \cdot V_{IN}^3(t) \\
&+ g_4 \cdot \left(1 - \frac{\sum_{k=1}^p G_{2k+1}(t)}{g_1}\right)^4 \cdot V_{IN}^4(t) + g_5 \cdot \left(1 - \frac{\sum_{k=1}^p G_{2k+1}(t)}{g_1}\right)^5 \cdot V_{IN}^5(t) + \dots
\end{aligned} \tag{6.20}$$

where  $V_{OUT}^{(1)}(t)$  is the total output signal after predistorting the input signal with one injection of the in-band distortion components. As shown in Section 5.3, the even-order terms of the PA polynomial model do not produce in-band distortion, whereas the odd-order terms generate in-band distortion components at the fundamental frequency, which are described analytically as the following mathematical operator:  $g_{2k+1} \cdot V_{IN}^{2k+1}(t) \rightarrow G_{2k+1}(t) \cdot V_{IN}(t)$ . The latter notation denotes that the in-band distortion component  $G_{2k+1}(t) \cdot V_{IN}(t)$  is produced by and has a one-to-one correspondence with the odd-order polynomial term  $g_{2k+1} \cdot V_{IN}^{2k+1}(t)$ . Consequently, at the fundamental frequency, each odd-order term of (6.16) outcomes in the corresponding distortion component:

$$\left(g_{2k+1} \cdot V_{IN}^{2k+1}(t)\right)^{FUND} = G_{2k+1}(t) \cdot V_{IN}(t). \tag{6.21}$$

Using (6.20) and (6.21), the output signal at the fundamental frequency after predistorting the input signal with one injection of the in-band distortion components can be expressed as:

$$\begin{aligned}
V_{OUT}^{(1)FUND}(t) &= g_1 \cdot V_{IN}(t) - \sum_{k=1}^p G_{2k+1}(t) \cdot V_{IN}(t) \\
&+ G_3(t) \cdot \left(1 - \frac{\sum_{k=1}^p G_{2k+1}(t)}{g_1}\right)^3 \cdot V_{IN}(t) + G_5(t) \cdot \left(1 - \frac{\sum_{k=1}^p G_{2k+1}(t)}{g_1}\right)^5 \cdot V_{IN}(t) + \dots
\end{aligned} \tag{6.22}$$

As can be seen from (6.22), after completing one injection, the original distortion components caused by  $\sum_{k=1}^p G_{2k+1}(t) \cdot V_{IN}(t)$  are compensated for. Indeed, the obtained expression can be re-written as:

$$\begin{aligned}
V_{OUT}^{(1)FUND}(t) &= g_1 \cdot V_{IN}(t) + G_3(t) \cdot \left[ -1 + \left( 1 - \frac{\sum_{k=1}^p G_{2k+1}(t)}{g_1} \right)^3 \right] \cdot V_{IN}(t) \\
&+ G_5(t) \cdot \left[ -1 + \left( 1 - \frac{\sum_{k=1}^p G_{2k+1}(t)}{g_1} \right)^5 \right] \cdot V_{IN}(t) + \dots
\end{aligned} \tag{6.23}$$

After expanding the brackets in (6.23), it can be shown that the initial distortion components  $G_{2l+1}(t)$  are compensated for. Nevertheless, the new distortion components caused by the injected signal appear. Therefore, it is necessary to recalculate the new in-band distortion components and to compensate them during the next iteration. The new predistorted input signal at the second iteration looks like:

$$V_{IN}^{(2)}(t) = V_{IN}(t) - \frac{\sum_{k=1}^p G_{2k+1}^{(1)}(t)}{g_1} \cdot V_{IN}(t), \tag{6.24}$$

where  $G_{2k+1}^{(1)}(t)$  is the magnitude factor of the  $(2k+1)$ -order in-band distortion component after the first iteration. It is obtained from (6.23) as following:

$$G_{2k+1}^{(1)}(t) = G_{2k+1}(t) \cdot \left( -1 + \left( 1 - \frac{\sum_{l=1}^p G_{2l+1}(t)}{g_1} \right)^{2k+1} \right). \tag{6.25}$$

Similarly, the new in-band distortion components are calculated and the expressions for the injected signals at further iterations are obtained. On the  $m$ -th iteration, the predistorted input and the corresponding output signals can be written as:

$$V_{IN}^{(m)}(t) = V_{IN}(t) - \frac{\sum_{k=1}^p G_{2k+1}^{(m-1)}(t)}{g_1} \cdot V_{IN}(t), \tag{6.26}$$

$$V_{OUT}^{(m)FUND}(t) = g_1 \cdot V_{IN}(t) + \left( \sum_{k=1}^p G_{2k+1}^{(m)}(t) \right) \cdot V_{IN}(t), \tag{6.27}$$

$$G_{2k+1}^{(m)}(t) = G_{2k+1}^{(m-1)}(t) \cdot \left( -1 + \left( 1 - \frac{\sum_{l=1}^p G_{2l+1}^{(m-1)}(t)}{g_1} \right)^{2k+1} \right). \tag{6.28}$$

where  $n=2p+1$  – is the order of the polynomial model; and  $G_{2l+1}^{(m)}(t)$  is the magnitude factor of an odd (third, fifth, seventh etc.) in-band distortion component at the  $m$ -th

iteration. Equations (6.26)-(6.28) represent the general mathematical model for the proposed baseband iterative injection DPD technique with  $m$  injections and  $n$ -order polynomial model. The distortion components at the next iteration are smaller than those at the previous iteration, which will be shown in Section 6.2.4 of this Chapter.

### 6.2.3 Operation of the Proposed Digital Predistorter

The proposed baseband digital predistorter incorporates iterative injection of the in-band distortion components, which are generated using the following parameters: number of injections  $m$ , polynomial coefficients  $g_{2k+1}$ ,  $k \in [1; \frac{n-1}{2}]$  of the  $n$ -order nonlinear model, and coefficients  $b_{2k+1}$  defined by Table 5.1. The latter is fixed, whereas the parameters  $m$  and  $g_{2k+1}$  depend on the particular system and can be adjusted. The proposed DPD generally requires iteratively updating the magnitude factors of the injected signals for each injection, which can be accomplished by a software algorithm in a DSP block. However, as described in Section 6.2.2, for weakly nonlinear systems, the proposed DPD parameters are calculated directly from the input signal, and hence the predistorter is suitable for hardware implementation. Operation of both the iterative and direct forms of the proposed DPD is presented below.

Figure 6-1 illustrates the operation of the proposed digital baseband predistorter with iterative injection algorithm for software implementation. The signal source generates input data samples, which are mapped to the required modulation type and split into the  $I$  and  $Q$  components. The input  $I$  and  $Q$  signals are used to calculate the mean value  $V$  of the input signal magnitude.  $I$  and  $Q$  are multiplied by  $1/V$  for normalisation. Further, the mean value  $V$  of the input signal magnitude is calculated.  $I$  and  $Q$  are multiplied by  $1/V$  for normalisation. This procedure is done in order to achieve  $V = \text{average}(|V_s(t)|)$  and not to affect the mean power level by predistortion. Normalised signals  $I^{norm}$  and  $Q^{norm}$  are subjected to the proposed baseband predistortion (6.26)-(6.28). After that, the signals are multiplied by  $V$  for de-normalisation, filtered with low-pass raised-cosine filters, and transferred to the I/Q modulator. Obtained RF signal is passed through the PA and further transferred to the RF output of the transmitter.

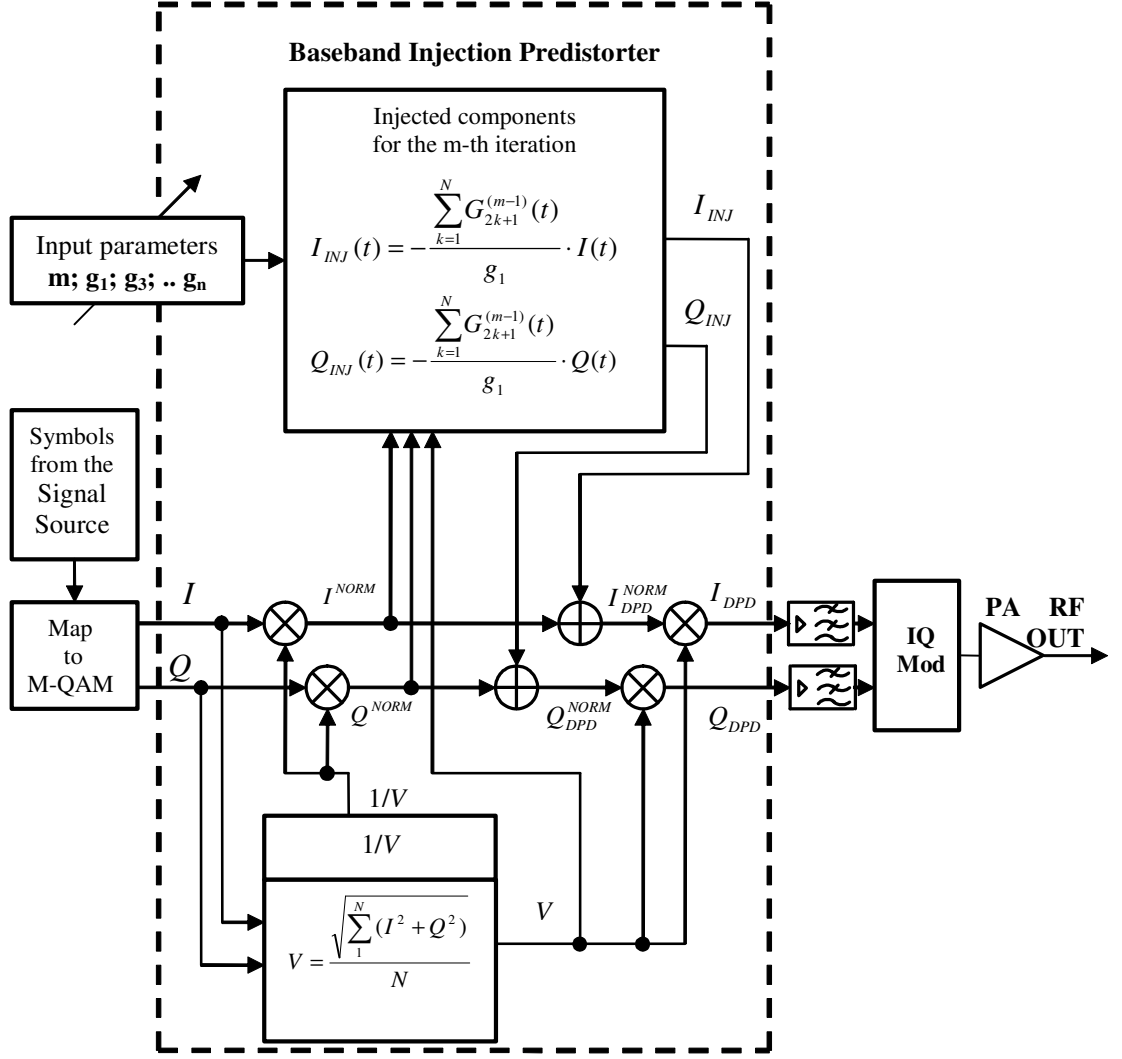


Figure 6-1: Block diagram of the proposed digital baseband predistorter using iterative injection of the in-band distortion components

Figure 6-2 illustrates the block diagram of the simplified for hardware implementation version of the proposed digital baseband predistorter with direct parameters' calculation algorithm for linearising weakly nonlinear systems. The baseband block generates  $I$  and  $Q$  signals together with the  $I^2(t) + Q^2(t)$  component. The latter is split into two parts, each of them used for calculating the corresponding injected signal. The first part is simply phase-inverted and multiplied by  $\alpha = \frac{3 \cdot V^2 \cdot g_3}{4 \cdot g_1}$ , whereas the second part is squared and multiplied by  $\beta = \frac{27 \cdot V^4 \cdot g_3^2}{16 \cdot g_1^2}$ . After that, the obtained signals are combined and multiplied by the input  $I$  and  $Q$  components in each

branch and injected into the original I and Q signals. The predistorted signals are filtered with low-pass raised-cosine filters and transferred to the I/Q modulator. Finally, the obtained RF signal is passed through the PA and further transferred to the RF output of the transmitter.

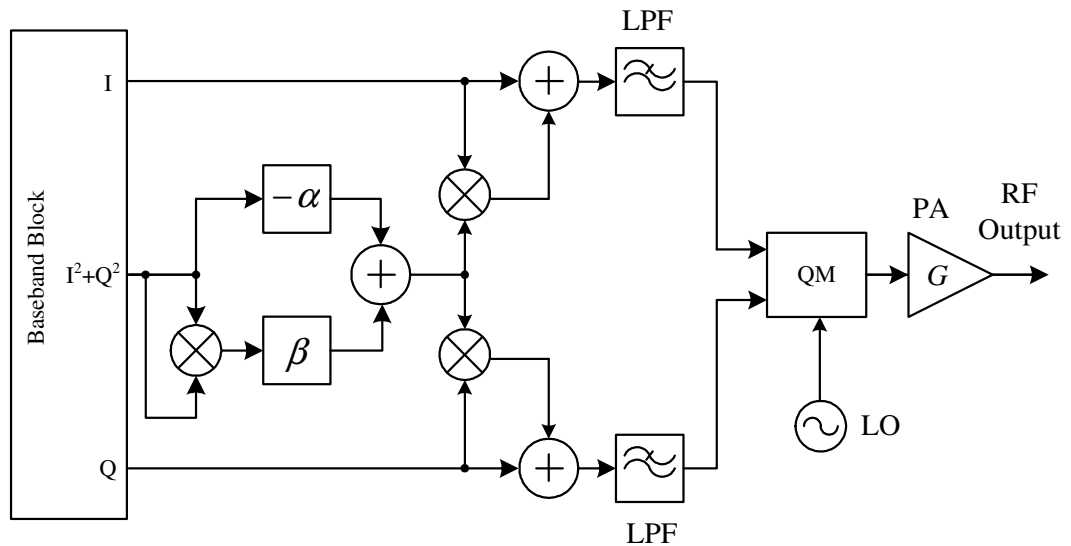


Figure 6-2: Hardware implementation of the simplified for weakly nonlinear systems proposed digital baseband predistorter using direct generation of the injected in-band distortion components

#### 6.2.4 Computational Complexity and Linearising Performance

The developed iterative injection technique allows increasing linearising performance and overcoming the distortion compensation limit by increasing the number of iterations  $m$ . However, in practice increasing the number of injections also results in higher DSP computational complexity. Therefore, a compromise between the linearising performance of the predistorter and its DSP complexity must be sought.

The computational complexity of the proposed nonlinearity compensation method is determined by the number of iterations  $m$  and the order of the PA model  $n$ . The proposed method does not require storage of complex LUTs, only  $g$ - and  $b$ -coefficients need to be tabulated, the number of which is very small and depends on the model order  $n$ . Therefore, the computational complexity of the proposed method is mainly attributed to the number of mathematical operations for each iteration. The required mathematical

operations are limited to the real multiplications and additions, as can be seen from (6.26) and (6.28). Table 6.1 presents the estimated computational complexity for the proposed nonlinearity compensation method depending on the number of iterations and the polynomial order. The values presented in Table 6.1 can be generalised as follows: the required number of stored coefficients equals to  $n+1$ ; the required number of real multiplications is  $\frac{m}{2} \cdot (3n+1)+1$ ; and the required number of real additions is  $\frac{n-1}{2} \cdot (3m-2)$ .

**TABLE 6.1:** Computational complexity of the proposed DPD

| Polynomial order ( $n$ ) | Number of coefficients | Number of real multiplications | Number of real additions     |
|--------------------------|------------------------|--------------------------------|------------------------------|
| 3                        | 4                      | $6+5 \cdot (m-1)$              | $1+3 \cdot (m-1)$            |
| 5                        | 6                      | $9+8 \cdot (m-1)$              | $2+6 \cdot (m-1)$            |
| 7                        | 8                      | $12+11 \cdot (m-1)$            | $3+9 \cdot (m-1)$            |
| 9                        | 10                     | $15+14 \cdot (m-1)$            | $4+12 \cdot (m-1)$           |
| $n$                      | $n+1$                  | $\frac{m}{2} \cdot (3n+1)+1$   | $\frac{n-1}{2} \cdot (3m-2)$ |

$m$  - number of injections

Figure 6-3 presents the dependence of linearisation degree on the number of injections for the proposed DPD technique (6.26)-(6.28). The linearisation degree is quantified as the improvement in spectral regrowth. The curve is obtained by simulating a power amplifier based on a MOSFET active device fed with a 5-MHz 16-QAM-modulated signal in Advanced Design System (ADS). In Figure 6-3, the spectral regrowth suppression for one injection of the in-band distortion components corresponds to the case of conventional baseband DPD, which usually offers from 10 to 15 dB improvement. As the number of injections increases, the spectral regrowth suppression gets stronger and converges after five injections. The Figure demonstrates that the proposed iterative baseband injection DPD can bring improvement of more than 33 dB into the spectral regrowth suppression performance. From Figure 6-3 one can see that the linearisation degree of the proposed DPD increases with the increase in number

of injections. It means that the proposed DPD is adjustable and can be tuned to achieve the best ratio of linearisation degree to computational complexity for a particular application.



Figure 6-3: Dependence of the spectral regrowth suppression on the number of injections for a 5-MHz 16-QAM signal

### 6.3. Verification of the Proposed DPD by Simulations

This Section presents simulation results for verifying feasibility of the proposed DPD technique. Initially, a simplified for hardware implementation version of the predistorter is designed in ADS and its spectral re-growth suppression improvement is tested for different modulation types. Then, performances of the proposed iterative components injection DPD technique are investigated for different types of signals using a Matlab-ADS co-simulation system. The Matlab-ADS co-simulation system is developed in order to carry out simultaneous real-time simulations of the DSP operations, used for generating and predistorting the in-phase and quadrature signals, and the RF path signal processing, including modulation and amplification.

### 6.3.1 Simulations Setup and Results for the Direct Injection DPD

The ADS circuit for simulating performances of the proposed digital predistorter, based on the direct injection of the in-band distortion signals, is presented in Figure 6-4. The presented block diagram includes a 64-QAM signal source, digital predistorter, Digital-to-Analogue Converter (DAC), I/Q modulator and the PA unit. The  $I^2(t) + Q^2(t)$  signal is generated in the baseband block and used for predistorting the input  $I$  and  $Q$  signals as follows:

$$I_{\text{DPD}}(t) = \left\{ 1 - \frac{3V^2 g_3}{4g_1} [I^2(t) + Q^2(t)] \right\} I(t), \quad (6.29)$$

$$Q_{\text{DPD}}(t) = \left\{ 1 - \frac{3V^2 g_3}{4g_1} [I^2(t) + Q^2(t)] \right\} Q(t). \quad (6.30)$$

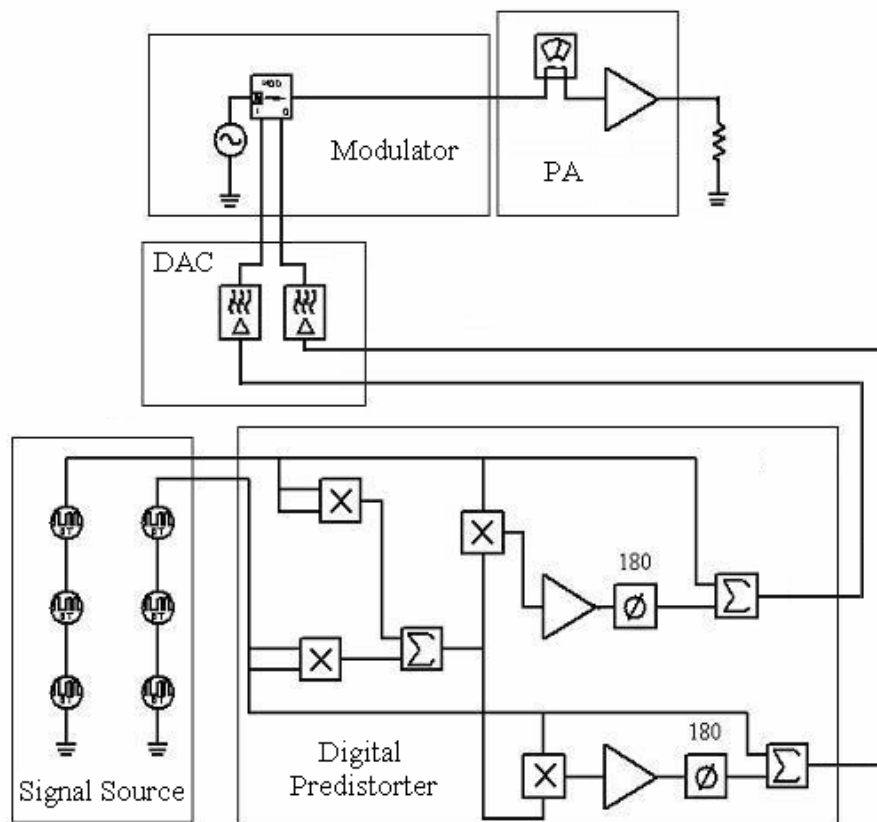


Figure 6-4: Simulation test bed for verifying performances of the predistorter with direct injection of the distortion components

The power amplifier used for simulations is taken from the ADS library. It has a 33-dB gain and the 1-dB compression point at 23 dBm output power. In order to quantify the nonlinear behaviour and extract the polynomial model of the PA, its gain and output power dependences on the input power level are investigated. The simulated variations of the PA gain and output power versus input power are presented in Figure 6-5. From the obtained AM/AM characteristic, the odd-order  $g$ -coefficients are extracted:  $g_1 = 38$ ;  $g_3 = -111$ ;  $g_5 = 112$ . Therefore, the fundamental-frequency model for the PA can be written as:

$$V_{OUT}^{FUND}(t) = 38 \cdot V_{IN}(t) - 83 \cdot |V_S(t)|^2 \cdot V_{IN}(t) + 70 \cdot |V_S(t)|^4 \cdot V_{IN}(t). \quad (6.31)$$

The coefficient of determination for the model (6.31) equals to  $r^2 = 0.986$ , which indicates high quality of fit. Further, the predistorter coefficients are calculated according to the extracted model. The spectral re-growth suppression performance of the proposed predistorter is investigated for QPSK, 16-QAM and 64-QAM signals at 3.5 GHz carrier frequency and symbol rate of 1726 kHz. The signals are passed through the PA with the input power level of -10 dBm. Simulation results for the QPSK, 16-QAM and 64-QAM input signals are presented in Figure 6-6. The Figure depicts improvements in spectral re-growths in the range of 12 to 17 dB, achieved by the use of the proposed predistorter.

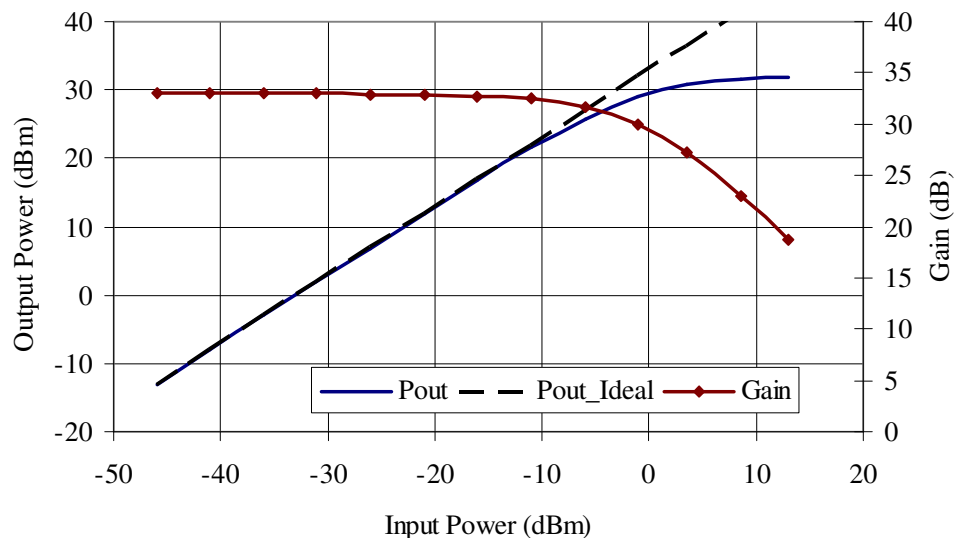
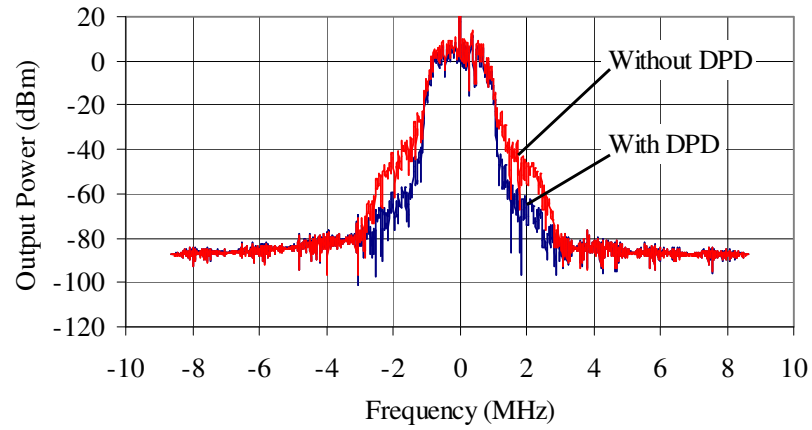
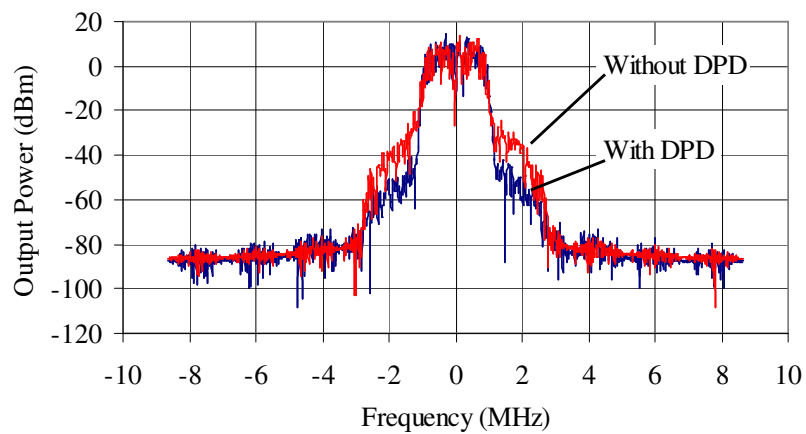


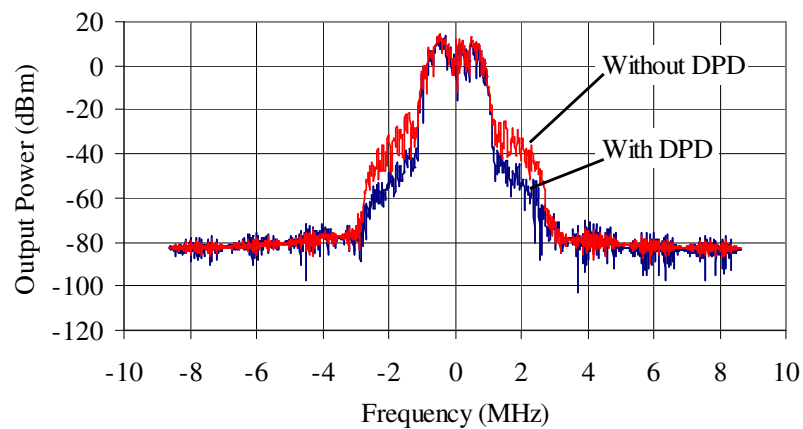
Figure 6-5: Simulated output power and gain versus input power for the considered PA



(a)



(b)



(c)

Figure 6-6: Simulated spectral re-growth without and with the proposed DPD using direct injection of the distortion components: (a) QPSK input signal; (b) 16-QAM input signal; (c) 64-QAM input signal

### 6.3.2 Developed Matlab-ADS Co-Simulation System

For investigating performances of the proposed DPD, based on iterative injecting of the in-band distortion components, a Matlab-ADS co-simulation system is developed. As the proposed predistorter is intended for the software implementation, the Matlab part of the system includes the DSP algorithm, used for generating the predistorted I and Q signals, whereas the ADS part incorporates simulations of the RF path of the transmitter.

A joint simulation of DSP operations in Matlab and RF circuit performances in ADS offers wide possibilities by combining advantages of the both softwares:

- simplicity of generating and processing the baseband digital I and Q signals for any modulation type in Matlab;
- Matlab is a powerful instrument for executing mathematical computations and predistorting I and Q signals;
- wide possibilities of behavioural modelling in Matlab;
- network analysis in ADS includes a wide range of simulation types (Envelope, Transient, Harmonic Balance, etc.);
- ADS provides a large number of test benches and device models;
- ADS is a powerful instrument for RF simulation, incorporating measurement tools close to real-life devices (spectrum analysers, timed devices etc).

For the purpose of investigating performances of the proposed predistorter, the Matlab-ADS co-simulation system can be designed according to two main layouts. The first one implies generating digital baseband I and Q signals in Matlab and transferring them to ADS modulation and amplification. This case corresponds to the signal processing in a real predistorter, where all DSP operations are carried out in a digital baseband block, and the predistorted signal is further passed to the RF path of the transmitter. The second layout implies generating the final modulated signal in Matlab and transferring it to the ADS part, where the RF signal is re-created with the assigned carrier frequency and symbol rate. The general functional diagrams for the described layouts are presented in Figure 6-7.

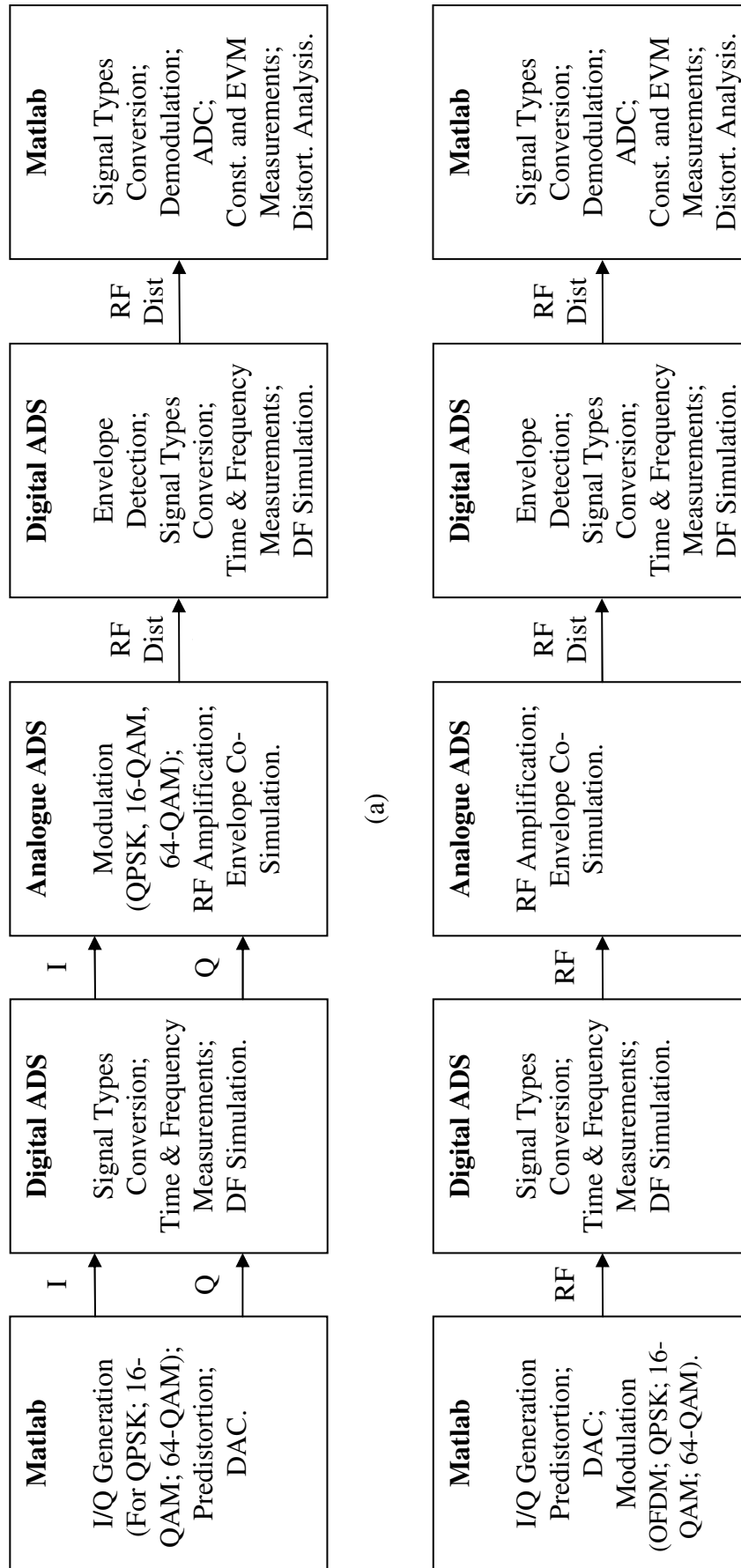


Figure 6-7: General functional diagrams for the Matlab-ADS co-simulation systems: (a) generating a digital baseband signal in Matlab; (b) generating a final RF signal in Matlab

As can be seen from the Figure, the main difference between the layouts is the location of I/Q modulator. If modulation is carried out in Matlab, it is assumed to be ideal, and the effects of I/Q imbalance and modulator imperfections are not included in the simulation. On contrary, if the I/Q modulator is simulated in ADS, the real-life imperfections can be included in the simulation.

The application of the proposed DPD technique for compensating real-life I/Q imperfections will be one of the directions for the future work. Another area of the future work includes implementation of the behavioural model for a real PA in Matlab and design of a Matlab-ADS co-simulation system, which incorporates modelling of RF amplification and distortion not by an ADS library model, but by the extracted Matlab behavioural model for the real PA. This layout would offer wide possibilities of tuning and examining the predistorter before conducting the real experiment.

### **6.3.3 Matlab-ADS Simulation Setup for Verifying the Iterative Injection DPD**

In order to verify performances of the proposed predistortion method, a Matlab-ADS co-simulation test bed has been designed according to the layout presented in Figure 6-7 (a). The main circuit for the test bed is illustrated in Figure 6-8.

It consists of a Matlab signal source, signal converters, time- and frequency-domain measurement blocks, analogue subcircuits for the I/Q modulation and RF signal amplification, and a Matlab measurement block.

The input signal is generated in Matlab according to the algorithm described below. It is transferred to the ADS digital circuit in a complex matrix form by the Matlab signal source block, as shown in Figure 6-8. The signal is further split into I and Q components, which are converted using two blocks: “Matrix unpack” for transforming the input matrix to the string and “Floating Point to Timed” for converting the signal from the floating point or real format to the timed format with assigning the time step. “Timed Data Collector” and “Spectrum Analyser” measurement blocks are used in the I and Q branches for capturing and plotting the signals in the time and frequency domains. “Up Sample” blocks are introduced before the spectrum analysers in order to increase the captured frequency band.



The modulation is accomplished in the ADS analogue sub-circuit, which is presented in Figure 6-9. The sub-circuit operates under the “Envelope” simulation controller and includes a local oscillator, I/Q modulator and low-pass filters, which realise the digital-to-analogue conversion procedure. After modulation, the obtained RF signal is returned to the main ADS digital circuit, as shown in Figure 6-8. “Envelope detector” blocks are used for providing simultaneous simulations of the “Data Flow” (Figure 6-8) and “Envelope” (Figure 6-9, 6-10) controllers.

Then, the RF signal is passed to the main amplifier sub-circuit, which is presented in Figure 6-10. It uses an ADS model of the power amplifier, which operates in its compression mode. The characteristics of the PA are investigated and presented below. After passing through the PA in the ADS analogue sub-circuit, the signal is returned to the main digital circuit operating under the Data Flow controller (Figure 6-8), where it is simulated in the time and frequency domains. The spectral re-growth characteristic and Adjacent Channel Power Ratio (ACPR) are evaluated in the spectrum analyser. The signal is further converted into the matrix form for processing in the Matlab measurement block. The Matlab block captures the amplified and distorted by the PA signal and demodulates it, in order to analyse the constellation diagram and Error Vector Magnitude (EVM). After that, the demodulated signal is returned to ADS, divided into I and Q components and converted to the timed form for examining the distorted baseband components in the time and frequency domains.

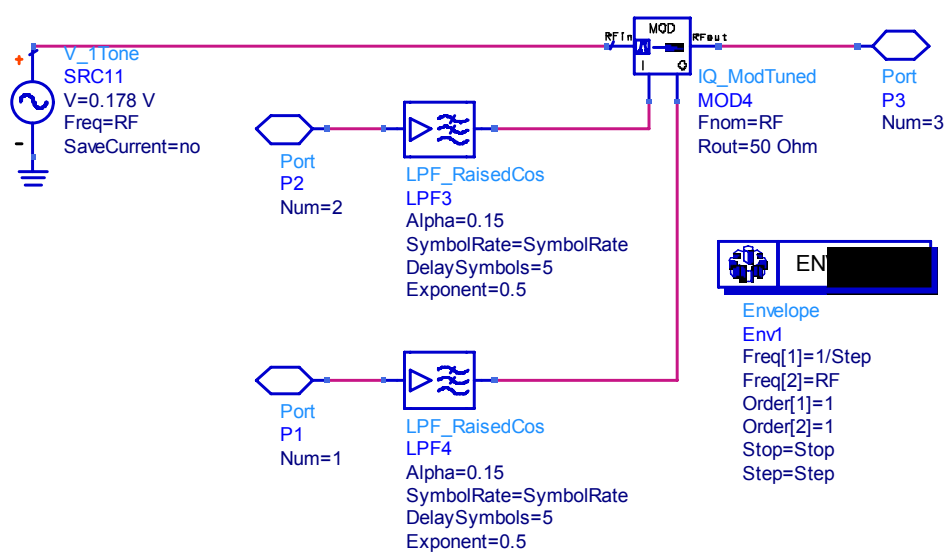


Figure 6-9: ADS analogue sub-circuit for the I/Q modulator

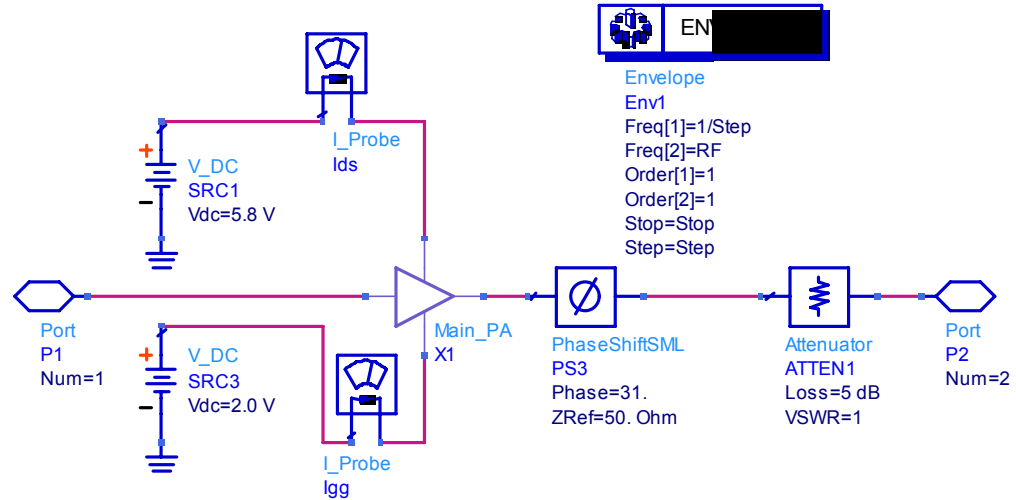


Figure 6-10: ADS analogue sub-circuit for the main PA

The Matlab signal source block diagram is presented in Figure 6-11. It is designed according to the proposed DPD method as described in Sections 6.2.2 and 5.2.3.  $N$  symbols of  $M$ -range are generated for the chosen modulation type. Then, these symbols are mapped to M-QAM with the I and Q components. Examples of the generated digital I and Q signals in the time and frequency domains for the QPSK, 16-QAM and 64-QAM modulation schemes together with the Matlab codes used for generating these signals are presented in Appendix-A. For instance, 16-QAM modulation has  $M=16$  and the range of symbols: 0, 1, 2 ... 15. For the considered 16-QAM modulation, I and Q can take one of the four possible values: -3, -1, 1, 3. Then, the mean value  $U$  of the input signal magnitude is calculated. The I and Q components are multiplied by  $1/U$  for normalisation. This procedure is introduced in order to achieve  $average(I^2 + Q^2) = 1$  and not to affect the mean power level by predistortion. Normalised signals  $I_n$  and  $Q_n$  are subjected to the proposed iterative baseband predistortion (6.26)-(6.28). After that, the signals are filtered with low-pass raised-cosine filters and multiplied by  $U$  for denormalisation. Predistorted  $I_{DPD}$  and  $Q_{DPD}$  are modulated in the IQ modulator. The final signal is transferred to the ADS main circuit for PA distortion simulations.

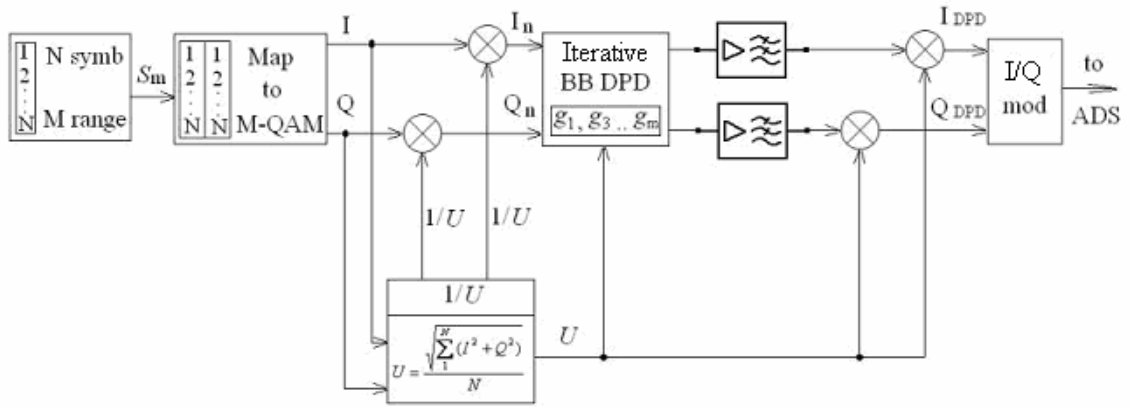


Figure 6-11: Functional diagram for the Matlab signal source

### 6.3.4 Simulation Results for the Proposed Iterative Injection DPD

Initially, the PA instantaneous nonlinear behaviour is investigated. The power amplifier has a 27-dB gain and the 1-dB compression point at 23 dBm output power. Figure 6-12 depicts the gain and output power dependence on the input power level for the considered PA.

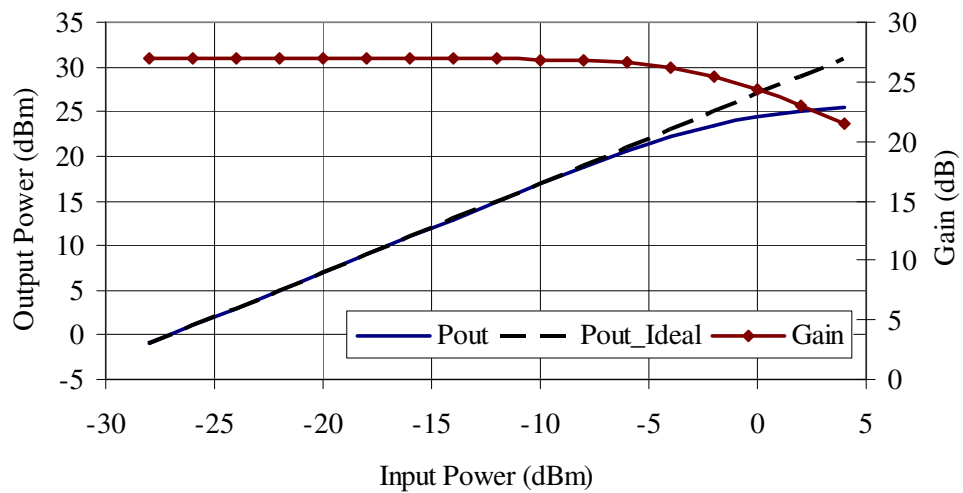


Figure 6-12: Simulated output power and gain versus input power for the considered PA

In order to extract  $g$ -coefficients for the fundamental-frequency model, the least-squares regression method is used. The obtained coefficients are:  $g_1 = 23$ ;  $g_3 = -103$ ;  $g_5 = 211$ . Consequently, the fundamental-frequency model for the PA can be written as:

$$V_{OUT}^{FUND}(t) = 23 \cdot V_{IN}(t) - 77 \cdot |V_S(t)|^2 \cdot V_{IN}(t) + 132 \cdot |V_S(t)|^4 \cdot V_{IN}(t). \quad (6.32)$$

The coefficient of determination for the model (6.32) equals to  $r^2 = 0.9994$ , which indicates a near perfect match. According to the extracted model, the predistorter coefficients are calculated. Firstly, the spectral re-growth suppression performance of the proposed predistorter is investigated for the different number of injections for a single-carrier QPSK, and multi-carrier 256-OFDM 64-QAM WiMAX signals at 3.5 GHz carrier frequency.

Figure 6-13 shows the QPSK spectral re-growths without predistortion and with the proposed iterative DPD using 3 and 6 injections. The simulation has been carried out with a carrier frequency of 3.5 GHz, symbol rate 1726 kHz, and the input power level of -3 dBm. From Figure 6-13 one can observe, that the proposed digital predistortion with 3 injections offers a 20-dB improvement, whereas with the 6-injections DPD, the improvement in spectral re-growth is up to 35 dB.

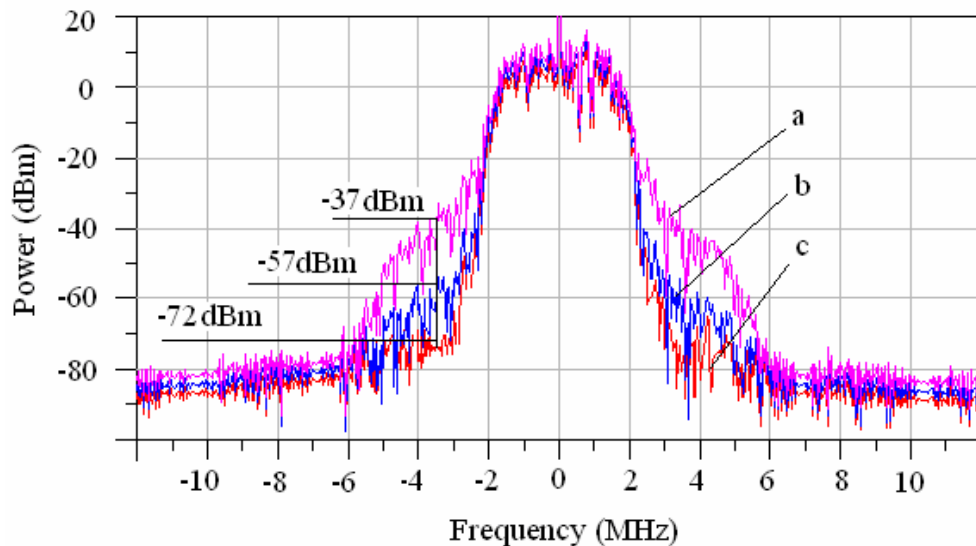


Figure 6-13: Spectral re-growth improvement for a QPSK signal: (a) without DPD; (b) proposed DPD with 3 injections; (c) proposed DPD with 6 injections

Figure 6-14 presents spectral re-growths for the 7-MHz 256-OFDM 64-QAM WiMAX signal at 3.5-GHz carrier without predistortion and with the proposed iterative

DPD using different number of injections. The simulation has been carried out with the input power level equal to -3 dBm. From Figure 6-14 one can observe that the proposed digital predistortion with 1 injection offers a 12-dB improvement in spectral re-growth, whereas the DPD with three and six injections offer a 22-dB and 31-dB improvement respectively.

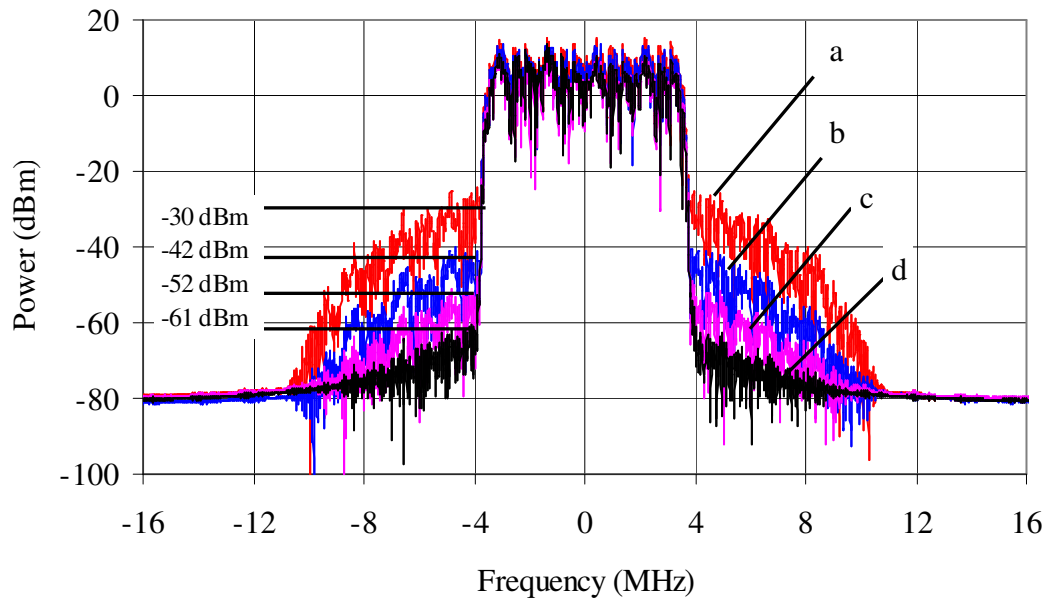


Figure 6-14: Spectral re-growth improvement for a 256-OFDM 64-QAM signal: (a) without DPD; (b) proposed DPD with 1 injection; (c) proposed DPD with 3 injections; (d) proposed DPD with 6 injections

Further, performances of the proposed predistorter with 6 injections are examined for a 7-MHz 256-OFDM 16-QAM WiMAX signal at 3.5 GHz carrier frequency. The spectral re-growth suppression, achieved by the DPD at 0-dBm input power level, is presented in Figure 6-15. The improvement of up to 32 dB can be observed from the Figure.

Sweeping the output power level in the range from -10 dBm to 25 dBm, Adjacent Channel Power Ratio (ACPR) and Error Vector Magnitude (EVM) are simulated. The obtained ACPR results for the 8-MHz lower and upper offsets are presented in Figure 6-16. As can be seen from the Figure, the proposed DPD technique brings up to 22 dB improvements in ACPR.

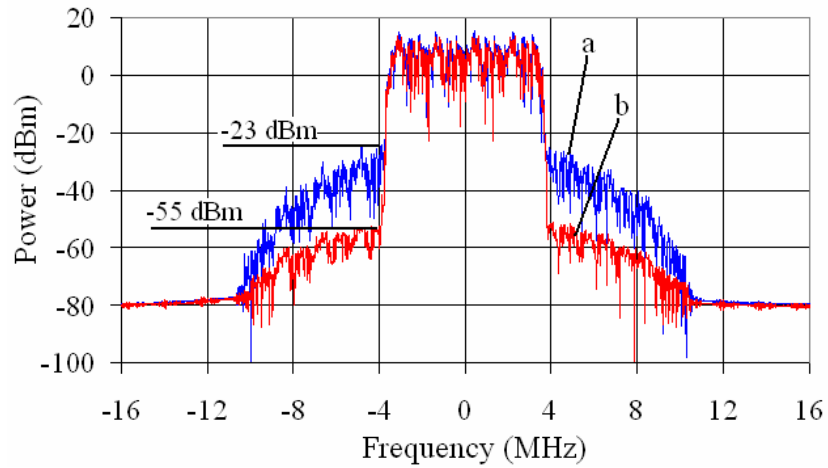


Figure 6-15: Spectral re-growth improvement for a 7-MHz 256-OFDM 16-QAM signal:  
 (a) without DPD; (b) proposed DPD with 6 injections

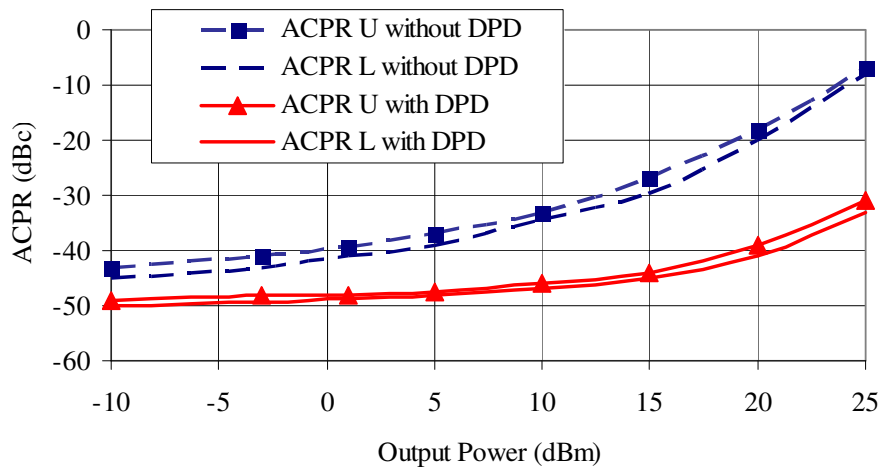


Figure 6-16: ACPR for a 7-MHz 256-OFDM 16-QAM signal at 8-MHz upper and lower offsets without DPD and with the proposed DPD with 6 iterations

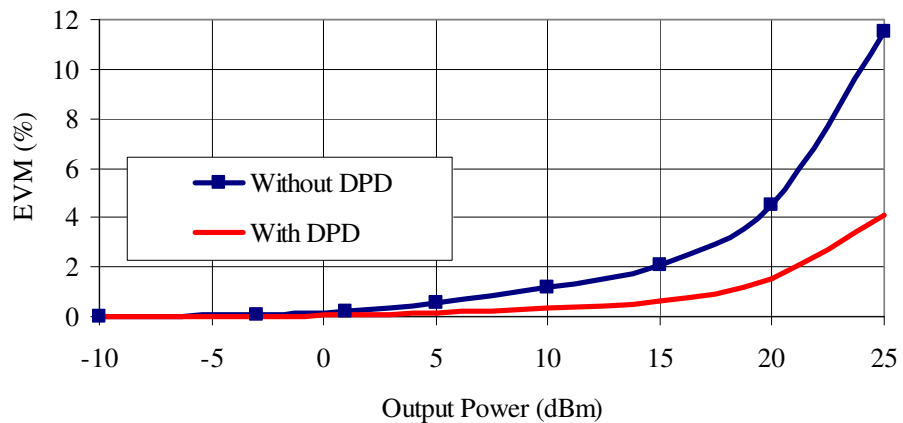


Figure 6-17: EVM verses output power for a 7-MHz 256-OFDM 16-QAM signal without DPD and with the proposed DPD with 6 iterations

Figure 6-17 illustrates the dependence of EVM on output power level for the original PA without predistortion and for the complete DPD system. By taking a closer look at Figures 6-16 and 6-17, a conclusion can be made, that the proposed technique effectively reduces nonlinear distortions for a wide power range. Particularly, the system linearity is significantly increased for high powers, where the PA operates at saturation.

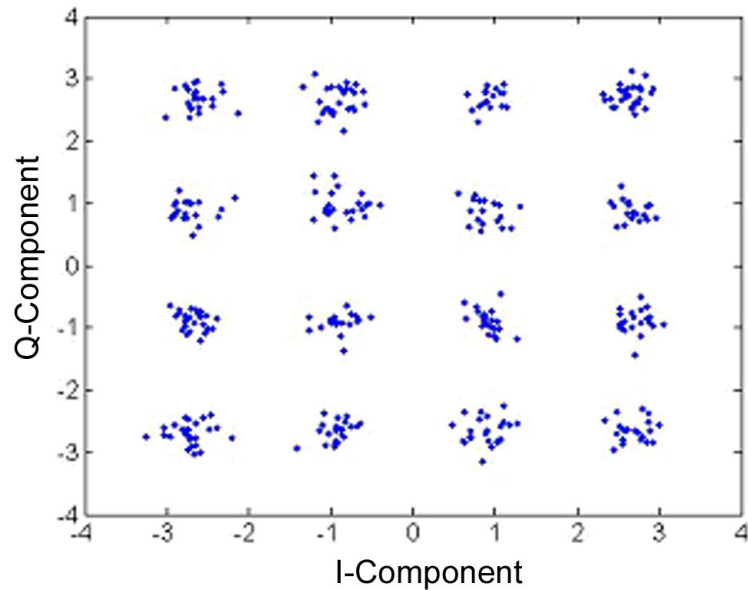


Figure 6-18: Demodulated 16-QAM constellation without DPD ( $P_{in} = -3$  dBm)

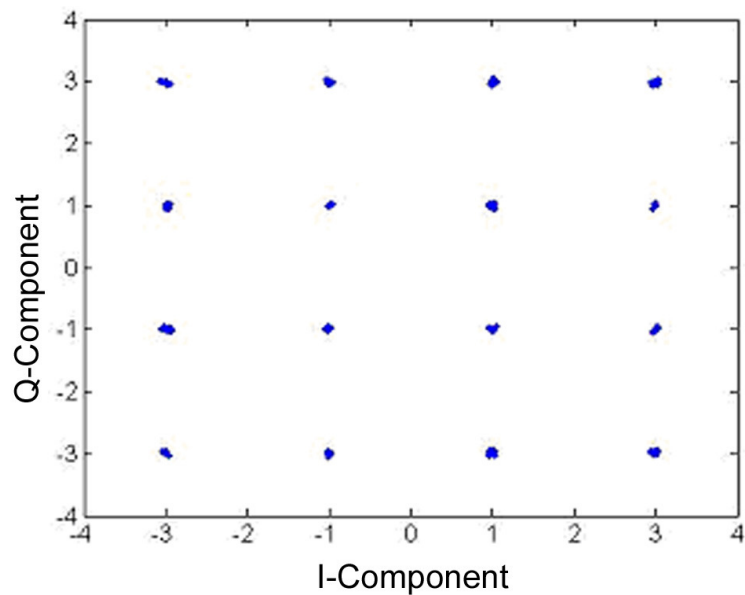


Figure 6-19: Demodulated 16-QAM constellation with 6-iterations DPD ( $P_{in} = -3$  dBm)

Finally, the demodulated constellation diagram is obtained by the Matlab measurement block for the considered system without DPD, as shown in Figure 6-18, and with the proposed iterative DPD using 6 injections, as shown in Figure 6-19. The constellation diagrams are received after passing the PA at -3-dBm input power level. Significant improvements can be observed comparing Figures 6-18 and 6-19.

## **6.4. Experimental Verification and Results**

In order to accomplish experimental verification of the proposed DPD technique, a laboratory test bed has been designed. The test bed includes a Digital Signal Processing (DSP) part realised in a Personal Computer (PC) and a Radio-Frequency (RF) part. The proposed predistorter is implemented in the DSP part. The RF sub-system, which includes the power amplifier, is depicted below in Section 6.4.1. The implemented predistorter operation was described above in Section 6.2.3.

This Section presents the experimental results for the power amplifier Mini-Circuits ZFL-500. The PA is a low-power low-noise wideband amplifier with the gain of 20 dB and the frequency range of 0.05 – 500 MHz intended for the VHF/UHF instrumentation and laboratory applications. The data sheet for the PA is presented in Appendix-B. ZFL-500 has the 1-dB compression point at 9-dBm output power. The PA exhibits symmetrical memory effects, which are quantified below in Section 6.4.2. The experimental investigations are carried out for the input power level of -10 dBm. At this level, the PA exhibits nonlinear behaviour.

The Section depicts the PA characterisation for the purpose of designing the predistorter and presents the experimental results for verifying the DPD linearising performances for QPSK and 16-QAM modulated signals.

### **6.4.1 Hardware Setup**

The experimental setup that was designed for verifying the performances of the proposed [6.1]-[6.4] and conventional [6.5]-[6.7] digital predistortion techniques is shown in Figure 6-20. It consists of a Personal Computer (PC), Electronic Signal Generator (ESG) E4433B, Device Under Test (DUT) and Vector Signal Analyser

(VSA) E4406A. The ESG E4433B has the frequency range of 205 kHz to 4 GHz and the power range of -135 dBm to 7 dBm according to the specification [6.8]. The VSA E4406A has the frequency range of 7 MHz to 314 MHz and 329 MHz to 4 GHz, the frequency span of up to 10 MHz and the maximum measurement input power of up to +30 dBm (1 W) according to the specification [6.9].

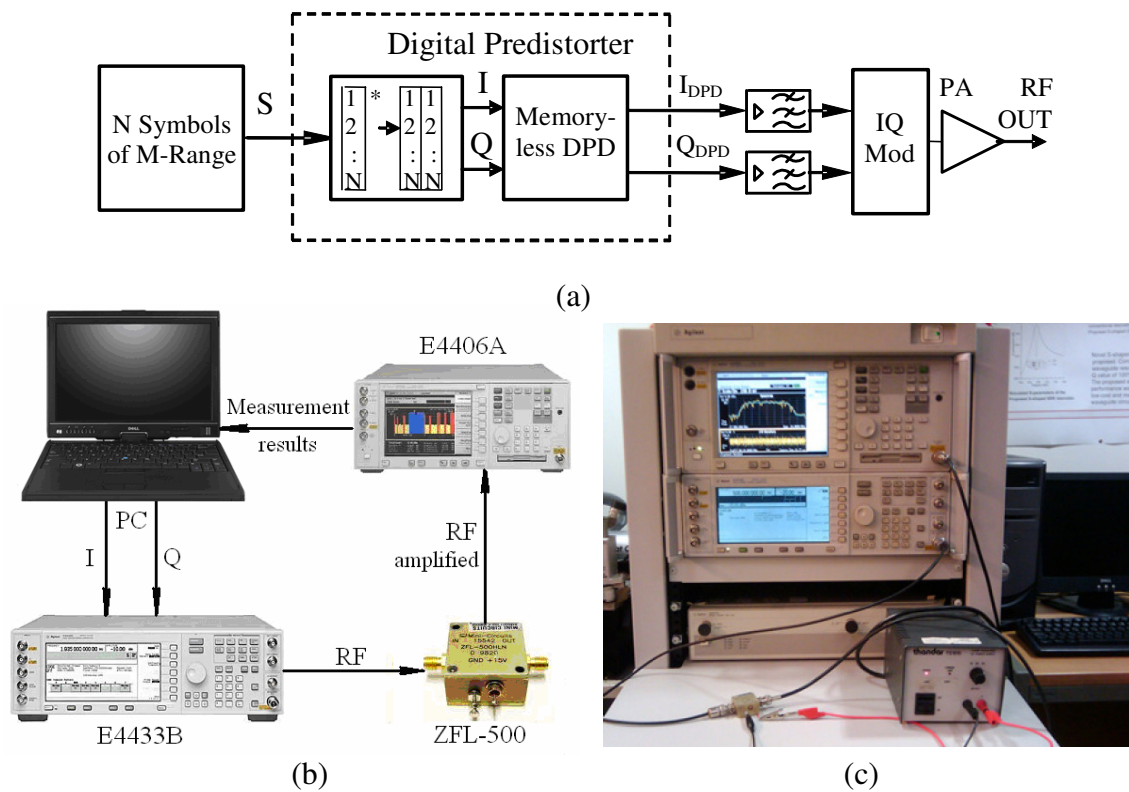


Figure 6-20 Experimental setup for verifying digital predistorters: (a) Functional diagram; (b) Experimental setup; (c) Hardware test-bench

The power amplifier used for the experiments is a 20-dB gain 1-dB compression at 9 dBm output power Mini-Circuits ZFL-500 PA with the frequency range of 0.05 - 500 MHz. In the experimental setup shown in Figure 6-20, the DSP part is implemented in a PC, whereas the RF part is realised in the ESG-DUT-VSA system. The proposed DPD is implemented in Matlab according to the procedure described in Section 6.2.3. The parameters of the predistorter are tuned in order to reflect the nonlinear behaviour of the power amplifier used as the DUT. For this purpose, the PA characterisation is accomplished in order to extract the nonlinear model coefficients. The characterisation results for the considered ZFL-500 amplifier are presented in Sections 6.4.2.

The initial data symbols are generated using a pseudorandom sequence PN9 and mapped to the chosen modulation scheme, as shown in Figure 6-20 (a). The pseudorandom sequence PN9 used in the experiments consists of 512 bits, which are presented in Appendix-C in the binary and hexadecimal formats. The sequence is pre-programmed in the ESG (E4433B) and used for representing the signal source binary data during experiments. The mapping schemes for the QPSK and 16-QAM modulation are given in Appendix-C.

The obtained complex signal is further divided into I and Q components and subjected to the proposed digital predistortion by the “Memoryless DPD” block, which realises the proposed distortion components iterative injection DPD technique described in Section 6.2.2. The mean value  $V$  of the input signal magnitude is calculated.  $I$  and  $Q$  are multiplied by  $1/V$  for normalisation. This procedure is performed in order to achieve  $average(I^2(t) + Q^2(t)) = 1$  and not to affect the mean power level by predistortion. The normalised signals  $I^{norm}$  and  $Q^{norm}$  are subjected to the proposed DPD, as described in Sections 6.2.2-6.2.3. After that, the signals are multiplied by  $V$  for de-normalisation.

The predistorted I and Q signals are uploaded into the ESG (E4433B), which executes the operations of Digital-to-Analogue Converting (DAC) and modulating. The modulated RF signal from the output of the signal generator is passed through the DUT and transferred to the VSA (E4406A) for measurements. The measurement results are downloaded to the PC for comparison and analysis.

## 6.4.2 PA Characterisation

In order to compensate for the PA nonlinear behaviour and memory effects by the proposed DPD technique, the amplifier needs to be characterised. This includes measuring its transfer function and frequency-dependent performances. The former is used to extract the polynomial  $g$ -coefficients for the memoryless part of the predistorter. The latter is exploited for obtaining the frequency-response coefficients if pre-equalisation of memory effects is necessary for the PA.

For measuring the nonlinear transfer function of the considered 20-dB gain 1-dB compression point at 9-dBm output power PA ZFL-500, an RF tone at 500 MHz frequency is generated by the ESG E4433B with the power varying in the range of -30...-3 dBm. The signal is passed through the PA and captured in the VSA E4406A,

where the output signal power is measured. The variations of output power and gain versus input power are presented in Figure 6-21.

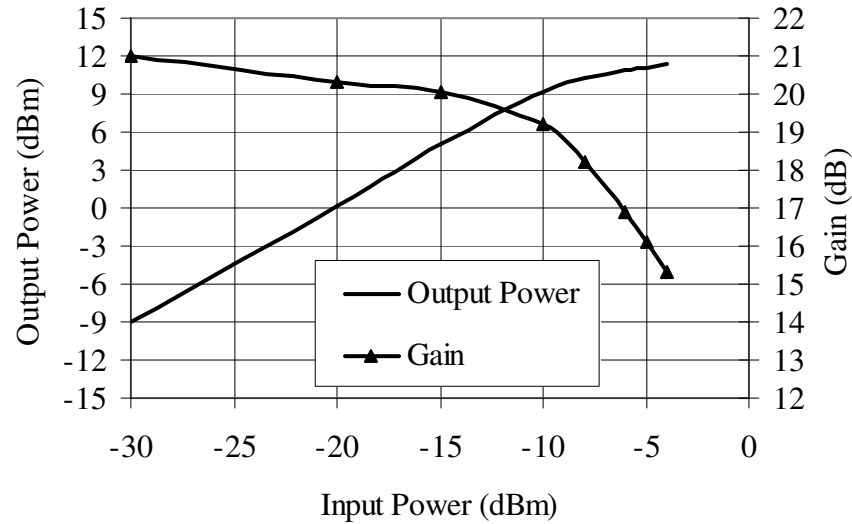


Figure 6-21: Measured output power and gain versus input power for the considered PA

The measured transfer characteristic for ZFL-500 is processed for extracting  $g$ -coefficients of the PA polynomial model, as described in Section 5.3. The dependence of the output voltage on the input voltage is obtained from the measured results, as shown in Figure 5-11. Then, using the frequency-response and Least-Squares Regression (LSR) methods, the PA model is extracted. As the operational input power is chosen to -10 dBm, the order of the polynomial model must correspond to the number of harmonics appearing at the PA output at this power level. By taking a closer look at the PA frequency response at -10 dBm input power, presented in Table 5.2, one can see the number of generated harmonics equals to five. Therefore, the polynomial model is sought in the form:

$$V_{OUT}^{FUND}(t) = g_1 \cdot V_{IN}(t) + \left[ \sum_{k=1}^N b_{2k+1} g_{2k+1} V_S^{2k} \right] \cdot V_{IN}(t), \quad (6.33)$$

where  $N=2$ ; and  $b_3=3/4$ ,  $b_5=5/8$  are determined by Table 5.1.

From the measured transfer characteristic, the odd-order  $g$ -coefficients are calculated using the LSR method:  $g_1 = 10.7$ ;  $g_3 = -251.7$ ;  $g_5 = 2633.4$ . Therefore, the fundamental-frequency polynomial model extracted from the instantaneous nonlinear behaviour of the power amplifier can be written as:

$$V_{OUT}^{FUND}(t) = 10.7 \cdot V_{IN}(t) - 189 \cdot |V_S(t)|^2 \cdot V_{IN}(t) + 1646 \cdot |V_S(t)|^4 \cdot V_{IN}(t). \quad (6.34)$$

The accuracy of the model (6.33) can be verified by comparing the measured and modelled transfer characteristics plotted in Figure 5-11 and by calculating the coefficient of determination  $r^2$ , used to judge the quality of fit of a model to the measured data. The coefficient of determination for the model (6.33) equals to  $r^2 = 0.99$ , which indicates very high quality of fit.

In order to quantify memory effects of the considered PA ZFL-500 at the operational power level, the gain and 3<sup>rd</sup>-order intermodulation distortion (IM3) dependences on modulation frequency are measured. A two-tone test is used for measuring IM3. The unmodulated RF signals are placed around the centre frequency of  $f_{RF} = 500$  MHz with the tone spacing varying in the range of  $f_{spacing} = 10$  kHz...10 MHz. The measured gain and IM3 frequency-dependent characteristics at the input power level of -10 dBm are presented in Figures 6-22 and 6-23 respectively.

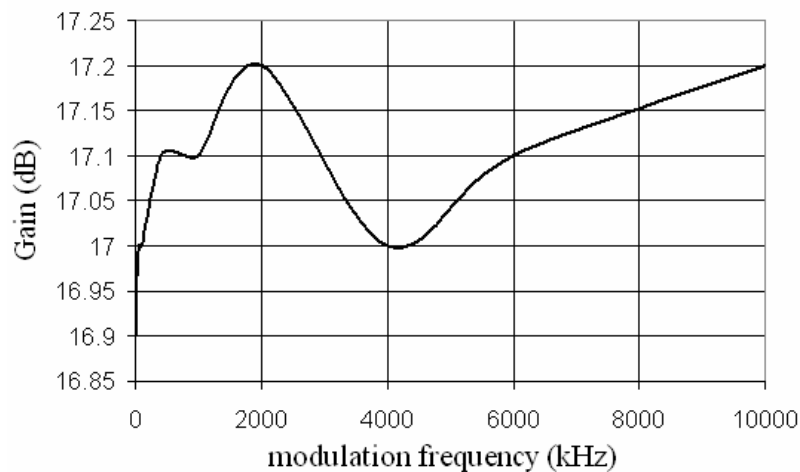


Figure 6-22: Measured gain of the PA (ZFL-500) at the input power level of -10 dBm

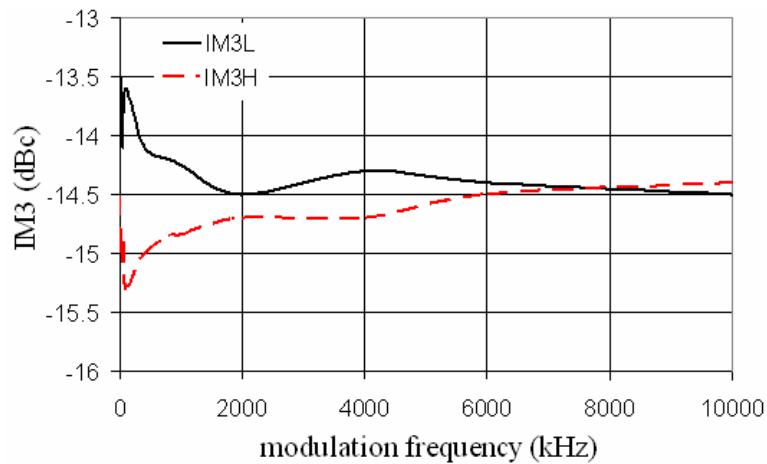


Figure 6-23: Measured IM3 of the PA at the input power level of -10 dBm

As can be observed from the Figures, the PA reveals low variations of the gain versus modulation frequency and a symmetrical distortion of the lower and higher intermodulation products (IM3L and IM3H). The measured gain and IM3 magnitude versus modulation frequency and output power and presented in Figures 6-24 and 6-25 respectively. Consequently, the considered PA ZFL-500 exhibits low symmetrical memory effects, which will not be considered for linearisation.

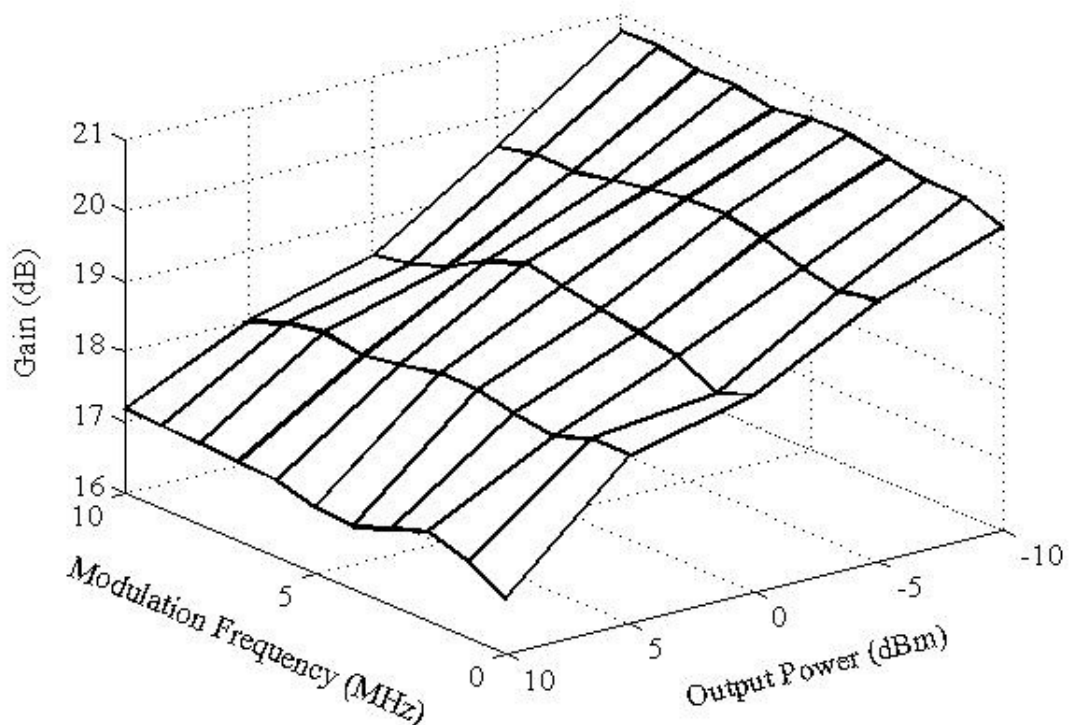


Figure 6-24: Measured gain characteristic of the PA ZFL-500 versus output power and modulation frequency

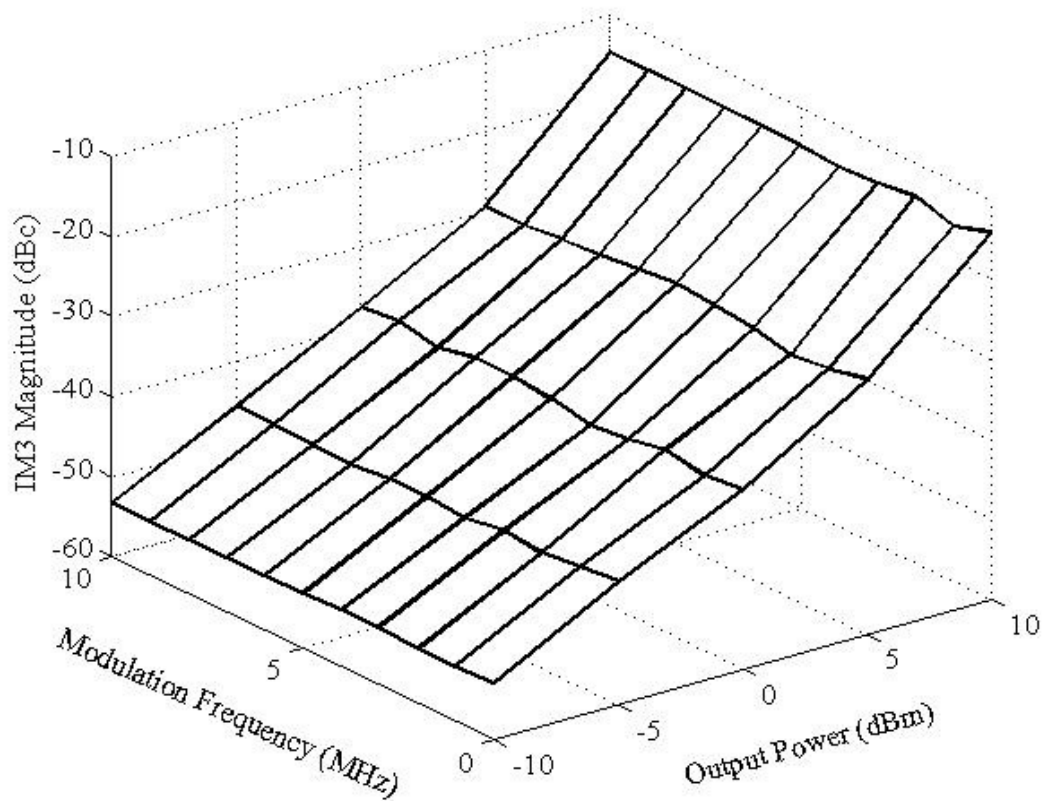


Figure 6-25: Measured IM3 characteristic of the PA ZFL-500 versus output power and modulation frequency

### 6.4.3 5-MHz QPSK Signal Case

For verifying the performances of the proposed [6.1]-[6.4] and conventional [6.5]-[6.7] DPD with a digitally modulated signal, a 5-MHz QPSK signal at -10 dBm input power level is used. As the QPSK modulation scheme includes one baseband power level, the magnitudes of I and Q signals are  $mag(I) = mag(Q) = 0.7071$  V, and the magnitude of the baseband voltage equals to 1 V.

The laboratory experiments are carried out using the test bed presented in Figure 6-20, where the proposed predistorter is implemented in Matlab according to the configuration shown in Figure 6-1. Initially, 512 bits of the PN9 sequence (see Appendix-C) are generated. The symbols are mapped to QPSK with I and Q levels of  $\pm 0.7071$  V. Further, the complex signal is split into I and Q components and subjected to the memoryless predistortion.

From the nonlinear model (6.2), the magnitude factors of the distortion components are calculated for the first injection as:  $G_3(t) = -189 \cdot |V_s(t)|^2$ ,  $G_5(t) = 1646 \cdot |V_s(t)|^4$ . Three iterations of the input signal predistortion are performed. The injected distortion-components' magnitude factors are updated for the 2<sup>nd</sup> iteration as:

$$G_3^{(1)}(t) = -189 \cdot |V_s(t)|^2 \cdot \left(-1 + \left(1 - \frac{-189 \cdot |V_s(t)|^2 + 1646 \cdot |V_s(t)|^4}{10.7}\right)^3\right), \quad (6.35)$$

$$G_5^{(1)}(t) = 1646 \cdot |V_s(t)|^4 \cdot \left(-1 + \left(1 - \frac{-189 \cdot |V_s(t)|^2 + 1646 \cdot |V_s(t)|^4}{10.7}\right)^5\right). \quad (6.36)$$

Further, for the 3<sup>rd</sup> iteration, the corresponding values of  $G_3^{(2)}(t)$  and  $G_5^{(2)}(t)$  are calculated as:

$$G_3^{(2)}(t) = G_3^{(1)}(t) \cdot \left(-1 + \left(1 - \frac{G_3^{(1)}(t) + G_5^{(1)}(t)}{10.7}\right)^3\right), \quad (6.37)$$

$$G_5^{(2)}(t) = G_5^{(1)}(t) \cdot \left(-1 + \left(1 - \frac{G_3^{(1)}(t) + G_5^{(1)}(t)}{10.7}\right)^5\right). \quad (6.38)$$

The updated distortion components are injected into the original in-phase and quadrature signals according to the proposed memoryless DPD as:

$$I_{DPD}^{(3)}(t) = I(t) - \frac{G_3^{(2)}(t) + G_5^{(2)}(t)}{10.7} \cdot I(t), \quad (6.39)$$

$$Q_{DPD}^{(3)}(t) = Q(t) - \frac{G_3^{(2)}(t) + G_5^{(2)}(t)}{10.7} \cdot Q(t). \quad (6.40)$$

The predistorted signals  $I_{DPD}$  and  $Q_{DPD}$  are transferred into the memory of the waveform generator Agilent E4433B and used for generating a 5-MHz QPSK-modulated RF signal at 500 MHz carrier. The obtained RF signal is passed through the PA and further transferred to the VSA for measurements.

The computational complexity of the designed predistorter includes the stored coefficients and mathematical operations necessary for the nonlinear memoryless compensating part of the lineariser. According to Table 6.1, for the 5<sup>th</sup>-order polynomial model and 3 injections, the number of required for the memoryless DPD coefficients equals to 6, whereas the number of real multiplications and additions equals to 25 and 14 respectively.

The measured spectra regrowth at the output of the power amplifier without DPD (a) and with the proposed DPD including three injections of the baseband distortion components (b) are presented in Figure 6-26. The spectra regrowth suppression improvement of up to 23 dB for a 5-MHz QPSK signal can be observed. Figure 6-27 shows the measured lower and upper ACPRs at the offset frequencies of 7 MHz without and with the proposed DPD. Both the ACPRs without predistortion are -15 dBc at 10 dBm output power, whereas the ACPRs for the case of using the proposed technique are -30 dBc at the same level. Therefore, an improvement of 15 dB is achieved by using the proposed baseband components iterative injection DPD.

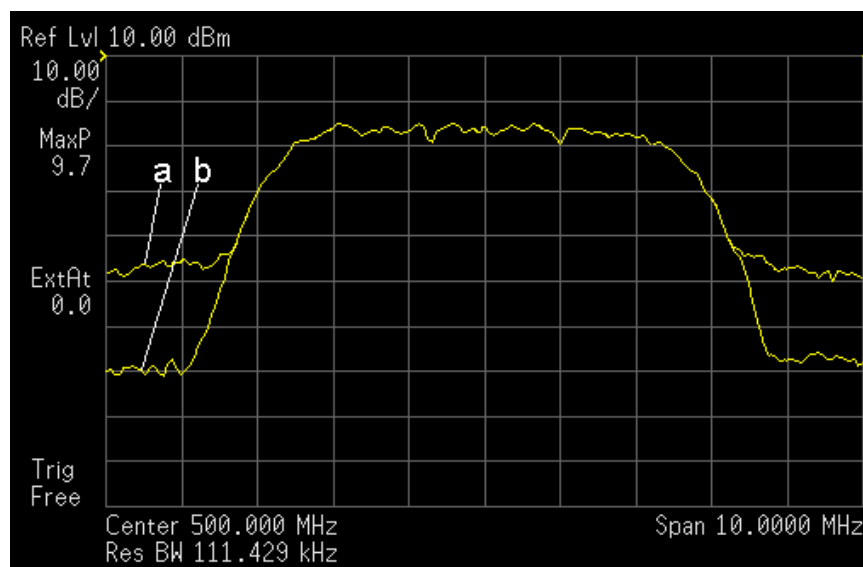


Figure 6-26. Measured output spectra of a 5-MHz QPSK signal at the output of the PA ZFL-500: (a) without DPD; (b) with the proposed DPD using 3 injections

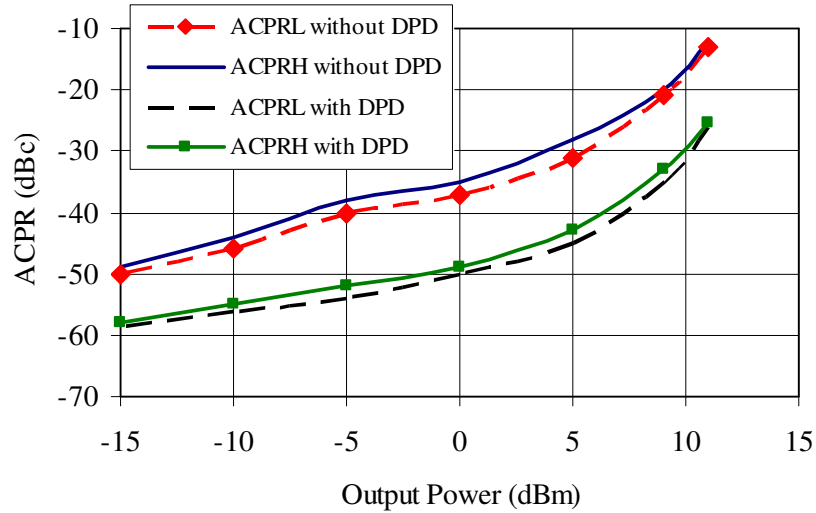


Figure 6-27. Measured ACPRs for 7-MHz offsets of a 5-MHz QPSK signal at the output of the PA ZFL-500 without DPD and with the proposed DPD using 3 injections

#### 6.4.4 3.5-MHz 16-QAM Signal Case

In this Section, the performances of the proposed predistorter [6.1]-[6.4] are verified and compared to the conventional distortion component injection DPD [6.5]-[6.7] using a 3.5-MHz 16-QAM digitally modulated signal with -10 dBm input power level. The 16-QAM modulation scheme includes three baseband power levels, as shown in Appendix-C. The baseband voltage and power levels for the considered signal are presented in Table 6.2.

**TABLE 6.2:** Voltage and power levels for the experiment

| $mag(I)$ , V | $mag(Q)$ , V | $mag(V_{BB})$ , V | $P_{BB}$ , dBm | $mag(V_{IN})$ , V | $P_{IN}$ , dBm |
|--------------|--------------|-------------------|----------------|-------------------|----------------|
| 0.32         | 0.32         | 0.45              | 3.12           | 0.05              | -16.88         |
| 0.32         | 0.96         | 1.01              | 10.11          | 0.10              | -9.89          |
| 0.96         | 0.96         | 1.36              | 12.66          | 0.14              | -7.34          |

$P_{LO} = -10$  dBm;  $V_{LO} = 0.1$  V

Using the test bed presented in Figure 6-20, the laboratory experiments are carried out for the proposed predistorter [6.1]-[6.4] designed according to the configuration depicted in Figure 6-1 and the conventional DPD incorporating the injection of the third- and fifth-order baseband distortion components [6.5]. 512 bits of the PN9 sequence (see Appendix-C) are generated and mapped to 16-QAM with I and Q levels of  $\pm 0.3203$  V and  $\pm 0.9608$  V. Further, the complex signal is split into I and Q components and subjected to the memoryless predistortion.

From the nonlinear model (6.34), the magnitude factors of the distortion components for the first injection are calculated as:  $G_3(t) = -189 \cdot |V_s(t)|^2$ ,  $G_5(t) = 1646 \cdot |V_s(t)|^4$ . Two iterations of the input signal predistortion are performed. The injected distortion-components' magnitude factors are updated for the 2<sup>nd</sup> iteration according to (6.35) and (6.36). Further, the obtained distortion components are injected into the original in-phase and quadrature signals according to the proposed memoryless DPD as:

$$I_{DPD}^{(2)}(t) = I(t) - \frac{G_3^{(1)}(t) + G_5^{(1)}(t)}{10.7} \cdot I(t), \quad (6.41)$$

$$Q_{DPD}^{(2)}(t) = Q(t) - \frac{G_3^{(1)}(t) + G_5^{(1)}(t)}{10.7} \cdot Q(t). \quad (6.42)$$

The predistorted signals  $I_{DPD}$  and  $Q_{DPD}$  are transferred into the memory of the waveform generator Agilent E4433B and used for generating a 3.5-MHz 16-QAM-modulated RF signal at 500 MHz carrier. The obtained RF signal is passed through the PA and further transferred to the VSA for measurements.

The computational complexity of the designed predistorter includes the stored coefficients and mathematical operations necessary for the nonlinear memoryless part of the lineariser. According to Table 6.1, for the 5<sup>th</sup>-order polynomial model and 2 injections, the number of required for the memoryless DPD coefficients equals to 6, whereas the number of real multiplications and additions equals to 17 and 8 respectively.

The measured spectra regrowth results at the output of the power amplifier ZFL-500 without DPD (a), with the conventional DPD (b), and with the proposed DPD (c) are presented in Figure 6-28. An improvement of up to 18 dB is achieved by the proposed DPD method with 2 injections, whereas a 12-dB improvement is obtained by the

conventional DPD method. Figure 6-29 shows the measured lower and upper ACPRs at the offset frequencies of 5 MHz without and with the proposed DPD. Both the ACPRs without predistortion approach -18 dBc at 12 dBm output power, whereas using the proposed technique, the ACPRs of up to -32 dBc are achieved at the same level. Therefore, an improvement of up to 14 dB is obtained by using the proposed baseband DPD method.

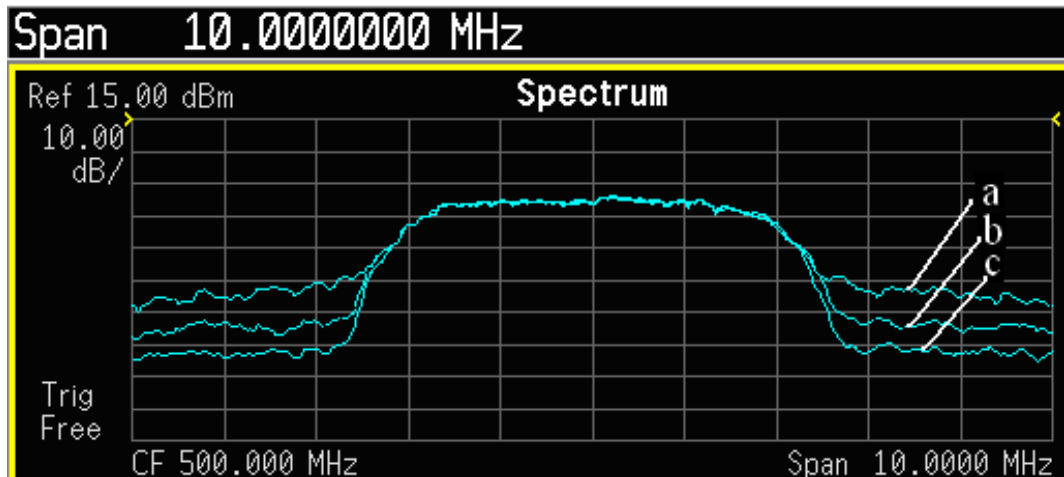


Figure 6-28. Measured output spectra of a 3.5-MHz 16-QAM signal at the output of the PA ZFL-500: (a) without DPD; (b) conventional baseband DPD; (c) proposed baseband DPD using 2 injections

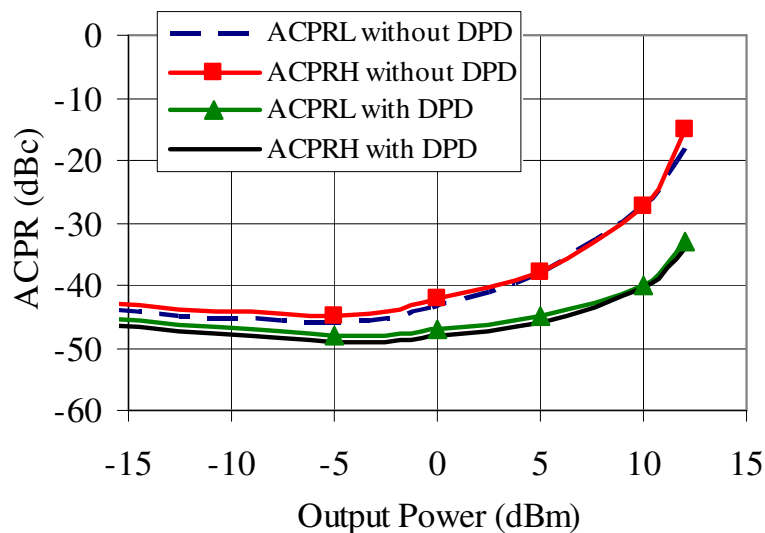


Figure 6-29. Measured ACPRs for 5-MHz offsets of a 3.5-MHz 16-QAM signal at the output of the PA ZFL-500 without DPD and with the proposed DPD using 2 injections

## 6.5. Conclusion

The proposed adjustable digital predistortion technique for linearising wireless transmitters incorporating the distortion components iterative injection method has been presented and verified by simulations and experimentally. The proposed solutions to the problems of linearisation of wireless transmitters depicted in the Chapter can be summarised as follows.

The distortion components iterative injection technique with adjustable ratio of linearisation degree to computational complexity was developed for the memoryless linearisation. The proposed memoryless DPD allows overcoming the distortion compensation limit particular to the injection techniques. The theoretical concept and practical operation of the proposed method were presented in the Chapter. The computational complexity and simulated performances were discussed. The proposed digital predistortion technique is adjustable for achieving the best ratio of linearisation degree to computational complexity for any particular application.

Advanced Matlab-ADS co-simulation system was developed for simultaneous simulations of the DSP and RF parts of the transmitter. The co-simulation system can be configured according to different layouts depending on simulation requirements. The proposed DPD was verified by simulations with QPSK, 16-QAM, 64-QAM, 256-OFDM 64-QAM and 256-OFDM 16-QAM signals. The results demonstrated high linearising performances and adjustability of the proposed DPD technique.

The feasibility of the proposed linearising technique was verified experimentally. The in-band distortion modelling method developed during the research work for calculating the predistorter parameters was experimentally proven to be accurate and convenient in practical use. The proposed distortion component iterative injection method demonstrated high linearising performances while tested with different types of signals and number of injections. The measured results proved the proposed distortion component iterative injection method offered significant improvements in the linearising performances with a reasonably low computational complexity compared to those of the conventional DPD. The tunability of the proposed technique was demonstrated during the experiments.

## 6.6. References

- [6.1] D. Bondar, and D. Budimir, "A new digital predistortion for linearity improvement and suppression of memory effects", in *Proc. European Microwave Week Conference EMW'09*, Roma, Italy, September 2009.
- [6.2] D. Bondar, and D. Budimir, "A Digital Predistorter for Wireless Transmitters", *International Journal of RF and Microwave Computer-Aided Engineering*, 2009 (accepted for publication).
- [6.3] D. Bondar, and D. Budimir, "Digital baseband predistortion of wideband power amplifiers with improved memory effects", in *Proc. IEEE Radio and Wireless Symposium RWS'09*, San-Diego, USA, pp. 284-287, January 2009.
- [6.4] D. Bondar, and D. Budimir, "Digital baseband components injection technique to enhance linearity in wideband wireless transmitters," *IEEE Transactions on Microwave Theory and Techniques*, Submitted.
- [6.5] N. Mizusawa, and S. Kusunoki, "Third- and fifth-order baseband component injection for linearisation of the power amplifier in a cellular phone," *IEEE Transactions on Microwave Theory and Techniques*, vol. 53, no. 4, pp. 3327-3334, Apr. 2005.
- [6.6] D. Bondar, and D. Budimir, "WiMax power amplifier linearization through injection of base-band components," in *Proc. 11<sup>th</sup> Int. Symp. Microw. Opt. Technol.*, Roma, Italy, pp. 293-297, Dec. 2007.
- [6.7] D. Bondar, D. Budimir, and B. Shelkovnikov, "Linearization of power amplifiers by baseband digital predistortion for OFDM transmitters," in *Proc. 18<sup>th</sup> Int. Crimean Conf. Microw. and Telecommun. Technology*, Sebastopol, Ukraine, vol. 1, pp. 270-271, Sept. 2008.
- [6.8] Agilent Technologies ESG family signal generators E4400-90323: User's Guide, April 2002.
- [6.9] Agilent Technologies E4406A VSA series transmitter tester: User's Guide, May 2007.

---

## 7. DIGITAL PREDISTORTION OF POWER AMPLIFIERS WITH IMPROVED MEMORY EFFECTS

### 7.1. Introduction

In the previous Chapter, the proposed memoryless DPD system with adjustable ratio of linearisation degree to computational complexity and enhanced linearising performances was described. However, as discussed in Chapter 4, memory effects may be present in real PAs, which often degrade the performances of linearisers. For this reason, a circuit able to compensate for the PA memory effects should be added to the proposed predistorter. In this Chapter, a DSP-based memory effects compensating technique is developed for the use in the proposed DPD system. The overall lineariser is intended for implementation as a Wiener or Hammerstein structure.

Moreover, in order to provide a possibility of adaptive realisation of the proposed predistorter, a close-loop version of the proposed predistorter is designed incorporating a feedback training scheme. An adaptive implementation of the DPD system would enable an automatic adjustment to environmental changes, such as temperature variations, sample deviations, or active device aging.

The Chapter includes a description of the developed baseband equalisation technique for compensating memory effects, simulation setup and results for verifying the memory-compensating method, adaptation procedure using an off-line training scheme, and experimental setup and results for verifying performances of the overall DPD system incorporating the proposed iterative injection memoryless predistorter and baseband equaliser for minimising memory effects.

The Chapter is structured as follows. The first part of this Chapter depicts a baseband equalisation method developed for minimising PA memory effects by digitally processing the baseband signal, which increases the linearising performance of the proposed DPD system and makes it suitable for wideband single- carrier and multi-carrier applications, such as UMTS and WiMAX. The main advantage of the proposed baseband equalisation technique compared to the conventional digital filtering is its simpler procedures of calculating and optimising the equaliser coefficients, which are

extracted directly from the gain and phase curves avoiding recursive algorithms. This results in a faster operation and lower circuit complexity.

Secondly, the baseband equaliser is verified by simulations using the developed Matlab-ADS co-simulation test bench. The simulations are carried out with a 12-dB gain 1-dB compression point at 25 dBm output power amplifier based on a MOSFET active device MRF9742. The PA exhibits memory effects. Its characterisation and the equaliser coefficients' extraction are demonstrated in the Chapter. The proposed equalisation algorithm is implemented in Matlab and used for pre-compensating the PA frequency-dependent behaviour.

Then, the adaptation procedure using an offline training scheme is depicted in the Chapter. The adaptive close-loop implementation of the proposed DPD system including memoryless linearisation and compensating of memory effects is presented and discussed.

Finally, this Chapter presents experimental setup and results for verifying performances of the complete predistorter, including the proposed solutions for compensating nonlinear distortions and memory effects. The experimental investigations are carried out for a wideband power amplifier Mini-Circuits ZHL-1042J excited with different types of signals. The PA is driven into saturation while the performances without and with the proposed predistortion are investigated. Different scenarios of the test signals are considered. Particularly, the experimental investigations are carried out for a 5-MHz WCDMA system at 2.1-GHz, and for a 5-MHz 16-QAM modulated signal at 3.5-GHz. The measured results verify the feasibility of the proposed predistortion and demonstrate improvements in the linearising performance compared to the conventional DPD.

## **7.2. Baseband Equalisation Technique for Compensating Memory Effects**

This Section presents the developed method for compensating frequency-dependent distortion behaviour of power amplifiers using adaptive equalisation of the baseband input signal. The equalisation method aims at enhancing the linearising performance of the conventional baseband DPD by minimising memory effects. The developed

technique incorporates multiplying discrete frequency points of the input signal by the equaliser coefficients, which are calculated from the inverse frequency response of the PA. Such an approach allows overcoming potential stability problems inherent in the IIR filters and coefficient identification complexity as well as adaptation difficulty typical for the FIR filters. Firstly, the proposed compensation algorithm is described mathematically. After that, the equaliser operation and the computational complexity are analysed for a general implementation design and for a simplified layout used in OFDM systems. Finally, the feasibility of the proposed method for compensating memory effects is verified by simulations using the developed Matlab-ADS co-simulation system.

### 7.2.1 Developed Compensation Algorithm

The frequency-dependent behaviour of a PA can be represented as a filter with the complex frequency response  $H(f, P_{IN})$ , which is dependent on the input power level, because, in general, variations of the PA transfer function are different at different powers. This behaviour is a direct consequence of memory effects described in Chapter 4. The method for compensating frequency-dependent behaviour considered in this Section is based on the idea of equalising the PA frequency response by means of multiplying the discrete frequency points of the input baseband signal with the inverse discrete frequency points of the frequency response  $H(f_k, P_{bb})$ .

Initially, the PA frequency-dependent transfer function needs to be analysed at the operating power level, in order to determine the optimal number of frequency points. For an OFDM signal, the procedure is simplified, as the number of frequency points is determined by the IFFT size. Thus, for a 256-OFDM 64-QAM WiMAX signal, the number of frequency points equals to 256.

There are several challenges in this approach, which need to be solved before implementing this method to a particular amplification system. First of all, the PA frequency response should be normalised, in order not to affect the mean power level. Secondly, to make the equalisation system adaptive to the baseband power level, the frequency response of the filter at all possible baseband power levels should be calculated and stored in an index table. Then, the frequency response coefficients

corresponding to the input power level will be taken from the index table for pre-compensation.

Assuming that memory effects and nonlinear behaviour can be compensated separately [7.1], [7.5], the values of  $H(f_k, P_{bb})$  are identified and stored as a matrix, where each column defines the frequency point and each row determines the baseband power level:

$$H(f_k, P_{bb}) = \begin{bmatrix} h(f_1, P_1) & h(f_2, P_1) & \dots & h(f_N, P_1) \\ h(f_1, P_2) & h(f_2, P_2) & \dots & h(f_N, P_2) \\ \vdots & \vdots & \vdots & \vdots \\ h(f_1, P_M) & h(f_2, P_M) & \dots & h(f_N, P_M) \end{bmatrix}, \quad (7.1)$$

where  $N$  is the number of frequency points and  $M$  is the number of power levels.

The number of the baseband power levels is determined by the modulation type used. Indeed, for a QPSK signal, the baseband amplitude level is constant, as the in-phase  $I(t)$  and quadrature  $Q(t)$  signals can take only +1 or -1 values. In the case of 16-QAM, there are four possible levels of the  $I(t)$  and  $Q(t)$  signals: -3, -1, 1, 3. As the baseband power level is proportional to  $I^2(t) + Q^2(t)$ , it can take one of three possible values corresponding to:  $1^2 + 1^2$ ,  $3^2 + 1^2$  and  $3^2 + 3^2$ . For the case of 64-QAM, there are eight levels for the  $I(t)$  and  $Q(t)$  signals and, therefore, ten possible values for the input power. For those values, the frequency response of the filter needs to be measured and tabulated.

Then, the input baseband signal is subjected to  $N$ -point Discrete Fourier Transform (DFT) operation:

$$S_F(k) = \sum_{n=1}^N S_T(n) \cdot e^{-j\frac{2\pi}{N}kn}, \quad (7.2)$$

where  $S_F(k)$  are the discrete frequency points of the input signal corresponding to the baseband signal samples  $S_T(n)$ .

After that, the obtained input baseband signal frequency points are multiplied with the corresponding values of  $H(f_k, P_{bb})$ , and the Inverse Discrete Fourier Transform (IDFT) operation is carried out:

$$S_T^1(n) = \frac{1}{N} \sum_{k=1}^N S_F(k) \cdot \frac{1}{H(f_k, P_{bb})} \cdot e^{j\frac{2\pi}{N}kn}. \quad (7.3)$$

The block diagram for the described baseband equalisation method is shown in Figure 7-1. As can be seen from the Figure, the equalisation is accomplished by

multiplying the DFT points of the input digital baseband signal by the corresponding value of  $1/H(f_k, P_{bb})$ . These values are initially measured for each power level and stored in a table. In order not to affect the mean power level,  $H(f_k, P_{bb})$  is normalised. To make the equalisation system adaptive to the input power level, the frequency response values at all possible power levels are extracted a priori.

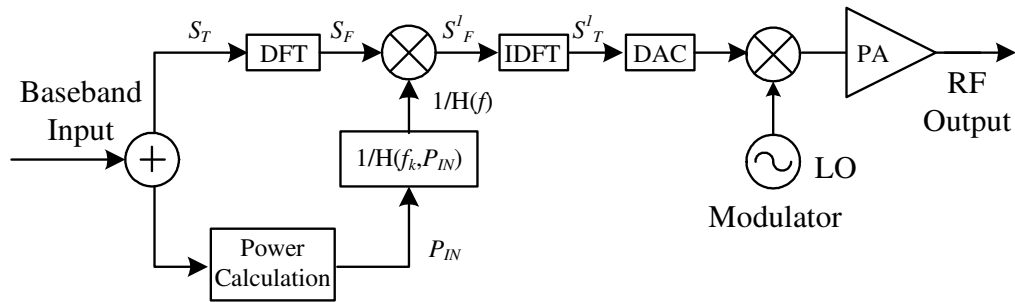


Figure 7-1: Block diagram of the developed baseband equalisation method

After performing the equalisation procedure, the predistorted signal is subjected to the IDFT, converted to the analogue form in the Digital to Analogue Converter (DAC), modulated and passed to the PA.

Extracting the frequency response values  $H(f_k, P_{bb})$  can be accomplished from the S-parameters of the power amplifier.  $S_{12}$  can be measured by a Performance Network Analyser (PNA). Alternatively, the training of the equaliser can be realised by exiting the PA with a tone signal at the frequency swept over the operational band and measuring the amplitude and phase of the output signal. In the same way, a real-time adaptation circuit can be implemented, which generates the input tone signal with the corresponding frequency and power level and measures the amplitude and phase of the output signal for updating the  $H(f_k, P_{bb})$  coefficients.

### 7.2.2 Implementation and Computational Complexity

The proposed baseband equaliser incorporates multiplying of the DFT samples of the input signal by the normalised inverse PA frequency response coefficients in the frequency domain. Generally, the procedure requires executing N-points DFT and IDFT procedures together with the multiplication of the signal frequency points by the

equaliser coefficients. However, for the case of OFDM systems, the technique can be significantly simplified, assuming that the variations of the PA transfer function within the range of one OFDM subcarrier are negligibly small comparing to those for the whole system bandwidth. In this case, the compensation of memory effects can be realised by multiplying each of the subcarrier symbols with the corresponding coefficient  $H(n, P_{bb})$ , where  $n = 0 \dots N-1$  is the number of the subcarrier.

A general block diagram for the proposed memory-compensating method is presented in Figures 7-2.  $N$  symbols of  $M$ -range are generated for the chosen modulation type and mapped to  $M$ -QAM. Obtained complex symbols are transformed into the frequency domain using DFT for equalisation. After multiplying by  $H(f_k, P_{bb})$ , the symbols are subjected to IDFT and passed to the memoryless nonlinearity compensation part of the predistorter.

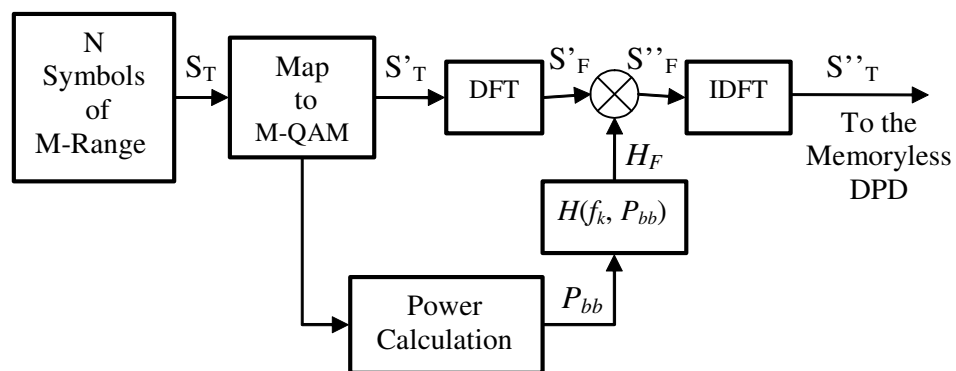


Figure 7-2: General block diagram of the proposed memory-compensating method

Figure 7-3 illustrates the operation of the proposed memory-compensating method for an OFDM system. The source generates binary data symbols, which are mapped to  $M$ -QAM in the corresponding block. For creating an OFDM symbol,  $N$  data samples are converted from the serial to parallel form and written in a matrix-column. The baseband power level for each of the  $M$ -QAM symbols is calculated and used for addressing the corresponding value of the frequency response coefficients  $H(n, P_{bb})$ .  $N$  data symbols are then multiplied by the corresponding coefficients and passed to the IDFT unit, where the pre-equalised OFDM symbol is created. A cyclic prefix is added, and the symbol is transferred to the memoryless part of the predistorter.

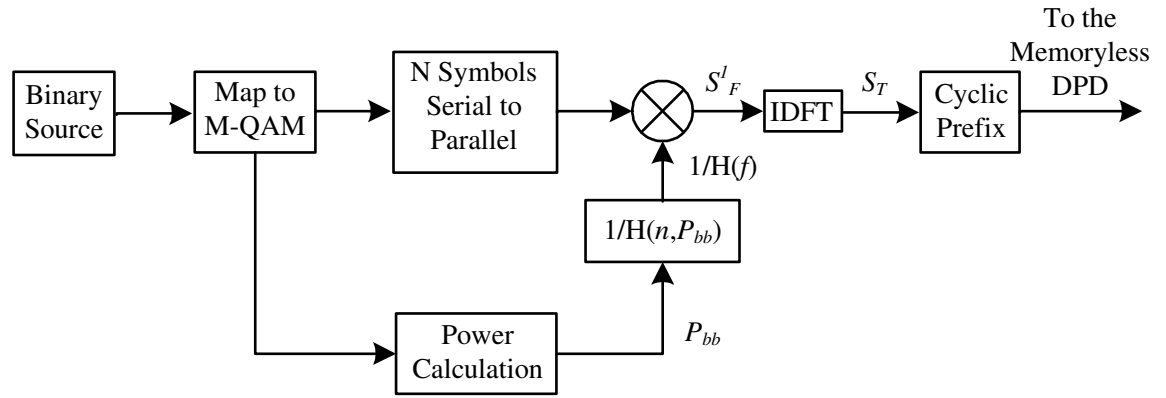


Figure 7-3: Block diagram of the proposed memory-compensating method for an OFDM system

The computational complexity of the proposed equalisation method can be estimated as the number of required DSP operations and the number of stored coefficients. The mathematical operations required for the method include N-points DFT and IDFT procedures and multiplying the frequency points by the complex-valued coefficients  $H(f_k, P_{bb})$ . For OFDM systems, the equaliser DSP operations are limited only to multiplications.

The number of stored coefficients is determined by the number of frequency points  $N$  and the modulation type. As described above, the frequency response coefficients need to be tabulated for all baseband power levels. The number of these levels depends on the modulation type. For QPSK, the baseband power level is constant, and hence the number of stored coefficients equals to the number of frequency points  $N$ . For 16-QAM, three power levels are possible, which means the number of stored coefficients equals to  $3N$ . Similarly, for 64-QAM  $10N$  coefficients need to be stored. Table 7.1 presents the required number of stored coefficients for each of the modulation types.

**TABLE 7.1:** Number of stored coefficients for the proposed equalisation method

| Number of DFT Points | Number of Stored Coefficients for QPSK | Number of Stored Coefficients for 16-QAM | Number of Stored Coefficients for 64-QAM |
|----------------------|--|--|--|
| $N$                  | $N$                                    | $3 \cdot N$                              | $10 \cdot N$                             |

### 7.3. Verification of the Memory Compensation Technique by Simulations

In this Section, verification of the proposed baseband equalisation method by simulations is presented. The procedure of designing and testing the equaliser includes the following steps. Firstly, the equaliser coefficients, which are used for compensating the frequency-dependent behaviour of the PA, are extracted from its simulated characteristics. Then, the proposed compensating algorithm is implemented in Matlab and used for predistorting the input I and Q signals. Finally, improvements in the signal constellation diagram, Error Vector Magnitude (EVM), and Adjacent Channel Power Ratio (ACPR) are investigated.

#### 7.3.1 Matlab-ADS Co-Simulation Test Bed

In order to verify the performances of the proposed predistortion method, a Matlab-ADS co-simulation test bed has been designed according to the layout presented in Figure 6-7 (b). The main circuit for the test bed is illustrated in Figure 7-4. It consists of a Matlab signal source, signal converters, time and frequency domain measurement blocks, RF subsystem with the Envelope simulation controller and a Matlab measurement block.

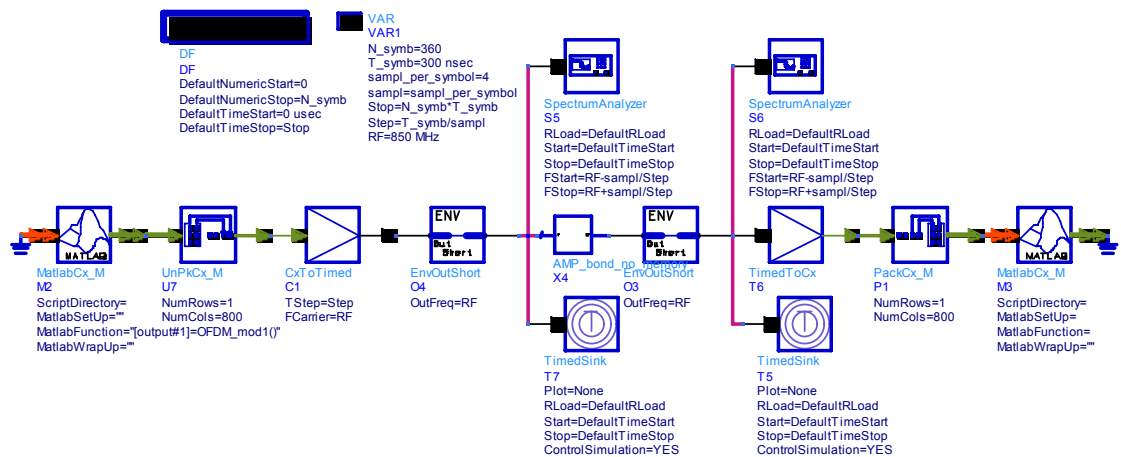


Figure 7-4: Main circuit for the designed Matlab-ADS co-simulation system

The input signal is generated in Matlab and pre-equalised according to the developed memory-compensating method. It is transferred to the ADS digital circuit in a complex matrix form, as shown in Figure 7-4. The signal is further converted using two blocks: “Matrix unpack” for transforming the input matrix to the string and “Complex to Timed” for converting the signal from the complex to timed format with assigning the time step, or the length of symbols, and the central RF carrier frequency. “Envelope detector” blocks are used for providing simultaneous simulations of the “Data Flow” (Figure 7-4) and “Envelope” (Figure 7-5) controllers. Then, the signal is passed to the RF sub-circuit for Envelope co-simulation. The RF sub-circuit, presented in Figure 7-5, contains a transistor-level model of the power amplifier exhibiting memory effects. The PA topology sub-circuit is shown in Figure 7-6.

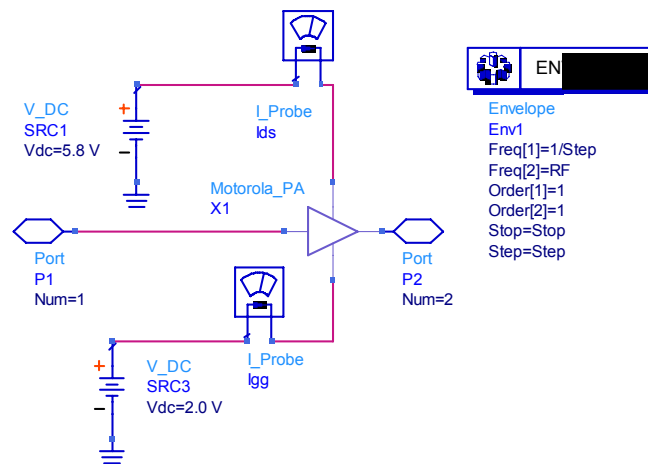


Figure 7-5: ADS analogue sub-circuit for the PA

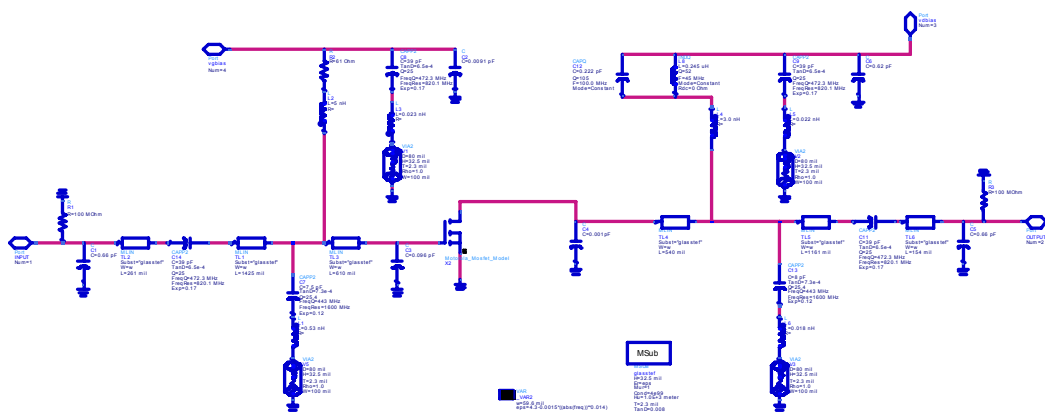


Figure 7-6: ADS sub-circuit for the PA transistor-level model

After passing through the PA in the ADS analogue sub-circuit with the Envelope simulation controller, the signal is returned to the main digital circuit operating under the Data Flow controller (Figure 7-4), where it is simulated in the time and frequency domains and converted into the matrix form for analysing in Matlab. The constellation diagram and EVM are captured in the Matlab measurement block. The ACPR is evaluated using the output spectrum analyser of the main layout, as in Figure 7-4.

### 7.3.2 PA Characterisation

The power amplifier used for simulations is the same as that in Section 4.4. It is based on a MOSFET active device MRF9742, and has a 12-dB gain and the 1-dB compression point at 25 dBm output power. The PA nonlinear behaviour and memory effects are investigated. Figure 7-7 shows the gain and output power dependence on the input power level for the considered PA at the centre frequency of 850 MHz.

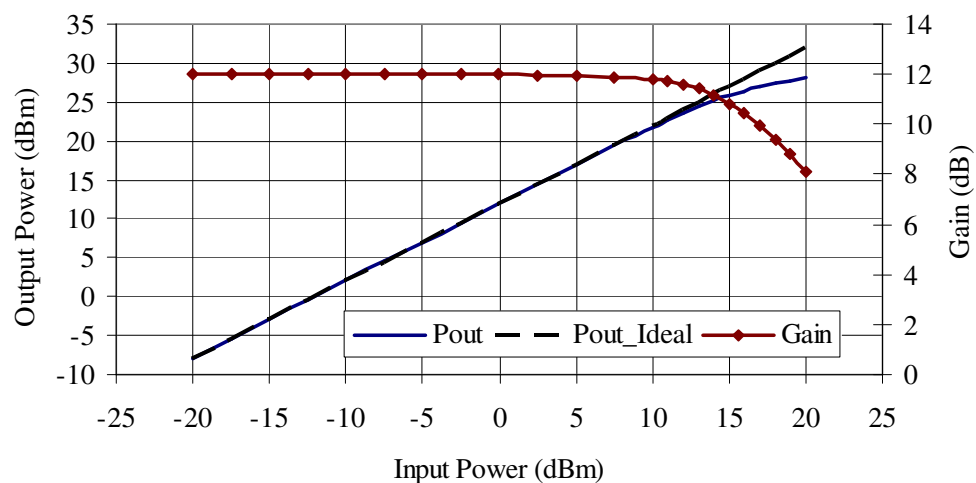


Figure 7-7: Simulated output power and gain versus input power for the considered PA

Quantification of the PA memory effects for a linear mode of operation was accomplished in Section 4.4 using the ADS and Matlab test beds. In this Section, the proposed equaliser is investigated for a wide dynamic range including the linear and compression modes of operation. The complex frequency-response coefficients are extracted from the PA gain and phase characteristics for different power levels. The amplifier characterisation is accomplished for the input power range of -20 ... 20 dBm.

The simulated dependences of gain and phase on modulation frequency for different input power levels are presented in Figures 7-8 and 7-9 respectively.

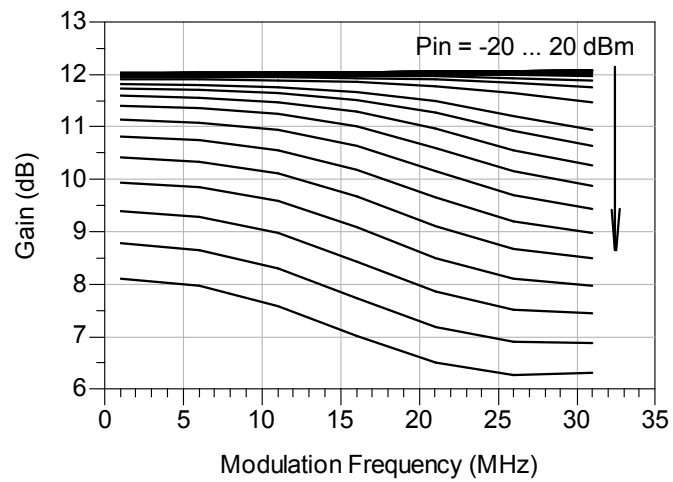


Figure 7-8: Simulated MRF9742 gain variations over modulation frequency due to memory effects

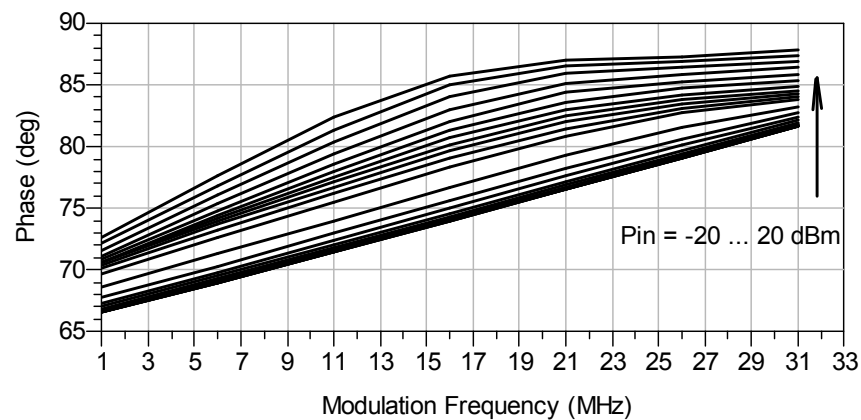


Figure 7-9: Simulated MRF9742 phase variations over modulation frequency due to memory effects

### 7.3.3 Equaliser Coefficient Extraction

For verifying the performances of the developed equalisation method by simulations, a 3.5-MHz 256-OFDM 16-QAM WiMAX signal with 0-dBm input power level is used. As the 16-QAM modulation scheme is applied to modulate each OFDM subcarrier, the number of baseband power levels equals to three. The baseband voltage and power levels for the considered signal are presented in Table 7.2. At these levels, the amplifier exhibits memory effects, but is not in saturation. The magnitude and phase of the normalised inverse frequency response of the considered PA (MRF9742) are extracted from the gain and phase curves for the corresponding input power levels. The magnitude of the input voltage is calculated using the following relation:

$$\text{mag}(V_{IN}) = \text{mag}(V_{LO}) \cdot \sqrt{\text{mag}(I)^2 + \text{mag}(Q)^2}, \quad (7.4)$$

where  $V_{LO}$  is the carrier voltage of the Local Oscillator (LO). Assuming a 50-ohm impedance, the input power level is related to the input voltage magnitude as:

$$P_{IN\_dBm} = 10 \cdot \log(10 \cdot \text{mag}(V_{IN})^2). \quad (7.5)$$

For 0-dBm carrier power, the corresponding voltage magnitude of the LO is  $\text{mag}(V_{LO}) = 0.316228$  V. Substituting the obtained value in (7.4) yields the quantities for  $\text{mag}(V_{IN})$  corresponding to 0-dBm carrier power. The resulting values of  $\text{mag}(V_{IN})$  and  $\text{mag}(P_{IN})$  are presented in Table 7.2.

**TABLE 7.2:** Voltage and power levels for simulations

| $\text{mag}(I)$ , V | $\text{mag}(Q)$ , V | $\text{mag}(V_{BB})$ , V | $P_{BB}$ , dBm | $\text{mag}(V_{IN})$ , V | $P_{IN}$ , dBm |
|---------------------|---------------------|--------------------------|----------------|--------------------------|----------------|
| 0.31                | 0.31                | 0.44                     | 2.84           | 0.14                     | -7.16          |
| 0.31                | 0.93                | 0.98                     | 9.83           | 0.31                     | -0.17          |
| 0.93                | 0.93                | 1.32                     | 12.38          | 0.42                     | 2.38           |

$P_{LO} = 0$  dBm;  $V_{LO} = 0.316228$  V

For the considered PA based on a Motorola MRF9742 active device, the normalised complex values  $H_{\text{NORM}}(f_k, P_{\text{IN}})$  are extracted from the gain and phase dependences (Figures 7-8, 7-9) at the input power levels of  $P_{\text{IN}_1} = -7.16$  dBm,  $P_{\text{IN}_2} = -0.17$  dBm and  $P_{\text{IN}_3} = 2.38$  dBm (Table 7.2). The magnitude and phase of the normalised frequency response  $H_{\text{NORM}}(f_k, P_{\text{IN}})$  for the considered signal and PA are presented in Figures 7-10 and 7-11 respectively.

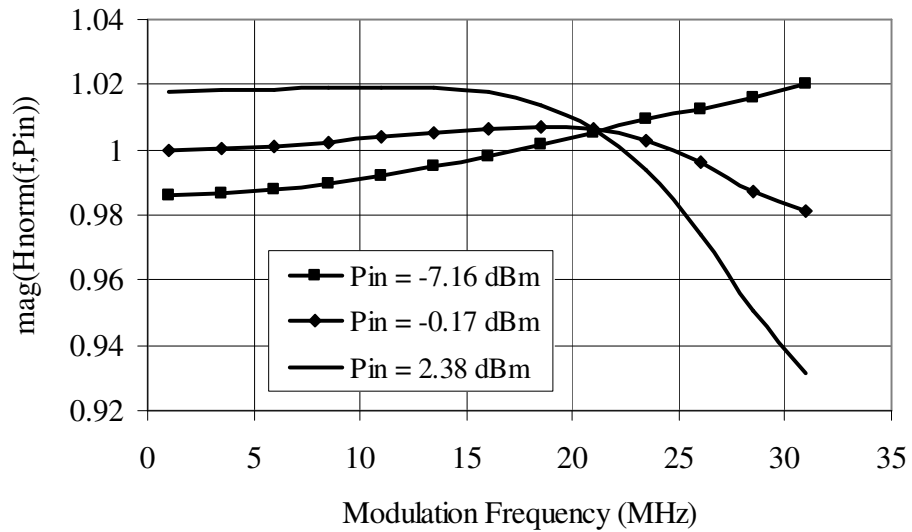


Figure 7-10: Magnitude of the normalised frequency response  $H_{\text{NORM}}(f_k, P_{\text{IN}})$  for three power levels

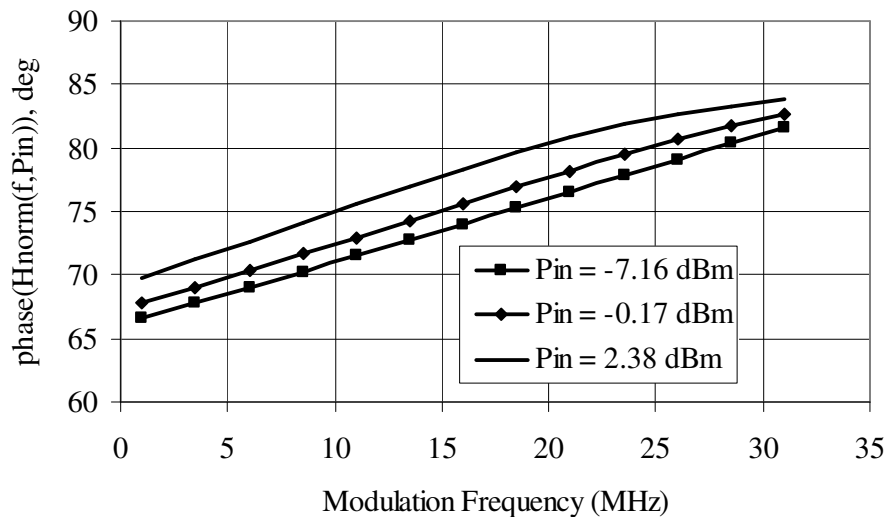


Figure 7-11: Phase of the normalised frequency response  $H_{\text{NORM}}(f_k, P_{\text{IN}})$  for three power levels

### 7.3.4 Simulated Results

To compensate for the PA memory effects, the equaliser, designed according to the block diagram in Figure 7-3, is implemented in the Matlab signal source unit (Figure 7-4), which generates a 3.5-MHz 256-OFDM 16-QAM signal. After mapping to 16-QAM, the symbols take one of three possible baseband power levels, which are detected by the “Power Calculation” block. The baseband signal is converted to the parallel form composed of 256 16-QAM symbols; each of them is multiplied by the equaliser coefficient corresponding to the number of the sub-carrier and the power level of the symbol. After multiplying the complex baseband signal is by  $1/H_{\text{NORM}}(f_k, P_{IN})$ , IDFT is performed, and an OFDM waveform is created. It passes the MRF9742 amplifier at an input power level of 0 dBm. Further, the signal is captured by the Matlab measurement block, demodulated according to the OFDM demodulation algorithm and analysed. An example of the Matlab OFDM demodulation code is presented in Appendix A. The constellation diagrams of the signal after passing through the PA without equalisation and with the developed pre-compensation of memory effects are presented in Figures 7-12 and 7-13 respectively. Comparing the two constellation diagrams, one can observe that the dispersion due to memory effects is almost eliminated.

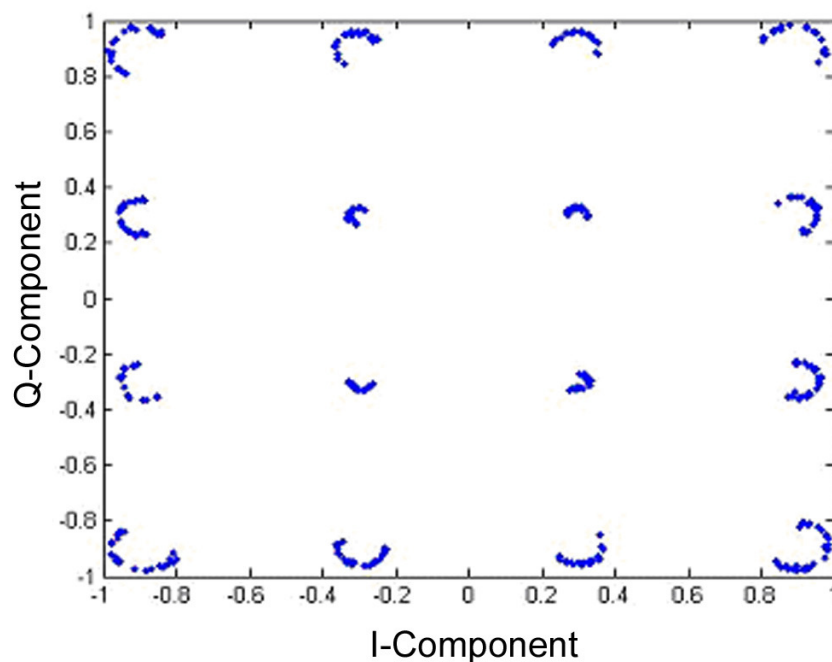


Figure 7-12: Demodulated constellation for the considered PA (MRF9742) without compensation of memory effects at  $P_{in} = 0$  dBm (EVM = 5.3 %)

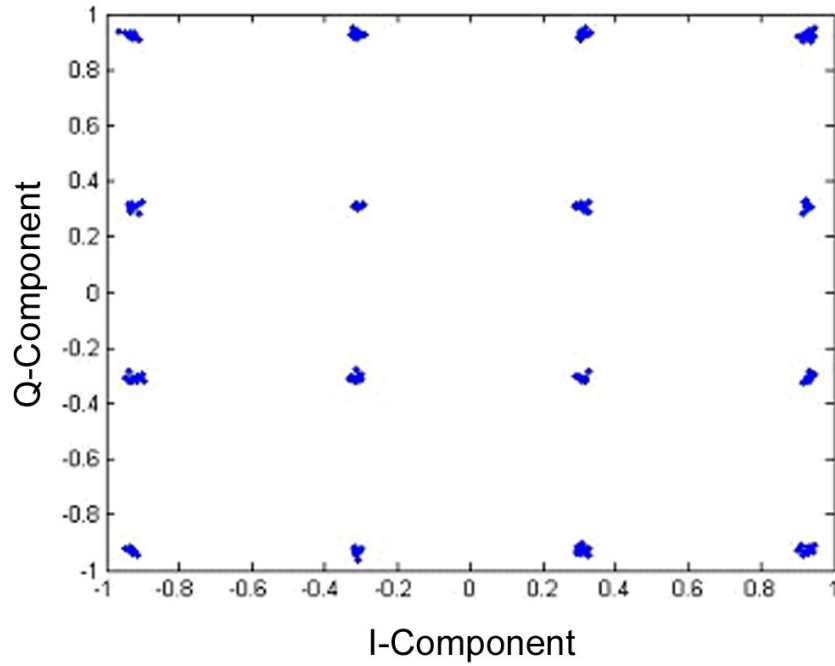


Figure 7-13: Demodulated constellation for the considered PA (MRF9742) using the developed baseband equalisation method at  $P_{in} = 0$  dBm (EVM = 0.97 %)

The captured data samples are processed by the Matlab measurement block, which calculates the error vector magnitude of the signal with and without compensation of memory effects. Using the demodulated I and Q samples, the EVM is calculated according to the following relation:

$$EVM = \frac{\sum_{k=1}^N \sqrt{[I_r(k) - I_i(k)]^2 + [Q_r(k) - Q_i(k)]^2}}{\sum_{k=1}^N \sqrt{I_i^2(k) + Q_i^2(k)}}, \quad (7.6)$$

where  $k$  is the sample index;  $I_i(k)$  and  $Q_i(k)$  are the ideal I and Q samples, whereas  $I_r(k)$  and  $Q_r(k)$  are the received I and Q samples respectively.

The calculated EVM for the demodulated signal without pre-equalisation (Figure 7-12) equals to 5.3 %, whereas the EVM for the demodulated signal with the developed pre-compensation of memory effects at the same power level (Figure 7-13) equals to 0.97 %. The significant reduction in EVM proves the feasibility of the developed baseband equalisation method and illustrates, that the frequency response  $H_{NORM}(f_k, P_{IN})$  was calculated accurately, and the pre-compensation of memory effects was performed correctly.

Further, the performances of the developed equalisation method are investigated for a wide power range including the linear and nonlinear modes. Varying the PA input power in the range of -20 ... 15 dBm, the EVM and ACPR characteristics are simulated for a 3.5-MHz 256-OFDM 16-QAM WiMAX signal.

EVM is calculated in the Matlab measurement block from the demodulated I and Q samples, as described above. Figure 7-14 depicts the simulated EVM versus power level for the considered PA with and without pre-equalisation of memory effects. As can be observed from the Figure, the proposed equaliser reduces the signal distortions in the linear and nonlinear modes.

ACPR is calculated by the spectrum analyser in the main ADS circuit from the RF signal captured after amplifying in the PA. 4-MHz offsets are chosen for calculating ACPRs of the higher and lower (ACPRH and ACPRL) adjacent channels. Figure 7-15 presents the simulated ACPR versus power level for the considered PA with and without pre-equalisation of memory effects. As can be observed from the Figure, the proposed equaliser reduces the spectrum spread and equalises the upper and lower intermodulation distortions.

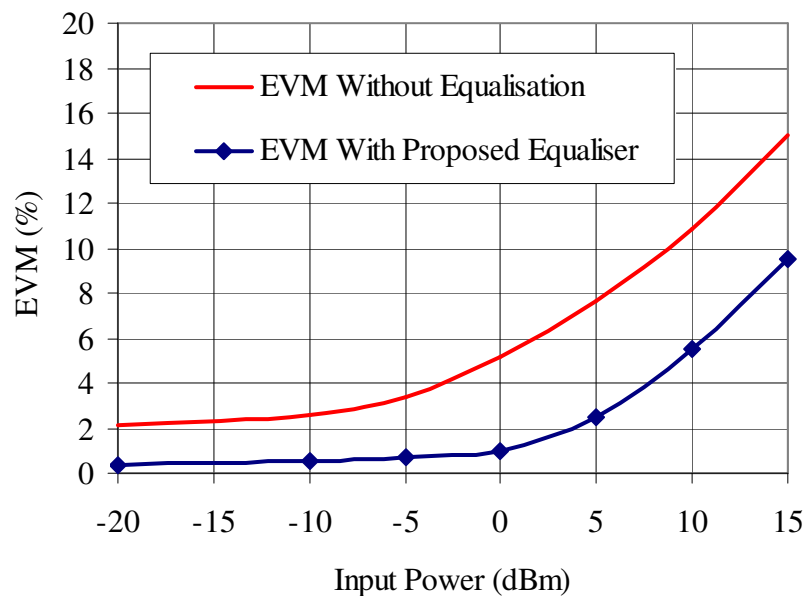


Figure 7-14: EVM versus input power with and without pre-equalisation for the considered PA exited with a 3.5-MHz 256-OFDM 16-QAM signal

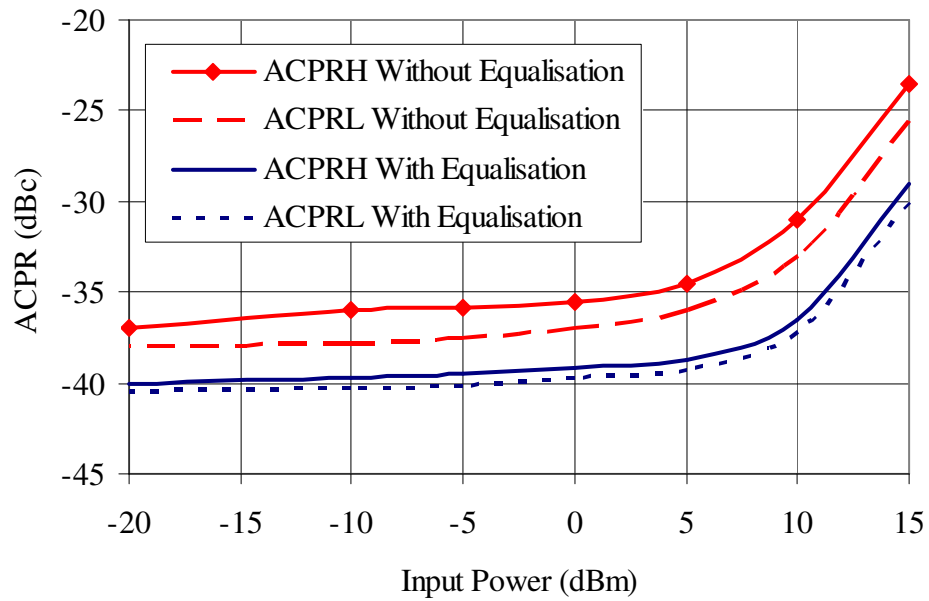


Figure 7-15: ACPRs at 4-MHz higher and lower offsets versus input power with and without pre-equalisation for the considered PA excited with a 3.5-MHz 256-OFDM 16-QAM signal

#### 7.4. Adaptation Procedure using Offline Training

This Section depicts a close-loop implementation of the proposed DPD including an adaptation circuit for optimising the predistorter coefficients according to environmental change, self-heating and other phenomena, which modify the electrical parameters of the PA. The adaptation method must update  $g$ -coefficients, used for compensating the nonlinear distortion, and the PA frequency response coefficients  $H(f_k, P_{bb})$ , which are required for minimising memory effects. Conventionally, adaptation procedures for optimising memory polynomial predistorters, such as those designed according to the Hammerstein or Wiener structures, include recursive algorithms for calculating the coefficients of the FIR filter taps [7.1]-[7.2]. However, such algorithms are time-consuming, as they require executing several iterations to achieve convergence. Alternatively, with the help of the FFT-based methods, the adaptation of the equaliser parameters can be accomplished by a single shot, as described in [7.3]-[7.5]. This includes exciting the PA with a training sequence, composed of equally spaced over the

operational bandwidth frequency points, which capture the information about the gain and phase frequency-dependent behaviour.

In this work, the adaptation of the predistorter coefficients for both the memoryless nonlinearity-compensation and memory-minimising parts are accomplished by a single shot using the feedback-based offline training scheme. In order to avoid the potential problems of the feedback linearisation, described in Chapter 3, the adaptation loop is designed to operate offline, and hence it is not in use during the operation of the predistorter. The adaptation chain is turned on only when required. The decision on executing the adaptation procedure is taken by comparing the mean square error between the input and demodulated output signals with the threshold. The extraction of  $g$ -coefficients is accomplished from the AM/AM characteristic using the Least-Squares Regression (LSR) approximation, as described in Section 5.3.2. The calculation of the frequency response coefficients  $H(f_k, P_{bb})$  is carried out using a training sequence, composed of equally spaced over the operational bandwidth frequency points.

The block diagram for the close-loop implementation of the proposed predistorter, including the memory nonlinearity compensation in the direct path and the adaptation circuit in the feedback path, is presented in Figure 7-16.



Figure 7-16: Close-loop adaptive implementation of the proposed predistorter using a feedback-based offline training scheme

The close-loop system consists of four main circuits: the digital predistorter, composed of the memory- and nonlinearity-compensation units; the main analogue circuit, including the I/Q modulator and the power amplifier, the analogue feedback circuit, which performs the inverse operations to those of the main analogue circuit, i.e. attenuating and demodulating the RF signal; and the digital adaptation circuit, composed of the adaptation controller, the block incorporating LSR algorithm for calculating  $g$ -coefficients and the sub-circuit for extracting  $H(f_k, P_{bb})$  coefficients.

The data source provides the baseband input symbols mapped to M-QAM. They are predistorted by the baseband equalisation circuit, as shown in Figure 7-2, and by the memoryless distortion-components injection DPD circuit, as shown in Figure 6-1. The predistorted signal is divided into two paths: one is fed to the adaptation controller, and the other is converted to the analogue form by the DAC, filtered with the low-pass filter, modulated in the I/Q modulator using an RF carrier signal from the LO and passed through the main PA. The amplified RF signal is coupled by the output coupler and directed to the feedback loop for analysis. In the analogue feedback chain, the signal is attenuated by the value of PA linear gain as:

$$V_{FB\_ATT}(t) = \frac{V_{FB}(t)}{G_{Linear}}. \quad (7.7)$$

Then, the fed-back attenuated signal is demodulated, filtered and converted to the digital form by the ADC. The obtained baseband signal is compared with the original one in the adaptation controller by means of calculating the Mean Square Error (MSE):

$$E[|e_k|^2] = \frac{\sum_{k=1}^n [|y_k - \tilde{y}_k|^2]}{n}, \quad (7.8)$$

where  $\tilde{y}_k$  and  $y_k$  are the  $k$ -th samples of the fed-back and original baseband signals respectively, and  $n$  is the number of considered samples.

If the obtained value of MSE is greater than the threshold, the adaptation circuit will be turned on. From the original and fed-back signals, a set of experimental data is obtained as  $N$  pairs of the input  $x_i$  and the corresponding output  $y_i$  variables:  $(x_1, y_1)$ ,  $(x_2, y_2)$ ,  $(x_3, y_3)$ , ...,  $(x_n, y_n)$ . Then, according to the LSR approximation algorithm, the  $g$ -coefficients for the predistorter are extracted, as described in Section 5.3.2.1. The coefficients are calculated directly by solving the linear system of equations:



## 7.5. Experimental Setup

In order to accomplish the experimental verification of the proposed DPD technique, a laboratory test bed has been designed. The test bed includes a Digital Signal Processing (DSP) part realised in a Personal Computer (PC) and a Radio-Frequency (RF) part. The proposed predistorter is implemented in the DSP part. The RF sub-system, which includes the power amplifier, is depicted below in Section 7.5.1. The implemented predistorter operation is described in Section 7.5.2.

### 7.5.1 Hardware Setup

The experimental setup that was designed for verifying the performances of the proposed [7.6]-[7.9] and conventional [7.10] digital predistortion techniques is shown in Figure 7-17. It consists of a PC, Electronic Signal Generator (ESG) E4433B, DUT ZHL-1042J and Vector Signal Analyser (VSA) E4406A.

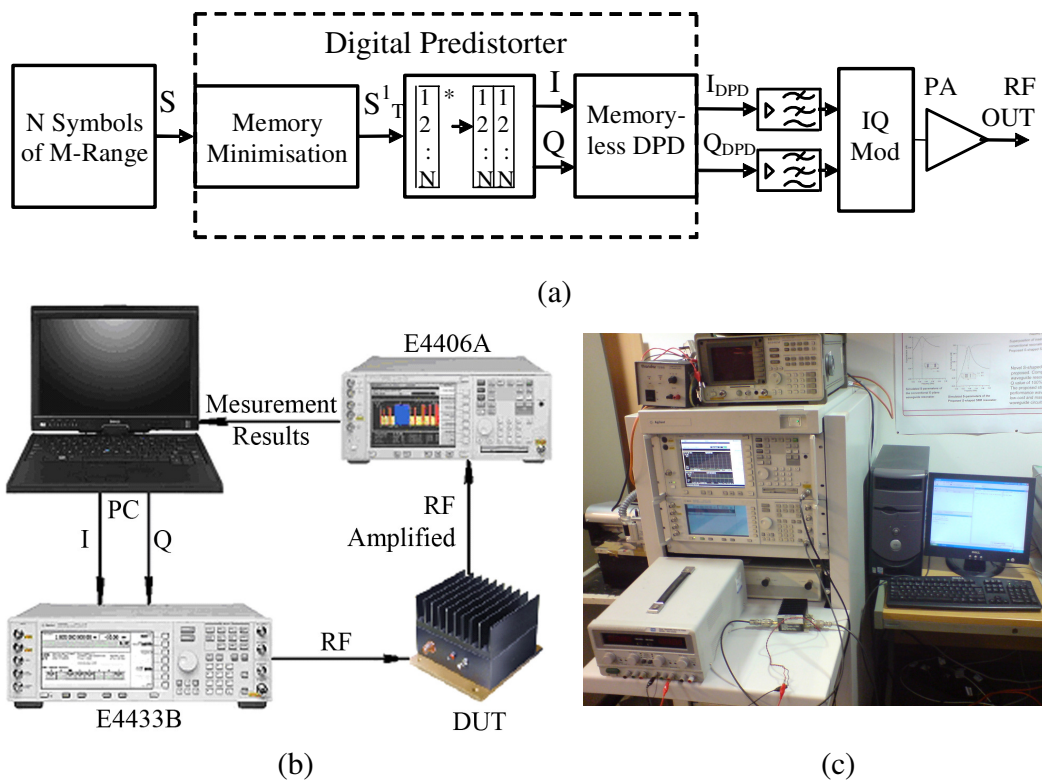


Figure 7-17: Experimental setup for verifying digital predistorters: (a) Functional diagram; (b) Experimental setup; (c) Hardware test-bench

The power amplifier used for the experiments is a 25-dB gain 1-dB compression at 20 dBm output power Mini-Circuits ZHL-1042J PA with the frequency range of 10 - 4200 MHz. The datasheet for the PA is presented in Appendix B.

The proposed DPD including the memoryless nonlinearity and memory effects compensating parts is implemented in Matlab according to the procedures described in Sections 6.2 and 7.2. The parameters of the predistorter are tuned in order to reflect the memory nonlinear behaviour of the power amplifier used as the DUT. For this purpose, the PA characterisation is accomplished in order to extract the nonlinear model and the baseband equaliser coefficients. The characterisation results for the considered ZHL-1042J amplifier are presented in Section 7.6.1.

The initial data symbols are generated and mapped to the chosen modulation scheme, as shown in Figure 7-17 (a). The obtained baseband signal is further subjected to the proposed digital predistortion including the baseband equalisation to compensate for the frequency-dependent behaviour and the memoryless DPD to compensate for the nonlinear distortion of the PA. The former is executed by the “Memory Minimisation” block, which is designed according to the developed baseband equalisation technique depicted in Section 7.2. The latter is accomplished by the “Memoryless DPD” block, which realises the proposed distortion components iterative injection DPD technique described in Section 6.2.

The predistorted I and Q signals are uploaded into the ESG (E4433B), which executes the operations of Digital-to-Analogue Converting (DAC) and modulating. The modulated RF signal from the output of the signal generator is passed through the DUT and transferred to the VSA (E4406A) for measurements. The measurement results are downloaded to the PC for comparison and analysis.

### **7.5.2 Implemented Predistorter Configuration**

The proposed digital predistorter configuration used in the experiments is presented in Figure 7-18. It consists of a baseband equalisation part for compensating memory effects, and a nonlinearity compensation part, designed according to the proposed baseband iterative injection technique.

The input symbols are generated using a pseudorandom sequence PN9 and mapped to the chosen modulation type by the corresponding mapping scheme. The

pseudorandom sequence PN9 used in the experiments consists of 512 bits, which are presented in Appendix-C in the binary and hexadecimal formats. The sequence is pre-programmed in the ESG (E4433B) and used for representing the signal source binary data during experiments. The mapping schemes for the QPSK and 16-QAM modulation are given in Appendix-C.

After mapping, the obtained complex symbols are predistorted as follows. Initially, they are transformed into the frequency domain using Fast Fourier Transform (FFT) with the aim to accomplish equalisation. After multiplying by  $H(f, P_{in})$ , the symbols are subjected to the inverse FFT (IFFT) procedure. The obtained complex signal is further divided into I and Q components and passed to the nonlinearity compensation block of the predistorter. The mean value  $V$  of the input signal magnitude is calculated.  $I$  and  $Q$  are multiplied by  $1/V$  for normalisation. This procedure is performed in order to achieve  $average(I^2(t) + Q^2(t)) = 1$  and not to affect the mean power level by predistortion. The normalised signals  $I^{norm}$  and  $Q^{norm}$  are subjected to the proposed DPD, as described in Section 6.2. After that, the signals are multiplied by  $V$  for de-normalisation. The predistorted signals  $I_{DPD}$  and  $Q_{DPD}$  are further transferred into the waveform generator (E4433B). In the ESG, the signals are filtered with low-pass raised-cosine filters and used for I/Q modulation. The obtained RF signal is passed through the PA.

In order to tune the parameters of the proposed predistorter to the DUT memory nonlinear behaviour, a training of the predistorter must be accomplished before carrying out the experimental validation. The training includes an extraction of the nonlinear  $g$ -coefficients and frequency response points  $H(f, P_{in})$  for a particular PA, as well as choosing an appropriate number of injections to achieve a sufficient linearising performance with a reasonably low level of computational complexity.

The remainder of this Chapter includes experimental results and discussions for the PA characterisation and extraction of the coefficients, tuning and computational complexity of the predistorter, and investigation of the DPD linearising performance for a low-memory PA and a PA exhibiting memory effects excited with different types of signals.

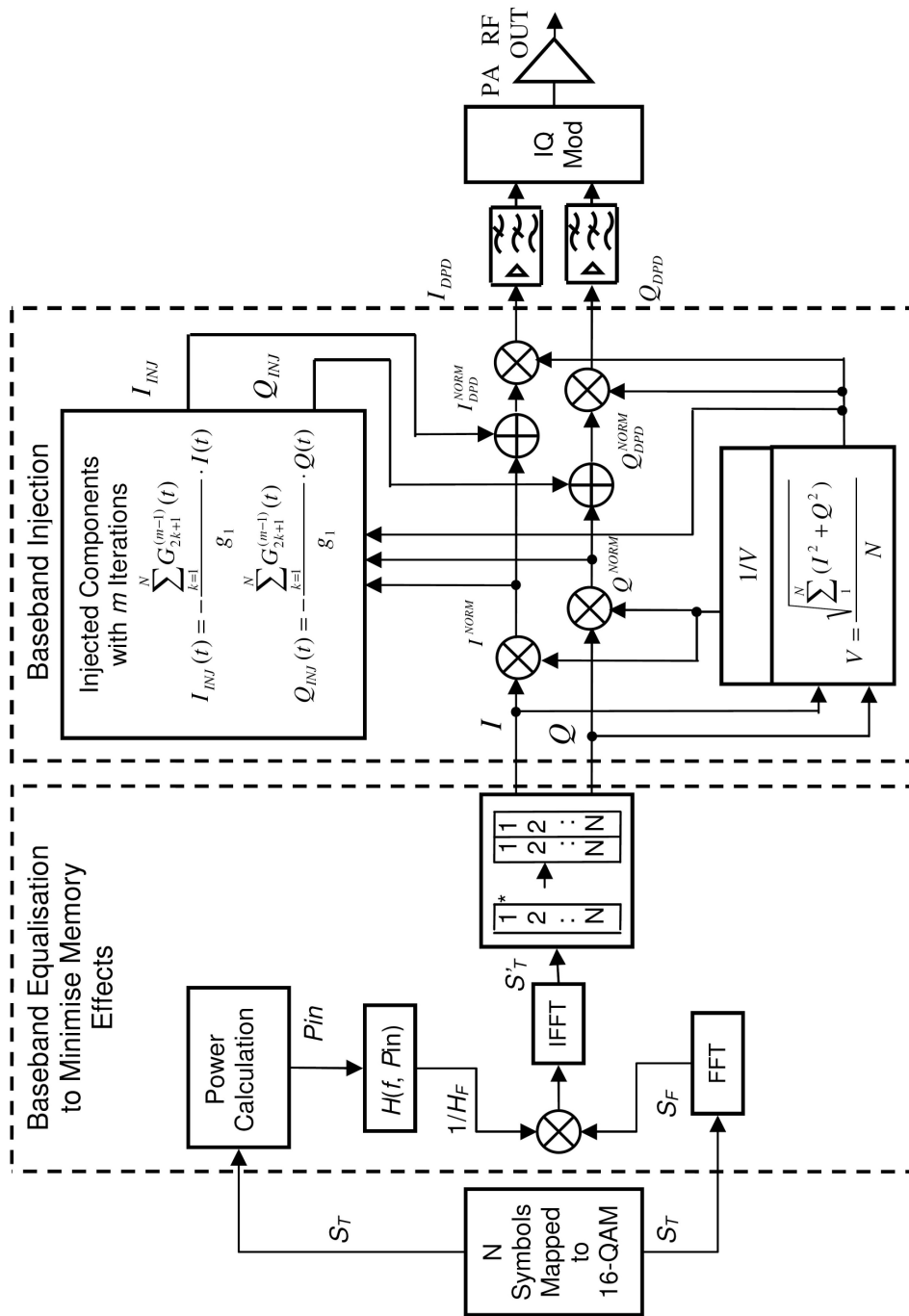


Figure 7-18: Block diagram of the proposed predistorter

## 7.6. Experimental Results for a Power Amplifier Exhibiting Memory Effects

This Section presents experimental results for the power amplifier Mini-Circuits ZHL-1042J. This is a medium-power low-noise wideband PA with high IP3 intended for laboratory and communication system applications. The amplifier has the 25 dB gain and the frequency range of 10 – 4200 MHz. The data sheet for the PA is presented in Appendix-B. ZHL-1042J has the 1-dB compression point at 20-dBm output power. The PA exhibits asymmetrical memory effects, which are quantified below in Section 7.6.1. The experimental validation is carried out for the input power levels of -3 dBm and -5 dBm. At these levels, the PA exhibits both the nonlinear behaviour and memory effects.

The Section depicts the PA characterisation for the purpose of predistorter design and presents the experimental results for verifying the DPD linearising performances for a 5-MHz WCDMA signal at 2.1 GHz carrier and a 5-MHz 16-QAM signal at 3.5 GHz carrier.

### 7.6.1 PA Characterisation

For characterising the PA, its transfer function and frequency-dependent performances are measured. The polynomial  $g$ -coefficients are extracted from the AM/AM characteristic, whereas the equaliser coefficients are obtained from the frequency response.

In order to measure the nonlinear transfer function of the considered 25-dB gain, 1-dB compression point at 20-dBm output power ZHL-1042J PA, an RF tone with varying input power is generated by the ESG E4433B. The RF signal is created with the frequencies of 2.1 GHz and 3.5 GHz and varying power in the range of -40...+5 dBm. Then, the RF tone is passed through the PA, and the output signal is directed to the VSA E4406A for measurements. Figures 7-19 and 7-20 present the output power and gain versus input power for the considered PA at 2.1 GHz and 3.5 GHz tones respectively.

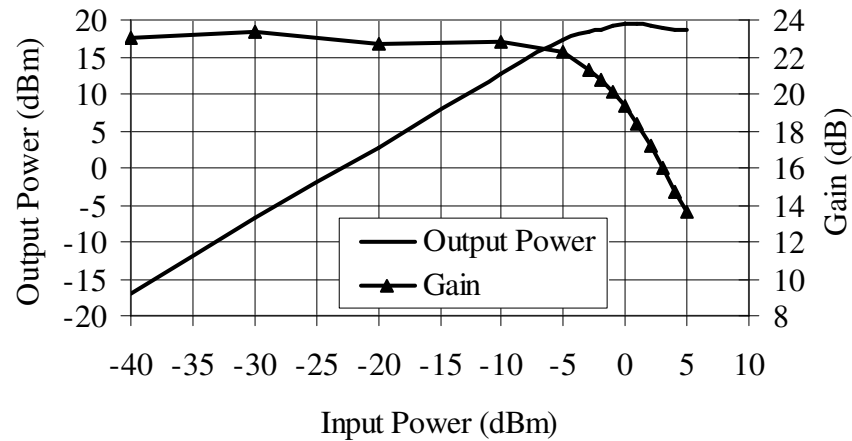


Figure 7-19: Measured output power and gain versus input power for the considered PA ZHL-1042J at 2.1 GHz

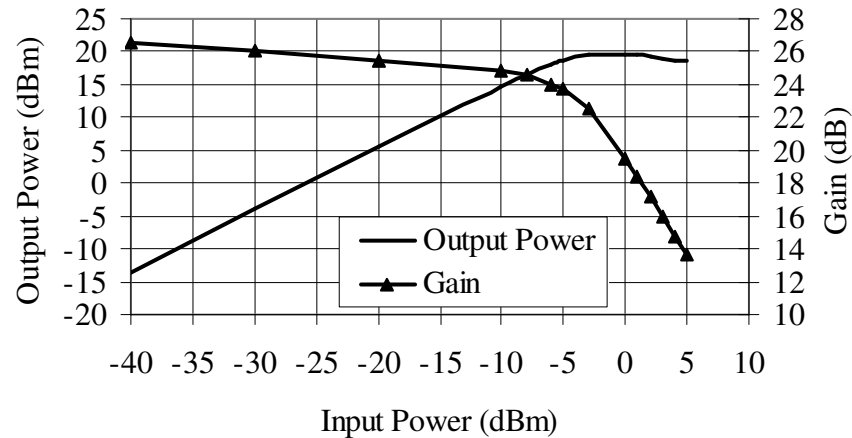


Figure 7-20: Measured output power and gain versus input power for the considered PA ZHL-1042J at 3.5 GHz

The measured transfer characteristics for ZFL-1042J at 2.1 GHz and 3.5 GHz carriers are processed for extracting  $g$ -coefficients of the PA polynomial model, as described in Section 5.3. The curves of output voltage versus input voltage are extracted from the measured results. Using the Least-Squares Regression (LSR) method, the polynomial model coefficients are calculated according to (5.38).

For the 2.1 GHz DPD system, the odd-order  $g$ -coefficients are obtained by the LSR method as follows:  $g_1=14.37$ ,  $g_3=-78.92$ ,  $g_5=146.08$ . Therefore, the extracted fundamental-frequency polynomial model for the DUT (ZHL-1042J) at 2.1 GHz looks like:

$$V_{OUT}^{FUND}(t) = 14.37 \cdot V_{IN}(t) - 59.19 \cdot |V_S(t)|^2 \cdot V_{IN}(t) + 91.3 \cdot |V_S(t)|^4 \cdot V_{IN}(t). \quad (7.14)$$

The accuracy of the obtained model is verified by comparing the measured and modelled transfer characteristics, as shown in Figure 7-21, and by calculating the coefficient of determination  $r^2$ . The coefficient of determination for the model equals to  $r^2 = 0.9915$ , which indicates high quality of fit. As can be observed from Figure 7-21, the modelled transfer function passes almost the same points as the measured one. Consequently, the obtained model (7.14) is accurate enough to represent the DUT nonlinear behaviour for the 2.1 GHz DPD system.

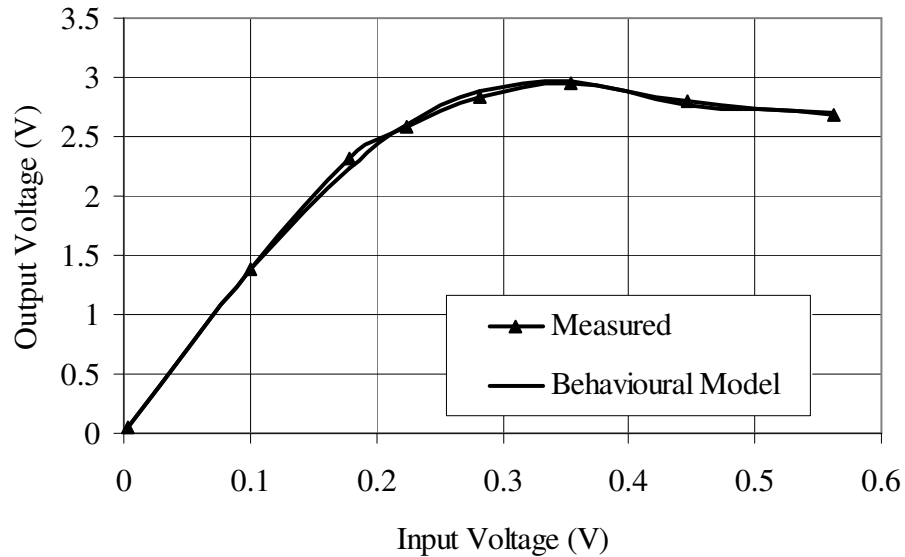


Figure 7-21: Comparison of the measured and 5<sup>th</sup>-order polynomial model transfer characteristics for the DUT ZHL-1042J at 2.1 GHz

For the 3.5 GHz DPD system,  $g$ -coefficients for the 5<sup>th</sup>-order polynomial model (5.38) look like:  $g_1=14.5$ ,  $g_3=-82.5$ ,  $g_5=157.4$ . Then, the 5<sup>th</sup>-order fundamental-frequency model for ZHL-1042J at 3.5 GHz can be written as:

$$V_{OUT}^{FUND}(t) = 14.5 \cdot V_{IN}(t) - 61.9 \cdot |V_S(t)|^2 \cdot V_{IN}(t) + 98.4 \cdot |V_S(t)|^4 \cdot V_{IN}(t). \quad (7.15)$$

The coefficient of determination for the obtained model equals to  $r^2 = 0.9434$ , which indicates medium-to-high accuracy. The measured and modelled by (7.15) transfer characteristics for the DUT (ZHL-1042J) are presented in Figure 7-22. By taking a closer look at the Figure, one can see that the modelled curve does not perfectly match

the measured one. Consequently, the accuracy of the obtained model (7.15) should be increased in order to reflect the nonlinear behaviour of the PA. This can be accomplished by increasing the number of terms in the polynomial model.

For the 7<sup>th</sup>-order polynomial model, the extraction of  $g$ -coefficients is repeated using the LSR procedure (See Section 5.3.2) with  $m=7$ . The obtained values are:  $g_1=14.7$ ,  $g_3=-87.7$ ,  $g_5=208.5$ ,  $g_7=-128.9$ . By substituting these quantities together with  $b_3=3/4$ ,  $b_5=5/8$ ,  $b_7=35/64$  into (5.35)-(5.37), the 7<sup>th</sup>-order fundamental-frequency model for the DUT (ZHL-1042J) at 3.5 GHz can be written as:

$$V_{OUT}^{FUND}(t) = 14.7 \cdot V_{IN}(t) - 65.7 \cdot |V_S(t)|^2 \cdot V_{IN}(t) + 130.3 \cdot |V_S(t)|^4 \cdot V_{IN}(t) - 70.5 \cdot |V_S(t)|^6 \cdot V_{IN}(t). \quad (7.16)$$

The coefficient of determination for the obtained model equals to  $r^2 = 0.9915$ , which indicates high quality of fit. The measured and modelled by (7.16) transfer characteristics are presented in Figure 7-23. As can be observed from the Figure, the modelled transfer function passes almost the same points as the measured one. Consequently, the obtained 7<sup>th</sup>-order model (7.16) is accurate enough to represent the DUT nonlinear behaviour for the 3.5 GHz DPD system.

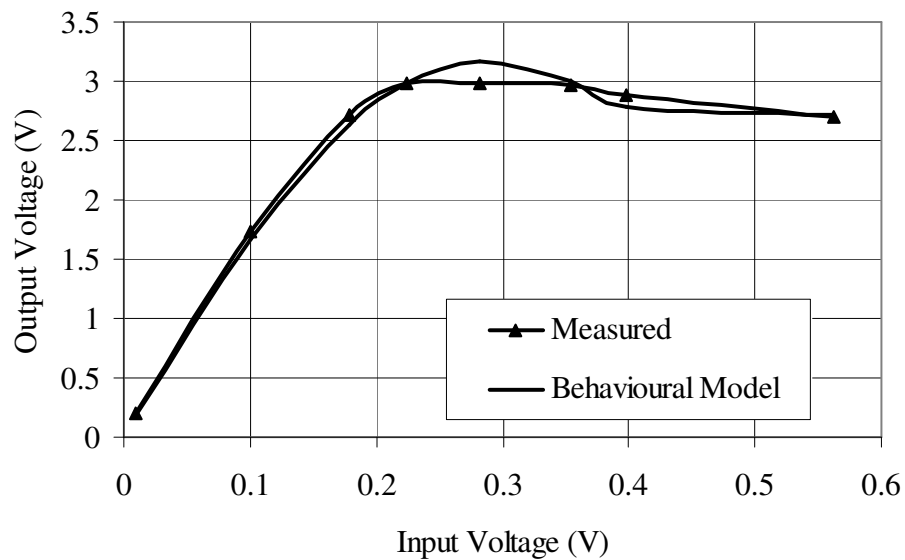


Figure 7-22: Comparison of the measured and 5<sup>th</sup>-order polynomial model transfer characteristics for the DUT ZHL-1042J at 3.5 GHz

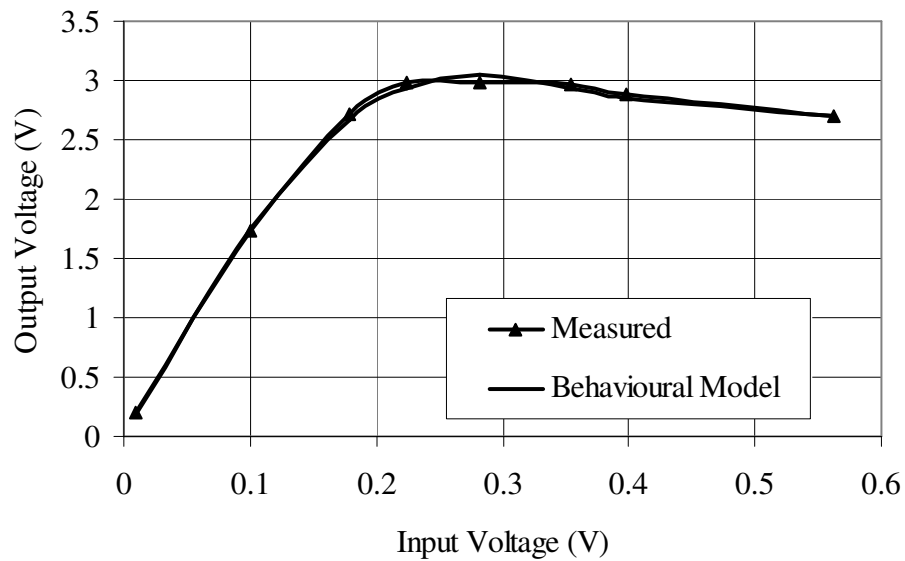


Figure 7-23: Comparison of the measured and 7<sup>th</sup>-order polynomial model transfer characteristics for the DUT ZHL-1042J at 3.5 GHz

In order to quantify memory effects of the considered PA ZHL-1042J, the gain and IM3 dependences on modulation frequency are measured using a two-tone test. The unmodulated RF signals are placed around the centre frequency of  $f_{RF} = 2.1$  GHz with the tone spacing varying in the range of  $f_{spacing} = 10$  kHz...10 MHz. The measured gain and IM3 frequency-dependent characteristics are presented in Figures 7-24 and 7-25 respectively.

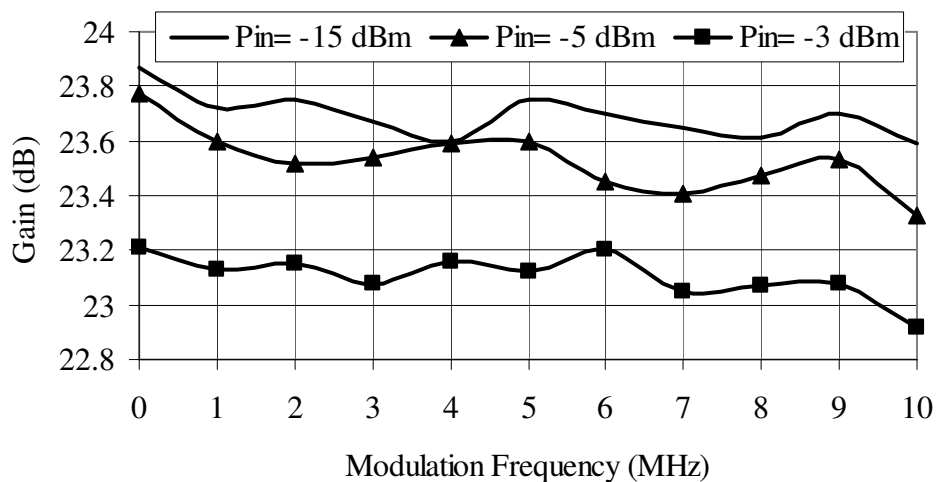


Figure 7-24: Measured gain of the PA ZHL-1042J versus modulation frequency

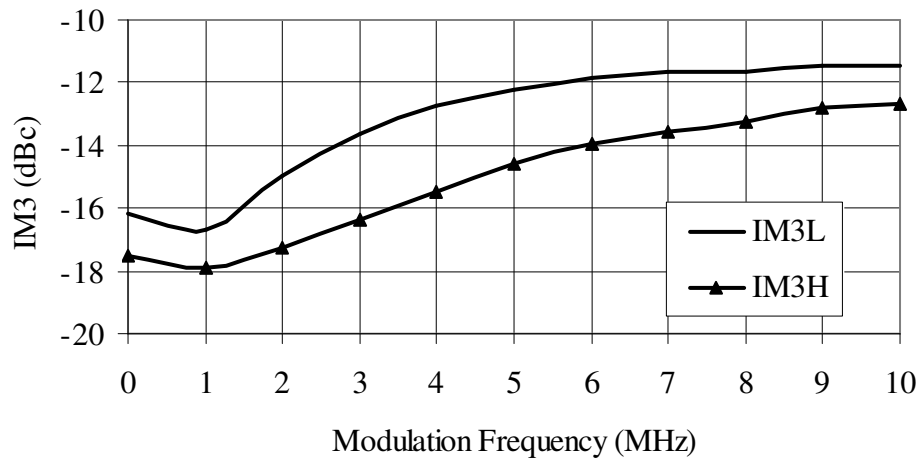


Figure 7-25: Measured higher and lower IM3 of the PA ZHL-1042J versus modulation frequency at the input power level of -3 dBm

As can be observed from the Figures, the PA reveals frequency-dependent variations of the gain and asymmetrical behaviour of the Lower and Higher Intermodulation products (IM3L and IM3H). Consequently, ZHL-1042J exhibits asymmetrical memory effects.

In order to equalise memory effects, the frequency-response extraction process is accomplished for the 2.1 GHz WCDMA and 3.5 GHz 16-QAM systems in Sections 7.6.2 and 7.6.3 respectively.

### 7.6.2 5-MHz WCDMA Signal Case

In this Section, the experimental results are presented for verifying the performances of the proposed and conventional DPD techniques using a 5-MHz WCDMA signal. The input power level is chosen to -3 dBm in order to account for both the memory effects and nonlinear behaviour of the DUT. As the QPSK modulation scheme is used in WCDMA signals, the baseband power level is constant, and the magnitudes of I and Q signals equal to  $\text{mag}(I) = \text{mag}(Q) = 0.7071$  V (see Appendix-C). The magnitude of the baseband voltage equals to 1 V. The frequency response coefficients are extracted for the operational power level of -3 dBm, corresponding to the input voltage of 0.2239 V calculated as  $\text{mag}(V_{IN}) = \text{mag}(V_{LO}) \cdot \sqrt{\text{mag}(I)^2 + \text{mag}(Q)^2}$ .

For the considered Mini-Circuits ZHL-1042J PA, the normalised complex frequency-response values  $H_{\text{NORM}}(f, P_{\text{IN}})$  are extracted from the gain and phase characteristics at the input power level of  $P_{\text{IN}} = -3$  dBm. The magnitude and phase of the normalised frequency response  $H_{\text{NORM}}(f, P_{\text{IN}})$  for the PA are presented in Figures 7-26 and 7-27 respectively.

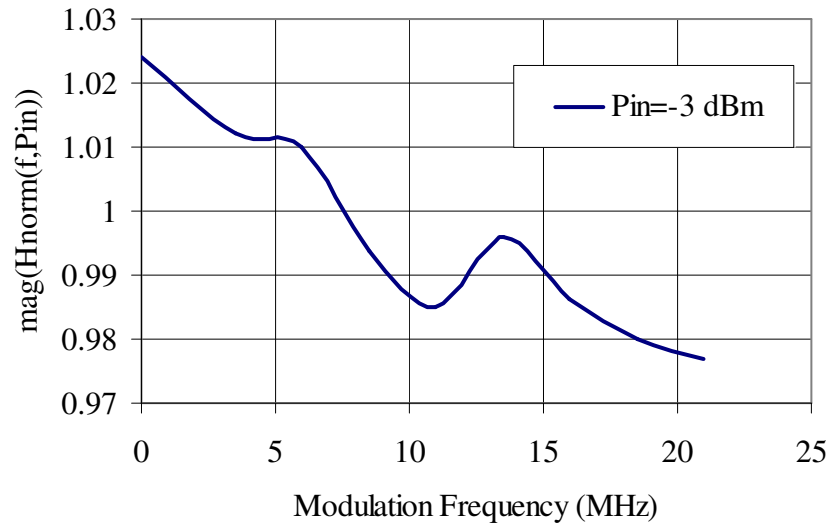


Figure 7-26: Magnitude of the normalised frequency response  $H_{\text{NORM}}(f, P_{\text{IN}})$  for the considered PA ZHL-1042J at -3 dBm input power level

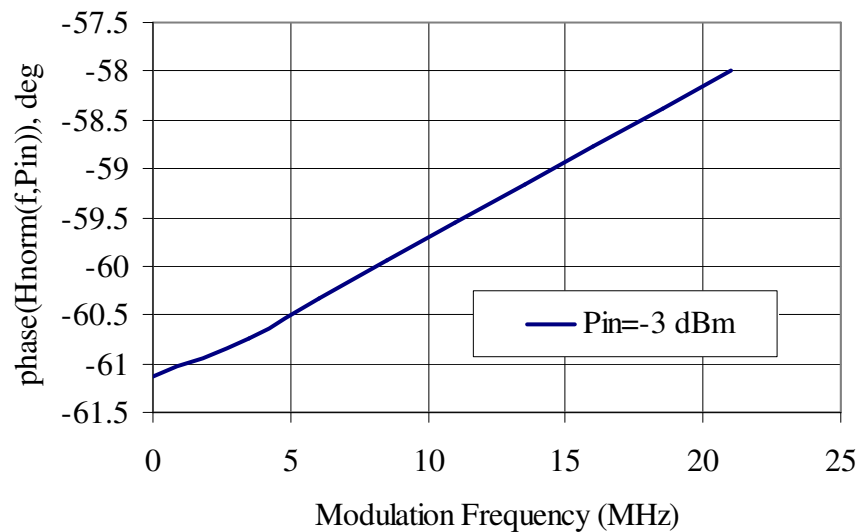


Figure 7-27: Phase of the normalised frequency response  $H_{\text{NORM}}(f, P_{\text{IN}})$  for the considered PA ZHL-1042J at -3 dBm input power level

The laboratory experiments are carried out using the test bed presented in Figure 7-17 with the proposed predistorter implemented in Matlab according to the block diagram depicted in Figure 7-18. The input pseudo-random sequence PN9 is generated and mapped to QPSK with I and Q levels of  $\pm 0.7071$  V. The baseband equalisation procedure is accomplished in order to pre-compensate the memory effects of the PA by multiplying the input signal with the complex frequency response coefficients in the frequency domain. For the considered ZHL-1042J PA and 5-MHz WCDMA input signal, 16 frequency points are used. Further, the complex signal is split into I and Q components and subjected to the memoryless predistortion.

From the 2.1-GHz fundamental-frequency polynomial model (7.14), the magnitude factors of the distortion components for the first injection are calculated as:  $G_3(t) = -59.2 \cdot |V_s(t)|^2$ ,  $G_5(t) = 91.3 \cdot |V_s(t)|^4$ . Three iterations of the input signal predistortion are performed. The injected distortion-components' magnitude factors are updated for the 2<sup>nd</sup> iteration as:

$$G_3^{(1)}(t) = -59.2 \cdot |V_s(t)|^2 \cdot \left(-1 + \left(1 - \frac{-59.2 \cdot |V_s(t)|^2 + 91.3 \cdot |V_s(t)|^4}{14.37}\right)^3\right), \quad (7.17)$$

$$G_5^{(1)}(t) = 91.3 \cdot |V_s(t)|^4 \cdot \left(-1 + \left(1 - \frac{-59.2 \cdot |V_s(t)|^2 + 91.3 \cdot |V_s(t)|^4}{14.37}\right)^5\right). \quad (7.18)$$

Further, for the 3<sup>rd</sup> iteration, the corresponding values of  $G_3^{(2)}(t)$  and  $G_5^{(2)}(t)$  are calculated as:

$$G_3^{(2)}(t) = G_3^{(1)}(t) \cdot \left(-1 + \left(1 - \frac{G_3^{(1)}(t) + G_5^{(1)}(t)}{14.37}\right)^3\right), \quad (7.19)$$

$$G_5^{(2)}(t) = G_5^{(1)}(t) \cdot \left(-1 + \left(1 - \frac{G_3^{(1)}(t) + G_5^{(1)}(t)}{14.37}\right)^5\right). \quad (7.20)$$

The updated distortion components are injected into the original in-phase and quadrature signals according to the proposed memoryless DPD as:

$$I_{DPD}^{(3)}(t) = I(t) - \frac{G_3^{(2)}(t) + G_5^{(2)}(t)}{14.37} \cdot I(t), \quad (7.21)$$

$$Q_{DPD}^{(3)}(t) = Q(t) - \frac{G_3^{(2)}(t) + G_5^{(2)}(t)}{14.37} \cdot Q(t). \quad (7.22)$$

The predistorted signals  $I_{DPD}$  and  $Q_{DPD}$  are transferred into the memory of the waveform generator Agilent E4433B and used for generating a 5-MHz WCDMA signal at 2.1 GHz carrier. The obtained RF signal is passed through the PA and further transferred to the VSA for measurements.

The computational complexity of the designed predistorter is estimated as the number of stored coefficients and mathematical operations required for the memoryless and memory-compensating parts of the DPD. According to Table 6.1, for the 5<sup>th</sup>-order polynomial model and 3 injections, the number of required for the memoryless DPD coefficients equals to 6, whereas the number of real multiplications and additions equals to 25 and 14 respectively. According to Table 7.1, for a QPSK signal, the number of complex multiplications and stored coefficients is equivalent to the number of frequency points, which in the experiment equals to 16. Therefore, the overall computational complexity of the designed predistorter can be estimated as follows. The total number of stored coefficients equals to 22. The total number of multiplications and additions is 41 and 14 respectively. Also, 16-points DFT and IDFT procedures are required.

The measured spectra regrowth at the output of the power amplifier without DPD (a), with the conventional DPD (b) and with the proposed DPD including three injections of the baseband distortion components and pre-compensation of PA memory effects (c) are presented in Figure 7-28.

The spectra re-growth improvement of up to 25 dB is achieved by using the proposed method, whereas only a 12 dB improvement on average is obtained by using the conventional DPD. Figure 7-29 shows the measured higher and lower ACPRs at the offset frequencies of 7 MHz without and with the proposed DPD. As can be seen from the Figure, ACPR without DPD approaches -15 dBc for high power levels, whereas both the ACPRs are below -31 dBc when the proposed DPD is used. Therefore, the proposed predistortion technique brings a 16-dB improvement in ACPR.

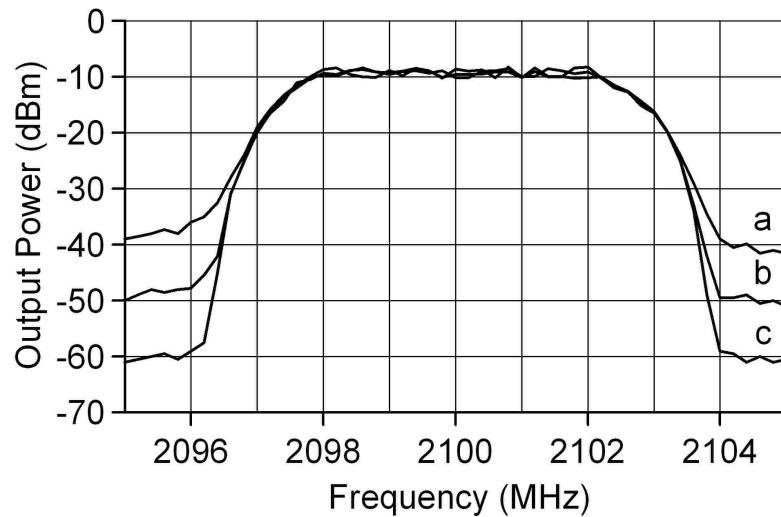


Figure 7-28: Measured output spectra of a 5-MHz WCDMA signal with a 2.1 GHz carrier at the output of the PA ZHL-1042J: (a) without DPD; (b) conventional DPD; (c) proposed DPD using 3 injections and pre-compensation of the memory effects

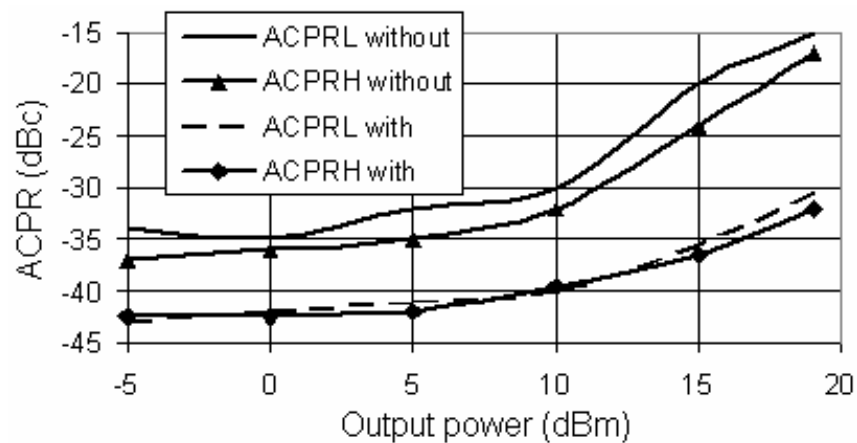


Figure 7-29: Measured ACPRs for 7-MHz offsets of a 5-MHz WCDMA signal with 2.1 GHz carrier at the output of the PA ZHL-1042J without DPD and with the proposed DPD using 3 injections and pre-compensation of the memory effects

### 7.6.3 5-MHz 16-QAM Signal Case

In this Section, the performances of the proposed predistorter are verified experimentally using a 5-MHz 16-QAM digitally modulated signal at -5 dBm input power. The 16-QAM modulation scheme includes three baseband power levels, as shown in Appendix-C. The baseband voltage and power levels for the considered signal are presented in Table 7.3. The magnitude and phase of the normalised inverse frequency response of the considered PA (ZHL-1042J) are extracted from the gain and phase curves for the corresponding power levels. The magnitude of the input voltage is calculated as  $mag(V_{IN}) = mag(V_{LO}) \cdot \sqrt{mag(I)^2 + mag(Q)^2}$ , where  $V_{LO}$  is the carrier voltage of the Local Oscillator (LO). For a 50-ohm impedance, the input power level is related to the input voltage magnitude as  $P_{IN\_dBm} = 10 \cdot \log(10 \cdot mag(V_{IN})^2)$ . For -5-dBm carrier power, the corresponding voltage magnitude of the LO is  $mag(V_{LO}) = 0.1778$  V. Then, the values of  $mag(V_{IN})$  and  $mag(P_{IN})$  corresponding to -5-dBm carrier power are calculated, as shown in Table 7.3.

For the considered Mini-Circuits ZHL-1042J PA, the normalised complex frequency-response values  $H_{NORM}(f, P_{IN})$  are extracted from the gain and phase characteristics at the input power levels of -11.88 dBm, -4.89 dBm and -2.34 dBm. The magnitude and phase of the normalised frequency response  $H_{NORM}(f, P_{IN})$  for the PA are presented in Figures 7-30 and 7-31 respectively.

**TABLE 7.3:** Voltage and power levels for the experiment

| $mag(I)$ , V | $mag(Q)$ , V | $mag(V_{BB})$ , V | $P_{BB}$ , dBm | $mag(V_{IN})$ , V | $P_{IN}$ , dBm |
|--------------|--------------|-------------------|----------------|-------------------|----------------|
| 0.32         | 0.32         | 0.45              | 3.12           | 0.08              | -11.88         |
| 0.32         | 0.96         | 1.01              | 10.11          | 0.18              | -4.89          |
| 0.96         | 0.96         | 1.36              | 12.66          | 0.24              | -2.34          |

$P_{LO} = -5$  dBm;  $V_{LO} = 0.1778$  V

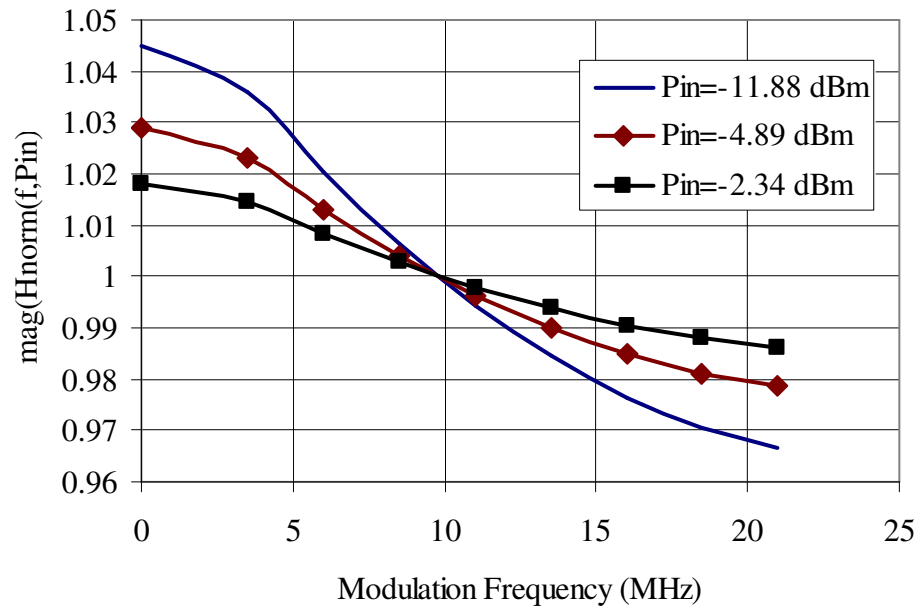


Figure 7-30: Magnitude of the normalised frequency response  $H_{\text{NORM}}(f, P_{\text{IN}})$  for the considered PA ZHL-1042J at three input power levels

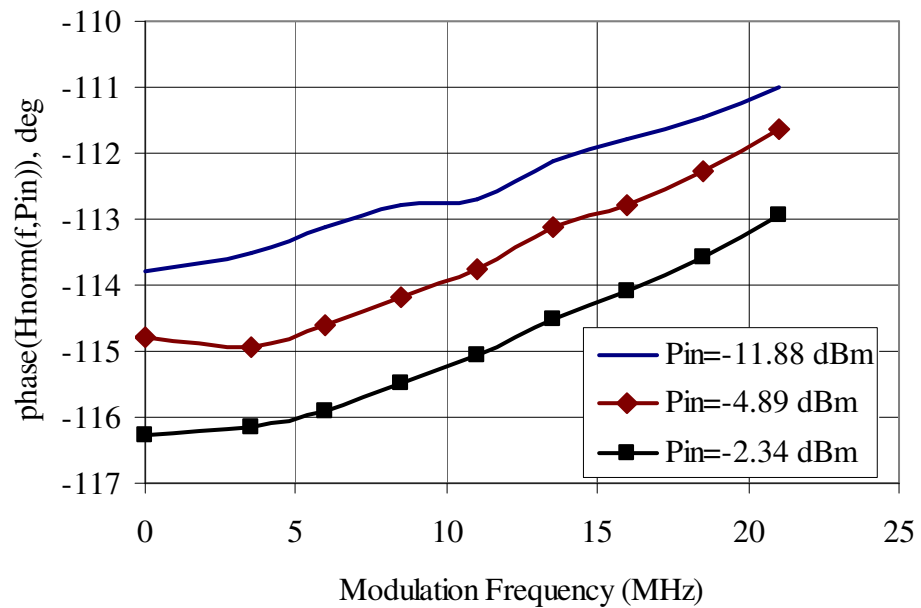


Figure 7-31: Phase of the normalised frequency response  $H_{\text{NORM}}(f, P_{\text{IN}})$  for the considered PA ZHL-1042J at three input power levels

Using the test bed presented in Figure 7-17, the laboratory experiments are carried out for the proposed predistorter, which is implemented in Matlab according to the configuration depicted in Figure 7-18. 512 bits of the PN9 sequence (see Appendix-C)

are generated and mapped to 16-QAM with I and Q levels of  $\pm 0.3203$  V and  $\pm 0.9608$  V. The baseband equalisation procedure is accomplished in order to pre-compensate the memory effects of the PA by multiplying the input signal with the complex frequency response coefficients in the frequency domain. For the considered ZHL-1042J PA and 5-MHz 16-QAM input signal, 16 frequency points are used. Further, the complex signal is split into I and Q components and subjected to the memoryless predistortion.

From the nonlinear model (7.16), the magnitude factors of the distortion components for the first injection are calculated as:  $G_3(t) = -65.7 \cdot |V_s(t)|^2$ ,  $G_5(t) = 130.3 \cdot |V_s(t)|^4$ , and  $G_7(t) = -70.5 \cdot |V_s(t)|^6$ . Three iterations of the input signal predistortion are performed. The injected distortion-components' magnitude factors are updated for the 2<sup>nd</sup> iteration as:

$$G_3^{(1)}(t) = -65.7 \cdot |V_s(t)|^2 \cdot \left(-1 + \left(1 - \frac{-65.7 \cdot |V_s(t)|^2 + 130.3 \cdot |V_s(t)|^4 - 70.5 \cdot |V_s(t)|^6}{14.7}\right)^3\right), \quad (7.23)$$

$$G_5^{(1)}(t) = 130.3 \cdot |V_s(t)|^4 \cdot \left(-1 + \left(1 - \frac{-65.7 \cdot |V_s(t)|^2 + 130.3 \cdot |V_s(t)|^4 - 70.5 \cdot |V_s(t)|^6}{14.7}\right)^5\right), \quad (7.24)$$

$$G_7^{(1)}(t) = -70.5 \cdot |V_s(t)|^6 \cdot \left(-1 + \left(1 - \frac{-65.7 \cdot |V_s(t)|^2 + 130.3 \cdot |V_s(t)|^4 - 70.5 \cdot |V_s(t)|^6}{14.7}\right)^7\right). \quad (7.25)$$

For the 3<sup>rd</sup> iteration, the corresponding values of  $G_3^{(2)}(t)$ ,  $G_5^{(2)}(t)$  and  $G_7^{(2)}(t)$  are calculated as:

$$G_3^{(2)}(t) = G_3^{(1)}(t) \cdot \left(-1 + \left(1 - \frac{G_3^{(1)}(t) + G_5^{(1)}(t) + G_7^{(1)}(t)}{14.7}\right)^3\right), \quad (7.26)$$

$$G_5^{(2)}(t) = G_5^{(1)}(t) \cdot \left(-1 + \left(1 - \frac{G_3^{(1)}(t) + G_5^{(1)}(t) + G_7^{(1)}(t)}{14.7}\right)^5\right), \quad (7.27)$$

$$G_7^{(2)}(t) = G_7^{(1)}(t) \cdot \left(-1 + \left(1 - \frac{G_3^{(1)}(t) + G_5^{(1)}(t) + G_7^{(1)}(t)}{14.7}\right)^7\right). \quad (7.28)$$

The updated distortion components are injected into the original in-phase and quadrature signals according to the proposed memoryless DPD as:

$$I_{DPD}^{(3)}(t) = I(t) - \frac{G_3^{(2)}(t) + G_5^{(2)}(t) + G_7^{(2)}(t)}{14.7} \cdot I(t), \quad (7.29)$$

$$Q_{DPD}^{(3)}(t) = Q(t) - \frac{G_3^{(2)}(t) + G_5^{(2)}(t) + G_7^{(2)}(t)}{14.7} \cdot Q(t). \quad (7.30)$$

The predistorted signals  $I_{DPD}$  and  $Q_{DPD}$  are transferred into the memory of the waveform generator Agilent E4433B and used for generating a 5-MHz 16-QAM-modulated RF signal at 3.5 GHz carrier. The obtained RF signal is passed through the PA and further transferred to the VSA for measurements.

The computational complexity of the designed predistorter is estimated as follows. According to Table 6.1, for the 7<sup>th</sup>-order polynomial model and 3 injections, the number of required for the memoryless DPD coefficients equals to 8, whereas the number of real multiplications and additions equals to 34 and 21 respectively. For the 16-QAM equalisation system, the number of complex multiplications is equivalent to the number of frequency points, whereas the number of stored coefficients equals to the number of frequency points times three, as shown in Table 7.1. For the considered DPD system excited with a 16-QAM input signal, the number of stored coefficients equals to 48, whereas the number of complex multiplications equals to 16. Therefore, the overall computational complexity of the designed predistorter can be described as follows. The total number of stored coefficients equals to 56. The total number of multiplications and additions is 50 and 21 respectively. Also, 16-points DFT and IDFT procedures are required for the operation of the predistorter.

The measured spectra regrowth results at the output of the power amplifier ZHL-1042J without DPD (a) and with the proposed DPD (b) are presented in Figure 7-32. A spectra regrowth improvement of up to 25 dB can be observed for a 5-MHz 16-QAM signal by using the proposed predistortion technique with 3 injections. Figure 7-33 shows the measured ACPRs for the higher (ACPRH) and lower (ACPRL) adjacent channels at the offset frequencies of 7 MHz without and with the proposed DPD. The improvement of up to 18 dB can be observed.

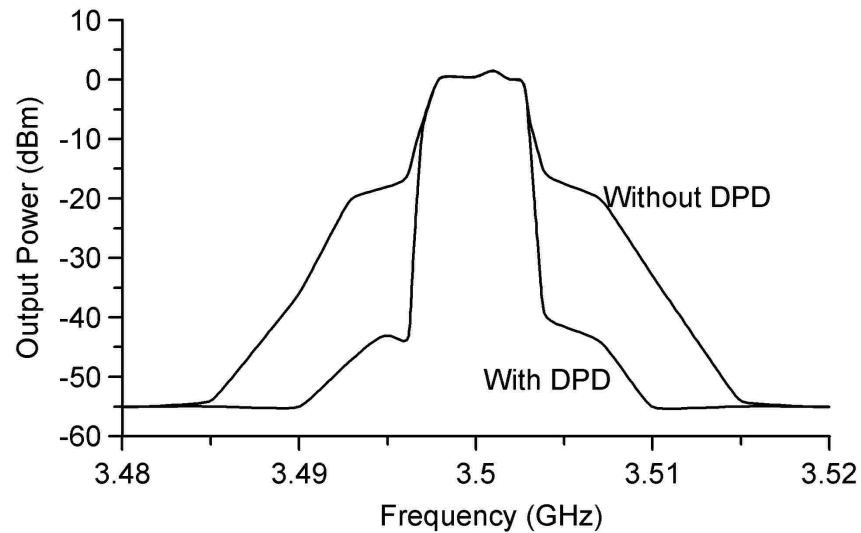


Figure 7-32. Measured output spectra of a 5-MHz 16-QAM signal at the output of the PA ZHL-1042J at 3.5 GHz: (a) without DPD; (b) proposed baseband DPD using 3 injections and pre-compensation of the memory effects

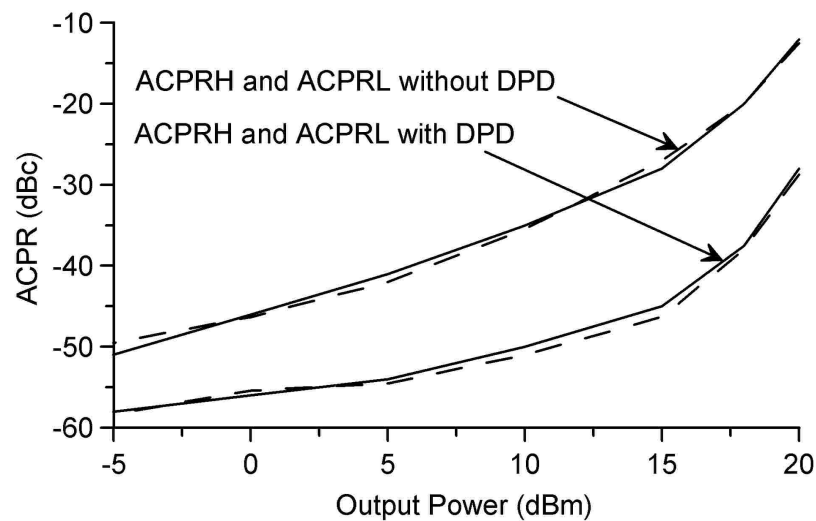


Figure 7-33. Measured ACPRs for 7-MHz offsets of a 5-MHz 16-QAM signal at the output of the PA ZHL-1042J without DPD and with the proposed DPD using 3 injections and pre-compensation of the memory effects

## 7.7. Conclusion

The proposed digital predistortion technique for linearising wideband wireless transmitters incorporating the distortion components iterative injection and baseband equalisation methods has been presented and verified by simulations and experiments.

The baseband equalisation method was developed for compensating PA memory effects. The theoretical concept, practical implementation and computational complexity of the proposed equalisation method were depicted in the Chapter. The memory-compensation performances of the method were verified by simulations. Memory effects quantification procedures were described in the Chapter and executed during the simulations. The PA characterisation and equaliser coefficients extraction procedures were described.

The baseband equalisation method was verified by simulations with a 3.5-MHz 256-OFDM 16-QAM signal. The results demonstrated high distortion-improvement performances of the equalisation technique.

An adaptation circuit using the offline training scheme was incorporated into the predistorter for enabling its adaptivity to environmental conditions and self-heating.

The feasibility and performances of the complete lineariser including the proposed iterative injection memoryless predistorter and baseband equaliser for minimising memory effects were verified experimentally. The proposed distortion component iterative injection method demonstrated high linearising performances while tested with different power amplifiers, types of signals, and number of injections. The developed baseband equalisation technique was experimentally verified with different signal bandwidths and PA exhibiting asymmetrical memory effects.

The measured results prove the proposed distortion component iterative injection method together with the baseband equalisation technique offer significant improvements in the linearising performances with a reasonably low computational complexity compared to those of the conventional DPD.

## 7.8. References

- [7.1] T. Liu, S. Boumaiza, and F. M. Ghannouchi, "Augmented Hammerstein predistorter for linearization of broad-band wireless transmitters", *IEEE Trans. on Microwave Theory and Techniques*, vol. 54, no. 4, pp. 1340-1349, June 2006.
- [7.2] T. Liu, S. Boumaiza, and F. M. Ghannouchi, "Pre-compensation for the dynamic nonlinearity of wideband wireless transmitters using augmented Wiener predistorters", In *Proc. Asia-Pacific Microwave Conference (APMC)*, vol. 4, pp. 4-7, Suzhou, China, Dec. 2005.
- [7.3] S. Armour, A. Nix, and D. Bull, "Complexity evaluation for the implementation of a pre-FFT equalizer in an OFDM receiver", *IEEE Trans. on Consumer Electronics*, vol. 46, no. 3, pp. 428-437, Aug. 2000.
- [7.4] T. Ramashri, and P. G. Reddy, "Adaptive channel equalizer and DTMF detection", *ARPN Journal of Engineering and Applied Science*, vol. 3, no. 2, pp. 31-34, Apr. 2008.
- [7.5] T. Wang and J. Ilow, "Compensation of nonlinear distortions with memory effects in OFDM transmitters," in *Proc. IEEE Global Telecomm. Conf.*, vol. 4, pp. 2398-2403, Dallas, USA, Nov. 2004.
- [7.6] D. Bondar, and D. Budimir, "A new digital predistortion for linearity improvement and suppression of memory effects", in *Proc. European Microwave Week Conference EMW'09*, Roma, Italy, September 2009.
- [7.7] D. Bondar, and D. Budimir, "A Digital Predistorter for Wireless Transmitters", *International Journal of RF and Microwave Computer-Aided Engineering*, 2009 (accepted for publication).
- [7.8] D. Bondar, and D. Budimir, "Digital baseband predistortion of wideband power amplifiers with improved memory effects", in *Proc. IEEE Radio and Wireless Symposium RWS'09*, San-Diego, USA, pp. 284-287, January 2009.
- [7.9] D. Bondar, and D. Budimir, "Digital baseband components injection technique to enhance linearity in wideband wireless transmitters," *IEEE Transactions on Microwave Theory and Techniques*, Submitted.

- [7.10] N. Mizusawa, and S. Kusunoki, "Third- and fifth-order baseband component injection for linearisation of the power amplifier in a cellular phone," *IEEE Transactions on Microwave Theory and Techniques*, vol. 53, no. 4, pp. 3327-3334, Apr. 2005.

## 8. CONCLUSION

This Chapter presents overall conclusions to the performed research work, including a summary of the thesis, original contributions to knowledge and suggestions for the future work.

### 8.1. Thesis Summary

In wireless communication systems, the design of linear and efficient transmitters for base stations and terminals is a major task. As the most important part of a transmitter is the power amplifier, a great concern is given for enhancing the PA performances. A common approach for achieving both the high linearity and efficiency is to design a PA operating in a nonlinear efficient mode and to provide its linearisation by an external device. Therefore, linearisation of power amplifiers is becoming one of the most important issues in wireless communication systems.

In this thesis, a comprehensive research work on the topic of linearisation of power amplifiers for wireless communication systems has been presented. An advanced adjustable linearisation technique incorporating the iterative digital predistortion method for memoryless nonlinearity compensation and the baseband equalisation method for minimising memory effects had been developed during the research work. The theoretical concept, practical implementation and validation of the proposed technique by simulations and experiments were depicted in the thesis.

The research work included the following areas. Initially, PA parameters, classes of amplification, the trade-off between efficiency and linearity, nonlinear analysis and characteristics used to quantify PA performances were described. A comparative review of the existing linearisation techniques was accomplished with highlighting the advantages and shortcomings of each method. As digital predistortion is one of the most cost-effective, easily integrated and flexible linearisation methods, it was chosen as a basis for the development of the proposed technique. A study of the origins, types and consequences of memory effects, as well as an overview of the methods used to quantify, model and compensate for memory effects, was presented. As the baseband equalisation technique offers a minimisation of the memory effects in wideband

communication systems by digitally processing the input signal without modifying the RF part of the transmitter, the method was implemented as the memory-compensating part of the lineariser. Proposed solutions to the problem of linearisation of wideband power amplifiers were presented, including the in-band distortion modelling technique, the baseband distortion component iterative injection DPD and the baseband equalisation method. In order to develop a compact and convenient procedure of characterising the PA nonlinearity and calculating the predistorter parameters, a generalised in-band distortion modelling technique was proposed. Two model extraction procedures based on the frequency response analysis and least-squares polynomial regression analysis were developed and experimentally examined in the research work. In order to overcome the distortion compensation limit inherent in injection techniques, an advanced baseband distortion components iterative injection DPD was developed. In addition, a Matlab-ADS co-simulation system was developed for carrying out enhanced simulations and utilising the advantages of both the softwares. The proposed overall linearisation technique was validated by simulations and by experiments with different types of signals and power amplifiers. The simulated and measured results proved the feasibility of the proposed method and showed its high linearising performance and adjustability. Detailed conclusions to each of the areas of the current research work are presented below.

In Chapter 2, the general parameters of RF power amplifiers were introduced together with the description of the amplification principle, classes of amplification and nonlinear analysis. The main parameters, such as gain, conduction angle, 1dB compression point and TOI, were defined and the relations between them discussed. The measures of the PA linearity and efficiency were presented. A description of the classes of operation and their relation to the conduction angle and efficiency of PAs were discussed. Efficiency and linearity trade-off was introduced. The nonlinear analysis using power series was described. The main characteristics and phenomena related to nonlinear distortions were discussed. Particularly, AM/AM and AM/PM distortions, EVM, HD, IM, CM and ACPR were depicted.

In Chapter 3, a comparative overview of linearisation techniques was presented, including the feedback, feedforward, envelop elimination and restoration, linear amplification using nonlinear components, injection techniques analogue predistortion and digital predistortion. The main advantages and drawbacks of the linearisation techniques are summarised below. The feedback methods have a high cancellation

performance and relatively high efficiency, but exhibit stability problems and bandwidth limitations. The feedforward methods offer very high linearising performance with high stability and bandwidth, but they have low efficiency and high circuit complexity. The EER technique has a high efficiency, but low cancellation performance and moderate bandwidth, also suffering from stability problems and practical implementation difficulties. The LINC method is theoretically suitable for increasing both the efficiency and linearity of a PA, but is extremely sensitive to real-life device imperfections, and hence is difficult for practical implementation. The frequency products injection techniques are simple and efficient, but also extremely sensitive to the phase shift, and hence unstable and problematic for wideband systems. Analogue predistortion is simple in implementation and able to linearise wideband PAs, but suffers from low-to-moderate linearising performance and adaptation difficulties. The digital predistortion methods are simple in implementation and integration, also exhibiting high efficiency, as they do not require additional RF components. However, the conventional LUT and polynomial DPD techniques offer only moderate linearising performance and have high DSP computational complexity. The baseband components injection DPD has a potential of achieving high linearising performance, while maintaining relatively low computational complexity. For this reason, the method was selected as a basis for the advanced DPD technique developed in this thesis.

In Chapter 4, memory effects of power amplifiers were studied, including the reasons behind memory effects and their impact on the PA behaviour. Depending on the origins, memory effects are categorised as electrical and thermal. The electrical memory effects are mainly produced by reactive elements of the PA biasing and matching circuits. They are typical for wideband transceivers. The thermal memory effects are attributed to varying temperature-dependent electrical parameters of power amplifiers. They are the dominant source of memory effects for narrowband systems. Depending on the distortion behaviour, memory effects are classified as symmetrical and asymmetrical. The symmetrical memory effects can easily be compensated by a filter, whereas the asymmetrical memory effects present more challenges to the transmitter design and need to be compensated by special circuits. For quantification of memory effects, a single-tone, two-tone or digitally modulated test can be used. The coefficients for the memory equalisation circuits can be calculated using a single-tone or two-tone test, whereas the digitally modulated test is particularly helpful in assessing the performances of the complete system. The main approaches for compensating memory

effects were described in Chapter 4. They are the impedance optimisation, envelope filtering, envelope injection and baseband equalisation techniques. The first method is able to improve the electrical memory effects by flattening the impedances over the frequency band. However, the method is difficult in practical implementation, time consuming and requires a significant hardware modification. The envelope filtering technique is simple, as it requires only one filter. However, the method is unstable and not suitable for compensating for the asymmetrical memory effects. The envelope injection technique is able to minimise both the symmetrical and asymmetrical memory effects. However, the method increases the circuit's complexity and requires additional RF components. Moreover, the envelope filtering and envelope injection techniques have practical difficulties in providing initial tuning and maintaining the proper phase and amplitude relations. The most promising tool for minimising memory effects is the baseband equalisation technique, which allows pre-compensating the frequency-dependent behaviour by digitally processing the input signal without modifying the RF path. The method is simple and convenient for the software implementation, whereas it may significantly increase the circuit's complexity if implemented in hardware.

In Chapter 5, the modelling techniques for representing PA memory nonlinear behaviour were examined. A generalised in-band distortion modelling technique was developed and verified experimentally, which enabled a quick and convenient characterisation of a PA and calculating the predistorter coefficients by the derived formulae. Two alternative nonlinear model extraction techniques based on the PA frequency-response analysis and least-squares polynomial regression method were developed and discussed. The proposed in-band distortion modelling technique together with the model extraction procedures were examined and verified experimentally. The experimental results proved the feasibility and accuracy of the proposed modelling methods and revealed the trade-off between the model extraction techniques: the model extraction procedure based on the least-squares polynomial regression offers a higher accuracy, nevertheless suffers from a higher time consumption and complexity compared to those of the PA frequency-response analysis. A comprehensive overview of the memory nonlinear modelling techniques was accomplished including the Volterra series; the models addressing linear memory, which are a two-box Wiener, two-box Hammerstein and three-box Wiener-Hammerstein models; and the models addressing nonlinear memory, which are a nonlinear feedback, nonlinear cascade and parallel Wiener models. The Volterra series is the most generalised and comprehensive

approach for representing both the nonlinear behaviour and memory effects. However, the practical difficulty of calculating the Volterra kernels increases the complexity of the method and restricts its application to only weakly nonlinear systems. Assuming that the memory effects and nonlinear behaviour of a PA can be represented by separate blocks, special cases of the Volterra series are derived, which are called the Wiener or Hammerstein models depending on the order, in which the nonlinear and memory blocks are connected.

In chapter 6, the proposed memoryless digital predistortion technique with adjustable ratio of linearisation degree to computational complexity based on the distortion components iterative injection method was presented and verified by simulations and experiments. The proposed memoryless DPD allows overcoming the distortion compensation limit peculiar to the injection techniques. The theoretical concept and practical operation of the proposed iterative nonlinearity compensation method were depicted in the Chapter. The computational complexity and linearising performances were examined. The proposed digital predistortion technique is adjustable for achieving the best ratio of linearisation degree to computational complexity for any particular application. A Matlab-ADS co-simulation system was developed for providing powerful tools for simulating both the DSP and RF parts of a transmitter. The co-simulation system can be configured according to different layouts depending on the simulation requirements. The proposed DPD was verified by simulations with QPSK, 16-QAM, 64-QAM, 256-OFDM 64-QAM and 256-OFDM 16-QAM signals. The results demonstrated high linearising performances and adjustability of the proposed DPD technique. The feasibility and performances of the memoryless digital predistortion technique were verified experimentally. The proposed distortion component iterative injection method demonstrated high linearising performances while tested with different types of signals and number of injections. The measured results proved the proposed distortion component iterative injection method offered significant improvements in the linearising performance with a reasonably low computational complexity compared to those of the conventional DPD.

In chapter 7, a baseband equalisation technique for compensating memory effects of PAs was developed and verified by simulations and experiments. The theoretical concept, practical implementation and computational complexity of the proposed equalisation method were depicted in the Chapter. The memory-compensation performances of the method were verified by simulations using the developed Matlab-

ADS co-simulation system. The PA characterisation and equaliser coefficients' extraction procedures were described. The adaptation circuit using an offline training scheme was designed and incorporated into the predistorter for enabling its adaptivity to environmental conditions and self-heating. The feasibility and performances of the complete lineariser including the memoryless DPD sub-system and memory-compensating sub-system were verified experimentally with different signals and PAs exhibiting memory effects. The proposed digital predistorter with improved memory effects was tested for linearising a 5-MHz WCDMA system at 2.1 GHz and a 5-MHz 16-QAM system at 3.5 GHz. The measured results proved the proposed distortion component iterative injection method together with the baseband equalisation technique offered significant improvements in the linearising performance with a reasonably low computational complexity compared to those of the conventional DPD. The tunability of the proposed technique was demonstrated during the experiments. The proposed DPD can be adjusted to achieve the best ratio of linearisation degree to computational complexity for any particular application.

Overall, the current research work has achieved its aims of developing a digital predistortion system with enhanced performances by introducing the proposed solutions to the issues, which traditionally limit the characteristics of predistortion linearisers. Having implemented the proposed methods of baseband distortion components iterative injection for the memoryless nonlinearity compensation and the developed baseband adaptive equalisation technique for the memory effects compensation, an advanced digital predistorter with high linearising performances was designed. The feasibility and performances of the proposed DPD were validated by simulations using the developed Matlab-ADS co-simulation system and experiments with different power amplifiers and signal types. The measured results showed high linearising performances of the proposed predistorter and demonstrated its simple implementation and tunability.

## **8.2. Originality and Contribution to Knowledge**

This Section presents summary of the original developments including the developed techniques, circuits and systems, and the detailed contributions to knowledge provided by the research work.

### **8.2.1 Original Developments**

The overall developments to the area of digital predistortion of wideband wireless transmitters presented in the Thesis include the following techniques and systems.

The in-band distortion modelling technique together with the model extraction procedures based on the PA frequency-response analysis and least-squares polynomial regression have been developed and verified experimentally. The experimental results proved the feasibility and accuracy of the proposed modelling methods and revealed the trade-off between the model extraction techniques: the model extraction procedure based on the least-squares polynomial regression has a higher accuracy, but also a higher time consumption and complexity compared to those of the PA frequency-response analysis.

The distortion components iterative injection technique with adjustable ratio of linearisation degree to computational complexity was developed for the memoryless linearisation. The proposed memoryless DPD allows overcoming the distortion compensation limit peculiar to the injection techniques. The theoretical concept and practical operation of the proposed iterative nonlinearity compensation method were depicted in the thesis. The computational complexity and simulated performances were presented.

The baseband equalisation method was developed for compensating PA memory effects. The theoretical concept, practical implementation and computational complexity of the proposed equalisation method were depicted in the thesis. The memory-compensation performances of the method were verified by simulations. Memory effects quantification procedures were described in the thesis and executed during the simulations. The PA characterisation and equaliser coefficients extraction procedures were described.

An adaptation circuit using the offline training scheme was incorporated into the predistorter for enabling its adaptivity to environmental conditions and self-heating.

Advanced Matlab-ADS co-simulation system was developed for providing powerful tools for simulating both the DSP and RF parts of the transmitter. The co-simulation system can be configured according to different layouts depending on the simulation requirements. The proposed DPD was verified experimentally and by simulations with QPSK, 16-QAM, 64-QAM, 256-OFDM 64-QAM and 256-OFDM 16-QAM signals. The results demonstrated high linearising performances and adjustability of the proposed DPD technique.

### **8.2.2 Contributions to Knowledge**

The original contributions to knowledge presented in this research work can be summarised as follows.

- For the first time, a baseband distortion components iterative injection technique has been proposed. The technique is adjustable for achieving the best ratio of linearisation degree to computational complexity. The proposed DPD is able to increase the linearising performance of conventional predistorters with a reasonably low computational complexity and to overcome the distortion compensation limit peculiar to the injection methods.
- The dependence of linearisation degree and computational complexity on the number of injections was investigated for the proposed technique.
- Compact analytical expressions for the in-band distortion modelling were derived. A series of coefficients near the corresponding in-band distortion components was obtained. The proposed formulae simplified the process of PA characterisation and calculating the predistorter parameters. An experimental validation proved the feasibility and accuracy of the proposed modelling method.
- The methods of extracting PA polynomial model based on the frequency response analysis and least-squares polynomial regression analysis were developed and evaluated experimentally. The area of implementation, advantages and drawbacks of each of the method were discussed.

- A baseband equalisation technique was developed for compensating the PA memory effects by digitally processing the input signal without modifying the RF path. The theoretical concept and practical implementation of the method were discussed.
- The performances of the proposed predistorter were evaluated for different power amplifiers, types of signals and power levels, including 5-MHz WCDMA at 2.1 GHz, 5-MHz QPSK at 500 MHz, 3.5-MHz 16-QAM at 500 MHz and 5-MHz 16-QAM at 3.5 GHz cases. The proposed DPD was proven to have a higher linearising performance compared to the conventional one, with a possibility of adjusting the performances and computational complexity for any particular application.

### **8.3. Future Work**

One of the directions for the future work would be developing and applying the proposed DPD technique for compensating real-life *I/Q* imperfections in wireless transceivers. Upon achieving successful results, the method would be investigated for improving the linearity and compensating real-life imperfections of the complete transmitter, including the PA, modulator and other components.

Another area of the suggested future work includes designing of a Matlab-ADS co-simulation system, which incorporates behavioural modelling of real PAs in Matlab, rather than using ADS library models, and carrying out simulations with the obtained models of real devices. This approach would offer wide possibilities of tuning and examining the predistorter by simulations before conducting the real experiment.

Despite a thorough experimental validation of the proposed DPD with different types of signals has been carried out during the research process, performance measurements of the predistorter excited with various forms of WiMAX signals can be included in the future work. Conducting experimental investigations for the 256-OFDM 16-QAM and 256-OFDM 64-QAM signals and comparing the obtained results to the simulations would provide extra information regarding the performances of the proposed DPD and accuracy of the simulations.

In addition, a comprehensive examination of the optimal layouts of the proposed DPD for implementation in base stations and mobile terminals of various wireless

---

standards would become an area of the future work. The research would include determining the optimal number of injections and frequency points as well as the most favourable structure of the adaptation circuit for each application.

As variations in environmental conditions cause degrading of the lineariser performances, the adaptive implementation of the proposed predistorter would be preferable. However, the feedback-based adaptation methods significantly increase the circuit's complexity. Therefore, another area for the future work includes investigation of different adaptation methods to find the best compromise between accuracy and complexity.

After that, a real-life implementation of the designed adaptive close-loop DPD would become a part of further studies. The real-life experiments with the proposed adaptive predistorter would evaluate the overall performance of the system before mass production.

---

## LIST OF PUBLICATIONS

- [1] D. Bondar, and D. Budimir, "A Digital Predistorter for Wireless Transmitters," *International Journal of RF and Microwave Computer-Aided Engineering* (accepted); electronic version: vol. 19, no 4, pp. 453 – 459, April 2009.
- [2] D. Bondar, and D. Budimir, "Digital baseband components injection technique to enhance linearity in wideband wireless transmitters," *IEEE Transactions on Microwave Theory and Techniques* (in preparation).
- [3] D. Bondar, D. Budimir, N. D. Lopez, X. Jiang, D. Maksimovic and Z. Popovic, "Linearisation of class-E power amplifier using digital baseband predistortion," *IEEE Radio and Wireless Symposium RWS'10*, San-Diego, USA, (submitted).
- [4] D. Bondar, and D. Budimir, "A new digital predistortion for linearity improvement and suppression of memory effects," in Proc. *European Microwave Week Conference EMW'09*, Roma, Italy, 28 September – 2 October 2009.
- [5] D. Bondar, D. Budimir, and B. Shelkovnikov, "Distortion components iterative injection technique for linearization of power amplifiers," in Proc. *19th International Crimean Conference "Microwave & Telecommunication Technology," CRIMICO'2009*, Sevastopol, Ukraine, September 2009.
- [6] D. Bondar, and D. Budimir, "Distortion improvement of power amplifiers with digital predistortion," in Proc. *10<sup>th</sup> IEEE Wireless and Microwave Technology Conference WAMICON'09*, Clearwater, USA, April 2009.
- [7] D. Bondar, and D. Budimir, "Digital baseband predistortion of wideband power amplifiers with improved memory effects," in Proc. *IEEE Radio and Wireless Symposium RWS'09*, San-Diego, USA, pp. 284-287, January 2009.

- 
- [8] D. Bondar, and D. Budimir, "Spectrum regrowth reduction in power amplifiers using digital baseband signal injection," in *Proc. Asia Pacific Microwave Conference APMC'08*, Hong-Kong, China, December 2008.
- [9] D. Bondar, D. Budimir, and B. Shelkovnikov, "Linearization of power amplifiers by baseband digital predistortion for OFDM transmitters," in *Proc. 18th International Crimean Conference "Microwave & Telecommunication Technology" CRIMICO'2008*, Sevastopol, Ukraine, vol. 1, pp: 270 – 271, September 2008.
- [10] D. Bondar, D. Budimir, and B. Shelkovnikov, "A new approach for non-linear analysis of power amplifiers," in *Proc. 18th International Crimean Conference "Microwave & Telecommunication Technology" CRIMICO'2008*, Sevastopol, Ukraine, vol. 1, pp. 125 – 128, September 2008.
- [11] D. Bondar, D. Budimir, and B. Shelkovnikov, "Minimizing memory effects in OFDM transmitters using adaptive baseband equalization," in *Proc. 18th International Crimean Conference "Microwave & Telecommunication Technology" CRIMICO'2008*, Sevastopol, Ukraine, vol. 1, pp. 272 – 275, September 2008.
- [12] D. Bondar, and D. Budimir, "WiMax power amplifier linearization through injection of base-band component," in *Proc. 11th International Symposium on Microwave and Optical Technology (ISMOT-2007)*, Roma, Italy, 17 – 21 December 2007.

## APPENDIX-A

### I/Q Generation using Matlab-ADS

The process of providing original and predistorted I/Q signals in the developed Matlab-ADS co-simulation system includes generation of the digital in-phase and quadrature signals in Matlab and re-calling it by ADS for simulations. The general layout for the ADS circuit, presented in Figure A-1 includes the block that is running Matlab program during the ADS simulations. The Matlab programs for generation QPSK, 16-QAM, 64-QAM and 64-OFDM 16-QAM signals are presented below. In Matlab, the symbols are generated digitally without assigning the carrier frequency and symbol rate, which is accomplished by the data flow (DF) simulation controller in ADS.

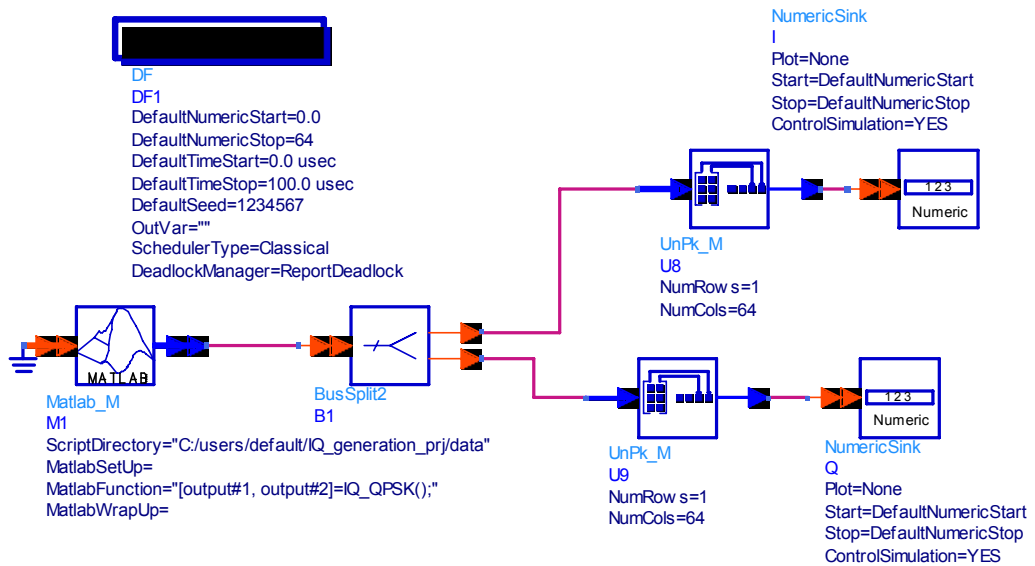


Figure A-1: I/Q generation circuit using Matlab and ADS

## Generating QPSK signal

```

function [I, Q]=IQ_QPSK() % Definition of a function without input
variables with output variables I and Q

N=64; % Number of generated symbols
M=4; % QPSK - rage of symbols {0,1,2,3}
X=randint(N,1,M); % Generation of a matrix-column with
dimension N x 1, which is composed of numbers in the range 0 ... M-1
Fd=1; % symbolrate, number of symbols per second (1Hz)
Fs=1*Fd; % samplerate: 1 sample per 1 symbol
Map=modmap(X,Fd,Fs,'qask',M); % mapping of X to M-QAM. Result is a
matrix with dimension N x 2 (2 columns)
I1=Map(:,1); % selection of the 1st column of the matrix
Q1=Map(:,2); % selection of the 2nd column of the matrix
C1=I1.^2+Q1.^2; % C1 - sum of the squares
U=mean(C1); % mean value
V=sqrt(U); % square root
I=I1/V; % Normalization by division I by the mean value
Q=Q1/V; % Normalization by division Q by the mean value
I=I'; % Transpose I from a column to a row (for export to ADS)
Q=Q'; % The same for Q

```

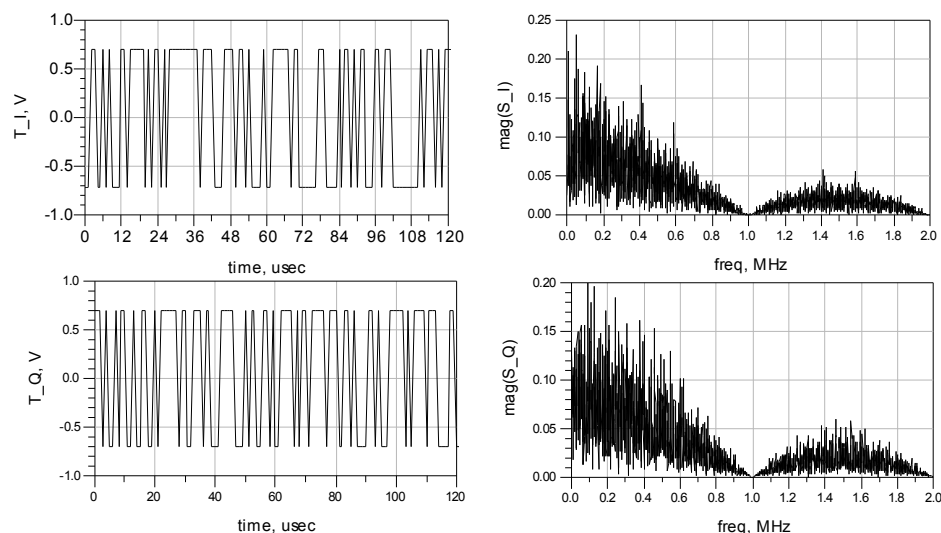


Figure A-2: Generated normalised digital I and Q signals for QPSK modulation in the time and frequency domains

## Generating 16-QAM signal

```

function [I, Q]=IQ_16QAM()
N=256;
M=16;
X=randint(N,1,M);
Fd=1;
Fs=1*Fd;
Map=modmap(X,Fd,Fs,'qask',M);
I1=Map(:,1);
Q1=Map(:,2);
C1=I1.^2+Q1.^2;
U=mean(C1);
V=sqrt(U);
I=I1/V;
Q=Q1/V;
I=I';
Q=Q';

```

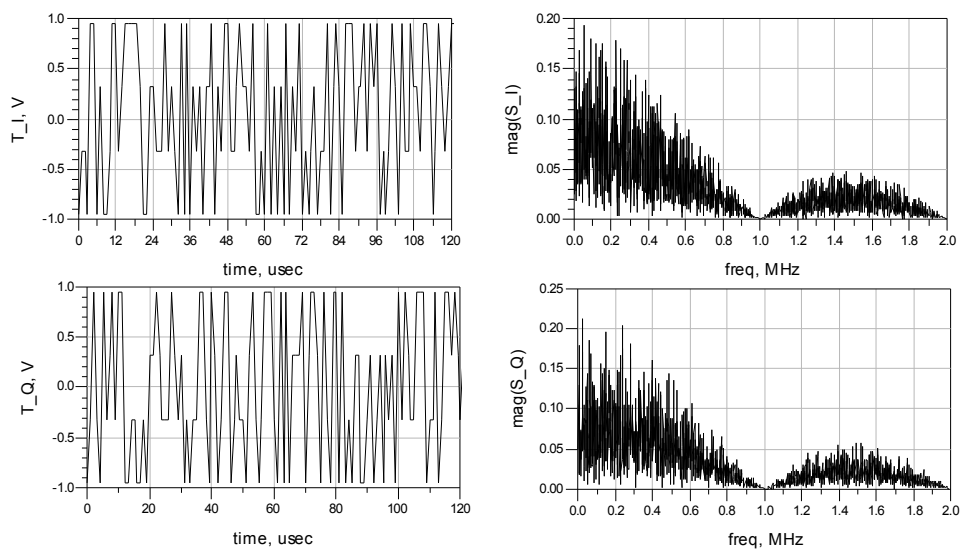


Figure A-3: Generated normalised digital I and Q signals for 16-QAM modulation in the time and frequency domains

## Generating 64-QAM signal

```

function [I, Q]=IQ_64QAM()
N=1024;
M=64;
X=randint(N,1,M);
Fd=1;
Fs=1*Fd;
Map=modmap(X,Fd,Fs,'qask',M);
I1=Map(:,1);
Q1=Map(:,2);
C1=I1.^2+Q1.^2;
U=mean(C1);
V=sqrt(U);
I=I1/V;
Q=Q1/V;
I=I';
Q=Q';

```

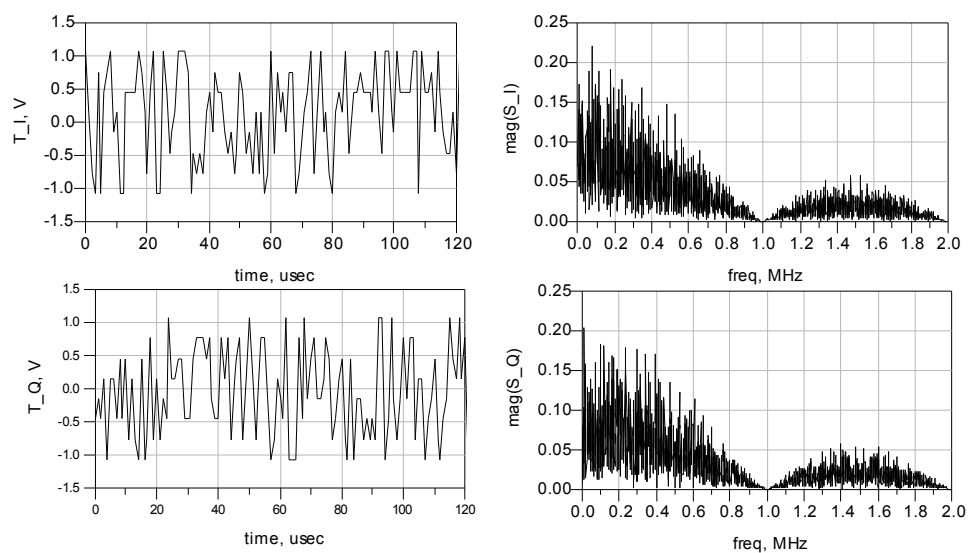


Figure A-4: Generated normalised digital I and Q signals for 64-QAM modulation in the time and frequency domains

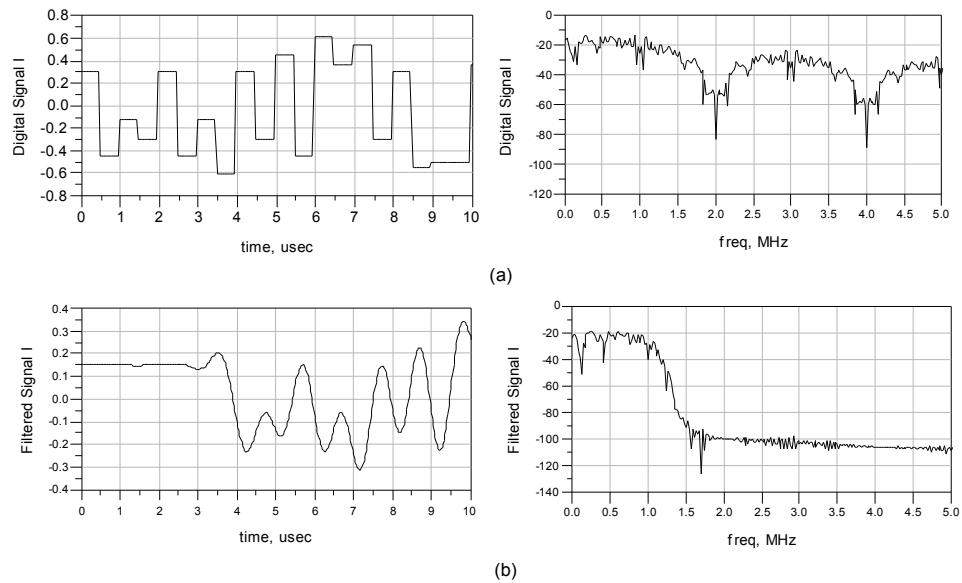


Figure A-5: Examples of the in-phase signal with 2-MHz symbol rate in the time and frequency domains: (a) original digital signal; (b) signal after DAC by raised-cosine filtering with the delay of 7 symbols and bandwidth equal to the symbol rate

## Generating 64-OFDM 16-QAM signal

```
function [I2, Q2]=OFDM_mod2() % Definition of a function without input
variables with output variables I2 and Q2
```

```
clear all;
```

```
% 16QAM 64OFDM
% FFT=64 => modulated data per OFDM frame = 64 - Guard_high -
Guard_low= 64-13-14-1 = 36 symbols
```

```
% then binary data per OFDM frame is 4*36 = 144 (because 16QAM gives
4 bits per carrier)
```

```
Ndata=360; % # of all transmitted data
Ns=36; % # of data symbols per OFDM frame
Nd=144; % # of data bits per OFDM frame
```

```
% how many frames needed for this amount of data
```

```

Nfr=10; % Nfr=chastnoe(Ndata/Ns)+1

FFT=64; % FFT size. it can be:
        % FFT = 64
        % FFT = 128
        % FFT = 256
        % FFT = 512
        % FFT = 1024
        % FFT = 2048

rate=3/4; % coding rate. it can be:
        % rate = 1/2
        % rate = 2/3
        % rate = 3/4

n=8/7; % sampling factor

Nc=Nd/n; % # of coded bits per OFDM symbol

Np=8; % # of pilot subcarriers

Ngl=13; % # of low guard subcarriers
Ngh=14; % # of high guard subcarriers
Ngen=28;

m=2; % it is used for cyclic prefix calculations. it could be:
      % m=2 G=1/4
      % m=3 G=1/8
      % m=4 G=1/16
      % m=5 G=1/32
G=1/2^m; % Cyclic prefix
CPx=G*FFT;

M=16; % range of symbols

% bits per sub carrier:

%      BPSK  1  M = 2*1=2    1 0
%      QPSK  2  M = 2*2=4    00 10 01 11
%      16QAM 4  M = 2*4=16   0000 0001 ... 1111
%      64QAM 6  M = 2*6=64   000000 000001 ... 111111

% vector initialization
X=zeros(Ndata,1);
Y1=zeros(Ndata,1);
Y2=zeros(Ndata,1);
Y3=zeros(FFT,1);
Y4=zeros(FFT,1);
Y5=zeros(Nfr*(FFT+CPx),1);
Y=zeros(1,Nfr*(FFT+CPx));
NGL=zeros(Ngl,1);
NGH=zeros(Ngh,1);
NGEN=zeros(Ngen,1);

% random integer generation by M kinds
X = randint(Ndata, 1, M);

% digital symbol mapped as analog symbol
Map = modmap(X, 1, 1, 'qask', M);

```

```

I1=Map(:,1);           % selection of the 1st column of the matrix
Q1=Map(:,2);           % selection of the 2nd column of the matrix
C1=I1.^2+Q1.^2;        % C1 - sum of the squares I1 and Q1

U=mean(C1);            % mean C1
V=sqrt(U);             % square root from U
I=I1/V;                % In order to have mean(I^2+Q^2)=1
Q=Q1/V;                % In order to have mean(I^2+Q^2)=1
Y1=[I Q];

% covert to the complex number
Y2=Y1;

for i=0:(Nfr-1)

    Y3=zeros(FFT,1);
    Y4=zeros(FFT,1);

    % insert guard low and guard high and guard DC into data vector
    %Y3=[NGL;Y2(i*Ns+1:Ns/2+i*Ns,1);0;Y2(Ns/2+1+i*Ns:Ns+i*Ns,1);NGH];
    Y3=[Y2(i*Ns+1:Ns/2+i*Ns,1);NGEN;Y2(Ns/2+1+i*Ns:Ns+i*Ns,1)];

    % IFFT from frequency to time transition
    Y4=ifft(Y3);

    % adding cyclic prefix (from the end of time vector to the
    beginning)
    Y5(i*(FFT+CPx)+1:CPx+i*(FFT+CPx),1)=Y4(FFT-CPx+1:FFT,1);

    Y5(CPx+i*(FFT+CPx)+1:FFT+CPx+i*(FFT+CPx),1)=Y4;

end;

% filtering
%nsamp=4;

Y5=rcosflt(Y5,1,4,'fir/sqrt',0.25,10);

BB1=Y5(:,1);
BB2=Y5(:,2);

I2=BB1';
Q2=BB2';

```

## De-modulating 64-OFDM 16-QAM signal

```

function [out1]=OFDM_demod1(Y) % Definition of a function with input
variable Y and output variable out1

out1=Y;

% 16QAM 64OFDM
% FFT=64 => modulated_data_per_OFDM_frame = 64 - Guard_high -
Guard_low= 64-13-14-1 = 36 symbols

% then binary data per OFDM frame is 4*36 = 144 (because 16QAM gives
4 bits per carrier)

Ndata=360; % # of all transmitted data
Ns=36;     % # of data symbols per OFDM frame
Nd=144;    % # of data bits per OFDM frame

% how many frames needed for this amount of data
Nfr=Ndata/Ns; % Nfr=chastnoe(Ndata/Ns)+1

FFT=64;    % FFT size. it can be:
           % FFT = 64
           % FFT = 128
           % FFT = 256
           % FFT = 512
           % FFT = 1024
           % FFT = 2048

Fd=1;      % sampling rate before filtering
Fs=4;      % sampling rate after filtering
fd=0;      % fd = filter delay

rate=3/4;  % coding rate. it can be:
           % rate = 1/2
           % rate = 2/3
           % rate = 3/4

n=8/7;     % sampling factor

Nc=Nd/n;   % # of coded bits per OFDM symbol

Np=8;      % # of pilot subcarriers

Ngl=13;    % # of low guard subcarriers
Ngh=14;    % # of high guard subcarriers
Ngen=28;

m=2;      % it is used for cyclic prefix calculations. it could be:
           % m=2   G=1/4
           % m=3   G=1/8
           % m=4   G=1/16
           % m=5   G=1/32

```

```
G=1/2^m;      % Cyclic prefix
CPx=G*FFT;

M=16;         % range of symbols

Y6=Y';

for ii=0:Nfr-1

    Y7=zeros(FFT,1);
    Y8=zeros(FFT,1);
    Y7=Y6(ii*(fd+CPx+FFT)+1+fd+CPx:ii*(fd+CPx+FFT)+fd+CPx+FFT,1);
    Y8=fft(Y7,FFT);
    Y9(ii*Ns+1:ii*Ns+Ns/2,1)=Y8(1:Ns/2,1);
    Y9(ii*Ns+Ns/2+1:ii*Ns+Ns,1)=Y8(Ns/2+Ngen+1:Ns/2+Ngen+Ns/2,1);

end;

figure(2);
plot(Y9, '.');
```

# APPENDIX-B

## Data Sheets for the Power Amplifiers

### Coaxial Amplifier

### ZFL-500

50Ω Low Power 0.05 to 500 MHz



SMA version shown

CASE STYLE: Y460

#### Features

- wideband, 0.05 to 500 MHz
- rugged, shielded case
- low noise, 5.3 dB typ.
- protected by US Patent, 6,943,629

#### Applications

- instrumentation
- lab use
- VHF/UHF

| Connectors           | Model       | Price   | Qty.  |
|----------------------|-------------|---------|-------|
| SMA                  | ZFL-500     | \$69.95 | (1-9) |
| BNC                  | ZFL-500-BNC | \$74.95 | (1-9) |
| BRACKET (OPTION "B") |             | \$2.50  | (1+)  |

#### Amplifier Electrical Specifications

| MODEL NO. | FREQUENCY (MHz) |       | GAIN (dB) |               | MAXIMUM POWER (dBm)  |                   |              | DYNAMIC RANGE  |     | VSWR (:1) Typ. |               | DC POWER          |  |
|-----------|-----------------|-------|-----------|---------------|----------------------|-------------------|--------------|----------------|-----|----------------|---------------|-------------------|--|
|           | $f_l$           | $f_u$ | Min.      | Flatness Max. | Output (1 dB Compr.) | Input (no damage) | NF (dB) Typ. | IP3 (dBm) Typ. | In  | Out            | Volt (V) Nom. | Current (mA) Max. |  |
| ZFL-500   | 0.05            | 500   | 20        | ±1.0          | L                    | U                 | 5.3          | +18            | 1.9 | 1.9            | 15            | 80                |  |

Open load is not recommended, potentially can cause damage.  
With no load derate max input power by 20 dB

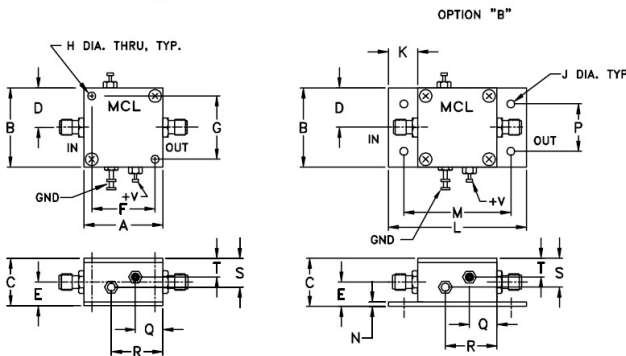
L= low range ( $f_l$  to  $f_l/2$ )

U= upper range ( $f_u/2$  to  $f_u$ )

#### Maximum Ratings

|                       |                |
|-----------------------|----------------|
| Operating Temperature | -20°C to 71°C  |
| Storage Temperature   | -55°C to 100°C |
| DC Voltage            | +17V Max.      |

#### Outline Drawing



#### Outline Dimensions (inch/mm)

|       |       |       |       |       |       |       |      |      |       |
|-------|-------|-------|-------|-------|-------|-------|------|------|-------|
| A     | B     | C     | D     | E     | F     | G     | H    | J    | K     |
| 1.25  | 1.25  | .75   | .63   | .36   | 1.000 | 1.000 | .125 | .125 | .46   |
| 31.75 | 31.75 | 19.05 | 16.00 | 9.14  | 25.40 | 25.40 | 3.18 | 3.18 | 11.68 |
| L     | M     | N     | P     | Q     | R     | S     | S    |      | wt.   |
| 2.18  | 1.688 | .06   | .750  | .50   | .80   | .45   | .29  |      | grams |
| 55.37 | 42.88 | 1.52  | 19.05 | 12.70 | 20.32 | 11.43 | 7.37 |      | 38    |



INTERNET <http://www.minicircuits.com>

P.O. Box 350166, Brooklyn, New York 11235-0003 (718) 934-4500 Fax (718) 332-4661

Distribution Centers NORTH AMERICA 800-654-7949 • 417-335-5935 • Fax 417-335-5945 • EUROPE 44-1252-832600 • Fax 44-1252-837010

Mini-Circuits ISO 9001 & ISO 14001 Certified

# Coaxial Amplifier

## ZHL-1042J

50Ω Medium Power 10 to 4200 MHz

### Features

- wideband, 10 to 4200 MHz
- high IP3, +30 dBm typ.
- low noise, 6 dB typ.

### Applications

- laboratory
- communication systems



|                  |           |          |       |
|------------------|-----------|----------|-------|
| CASE STYLE: NN92 |           |          |       |
| Connectors       | Model     | Price    | Qty.  |
| SMA              | ZHL-1042J | \$495.00 | (1-9) |

### Electrical Specifications

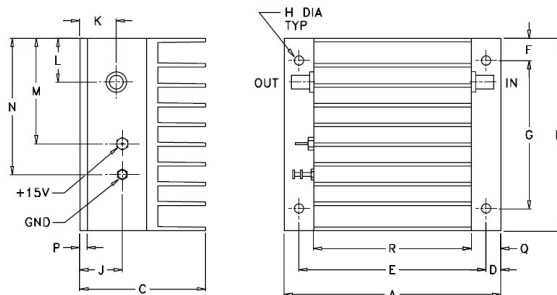
| MODEL NO. | FREQ. (MHz) |       | GAIN (dB) |      |      | MAXIMUM POWER OUTPUT (dBm) |                   | DYNAMIC RANGE |                | VSWR (-1) Typ. |     | DC POWER      |                  |
|-----------|-------------|-------|-----------|------|------|----------------------------|-------------------|---------------|----------------|----------------|-----|---------------|------------------|
|           | $f_c$       | $f_u$ | Typ.      | Min. | Max. | (1 dB Compr.)              | Input (no damage) | NF (dB) Typ.  | IP3 (dBm) Typ. | In             | Out | Volt (V) Nom. | Current (A) Max. |
| ZHL-1042J | 10          | 4200  | —         | 25   | ±1.5 | +20                        | +10               | 6             | +30            | 2.5            | 2.5 | 15            | 0.330            |

Open load is not recommended, potentially can cause damage.  
With no load derate max input power by 20 dB

### Maximum Ratings

|                       |                |
|-----------------------|----------------|
| Operating Temperature | -20°C to 65°C  |
| Storage Temperature   | -55°C to 100°C |
| DC Voltage            | +20V Max.      |

### Outline Drawing



### Outline Dimensions (inch/mm)

|       |       |       |      |       |      |       |      |       |       |       |       |       |      |       |       |       |
|-------|-------|-------|------|-------|------|-------|------|-------|-------|-------|-------|-------|------|-------|-------|-------|
| A     | B     | C     | D    | E     | F    | G     | H    | J     | K     | L     | M     | N     | P    | Q     | R     | wt    |
| 3.66  | 3.25  | 2.13  | .25  | 3.16  | .38  | 2.50  | .156 | .72   | .64   | .74   | 1.78  | 2.30  | .125 | .50   | 2.66  | grams |
| 92.96 | 82.55 | 54.10 | 6.35 | 80.26 | 9.65 | 63.50 | 3.96 | 18.29 | 16.26 | 18.80 | 45.21 | 58.42 | 3.18 | 12.70 | 67.56 | 440.0 |



P.O. Box 350166, Brooklyn, New York 11235-0003 (718) 934-4500 Fax (718) 332-4661 For detailed performance specs & shopping online see Mini-Circuits web site



The Design Engineers Search Engine Provides ACTUAL Data Instantly From MINI-CIRCUITS At: [www.minicircuits.com](http://www.minicircuits.com)

RF/IF MICROWAVE COMPONENTS

REV OR  
M69088  
ZHL-1042J  
070510  
Page 1 of 2

## APPENDIX-C

### Experimental Signal Generation

#### Pseudorandom Sequence PN9

The pseudorandom sequence PN9 consists of 512 bits, which are given below in the binary and hexadecimal formats. The sequence is pre-programmed in the ESG E4433B and used for representing the signal source binary data during experiments.

PN9 in the Hexadecimal Format

|            |   |   |   |   |   |   |   |   |
|------------|---|---|---|---|---|---|---|---|
| <b>0</b>   | F | F | 8 | 3 | D | F | 1 | 7 |
| <b>20</b>  | 3 | 2 | 0 | 9 | 4 | E | D | 1 |
| <b>40</b>  | E | 7 | C | D | 8 | A | 9 | 1 |
| <b>60</b>  | C | 6 | D | 5 | C | 4 | C | 4 |
| <b>80</b>  | 4 | 0 | 2 | 1 | 1 | 8 | 4 | E |
| <b>A0</b>  | 5 | 5 | 8 | 6 | F | 4 | D | C |
| <b>C0</b>  | 8 | A | 1 | 5 | A | 7 | E | C |
| <b>E0</b>  | 9 | 2 | D | F | 9 | 3 | 5 | 3 |
| <b>100</b> | 3 | 0 | 1 | 8 | C | A | 3 | 4 |
| <b>120</b> | B | F | A | 2 | C | 7 | 5 | 9 |
| <b>140</b> | 6 | 7 | 8 | F | B | A | 0 | D |
| <b>160</b> | 6 | D | D | 8 | 2 | D | 7 | D |
| <b>180</b> | 5 | 4 | 0 | A | 5 | 7 | 9 | 7 |
| <b>1A0</b> | 7 | 0 | 3 | 9 | D | 2 | 7 | A |
| <b>1C0</b> | E | A | 2 | 4 | 3 | 3 | 8 | 5 |
| <b>200</b> | E | D | 9 | A | 1 | D | E | 1 |

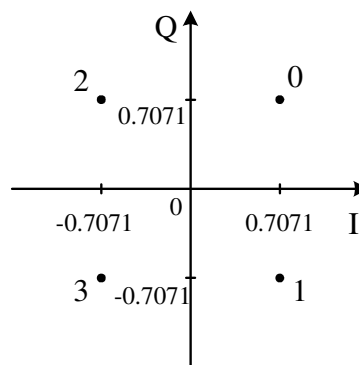
PN9 in the Binary Format (Transposed)

| 0 | 20 | 40 | 60 | 80 | A0 | C0 | E0 | 100 | 120 | 140 | 160 | 180 | 1A0 | 1C0 | 200 |
|---|----|----|----|----|----|----|----|-----|-----|-----|-----|-----|-----|-----|-----|
| 1 | 0  | 1  | 1  | 0  | 0  | 1  | 1  | 0   | 1   | 0   | 0   | 0   | 0   | 1   | 1   |
| 1 | 0  | 1  | 1  | 1  | 1  | 0  | 0  | 0   | 0   | 1   | 1   | 1   | 1   | 1   | 1   |
| 1 | 1  | 1  | 0  | 0  | 0  | 0  | 0  | 1   | 1   | 1   | 1   | 0   | 1   | 1   | 1   |
| 1 | 1  | 0  | 0  | 0  | 1  | 0  | 1  | 1   | 1   | 0   | 0   | 1   | 1   | 0   | 0   |
| 1 | 0  | 0  | 0  | 0  | 0  | 1  | 0  | 0   | 1   | 0   | 1   | 0   | 0   | 1   | 1   |
| 1 | 0  | 1  | 1  | 0  | 1  | 0  | 0  | 0   | 1   | 1   | 1   | 1   | 0   | 0   | 1   |
| 1 | 1  | 1  | 1  | 0  | 0  | 1  | 1  | 0   | 1   | 1   | 0   | 0   | 0   | 1   | 0   |
| 1 | 0  | 1  | 0  | 0  | 1  | 0  | 0  | 0   | 1   | 1   | 1   | 0   | 0   | 0   | 1   |
| 1 | 0  | 1  | 1  | 0  | 1  | 0  | 1  | 0   | 1   | 1   | 1   | 0   | 0   | 0   | 1   |
| 0 | 0  | 1  | 1  | 0  | 0  | 0  | 1  | 0   | 0   | 0   | 1   | 0   | 0   | 0   | 0   |
| 0 | 0  | 0  | 0  | 1  | 0  | 0  | 0  | 0   | 1   | 0   | 0   | 0   | 1   | 1   | 0   |
| 0 | 0  | 0  | 1  | 0  | 0  | 1  | 1  | 1   | 0   | 0   | 1   | 0   | 1   | 0   | 1   |
| 0 | 1  | 1  | 0  | 0  | 0  | 0  | 1  | 1   | 0   | 1   | 1   | 1   | 1   | 0   | 1   |
| 0 | 0  | 1  | 1  | 0  | 1  | 1  | 1  | 0   | 0   | 1   | 0   | 0   | 0   | 1   | 0   |
| 1 | 0  | 0  | 0  | 0  | 1  | 0  | 1  | 0   | 1   | 1   | 0   | 1   | 0   | 0   | 1   |
| 1 | 1  | 1  | 1  | 1  | 0  | 1  | 1  | 0   | 0   | 1   | 0   | 0   | 1   | 0   | 0   |
| 1 | 0  | 1  | 1  | 0  | 1  | 1  | 1  | 1   | 1   | 1   | 0   | 0   | 1   | 0   | 0   |
| 1 | 1  | 0  | 1  | 0  | 1  | 0  | 0  | 1   | 1   | 0   | 0   | 1   | 1   | 0   | 0   |
| 0 | 0  | 0  | 0  | 0  | 1  | 1  | 0  | 0   | 0   | 1   | 1   | 0   | 0   | 1   | 0   |
| 1 | 0  | 0  | 0  | 1  | 1  | 0  | 1  | 0   | 0   | 1   | 0   | 1   | 1   | 1   | 1   |
| 1 | 1  | 1  | 0  | 1  | 0  | 0  | 0  | 1   | 0   | 1   | 1   | 0   | 0   | 0   | 1   |
| 1 | 1  | 0  | 1  | 0  | 1  | 1  | 0  | 0   | 1   | 0   | 1   | 1   | 0   | 0   | 1   |
| 1 | 1  | 1  | 0  | 0  | 0  | 1  | 1  | 1   | 1   | 1   | 0   | 1   | 1   | 1   | 0   |
| 1 | 0  | 0  | 0  | 0  | 0  | 1  | 1  | 0   | 1   | 0   | 1   | 1   | 0   | 1   | 1   |
| 0 | 1  | 1  | 1  | 0  | 1  | 1  | 0  | 0   | 0   | 0   | 0   | 1   | 0   | 1   | 1   |
| 0 | 1  | 0  | 1  | 1  | 1  | 1  | 1  | 0   | 1   | 0   | 1   | 0   | 1   | 0   | 1   |
| 0 | 0  | 0  | 0  | 0  | 0  | 1  | 0  | 1   | 0   | 0   | 1   | 0   | 1   | 0   | 1   |
| 1 | 1  | 1  | 0  | 0  | 1  | 0  | 1  | 1   | 1   | 0   | 1   | 1   | 1   | 0   | 0   |
| 0 | 0  | 0  | 0  | 1  | 1  | 1  | 0  | 0   | 1   | 1   | 1   | 0   | 1   | 0   | 0   |
| 1 | 0  | 0  | 1  | 1  | 1  | 1  | 0  | 1   | 0   | 1   | 1   | 1   | 0   | 1   | 0   |
| 1 | 0  | 0  | 0  | 1  | 0  | 0  | 1  | 0   | 0   | 0   | 0   | 1   | 1   | 0   | 0   |
| 1 | 1  | 1  | 0  | 0  | 0  | 0  | 1  | 0   | 1   | 1   | 1   | 1   | 0   | 1   | 1   |

## QPSK and 16-QAM Mapping

QPSK Map

| <b>S</b> | <b>I</b> | <b>Q</b> |
|----------|----------|----------|
| 0        | 0.7071   | 0.7071   |
| 1        | 0.7071   | -0.7071  |
| 2        | -0.7071  | 0.7071   |
| 3        | -0.7071  | -0.7071  |



16-QAM Map

| <b>S</b> | <b>I</b> | <b>Q</b> |
|----------|----------|----------|
| 0        | 0.3203   | 0.3203   |
| 1        | 0.9608   | 0.3203   |
| 2        | 0.3203   | 0.9608   |
| 3        | 0.9608   | 0.9608   |
| 4        | 0.3203   | -0.3203  |
| 5        | 0.3203   | -0.9608  |
| 6        | 0.9608   | -0.3203  |
| 7        | 0.9608   | -0.9608  |
| 8        | -0.3203  | 0.3203   |
| 9        | -0.3203  | 0.9608   |
| A        | -0.9608  | 0.3203   |
| B        | -0.9608  | 0.9608   |
| C        | -0.3203  | -0.3203  |
| D        | -0.9608  | -0.3203  |
| E        | -0.3203  | -0.9608  |
| F        | -0.9608  | -0.9608  |

